Photoconductivity, Noise, and related phenomena in some amorphous chalcogenide semiconductors

by

C. MAIN

Thesis presented for the degree of Doctor of Philosophy of the University of Edinburgh in the Faculty of Science.

December 1973

ACKNOWLEDGEMENTS

I should like to express my thanks to Dr. Alan E. Owen, for his foresight, guidance and encouragement throughout the course of this work.

The assistance of the technical staff of the Department of Electrical Engineering is gratefully acknowledged.

I should also like to thank Dr. J.M. Marshall, for many enlightening and critical discussions, and to express my appreciation to colleagues in the Department for their friendship and assistance.

The financial assistance provided by the Science Research Council is gratefully acknowledged.

I am grateful to Mrs. Helen McKeating for her excellent setting out and typing of the text.

Finally, I should like to thank my wife Sandra for her patience and understanding during the writing of the thesis, especially in the last few months.

(ABSTRACT)

Measurements of photoconductivity and noise in two representative amorphous chalcogenide compounds, As_2Te_3 and As_2Se_3 were made, in conjunction with standard optical and electrical studies. Such measurements can give detailed information on carrier transport, kinetics, and the distribution of electron states in these materials.

A general review of band structure and electrical properties of amorphous semiconductors is given, with particular reference to the chalcogenides.

The salient features of photoconductivity in the chalcogenides are described, and a general approach to the problem is described and developed, for a photoconductor with arbitrary trap distribution. The analysis is applied in this work to a simple discrete trap model in an 'Occam's razor' approach. Other models, involving continuous distributions of localised states, are reviewed.

An account is given of the design and operation of the experimental systems employed in the study of steady state and transient photoconductivity. Extensive use is made of convenient semiconductor optical sources (e.g. a GaAs laser).

The general features of semiconductor noise are reviewed, and an expression for the generation-recombination noise spectrum is developed for the same discrete trap model, which illustrates why the chalcogenide glasses have

an apparently low noise. Experimental considerations are reviewed, and the measurement of noise spectra is described.

Experimental results on optical, electrical, photoconductive and noise properties are presented and discussed. The interpretations for As_2Te_3 and As_2Se_3 are similar. Several groups of localised states, within the mobility gap, are identified and characterised and their roles in trapping and recombination are discussed. The effects of applied electric field on transport are discussed in terms of band and hopping conduction.

CONTENTS

Page

8. AMORPHOUS As_2Te_3 : EXPERIMENTAL RESULTS AND DISCUSSION.

CHAPTER 1

INTRODUCTION

1.1 THE STUDY OF AMORPHOUS SEMICONDUCTORS

Since the advent of quantum mechanics, the field of crystalline semiconductors in particular has received much attention, resulting in a large body of well established theory, and a wide range of applications for semiconductor devices.

The theoretical approach for the behaviour of electrons in such materials is facilitated by the periodicity of a perfect crystal structure. The theory demonstrates that there exist bands of allowed energy for electrons extending throughout the crystal, separated by forbidden gaps, and describes the distribution of electrons in these bands.

Little modification is required for the theory to cope with small departures from perfect periodicity in real crystals, associated with lattice vibrations and structural imperfections such as dislocations and impurities, although such defects profoundly influence electron transport, by scattering and trapping.

The optical and electrical properties of crystalline semiconductors vary over a wide range. Conductivities, usually temperature dependent, lie between 10^{2} and 10^{-10} $Ohm^{-1}\ m^{-1}$, while carrier mobilities are found between 10^{-6} and $10^{-1}\ m^{2}\ V^{-1}\ s^{-1}$, or greater, and bandgaps, between 0.2 and 2.0 eV.

There exists, however, a large group of disordered materials, including non-crystalline solids, and liquids, which exhibit many typical semiconducting characteristics, and for which there is, as yet, no complete theoretical framework.

A rough but convenient classification of such materials is into two groups : amorphous chalcogenides and amorphous transition metal oxides. The chalcogenides consist in general of combinations of S, Se, or Te with Si, Ge, P, As, Sb, Bi, Tl, Pb, etc., while the second group contains a transition metal oxide as a major constituent - e.g. V_2O_5, Fe_2O_3, MnO, etc. Other materials not included above can also be prepared in non-crystalline form - the elements Si, Ge, C, and others. This work is concerned with materials in the chalcogenide group.

A distinction should be made between the descriptions 'vitreous' or 'glassy', and 'amorphous'. The former refers to solids which can be prepared in bulk form, by cooling from the melt without crystallisation. Such materials may be expected to reflect in their structure, that of the liquid, though this is not always the case. At any rate the thermal history and characteristic parameters, such as a glass transition temperature, T_g can be fairly well defined. Some materials e.g. Si, Ge, can only be prepared in disordered form by deposition from vapour, as thin films, where the description 'amorphous' is more appropriate, and a relationship with some liquid structure is not well defined.

Most materials which can be prepared in bulk glassy form can also be prepared in disordered form by vapour deposition, and this includes the materials studied in this work. Although in many cases the thin films have similar structural properties and exhibit behaviour similar to bulk prepared samples - e.g. thermal behaviour with a 'glass transition', they are probably not identical. Hence the vapour deposited films used in this work will be described as amorphous.

Structural studies of many vitreous and amorphous materials - e.g. of the radial distribution function (r.d.f.), have shown that there is usually considerable 'short range order' over a few interatomic distances, and the local environment of a given atom is often similar to that in the analogous crystal, if it exists. Long range order, over many interatomic distances, is not preserved, however.

An electronic theory for those materials must explain the existence of an electron band structure in non-periodic lattices - e.g. as evidenced by optical properties. Furthermore, transport studies indicate very short carrier mean free paths, shorter than a free electron wavelength, and of the order of an interatomic spacing, which makes the application of existing band theory less than certain.

It is now generally agreed that the existence of short range order can result in a band structure, in many cases similar to that of the crystalline modification, but that the lack of long range order can introduce tails of localised states of high density extending into the

forbidden gap. The form and extent of this distribution, and the nature of the states, is still a matter for debate, however, and hence constitutes an important field for research.

The presence of a high density of localised states can greatly influence the electrical properties of amorphous semiconductors. The disorder which gives rise to them will greatly increase scattering effects for carriers in extended states. The transport of these 'free' carriers can be interrupted by trapping in localised states, thus drastically reducing the effective drift velocity. Transport can also occur by carriers hopping between localised states, with a much lower mobility than in extended states.

Some of the most important questions which arise concern the distinction between extended and localised states and the energy region in the density of states where the transition between the two occurs. Does the carrier mobility drop sharply or smoothly with decreasing energy? How do carriers behave in barely delocalised states, where the mean free path is very short?

Another important point is the relative insensitivity of electrical properties of amorphous semiconductors to impurities. Small amounts of impurities have marked effects on the electrical properties of crystalline semiconductors, but with a few exceptions, this is not the case in amorphous semiconductors. An explanation for this is that the 'dopant' atoms can easily have their valence requirements satisfied in the environment of a disordered material, and

hence do not give rise to defect levels.

Nevertheless much of the experimental evidence suggests, especially in the simpler 'compound' chalcogenides, that there may exist fairly discrete levels of localised states associated perhaps with quite well defined structural defects. Such states may serve to 'pin' the Fermi level in many materials, or may also appear against the background of the tails of states.

Experimental investigations aimed at deducing band structure and transport mechanisms are therefore essential to provide a framework upon which theory can be tested and built.

1.2 NON EQUILIBRIUM PROPERTIES OF SEMICONDUCTORS

The thermal equilibrium distribution of electrons among the available states in a semiconductor is described by Fermi-Dirac statistics, and relies on electron transitions between the states, i.e. it is a dynamic equilibrium. Some powerful methods of investigating the band structure and carrier transport in semiconductors involve a study of the behaviour when there are departures from this equilibrium.

The introduction of localised states generally alters the detailed nature of this equilibrium to a great extent, and methods which disturb the equilibrium will reveal their presence. The transitions involved may be loosely grouped under headings; generation, recombination, trapping, and trap release. While in a 'trap-free' semiconductor, recombination of electrons and holes occurs via a band-band

transition, in the presence of even a small localised state density, recombination via localised states may predominate. The presence of a large 'reservoir' of trapped carriers can also slow down or add an 'inertia' to the kinetics.

The nature of the electron distribution can be understood and investigated on three levels, involving increasingly fundamental concepts. Firstly, the values given by the Fermi function, are merely time averages, e.g. of carrier densities, which can be observed in conductivity measurements. At the second level, the transition kinetics, described by mass-action laws, which produce the steady state or equilibrium distribution, can be studied by photoconductivity techniques.

Thirdly, the statistical nature of the transition processes, which results in the macroscopic mass-action law description can be investigated by noise measurements.

In photoconductivity measurements, disequilibrium is produced by excess optical excitation, (normally band-band) of electrons and holes. A new steady state distribution is reached which can be partly monitored by conductivity measurements i.e. the density of those carriers responsible for conduction. If the excitation is modulated, further information on transition kinetics can be obtained from the time dependence of photocurrent. Spatial effects and transport can also be investigated more directly, using inhomogeneous excitation.

The statistical nature of the processes leading to equilibrium (or steady state) can result in fluctuations

in the electron distribution about the average and hence conductivity fluctuations, generally termed 'generation-recombination noise'. (Other types of noise - e.g. shot noise, will not be considered in detail here). Strictly speaking, in the absence of excess generation, this is not a non-equilibrium property, but the same physical concepts and mathematical formalism can be used to analyse these naturally occurring departures from the average electron distribution. The information obtained from noise measurements can therefore be used to augment that from photoconductivity studies.

1.3 PHOTOELECTRIC PROPERTIES AND APPLICATIONS OF AMORPHOUS SEMICONDUCTORS

Amorphous semiconductors exhibit a wide range of optical and photoelectric properties, also observed in crystalline semiconductors, which can be used to investigate the fundamental electronic parameters of the materials, and which have also led to a number of important applications.

Such properties include photoconductivity, photoluminescence, barrier and bulk photovoltages and internal and external photoemission. All of those have been used to probe the nature and density of states in a number of materials.

Two of the most important applications at present are in electrophotography - e.g. the 'Xerox' process, and in television 'Vidicon' storage tubes. Here, the photoconducting properties of some of the more insulating materials, such as Se, As_2Se_3, Sb_2S_3, are used. Hence, a

great deal of research is being done on the photoconductive properties of these materials with a view to applications as well as from a fundamental point of view.

1.4 SWITCHING APPLICATIONS AND RELATED PHENOMENA

Recently, the observation of switching phenomena in devices utilising a number of amorphous chalcogenides or oxide glasses, has aroused considerable attention and provoked a great deal of fundamental and applied research. The basic 'amorphous switch' is a two terminal device which can be switched reversibly (threshold operation) or bi-stably (memory operation) between a high (OFF) and a low (ON) resistance, by application of suitable voltage or current pulses.

Such devices can be used in a number of applications such as controlling electroluminescent panel displays, or as computer memory elements. The use of amorphous semiconductors in electronic devices has a number of advantages over crystalline semiconductors. Sophisticated crystal growing and doping techniques are not required, especially as amorphous semiconductors are normally insensitive to impurities. The inbuilt disorder also results in resistance to radiation damage.

The mechanism of threshold switching, whether electronic, thermal, or a combination of the two, is still a matter for debate, although it is clear that bistable switching involves reversible structural transformations between amorphous and crystalline states.

Structural alterations can also be induced optically and several new applications utilise this property, in electrophotography ('Ovography') and in laser addressed optical memories.

1.5 THE PURPOSE OF THE PRESENT WORK

The aim of this project was to develop and utilise photoconductivity and noise techniques for the study of band structure, carrier kinetics, and transport in amorphous semiconductors.

The materials chosen for the research were simple prototype 'compound' chalcogenides, As_2Se_3 and As_2Te_3 which serve as a better starting point for interpretation of results than the more complex multicomponent alloys. Furthermore, the two materials have significantly different properties, and could be described as representative of the two ends of the 'spectrum' of chalcogenides.

As_2Se_3 is a wide-gap semi-insulator, typical of the photoconductors used in electrophotography, while the relatively conducting As_2Te_3, although not a good switching material, is similar in many respects to typical switching alloys.

The research carried out, therefore, could hopefully help in understanding both the fundamental electronic properties of the materials, and the mechanisms involved in their applications.

A number of different models for photoconductivity in amorphous chalcogenides have been proposed. In the present work it was hoped that standard techniques could be

used, with some novel aspects, such as the use of semiconductor light sources - in a consistent way to test the validity of these models for the selected materials. Parameters such as carrier lifetimes, mobilities, and trap densities could then be extracted from experimental data.

Previous reports of noise in amorphous or vitreous chalcogenides give little information other than phenomenological aspects. It was hoped that noise studies could prove more fruitful than this, and augment or corroborate the interpretation of photoconductivity data.

CHAPTER 2

ENERGY BANDS, CONDUCTION AND STRUCTURE OF AMORPHOUS SEMICONDUCTORS

2.1 CRYSTALLINE SEMICONDUCTORS

2.1.1 BAND THEORY OF CRYSTALLINE SOLIDS

The application of wave mechanics to the problem of electrons in solids has provided the basis for the interpretation of thermal, optical, and electrical properties of semiconductors, in terms of 'band-theory'.

The form and restrictions on one electron wave functions in perfect periodic lattices can be obtained by solution of the Schrodinger wave equation and the Bloch theorem predicting solutions with the periodicity of the lattice. Two contrasting approaches have been employed - the 'tight binding' and 'nearly free electron' models.

In the tight binding approach the starting point is an isolated atom of the material, with the electrons arranged in specific configurations in a series of discrete allowed energies, around the nucleus. Interaction occurs between neighbouring atoms in the solid and the wave functions associated with individual atoms overlap. Tight binding theory assumes weak interaction and shows how the atomic wave functions'discrete energy levels - particularly for outer electrons, become spread into quasi continua or allowed bands, separated by forbidden regions.

The 'nearly free' electron model assumes strong interaction and large overlap of atomic wave functions. The allowed electron energies are quite different from the

atomic eigenvalues. In this treatment, the periodic potential of the ion cores (together with the average electron cloud potential) is small compared to the total energy of the electron. Again allowed and forbidden bands result. Both approaches are approximations and the choice of one or the other depends on the material in question.

The form of the bands - in particular the relation between electron energy E, and propagation constant or wave number k depend in detail on the lattice structure involved. In many cases there is a parabolic relation between E and k at the band edges and electrons in these states behave like free electrons in an electric field, but with an effective mass m^* not in general equal to the free electron mass.

The distribution of allowed electron states with energy is denoted by the function g(E) where g(E)dE is the volume density of states in the range E to E + dE. For free particles the parabolic E-k relation (in 2-dimensions) leads to a simple result

$$g(E) = \frac{8\sqrt{2\pi}}{h^3} \, m^{\frac{3}{2}} \, E^{\frac{1}{2}} \, m^{-3} \, J^{-1} \qquad 2.1.1$$

The form of g(E) in crystalline solids again depends on the lattice structure, but for parabolic band edges, the density of states near the edges is similar to that for free particles. Figure 2.1 shows schematically the form of g(E) for a simple cubic lattice.

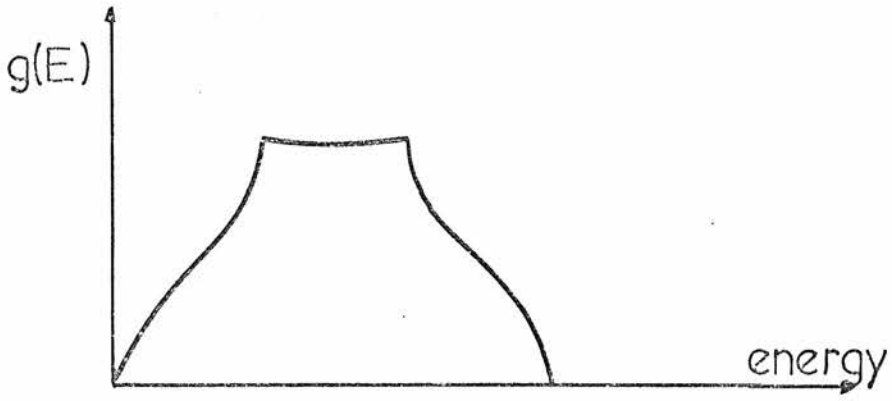

Fig 2.1 Simple cubic lattice. Density of states

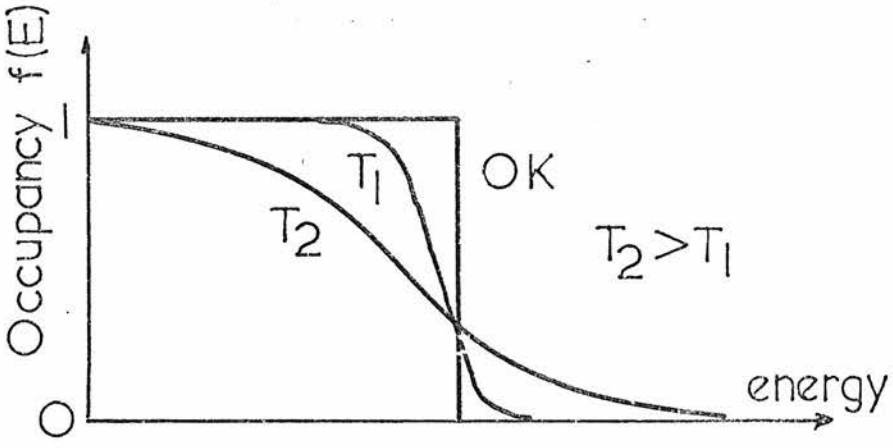

Fig 2.2 Fermi-Dirac Distribution function

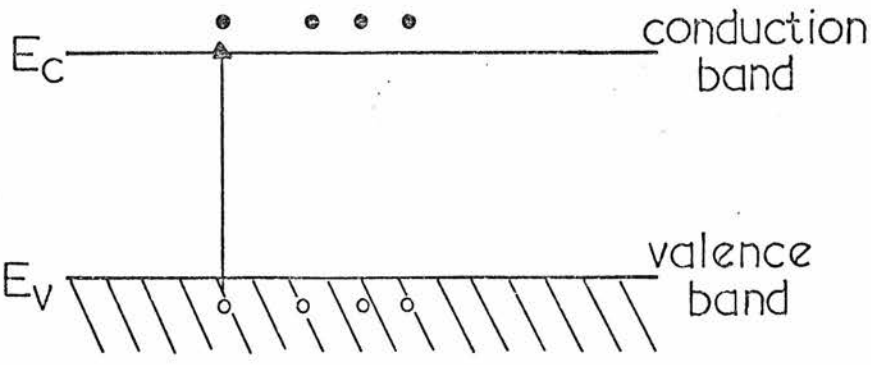

Fig 2.3 Charge carriers in an Intrinsic Semiconductor

2.1.2 THE FERMI DIRAC DISTRIBUTION

The available electrons in a solid in thermal equilibrium are distributed among the allowed states (extended and localised) according to Fermi-Dirac statistics. These statistics are appropriate to electrons as indistinguishable particles, occupying states in accordance with the Pauli exclusion principle, which allows each quantum state to accept only one electron. The occupation probability $f_o(E)$ for a given state of energy E, is

$$f_o(E) = \frac{1}{1 + \exp\left(\frac{E - E_F}{kT}\right)} \qquad 2.1.2$$

where E_F is the equilibrium Fermi level (at which $f_o(E) = \frac{1}{2}$) k is Boltzmann's constant, and T the absolute temperature. Thus in a distribution of states g(E), the density of occupied states n(E)dE within the range E to E + dE, can be written

$$n(E)dE = g(E)\, f_o(E)dE \qquad 2.1.3$$

At OK, all the states below E_F are occupied, and all those above, are empty. The value of E_F itself is temperature dependent, and the relation depends upon the form of the density of states, which through charge conservation requires that for all allowed energies

$$\int g(E)\, f_o(E)dE = \text{constant (all temperatures)} \qquad 2.1.4$$

i.e. asymmetry in g(E) will cause E_F to shift from its zero temperature position at T > 0. A further implicit temperature dependence arises from the effects of thermal expansion on the band structure often causing a decrease in allowed band separation with temperature.

Figure 2.2 illustrates the form of the equilibrium Fermi function for several temperatures. The 'step' form at OK is shown, while at higher temperatures the variation is shallower, and E_F may shift.

The detail of the processes whereby the equilibrium distribution is attained - i.e. by electron transitions between states, will be discussed later in chapter 3. For example, at temperatures greater than OK electrons can be excited into previously empty states (above E_F) by interaction with lattice vibrations or absorption of black-body radiation.

Electronic transport properties, under the influence of an applied electric field, involve a redistribution of electrons, which cannot occur in a full band. In semiconductors and insulators at OK, there are no partially full bands as in metals. The highest full band, the valence band, associated with bonding states, is separated from the lowest empty band, the conduction band, by a forbidden gap - i.e. E_F lies in this gap at OK.

Figure 2.3 illustrates schematically the electron distribution at finite temperature. In a semiconductor the band-band excitation provides a limited number of free electrons in the conduction band, and the empty states left in the valence band contribute to current flow, as

positive charge carriers or holes. The hole distribution can be described in a similar way to the electron distribution, using the complement of the Fermi function $\bar{f}_o(E) = [1 - f_o(E)]$.

The case described is that of an 'intrinsic' semiconductor. The presence of impurities or defects can introduce states into the band scheme which can significantly alter the electron distribution, giving rise to 'extrinsic' behaviour.

2.1.3 LOCALISED STATES

Localised states, for which the electron wave function does not extend throughout the crystal, occur for a number of reasons. Substitutional atoms of different valency than those which they replace, interstitial atoms and vacancies, are all common in crystalline semiconductors and give rise to localised states whose energy falls in the normally forbidden gap.

The 'defect' distorts the perfect periodicity of the lattice and can produce a region of lower potential energy for an electron or hole in its vicinity, resulting in a state sufficiently displaced from the allowed band as to lie in the forbidden gap.

For example, group V impurity atoms in crystalline Ge or Si, introduce monovalent 'donor' centres near the conduction band, which can be ionised to produce free electrons at temperatures at which intrinsic excitation is negligible.

Vacancies and interstitials can also result in localised states, where valence bonds are unsatisfied.

Such states as those mentioned above, often present a Coulomb attractive inverse square potential for the relevant carrier when they are not occupied by that carrier, hence in this state they may be described as 'Coulombic' centres. Other potential configurations are possible, however. For example, some centres associated with impurities such as Ni, Co, Fe, in Ge may, when neutral, present a moderately long range inverse fourth power potential, caused by interaction between a carrier and the polarisability of the centres[1].

Since the structural defects in crystals discussed above are usually well defined deviations from the fundamental lattice structure, the localised states will have well defined properties. For example, they may all lie at roughly the same energy, giving rise to a 'discrete level' of localised states within the gap.

The equilibrium occupancy function of equation 2.1.2, must be modified somewhat for localised states to take into account spin or orbital degeneracy. In the simplest case of a monovalent state with s-like wave function, the state may trap an electron of either spin ($\pm \frac{1}{2}$), but, having captured one electron, cannot normally capture another. This gives

$$f_o(E) = \frac{1}{1 + \frac{1}{2} \exp\left(\frac{E - E_F}{kT}\right)} \qquad 2.1.5$$

The spin degeneracy factor here, is 2, but can take other values for other types of localised state.

The processes by which the electron distribution is attained when localised states are present have produced a fairly loose nomenclature describing the roles played by the states. A state acts as a recombination centre for a given free carrier, if, having captured the carrier, the probability of capturing the opposite carrier is greater than that of thermal re-emission to the same band. An electron hole pair is therefore annihilated by this process - recombination via a localised state. For a shallow trap, the probability of thermal re-emission is greater than that of capture of an opposite carrier, and the state can be said to be in 'thermal contact' with one band. There is no qualitative difference between the two, as the difference is only one of relative probabilities[2]. The word 'trap' will be used as a general description, in this work.

A more detailed discussion on the various transitions and phenomenological trap parameters, such as capture cross sections, follows in chapter 3.

2.1.4 CARRIER TRANSPORT

Even in crystalline materials, the perfect periodicity giving rise to Bloch wave functions, does not exist at finite temperatures, due to lattice vibrations and impurities. The wave-function problem is altered to one where Bloch functions take part in scattering processes[3,4]. Electron and hole motion in the bands is interrupted by scattering events and the average distance travelled

between scattering events is the mean free path or shubweg. Analysis of the carrier distribution and behaviour under a perturbing force is effected by the Boltzmann transport equation[5]. Under the influence of an electric field this leads to the concept of free carrier mobility μ_o. In some crystalline semiconductors, e.g. Si, this can be as high as 10^{-1} m^2 V^{-1} s^{-1} or greater, with a shubweg approaching 10^{-6} m.

Apart from conductivity measurements a number of other measurements allow investigation of carrier distribution and transport processes - e.g. Hall effect, Magneto resistance, thermopower.

Localised states, as well as acting as scattering centres can have a drastic effect in their trapping role, on charge transport via extended states. A given carrier or group of carriers will have its motion in extended states interrupted by a series of trapping and release events, and the effective drift velocity will be reduced by the fraction of the time that a carrier is free. Consider a discrete trap level, density N_1, at energy E_1 acting as shallow traps for electrons. If the trapping time is τ_t and the release time τ_{tr}, then an effective trap-limited electron drift mobility μ_{nd} may be defined[6,7]

$$\mu_{nd} = \mu_{no} \frac{\tau_t}{\tau_t + \tau_{tr}} = \mu_{no} \left(1 + \frac{N_1}{N_c} \exp\left(\frac{E_c - E_1}{kT}\right)\right)^{-1} \quad 2.1.6$$

2.2 AMORPHOUS SEMICONDUCTORS

2.2.1 BAND STRUCTURE IN AMORPHOUS SEMICONDUCTORS

That many amorphous materials exhibit semiconductor behaviour and appear to have a forbidden gap as do crystalline semiconductors is evidenced by optical and electrical measurements[8]. Although the theory of electrons in such materials is not yet as advanced as that for crystals, a number of models with some common features have been proposed.

The disorder occurring in glassy and amorphous semiconductors arises from a number of causes. For example, phonons and impurities, structural disorder - e.g. fluctuations in bond length and angle, and compositional disorder in multicomponent materials. These produce spatial and potential fluctuations in the periodic potential environment of the electron.

Structural studies using techniques such as X-ray diffraction have shown that although the 'long range order' over say tens of angstroms, does not exist in amorphous materials, short range order, over a few atomic separations is present.[9] Thus, an atom in the amorphous modification of a substance can have the same co-ordination environment as in the crystal, and the local potential environment of an electron would be similar in both cases. Ioffe and Regel[10] conclude that an electron band-structure depends on short range order and should exist in amorphous materials as in crystals, subject to certain modifications.

Figure 2.4 shows some of the density of states models discussed in the literature. The band edges are no longer well defined, and 'tails' in the density of states extend into the previously forbidden gap. The exact nature and distribution of these states is still the subject of controversy, and it is probable that there is no one general band-structure model for amorphous semiconductors as indeed one does not exist for all crystalline semiconductors.

The consequences of long-range disorder on the band structure have been discussed by a number of authors. Gubanov[12], using a disorder parameter characteristic of the material considered small spatial perturbations in the periodic potential and formally related well-depth fluctuations. Linear combinations of unperturbed Bloch functions give the new solutions. In general, the results obtained show that the allowed bands broaden in energy, and have diffuse edges. Large short-range fluctuations produce large potential deviations and states below the unperturbed band-edge, which are localised.

Cohen[13] discussed, for clarity, density fluctuations in a binary alloy, say AB, where A is the major constituent. and considered the band structures for pure crystalline A and the substitutional alloy AB.

In the amorphous form, spatial fluctuations in the density of B produce states beyond the band edges of the AB crystal, which are localised - i.e. 'tail states'.

Cohen further postulates that, with sufficient disorder, which may occur in the multicomponent chalcogenides,

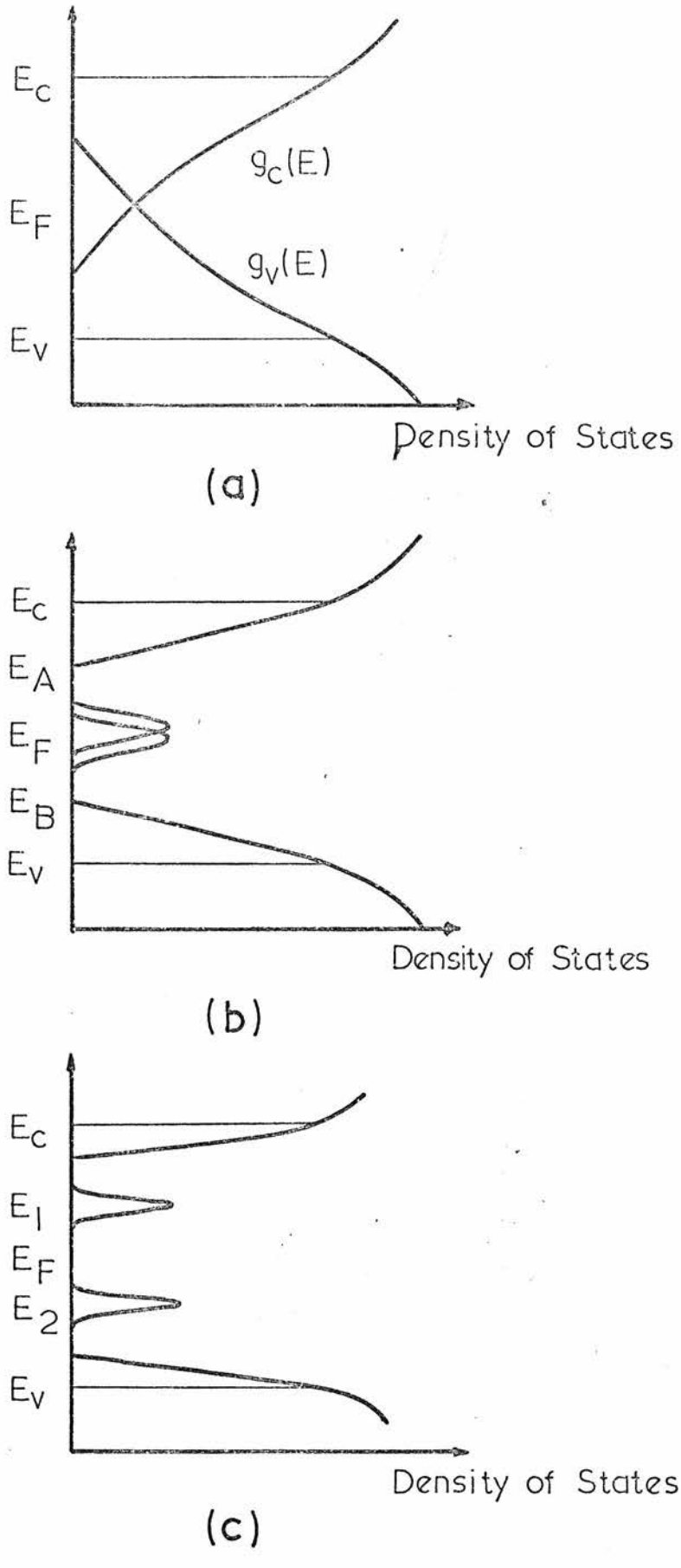

Fig 2.4 Density of States Models

(a) C.F.O.

(b) Mott-Davis

(c) 'Discrete' Levels

the tails of the conduction and valence bands may overlap - see figure 2.4.a. As the tail states retain the charge/occupancy nature of their appropriate 'parent' bands, the equilibrium Fermi level E_F, will be situated near the 'cross-over' with filled (negative) conduction band tail states below E_F, and empty (positive) valence band tail states above E_F. The density of those states at the Fermi level could be as high as 10^{25}-10^{26} m^{-3} eV^{-1}, pinning E_F quite effectively.

Mott[14] has discussed the nature of the electron states in amorphous semiconductors, using the model of a disordered impurity band ('Anderson band')[15] where fluctuation is introduced into the well depth in a periodic array. One form of the criterion for localisation is that electrons in such states do not contribute to the d.c. conductivity at OK, even if E_F lies in the range of these states. Andersons arguments apply to a whole band, and are extended by Mott to demonstrate that below a critical energy (and density of states) in the tail of a band, the states become localised. The consequences of this will be discussed later.

Apart from the more or less featureless tails in the density of states already mentioned, it seems likely that in many materials more definite structure in the density of states should exist[13]. For elements and simple compounds such as Se[11] As_2Se_3[9], and As_2Te_3[16] structural studies have indicated a high degree of short range order. Thus, defects in such materials can also be expected to be structurally well defined - e.g. broken

bonds, vacancies, chain ends, and would have reasonably well defined electron energy levels associated with them. The band structure could be similar to that of the analogous crystal, but with some 'smearing out' of the discrete localised levels, and band-tailing of relatively limited extent.

Mott[17] has pointed out that in such materials as amorphous Se, the band tailing should be less than ~ 0.2 eV in extent, and recent work[18] has shown that there do exist deeper states, perhaps not associated with the tails.

'Pinning' of the Fermi level by deep-lying states can be achieved in a similar manner to the 'C.F.O.' overlap model, and Mott[19] has proposed a model, shown in figure 2.4b, where two broadened overlapping centres in the forbidden gap, associated with dangling bonds, serve this purpose, while the localised band-tails may be fairly limited in extent. Again, there is no reason why a number of levels associated with different defects should not exist.

For example, Marshall and Owen[20] proposed a model, shown in figure 2.4c, for As_2Se_3, incorporating two fairly well defined 'bumps' of localised states in the forbidden gap. The states were 'coulombic', i.e. donors in the upper half and acceptors in the lower half of the gap, in almost equal concentrations. This phenomenon of 'auto-compensation' is fairly well known in crystalline semiconductors, and here served to maintain E_F in its roughly mid-gap position, at sufficiently high

temperature. There is now some doubt concerning the 'coulombic' nature of these centres, but the model, and the paper are still valid for say, neutral states.

As will be discussed in chapters 8 and 9, many of the results of the present investigation can be explained in terms of fairly discrete levels.

2.2.2 STRUCTURE AND BONDING IN As_2Se_3 AND As_2Te_3

The brief discussion on structure in this section deals mainly with the chalcogenide materials relevant to this work - As_2Se_3 and As_2Te_3.

Much of the investigation of the structure of the chalcogenides, has naturally centred on the simpler binary systems As_2S_3, As_2Se_3, and As_2Te_3[9,16,21-25].

Crystalline As_2Se_3, and As_2S_3 are known to be isomorphous,[22,26] and have pronounced layer structures. Figure 2.5 shows schematically a single layer viewed along the normal to the layer plane (010 plane). The network consists of shallow triangular pyramids joined together to form twelve-membered puckered rings. The bonding within the layer is covalent, and the co-ordination numbers are 3 for As, and 2 for Se or S. The layers are weakly bonded primarily by van der Waals interactions.

Studies of bulk glassy As_2Se_3, by X-ray diffraction methods[21] show that the first and second interatomic spacings are very similar to those in the crystal, and the co-ordination numbers are the same - i.e. the short range order is preserved. The layer structure is probably broken up to a certain extent, becoming more of

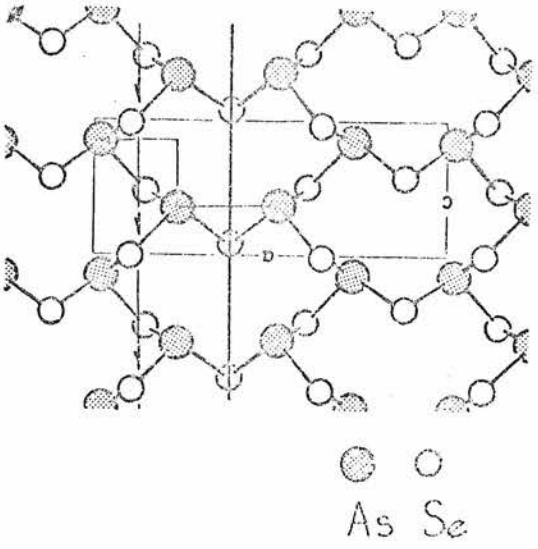

Fig 2.5 As_2Se_3 Crystal structure : plan view of single layer (ref 149)

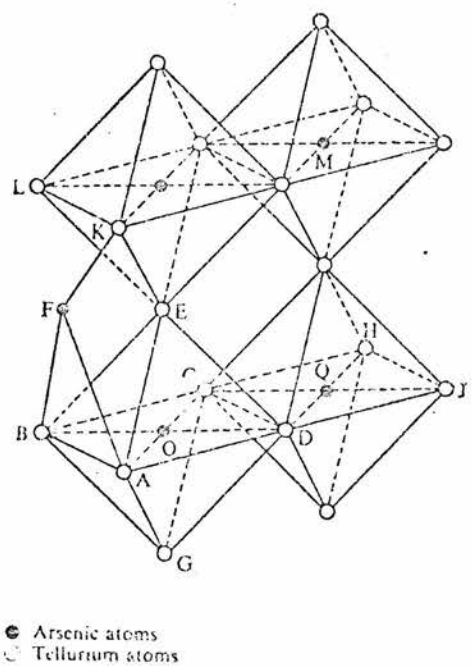

Fig 2.6 As_2Te_3 Crystal structure (ref 16)

a three dimensional network with layers cross-linked, or broken up into rings or smaller covalently bonded groupings. It is also possible that the layers can break down into chains.

Electron diffraction studies were carried out on evaporated films of As_2Se_3 and As_2Te_3, by Andrievskii et al[24]. In As_2Se_3 films, the values for the first and second interatomic distances are close to the values for the crystal, and the glass. The co-ordination numbers, however, for As (~ 6) and Se (~ 4) are higher than in the crystal and glass. It is probable then, that the structure of the thin films is significantly different from that of the bulk material.

During evaporation, some dissociation probably occurs, and the vapour may contain a number of small molecular units. The film structure is probably a three-dimensional network with little vestige of the layers in the crystal.

The structure of crystalline As_2Te_3[25,9] is somewhat different from that of crystalline As_2Se_3. Figure 2.6 shows the structure which consists of zig-zag chains in which the arsenic atoms are octahedrally and trigonally bound to the tellurium atoms. The arsenic atoms therefore have co-ordination numbers of 6 and 3 respectively, and the tellurium atoms, 3 or 2 - i.e. there is considerable ionic bonding. The structure could be interpreted as extreme crimping of the layer structure, with the layers bonded by the six fold co-ordinated As atoms.

Vaipolin et al[21] studied glasses in the system As_2Se_3 - As_2Te_3, and found increasing co-ordination

numbers with addition of Te. Assuming there to be layered structure in the glass, this was interpreted as 'cross linking' or 'spot welding' between layers, at points where the arsenic atoms were six-fold co-ordinated, although the bonding in the glasses was predominantly covalent. Fitzpatrick and Maghrabi[16], interpreted X-ray studies on glassy As_2Te_3 in terms of random covalently bonded $AsTe_{3/2}$ groupings, arranged in a three dimensional network, similar to glassy As_2Se_3. These authors therefore argued that the short-range order in As_2Te_3 changes significantly on crystallisation. The fact that crystalline As_2Te_3 is a degenerate semiconductor with metallic properties, while vitreous As_2Te_3 is semiconducting, gives weight to this argument.

Andrievskii's electron diffraction studies on evaporated As_2Te_3[24] reveal first and second interatomic distances very similar to those in the glass ~2.6 Å and ~ 3.9 Å respectively, and co-ordination numbers for As (~5.1) and Te (3.4) at room temperature, again rather higher than in the glass.

The formation of the electronic band structure in chalcogenides from molecular orbital states and the part played by short range order, has been discussed by a number of authors[14,27,28].

When the group VI elements appear in two-fold co-ordination, the upper part of the valence band in the solid is formed from their unshared, or 'lone-pair' states in π orbitals, while the conduction band is formed

from antibonding orbitals. This is in contrast to the tetrahedrally bonded semiconductors, such as Ge and Si, where the valence band is formed from bonding states.

For example, figure 2.7 shows the formation of bands in crystalline Se from the 4 p and 4 s states, as the atoms are brought together[27]. The p-states form the antibonding (conduction) and bonding bands, above and below the occupied lone-pair (valence) band, which lies close to the original 4 p energy level. The 4 s states, which in Ge are hybridised with the 4 p states, to form antibonding and bonding bands, lie well below the p states in Se. A similar situation will exist when the Se is bonded in two fold co-ordination with other atoms, such as As.

The effect of disorder on the band structure, and the formation of tails of localised states, have been estimated by Mott[14]. It is likely from the preceding discussion that the valence band is less affected by disorder than the conduction band, and has a narrower range of localised tail states. In the vitreous forms of the simpler binary 'compound' chalcogenides, such as As_2Se_3 and As_2Te_3, the valence band tail could be limited to ≤ 0.2 eV. As mentioned earlier, there may also exist several levels of localised states, in the forbidden gap, associated perhaps with broken bonds.

As the structure and bonding in amorphous films of As_2Se_3 and As_2Te_3 may be somewhat different from the bulk glasses, as mentioned above, the band structures could also be rather different. However, measurements/

measurements[18,20,29,30] of a number of electrical properties e.g. drift mobilities in evaporated films and thin bulk vitreous samples, of As_2Se_3, Se, and other chalcogenides, give very similar results, indicating that such differences must be small.

2.2.3 CONDUCTION IN AMORPHOUS CHALCOGENIDES

Transport of charge under the influence of an applied field can occur in a number of ways in amorphous semiconductors. These include

Normal extended state transport
Diffusive or percolative motion in 'barely delocalised' states
Hopping in localised band-tail states
Hopping in localised states near the Fermi level
Polaron hopping

These will be discussed with reference to the density of states model of figure 2.4b. For convenience, electron transport will be discussed, although hole conduction predominates in most materials.

Figure 2.8 which repeats the upper half of the density of states of figure 2.4b, shows schematically how the mobility $\mu(E)$ of carriers in the states is expected to vary with energy at a finite temperature, and gives the occupancy $f(E)$ (Fermi function) for those states. The overall conductivity may be thought of as contributions from a number of transport mechanisms operating in parallel, and can be expressed as

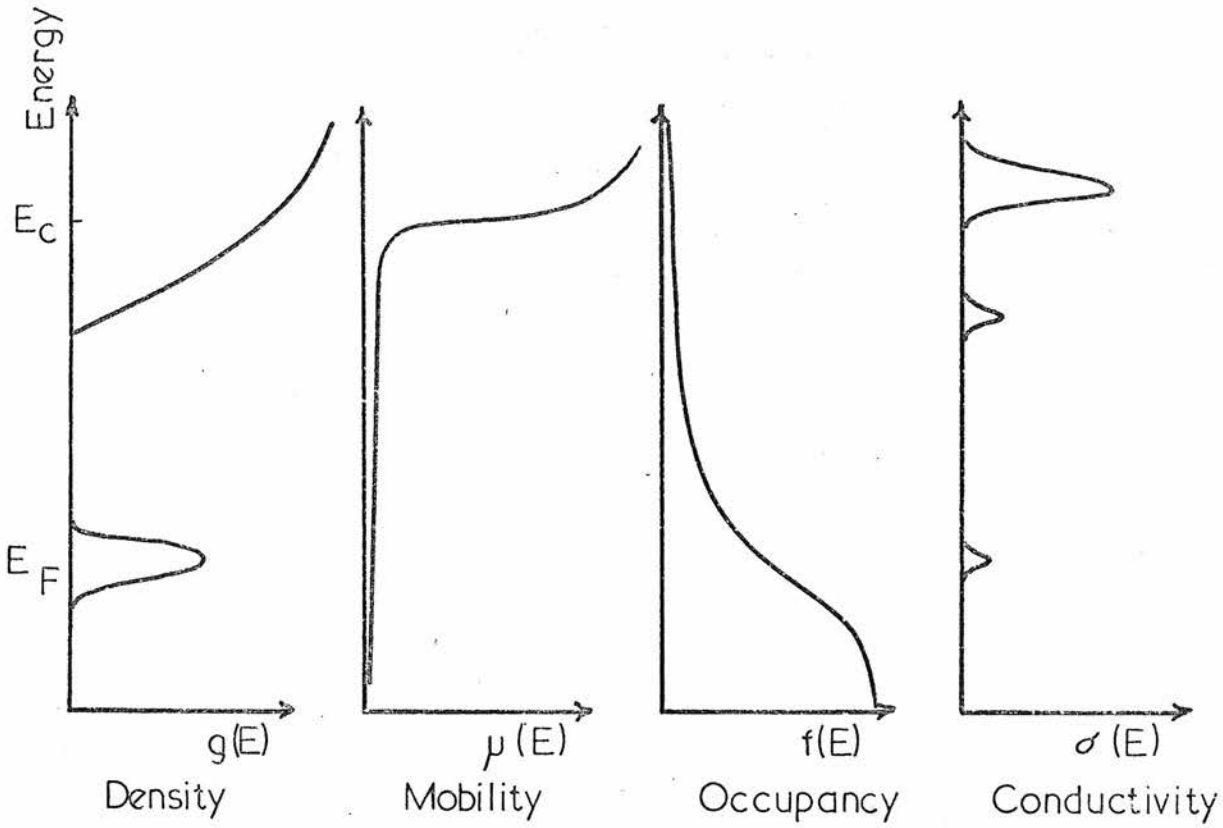

Fig 2.8 Contributions to Conductivity from States at Different Energies

$$\sigma = \int eg(E)\, f(E)\, \mu(E)\, dE \qquad 2.2.1$$

for electron transport, and figure 2.8 shows schematically the contributions to σ at various energies.

Well into the extended states, conventional electron transport is likely with a relatively long mean free path, i.e. much greater than an interatomic spacing, and a mobility perhaps greater than 10^{-2} m^2 V^{-1} s^{-1}. At room temperature however, the occupancy of those states will be very low and they will contribute little to the low field d.c. conductivity.

At energy E_c (and E_v in the valence band) the mobility is thought to drop by two to three orders of magnitude[13,14]. According to Mott[14] this is a fairly sharp mobility edge, as 'Anderson localisation' sets in, while Cohen[13] suggests a rather smoother variation starting above E_c.

Transport in states just above E_c (barely delocalised) was suggested to be diffusive[13] with a mean free path of the order of an interatomic spacing (~3 Å) and a mobility, μ_o, corresponding to diffusive motion

$$\mu_o = \frac{1}{6} \nu_{el} R^2/kT \sim 10^{-3} m^2 V^{-1} s^{-1} \qquad 2.2.2$$

where ν_{el} is an electronic frequency, of the order of 10^{15} Hz, and R is an average jump distance.

The contribution of this process to the conductivity is of the form

$$\sigma = \sigma_{ext} \exp\left(-\frac{E_c - E_F}{kT}\right) . \qquad 2.2.3$$

where the pre-exponential factor $\sigma_{ext} = eg(E_c)\, kT\mu_o$, has been estimated theoretically[14] to be of order $2 \times 10^4\ \Omega^{-1}\ m^{-1}$.

The mobility edge has also been interpreted in terms of a 'percolation threshold'[8,31] at E_c. Below E_c there are islands' of allowed localised regions, separated by potential barriers, while at $E \geq E_c$ the probability of an interconnected path through the material of allowed regions (channels) becomes finite.

Just below E_c, conduction will occur by thermally activated 'hopping' of carriers between localised states[17], and the mobility can be written

$$\mu_{hop} = \frac{1}{6}\nu_{ph}\, eR^2/kT \exp(-W/kT) \exp(-2\alpha R) \quad 2.2.4$$

where ν_{ph} is now a phonon frequency, $\sim 10^{12}$ Hz, $\exp(-2\alpha R)$ is a tunnelling factor, and W, a hopping activation energy. The conductivity contribution of the band tail may be written

$$\sigma_{hop(1)} = \sigma_1 \exp\left(-\frac{E_A - E_F}{kT}\right) \exp\left(-\frac{\Delta W}{kT}\right) \exp(-2\alpha R) \quad 2.2.5$$

where $\sigma_1 \lesssim 20\ \Omega^{-1}\ m^{-1}$ (17) E_A is the effective limit of the band-tail, and ΔW, hopping activation energy.

Hopping conduction in states near the Fermi level could also occur[14], with an even lower mobility, and a low activation energy, about half the width of the band of states at E_F. At very low temperatures Mott[32] argues that hopping to distant sites becomes more probable, and this gives

$$\log \sigma = A - BT^{-1/4} \quad 2.2.6$$

The total conductivity is the sum of all of these contributions, and the question arises as to which mechanism dominates in a given material under given conditions. Bearing in mind the 10^3 drop in mobility at E_c, in materials with band tailing of < 0.2 eV, it is probable that extended state conduction would dominate at room temperature. Some experimental results are reviewed in 2.2.4.

Emin et al[33] have recently suggested that small polaron conduction may occur in disordered chalcogenides. The polaron concept, originally applied to ionic materials involves the self-trapping of a carrier in the potential well associated with the carriers' distortion of the local lattice. This configuration is known as a small polaron when the carrier is localised on a single atomic site. The mobility is of the order of 10^{-5} m^2 V^{-1} s^{-1}, and the activation energy for conduction contains a generation term, and a hopping term, as does the hopping conductivity of equation 2.2.5

2.2.4 REVIEW OF ELECTRICAL PROPERTIES OF CHALCOGENIDES

This section reviews some of the main features of the electrical properties of disordered chalcogenides. More detailed discussion on the materials studied in this work - As_2Se_3 and As_2Te_3, e.g. on localised state distribution, will be given later.

The d.c. conductivities of many chalcogenide compositions gives a good straight line plot of $\log \sigma$ vs $1/T$ around room temperature, i.e.

$$\sigma = C \exp(-\frac{E_\sigma}{kT}) \qquad 2.2.7$$

where E_σ ranges from ~0.33 eV for GeTe[34] to 0.92 eV for As_2Se_3[35] and 1.05 eV for As_2S_3[35]. Typical values for the multicomponent switching alloys range between 0.45 and 0.55 eV. E_σ is usually about half the optical gap E_{opt}, so that the chalcogenides appear to have 'intrinsic' semiconductor behaviour. Room temperature conductivities vary between $\sim 10^{-1}\ \Omega^{-1}\ m^{-1}$ for $As_2Te_3Tl_2Se$, and $\sim 10^{-14}$ for As_2S_3. For many of those materials, C lies between 10^5 and $10^6\ \Omega^{-1}\ m^{-1}$, as pointed out by Stuke[36].

The temperature variation of the activation energy, estimated from optical gap measurements can be included in equation 2.2.7, i.e.

$$E_\sigma = E_\sigma(0) - \gamma' T \qquad 2.2.8$$

where γ' is roughly half the optical gap temperature coefficient, γ and $E_\sigma(0)$ is the extrapolated zero temperature value of the activation energy.

This gives $C = \sigma_o \exp(\frac{\gamma}{2k})$, and as γ is typically $\sim 5 \times 10^{-4}$ eV K^{-1} [37], σ_o is $\geq 10^4\ \Omega^{-1}\ m^{-1}$ for such materials, probably indicative of extended state transport, at room temperature. (The factor 2 in the temperature coefficient may be roughly justified by the observation that E_σ is about half the optical gap in these materials).

In some materials, e.g. As_2S_3[35], the value of C is much lower ($< 10^3$), and this may indicate the

predominance of hopping conduction at room temperature. Evaporated chalcogenide films often give $\log \sigma$ vs $1/T$ plots which curve off to lower slope, at low temperatures (< 150 K)[38]. This could be interpreted as a transition to hopping conduction, or in terms of a 'soft' mobility edge.

Using equation 2.2.1, for a linear tail of states, Davis and Mott[17] estimate that extended state conduction should predominate at room temperature, if the extent of the band tail is less than ~ 0.2 eV. Thus if there is extensive band tailing, as predicted by Cohen[13], e.g. for multicomponent alloys, then hopping may predominate at room temperature. Unfortunately, there is no unambiguous way of checking the extent of possible band tailing.

Finally, recent reports, e.g. by Emin et al[33], suggest that polaron conduction in disordered chalcogenides could give fairly high values of σ_o within an order of $10^4\ \Omega^{-1}\ m^{-1}$, a value which previously would have been taken to indicate, say diffusive transport in extended states[17,39]. The question as to whether band or hopping conduction predominates in such materials, is therefore still open.

Thermoelectric power measurements in liquid[40] and solid[41,33] chalcogenides have shown a positive coefficient S, indicating that hole transport predominates Its magnitude, of the order mV K^{-1}, is similar to that obtained in crystalline semiconductors, and it is inversely proportional to temperature. The thermoelectric

power can be written

$$S = \frac{k}{e} \left(\frac{E_s}{kT} + \text{constant} \right) \qquad 2.2.9$$

where E_s is a characteristic activation energy.

Again, results have been interpreted in terms of band and hopping conduction. In his measurements on liquids (in AsSeTe system), Edmond[40] assumed band conduction in an intrinsic semiconductor, with a higher hole mobility, and put $E_s = E_g/2$ where E_g is the gap between extended states, or mobility gap. He found $E_s > E_\sigma$ in these materials. Owen[42] assumed ambipolar conduction (electrons and holes) to resolve this discrepancy.

In contrast some recent measurements on solid chalcogenides by Emin et al[33], have given $E_s < E_\sigma$. Emin assumes polaron hopping conduction, and argues that $E_\sigma = E_s + \Delta W$, where ΔW is the hopping activation energy or mobility activation energy.

Hall effect measurements, in chalcogenides,[33,43-46] normally indicate n-type conduction, in contradiction to thermopower measurements. In addition, the Hall mobilities obtained are of the order 10^{-5} m^2 V^{-1} s^{-1}, which makes interpretation in terms of normal band-transport unrealistic, as the lower limit of microscopic mobility in extended states, even for 'diffusive' motion should be 10^{-4} - 10^{-3} m^2 V^{-1} s^{-1} [13,17].

Measurements by Male[43] on various liquid and vitreous chalcogenides revealed virtually no temperature dependence, as might be expected for extended state

transport. More recent measurements[33,44] in a number of chalcogenides give an activated Hall mobility with a small activation energy (< 0.1 eV).

When the mean free path is of the order of an interatomic spacing, as in diffusive band transport or when conduction is by hopping, it has been suggested[50,53] that a minimum of three sites are involved in the 'jump' processes leading to a Hall effect, and this could lead to the 'sign anomaly'.

There have been a number of theoretical treatments of the Hall effect in low mobility materials[47-52] but there seems to be a lack of detailed agreement.

Drift mobility. The drift mobility (μ_d) of carriers injected into high resistivity, low mobility materials such as Se[18,30], As_2Se_3[20,29], has been measured by a transit time technique developed by Spear[54]. The results have normally been interpreted in terms of trap-limited band transport, so the mobility activation energy gives the trap depth in the simplest case of a discrete level. Typical figures, for room temperature mobilities and activation energies, range from 10^{-5} m^2 V^{-1} s^{-1}, 0.21 - 0.28 eV (at low temperatures) for holes in Se[30] to $\sim 10^{-10}$ m^2 V^{-1} s^{-1} and 0.43 eV for holes in As_2Se_3[20] and it is normally found that the hole mobility is greater than the electron mobility.

a.c. conductivity. The a.c. conductivity $\sigma(\omega)$ has been observed to have a frequency dependence $\sigma(\omega) \propto \omega^n$ with $n \leq 1$, in the range of frequencies up to 10 MHz,

for many chalcogenides - e.g. As_2S_3[42], As_2Se_3[55], As_2Te_3[56]. This frequency dependence, and the relative insensitivity of $\sigma(\omega)$ in this range, to temperature, have led some authors[53,57] to interpret the effect in terms of hopping between localised states near the Fermi level. Typical densities (m^{-3} eV^{-1}) for these states, from such an interpretation range from $\sim 10^{24}$ for As_2S_3, to nearly 10^{27} for As_2Te_3.

Optical absorption. This will be discussed again in chapter 3. The fundamental absorption edge in amorphous chalcogenides is more diffuse than in the crystalline analogues. It is characterised by an exponential increase of absorption coefficient α with photon energy, up to values of $\alpha \sim 10^4 - 10^5$ m^{-1}, and at higher photon energies, tends to saturate, around $10^7 - 10^8$ m^{-1}.

The photon energy dependence at high energies, often fits an equation of the form

$$\alpha \sim (h\nu - E_{opt})^2/h\nu \qquad 2.2.10$$

where $h\nu$ is the photon energy, and E_{opt} an 'optical gap'. This has been observed in As_2Se_3[58] and As_2Te_3[59], among other materials.

Various explanations of this behaviour usually involve electron transitions which are energy conserving but do not conserve wave number, as in crystalline semiconductors. For example, Tauc[60] assumes that such transitions occur between extended states in parabolic band edges upon which the localised tails are superimposed,

so E_{opt} may not correspond to an actual density of states gap. Davis and Mott[17] assume that tail-band transitions are involved, so E_{opt} need not even reflect the gap between extended states.

To illustrate this last statement, it is often found that $E_{opt} > 2\ E_{\sigma}$, in chalcogenides - e.g. for As_2S_3 E_{opt} (extrapolated to OK) ~ 2.5 eV[61] and $2\ E_{\sigma} \sim 2.2$ eV[35].

It should be noted that the high mid-gap density of states indicated by a.c. conductivity methods, does not seem to contribute to optical absorption. Davis and Mott[17] argue that this might be so because the width of the localised state 'bump' near E_F on figure 2.4b, is small, so the total density (m^{-3}) is small. Fritzsche[8] argues that the optical transition matrix element is small for transitions involving those states. In phenomenological terms this means that they have a small 'cross section', a point which is borne out by this work.

Impurities. It has often been observed that impurities have little effect on the conductivity of various chalcogenides[62], while in crystalline semiconductors, small densities of impurity atoms can have a drastic effect. This has been interpreted[13] as implying that in these disordered materials, the structures are such that nearly all atoms have their valence requirements locally satisfied. Some impurities do have a marked effect, however[63,35]. For example, it has been found[35] that one atomic percent of silver increases the conductivity of As_2S_3 by 3 to 4 orders of magnitude.

Studies of the effects of departure from stoichiometry have also been carried out on some chalcogenides e.g. As - Se[35,64], where it was found that the conductivity was highest at the stoichiometric composition $As_{40}Se_{60}$, and the activation energy E_σ at its lowest. Hurst[64] interpreted this as due to mobility gap shrinkage.

2.2.5 HIGH FIELD EFFECTS

The d.c. conductivity of many chalcogenides, e.g. As_2Se_3[65], $Ge_{15}Te_{85}$[30], Si_{10} - Te_{48} - As_{30} - Ge_{12}[66] Ge - As - Te - S[38] has been observed to be electric field dependent, with a similar functional dependence for all the materials studied. Marshall and Miller[66] have reviewed a number of possible mechanisms for this behaviour which they express as :

$$\sigma(\mathcal{E}) = \sigma(0) \exp\left(\frac{e\,\mathcal{E}\,a(T)}{kT}\right) \qquad 2.2.11$$

where $\mathcal{E}$ is the applied electric field, and a(T) is a temperature dependent parameter with dimensions of length - an 'activation length', with room temperature value in the region of 10 Å - 40 Å, which increases linearly with decreasing temperature. Measurements[67] indicate that this 'single exponential' behaviour is followed even at fields as low as 10^5 V m^{-1}, and is independent of sample thickness over a wide range, from 10^{-6} to 10^{-3} m (probably higher).

Possible mechanisms for non-ohmic effects are listed below.

Injection effects

Field assisted hopping

Field modified thermal trap release/capture

Schottky effect

Hot carrier effects

Field stripping of traps

Injection effects. As discussed by Rose[2] and Lampert and Mark[68] single and double injection of carriers from injecting electrodes can give non-ohmic space charge limited behaviour due to increased carrier densities. For example, single carrier injection, when the Fermi level (or quasi-Fermi level) is within a uniform distribution of localised states, can give, using the present nomenclature.

$$\sigma(\mathcal{E}) = \sigma(0) \exp\left(\frac{\text{constant} \times \mathcal{E}}{k\,T \times l}\right) \qquad 2.2.12$$

where l is the interelectrode spacing.

The pronounced thickness dependence of this and other injection models (e.g. with shallow traps, or double injection), makes it inconsistent with the data, which appear to be due to a 'bulk' process. In addition, when mobility measurements are possible, as in Se, the drift mobility and conductivity have essentially the same field dependence[30], thus ruling out a carrier density effect.

Space charge injection cannot be altogether discounted for samples much thinner than 10^{-6} m, where it may contribute to switching effects.

Field assisted hopping. Various authors[19,69,70] have discussed the effects of high electric fields on hopping conduction. The effect should be similar in form to that observed in ionic conduction. An applied field will lower the energy required for a given 'down-field' hop, and raise the energy required for a given 'up field' hop, so equation 2.2.5 is modified to

$$\sigma(\mathcal{E}) = \sigma(0)\ \sinh\left(\frac{e\,\mathcal{E}\,R}{kT}\right)\ \exp\left(\frac{-\Delta W}{kT}\right)\ \exp(2\,\alpha\,R) \qquad 2.2.13$$

and at sufficiently high fields, this gives an exponential dependence.

Jump distances in hopping conduction are usually assumed to be of the order of interatomic spacings[71] while the data would indicate larger values (> 10 Å up to 50 Å). This seems unlikely, but Mott[71] points out that the tunnelling factor in equation 2.2.13, may be modified, and may be $\gg 1$, if the localised states wave function overlaps with a number of others.

Given that this might be so, there remains a fundamental objection to an interpretation in terms of hopping. At fields below $\sim 10^6$ V m^{-1}, hyperbolic sine behaviour should occur, while as pointed out, exponential behaviour prevails at fields as low as 10^5 V m^{-1}.

Field modified thermal trap release/capture. An electric field may enhance the probability of thermal ionisation of a localised state (reduce τ_{tr}) or modify

its trapping cross-section (change τ_t). The steady state redistribution of trapped and free charge produced, can give a field dependent conductivity.

In the Poole-Frenkel effect[72], depicted in figure 2.9, the ionisation energy of a centre with a coulombic potential is reduced by the field. In a simple one dimensional treatment, the potential is given by the expression $-e^2/4\pi\epsilon\epsilon_o x$, where ϵ is the relative high frequency dielectric constant, ϵ_o is the permittivity of free space, and x is the distance from the centre. In the absence of an applied field a trapped carrier must surmount a barrier of energy E_t, to enter the band (say, conduction band). The applied electric field lowers the potential by an amount $-e\mathcal{E}x$, and a maximum 'downfield' barrier is obtained at x_M which is smaller than the original barrier by an amount $\beta\mathcal{E}^{\frac{1}{2}}/kT$, where $\beta = (e^3/\pi\epsilon\epsilon_o)^{\frac{1}{2}}$. The trap release probability is increased by a factor $\exp(\beta\mathcal{E}^{\frac{1}{2}}/kT)$, and if other mechanisms (recombination trapping mobility) are field independent, and conduction is in extended states, this can give

$$\sigma(\mathcal{E}) = \sigma(0)\exp\left(\frac{\beta\mathcal{E}^{\frac{1}{2}}}{kT}\right) \qquad 2.2.14$$

Other treatments[73,74] treat the situation more thoroughly. Three dimensional geometry has been assumed[73,74] and carrier emission in all directions has been dealt with[74], assuming now that a carrier is free if it approaches within ~kT of the band edge. For coulombic potentials, Hartke showed that values of β up to 50% smaller than in the simple treatment were possible,

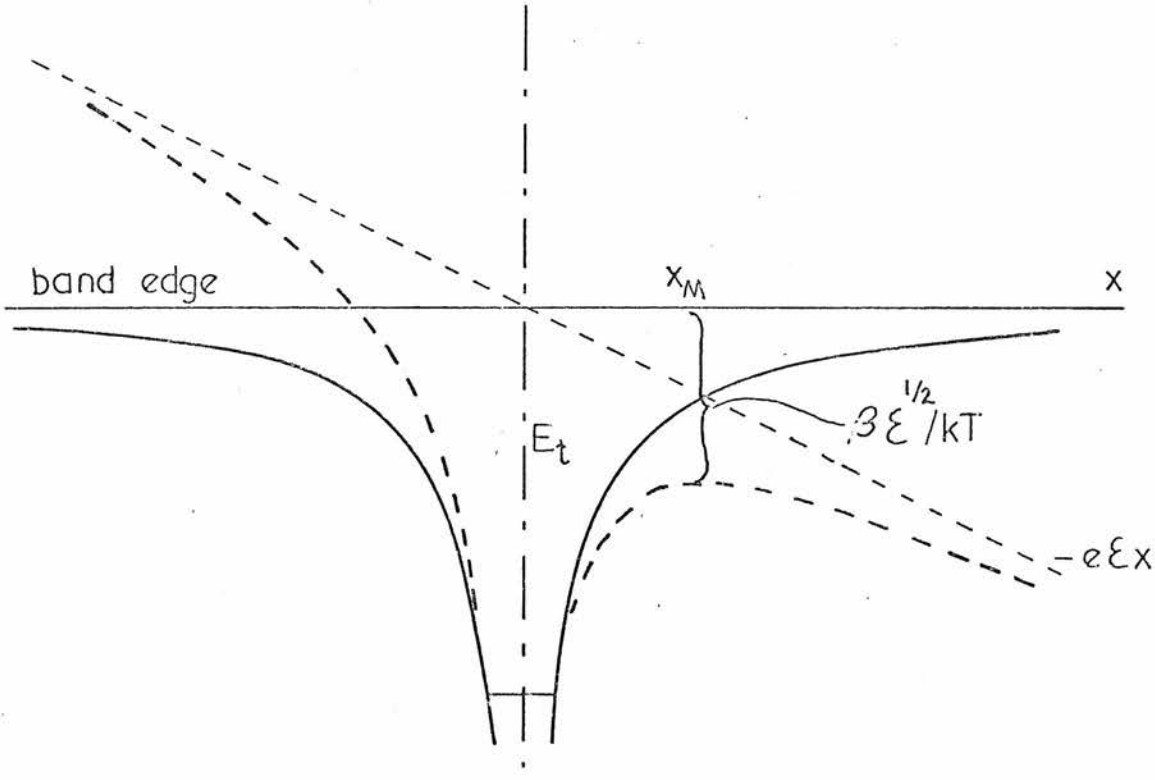

Fig 2.9 Mechanism of Poole Frenkel effect.

while Ieda et al demonstrated that hyperbolic sine behaviour should appear for fields below $\sim 2 \times 10^6$ V m^{-1}.

This last observation, and the square root exponent are again inconsistent with much of the data. Marshall and Miller[66] examined a number of other potential configurations e.g. 'neutral' centres with $1/x^4$ potential, square wells, and found that, although a linear exponent is approached for such wells, 'Ohmic' behaviour is predicted to high fields, in contradiction to observation. A similar result is found for interacting coulombic centres, where the potential barrier maximum is half way between centres ('Poole' effect)[75].

Dussel and Boer included in a classical treatment, the effects of a field dependent trapping capture cross section, combined with a Poole Frenkel release enhancing mechanism. Marshall and Miller again conclude that this would not lead to the observed behaviour.

The Schottky effect[76] which assumes field assisted thermal excitation of charge carriers across a metal-semiconductor contact, gives results similar to the Poole Frenkel effect, except that a lower field dependence is predicted, as a moving 'image' charge is now involved. Again this is not in agreement with the observations - especially those of a 'bulk' mobility field dependence - whereas Schottky effect is an electrode phenomenon.

Hot carrier effects. At sufficiently high fields, carriers moving in extended states may gain energy faster than they lose it to phonons. If the mean free time is ν^{-1}, then a critical field, above which this occurs, is given approximately, by[66]

$$\mathcal{E}_{crit} \simeq (kT\nu/2e\mu_o)^{\frac{1}{2}} \qquad 2.2.15$$

and for $\mu_o \sim 10^{-4}$ m^2 V^{-1} s^{-1}, $E_{crit} \sim 10^7$ V m^{-1}.

As this occurs, carriers move into extended states of higher energy. If the mobility in the band increases with energy[13] as in figure 2.8, in contrast with the situation in crystalline semiconductors, the conductivity can rise rapidly, and avalanching effects can occur[19,77]. This of course does not explain the low field effects observed, but may be important, e.g. in switching.

Field 'stripping' of traps. Trapped carriers may tunnel directly out of traps into extended states, through the intervening potential barrier, in the 'down field' direction, when an electric field is applied. The barrier width should be reduced to ~ 50 Å for significant tunnelling to occur, and for the relatively deep traps observed in, say, drift mobility measurements (e.g. 0.43 3V in As_2Se_3), fields of the order of 10^8 V m^{-1} would be required, much higher than those at which non-ohmic effects are observed.

Mott[19] and Marshall and Miller[66] have pointed out that carriers in localised states in band tails, close to the mobility edge, could be very susceptible to tunnelling into extended states. This effect could occur

at fairly low fields if the mobility varies rapidly with energy, giving a short tunnelling distance between 'localised' and 'extended' states, at such fields. This could account for the apparent lack of a transition to 'ohmic' behaviour at low fields, and its ubiquitous appearance in widely different materials which, although they might contain different distributions of deep levels, may all possess band tails and mobility edges. The detailed nature of the mobility edge may not matter too much.

Such a field stripping of shallow traps, effectively delocalises the states, and can be interpreted as a lowering of the mobility edge - hence changing the effective depth of deeper states also. The field could alternatively be pictured as unblocking percolation paths between allowed regions, - again effectively lowering the mobility edge.

Although detailed calculations have not yet been published, this interpretation of high field effects seems a plausible and attractive approach.

CHAPTER 3

OPTICAL PROPERTIES AND PHOTOCONDUCTIVITY IN AMORPHOUS SEMICONDUCTORS

3.1 OPTICAL PROPERTIES

3.1.1 OPTICAL CONSTANTS

The usual terminology for propagation of electromagnetic radiation is employed here. In an absorbing medium, the complex permittivity ϵ^* and complex refractive index n^*, are related as follows

$$n^* = n - ik = (\epsilon^*/\epsilon_o)^{\frac{1}{2}} = (\epsilon - \frac{j\sigma}{\omega})^{\frac{1}{2}} \epsilon_o^{-\frac{1}{2}} \qquad 3.1.1$$

where n is the refractive index, k the extinction coefficient, and all terms may be functions of frequency ω. The relation between the energy absorption coefficient $\alpha(\omega)$ and the high frequency a.c. conductivity $\sigma(\omega)$ is then

$$\alpha(\omega) = \frac{2k\omega}{c} = \frac{\sigma(\omega)}{\epsilon_o nc} \qquad 3.1.2$$

where c is the free space velocity of light.

3.1.2 INTERBAND TRANSITIONS

In crystalline semiconductors, the onset of electronic interband transitions when the photon energy $h\nu$ corresponds to the band gap, marks the fundamental absorption edge. The absorption coefficient α rises steeply to values around $\sim 10^8$ m^{-1}. The shape of the edge depends upon quantum mechanical considerations e.g. the nature of the wave functions in the valence and

conduction bands, and the density of states, which govern transition probabilities.

The probability of a transition eigenstates with wave functions ψ_m and ψ_n, and energies E_m and E_n, with electromagnetic perturbing force F, is proportional to the matrix element $|M_{mn}|^2$ where

$$M_{mn} = \int \psi_m^* F \psi_n \, d^3r \text{ (overall space)} \qquad 3.1.3$$

for optical excitation this simplifies to the matrix element of the dipole moment - the dipole approximation. Knowing the form of the wave functions and density of states[78], at the band edges, the form of the absorption edge can be found. For example, in the case of direct interband transitions, the absorption constant may be written

$$\alpha(\omega) = \frac{4h^2e^2}{\pi m^2 n\omega c} \int dk \; | M_{vc} |^2 \; \delta(E_c - E_v - h\omega)$$

where M_{vc} contains the wavevector selection condition, and $\delta(E_c - E_v - h\omega)$ contains the energy conservation selection rule.

In crystals, transitions involving only photons, are 'vertical' in momentum space, and the initial and final states have virtually the same wave number k, - 'direct transitions'. Indirect, 'non vertical' transitions involve emission or absorption of a phonon, with the attendant energy and momentum transfers.

A number of different situations can arise for either type of transition, depending upon the E - k relation at each band edge, and the matrix element's dependence on k. For example direct transitions may occur at $k \neq 0$, and be forbidden at $k = 0$. Direct transitions between states not at the band energy minima may predominate, so the measured optical gap E_{opt} need not equal the density of states gap $E_c - E_v$ although for indirect transitions, the agreement may be closer. Several 'types' of transition may occur simultaneously. Smith[79] discusses several such situations in crystalline semiconductors. For example, for direct and indirect 'allowed' transitions, the absorption coefficient is given by

$$\alpha = \text{const.}\ (h\nu - E_{opt})^{\frac{1}{2}} \quad \text{(direct)} \qquad 3.1.5$$

$$\alpha = \text{const.}\ (h\nu - E_{opt})^{2} \quad \text{(indirect)} \qquad 3.1.6$$

Absorption below the fundamental edge may occur due to exciton formation, when there is appreciable interaction between the electron hole pair created. For example, a series of exciton absorption lines corresponding to different excited states of the pair may be observed at energies $< E_{opt}$, and are normally

broadened by phonons and imperfections, to exciton 'bands'. The energy of an electron in such an excited state may therefore lie within the 'one-electron' forbidden gap.

As mentioned in 2.2.4, the optical gap in many semiconductors decreases linearly with temperature, above ~50 K.

$$\text{i.e.} \quad E_{opt}(T) = E_{opt,o} - \gamma T \qquad 3.1.7$$

Below ~50 K, the variation normally flattens off, so that $E_{opt}(0) < E_{opt,o}$. This variation is due to thermal effects e.g. expansion, on the band structure, and its implications for the conductivity temperature dependence were discussed in 2.2.4.

3.1.3 OPTICAL ABSORPTION IN AMORPHOUS SEMICONDUCTORS

In amorphous semiconductors, a fundamental absorption edge is retained, but is normally rather less steep than in crystalline semiconductors. An exponential tail at low photon energies, up to values of $\alpha \sim 10^5$ m^{-1}, is observed, in many cases, (Urbachs rule), followed by a tendency to saturation at high absorption coefficients $\alpha \sim 10^7 - 10^8$ m^{-1}.

No well defined optical gap appears, but several authors[17,80] have attempted to characterise the high photon energy absorption in terms of an 'optical gap' in the context of present models of amorphous semiconductors.

Tauc[80] considered transitions between extended states in parabolic band edges falling, or extrapolating

to zero at energies E_c' and E_v', slightly perturbed to give localised tails. Transitions between localised states, and between a localised and an extended state were considered unlikely. The k-selection condition was relaxed, as the value of k in barely delocalised states, where the shubweg is short, is uncertain. The transition matrix element is assumed to be energy independent, and this leads to

$$\alpha(\nu) = \text{const.} \; |M_{nm}|^2 \int g(E_c') \; g(E_v' + h\nu) dE \qquad 3.1.8$$

and gives

$$\alpha(\nu) = \text{const.} \; (h\nu - E_{opt})^2 / h\nu \qquad 3.1.9$$

where $E_{opt} = E_c' - E_v'$.

This form has been observed in a number of amorphous semiconductors, e.g. As_2Te_3[59], As_2Se_3[58], As_2S_3[58], but the optical gap obtained need not necessarily agree with the mobility gap E_g. Nor should the form be associated with an 'indirect gap' as given by equation 3.1.6, as the assumptions in the analysis are quite different.

Davis and Mott[17] using the Kubo-Greenwood[81] formalism, for $\sigma(\omega)$, assumed that k selection did not apply, and that the matrix element for transitions between localised and extended states was equal to that for extended-extended transitions. Transitions between localised states were considered unlikely, due to spatial separation.

An expression of the form of equation 3.1.8 for $\alpha(\nu)$ was derived, giving, for linear band tailing, as in figure 2.4b, the same relation as Tauc obtained, with $E_{opt} = E_C - E_B$, or $E_A - E_V$. Again this gap is not necessarily equal to the mobility gap E_g.

There have been several explanations for the exponential tail often observed in the absorption edge.[83] One possibility is that of transitions between localised states in exponentially distributed band edges[82]. Owen[39], and Davis and Mott[17], argue that this is unlikely as $|M_{mn}|^2$ must remain constant over a wide range of energy, and also, many different materials give similar exponential slopes.

Other explanations involve exciton absorption. Phonon broadening of an exciton line has been considered[84], and electric field broadening, by the presence of random internal fields, due to disorder, also seems plausible[85].

3.2 PHOTOCONDUCTIVITY IN AMORPHOUS SEMICONDUCTORS

3.2.1 THE CONTINUITY EQUATIONS

Interpretation of photoconductivity data is notoriously difficult, as many variables are involved : optical absorption and quantum efficiency; carrier trapping and recombination; transport of excess carriers; contact effects and inhomogenieties, to name but a few.

The continuity equations, (see e.g. van Roosbroeck[86]) describing the behaviour of excess carriers in semiconductors, can be written for the present experimental geometry, depicted in figure 3.1.

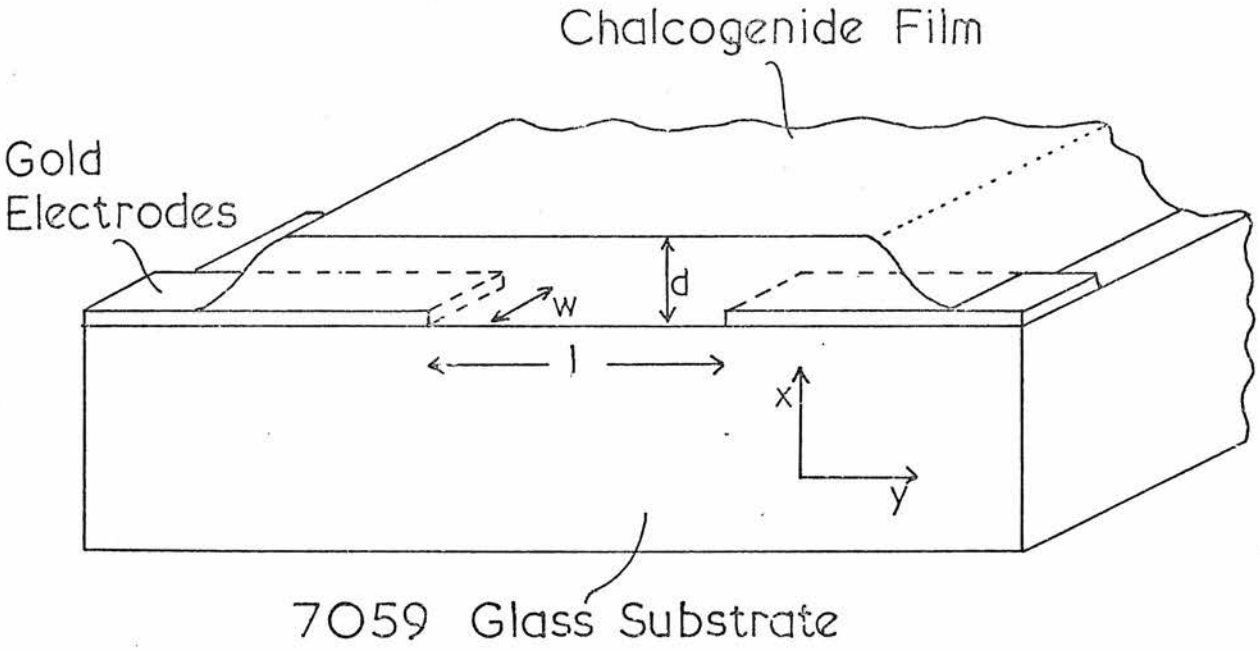

Fig 3.1 Sample Geometry.

This is a coplanar, or gap-cell structure, as described in section 4.2. The optical excitation is applied normal to the film surface (x direction) while the applied electric field is parallel to the film surface (y direction). It can be seen that optical absorption of the applied illumination will give rise to variations in generation rate and hence in carrier densities, in the x direction only, while it will be assumed that in most cases, the applied y-field does not introduce significant space charge, to distort the constant carrier distribution in the y-direction. A one-dimensional problem results. Thus, for holes and electrons in extended states, the continuity equations are

$$\frac{\partial p}{\partial t} = D_p \frac{\partial^2 p}{\partial x^2} - \mu_{po} \frac{\partial}{\partial x} (p \mathcal{E}_{int}) + H_p$$

$$\frac{\partial n}{\partial t} = D_n \frac{\partial^2 n}{\partial x^2} + \mu_{no} \frac{\partial}{\partial x} (n \mathcal{E}_{int}) + H_n \qquad 3.2.1$$

Taken term by term, H_p ahd H_n are kinetic terms, including optical generation, recombination, trapping etc. The diffusion term involves the free carrier diffusivities D_n and D_p; normally related to the free mobilities by the Einstein relations, and the drift terms involve the internal field $\mathcal{E}_{int}$ which produces drift currents in the x direction, when $D_p \neq D_n$ and when significant charge separation occurs. All terms may be dependent on x.

The set of necessary equations is completed by writing Poissons equation relating the internal field $\mathcal{E}_{int}$, to the net charge density $\rho(x)$

$$\frac{\partial \mathcal{E}_{int}}{\partial x} = \frac{4\pi e}{\epsilon \epsilon_o} \rho(x) \qquad 3.2.2$$

where $\rho(x)$ includes all charged states, extended and localised.

The discussion which follows deals mainly with the kinetic processes, although where possible, the effects of non uniform excitation, and attendant diffusion/ drift effects will be assessed.

An initial major assumption is that holes dominate the conductivity in amorphous chalcogenides. Experimental data, reviewed in chapter 2 confirm this. It is possible that this is due to the free hole density being greater than the free electron density, if conduction is via extended states. In turn this could be a result of asymmetric band tailing where the valence band is less affected by disorder than the conduction band (see 2.2.2), or if E_F is pinned 'off-centre' by localised states. Alternatively, the free hole mobility could be greater than the free electron mobility, - or both situations together.

3.2.2 OPTICAL GENERATION AND QUANTUM EFFICIENCY

Band-band generation, included in the kinetic terms of equation 3.2.1 consists of an equilibrium rate G_o, and an excess photogeneration rate ΔG. G_o may comprise

a number of possible mechanisms, such as phonon-aided transitions, absorption of black-body radiation, etc., while ΔG is assumed to be due to interband absorption of monoenergetic photons.

η, the generation quantum efficiency is defined as the number of 'free' electron-hole pairs produced per photon absorption. 'Free' here implies free to contribute to conduction after the initial generation. Subsequent rapid trapping or recombination may remove carriers but do not affect this definition.

Some experimental methods can effectively separate the generation and transport/trapping processes. Tabak and Warter[87], Pai and Ing[88] and others describe a charge collection technique in which a sandwich geometry is used. By integrating the transient current due to charge generated at one electrode by a flash of highly absorbed light, the total charge transported through the film can be measured (e.g. in Se) if recombination and electrode injection effects are negligible.

Other methods, such as those used here, can only give a relative value for η, and some knowledge of the transport and recombination properties is required to extract η from the photocurrent (ΔI) data.

In some amorphous chalcogenides, the relative quantum efficiency is constant over a range of photon energies from below the optical gap, to several times the gap energy (Fagen and Fritzsche[89]). The photoconductivity at energies below the optical gap was

thought to be due to transitions between the localised tail of one band, and the extended states of the other.

In some other chalcogenides, however, the absorption in the region of E_{opt} has a low quantum efficiency, and η does not saturate until the photon energy is about 0.5 eV above E_{opt}. This "non-photoconducting absorption" has been seen in Se[87,88,90] and As_2Se_3[91]. e.g. in Se, E_{opt} is estimated as 2.1 eV (Davis[92]), while η does not saturate till $h\nu \sim 2.6 - 2.8$ eV. Figure 3.2 shows the spectral dependence of α, and η, reported by several workers[93 - 97] for Se, taken from a paper by Hartke and Regensburger[90]. Most of those measurements were carried out by the technique mentioned above.

Some other salient features are that η has temperature and field dependences which vary with photon energy. In particular, Pai and Ing[88] found that at low photon energies (2.0 - 2.2 eV) the high field dependence could be fitted by a Poole-Frenkel expression

$$\eta \propto \exp\left(\frac{\beta\mathcal{E}^{\frac{1}{2}} - E_o}{kT}\right) \qquad 3.2.3$$

where the energy E_o decreases with increasing photon energy. The quantum efficiencies for electron and hole generation are roughly equal.

Several models have been proposed, varying in the detail which they treat, to account for this behaviour. These can be roughly subdivided into 'one electron state', and 'electron-hole interaction' models.

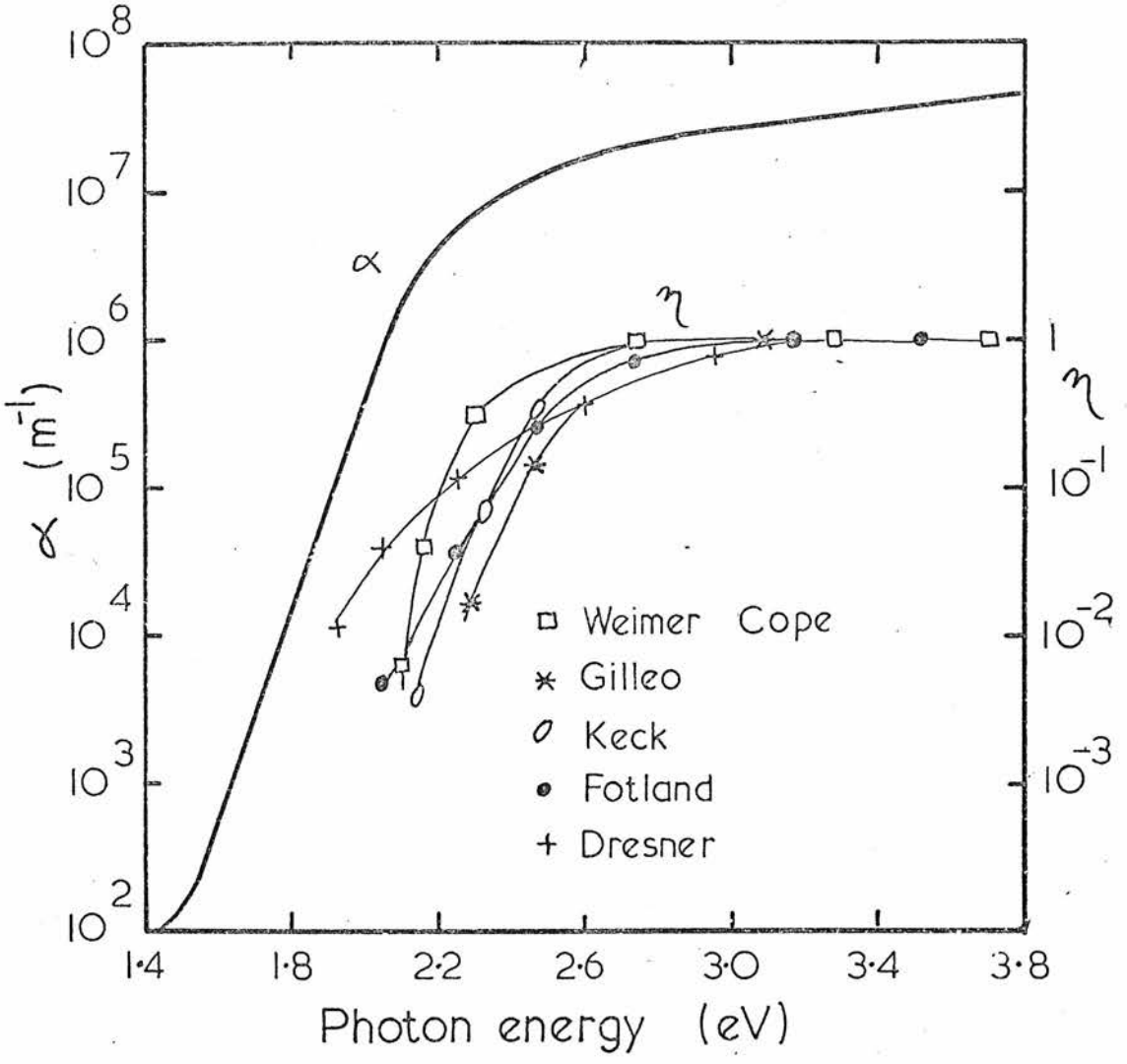

Fig 3 2 Optical Absorption and Quantum Efficiency in Se (ref 90)

A one electron state model has been proposed, e.g. by Lanyon[82]. Here a transition between a localised tail state and an extended state will produce one 'free' (say electron) and one trapped (hole) carrier. The quantum efficiency for hole generation would be less than unity if the recombination probability for the trapped carrier is greater than its thermal emission probability. The approximate equality of electron and hole responses over a wide range of photon energies[98] argues against this.

The interaction models may be subdivided into 'single-process' and 'two process' models.

Hartke and Regensburger[90] proposed a 2-process model, in which process 'P' involved direct interband transitions, with $\eta = 1$, and process 'N' produced excitons which were rapidly self trapped, and could not be ionised ($\eta = 0$). Lucovsky[100a] considers the molecular nature of Se, and the possibility of bound excitons as excited states of Se_8 ring molecules.

The quantum efficiency at photon energy $h\nu$ is then

$$\eta(\nu) = \frac{\epsilon''_P(\nu)}{\epsilon''_P(\nu) + \epsilon''_N(\nu)} \qquad 3.2.4$$

where $\epsilon''(\nu)$ is the imaginary part of the complex dielectric constant. Using optical data and the Kramers-Kronig relation, the non photoconducting absorption was associated with phonon aided transitions to a weakly bound exciton state.

The field dependence of η was associated with deep trapping and recombination effects - i.e. a range

limitation, by which at low fields, some carriers were lost. This is not consistent with much of the high field data, where with typical geometries, such a limitation does not apply.

One process models have been discussed by Tabak and Warter[89], Davis and Mott[17], and Knights[98] - in some detail. The essence of the classical treatment of this model is the probability of separating a photogenerated electron hole pair against their mutual coulomb attraction. Figure 3.3 illustrates some of the features of the model. For an interband transition with photon energy $h\nu$, the excess kinetic energy of the carriers, over the local coulomb potential, is

$$K.E. = (h\nu - E_{opt}) + e^2/4\pi\epsilon\epsilon_o r \qquad 3.2.5$$

This excess K.E. is lost by rapid thermalisation by phonon emission while the carriers move apart in diffusive motion with a short mean free path. The rate of loss of energy is expected to be rapid for such a case if k-selection rules are relaxed[17].

The separation after thermalisation, r_t can be found from random walk theory (diffusion) and the binding energy E_o at this separation, calculated[98]

$$r_t = \left(\frac{D(K.E)}{h\nu_p^2}\right)^{\frac{1}{2}} \qquad 3.2.6$$

$$E_o = \frac{e^2}{4\pi\epsilon\epsilon_o r_t} \qquad 3.2.7$$

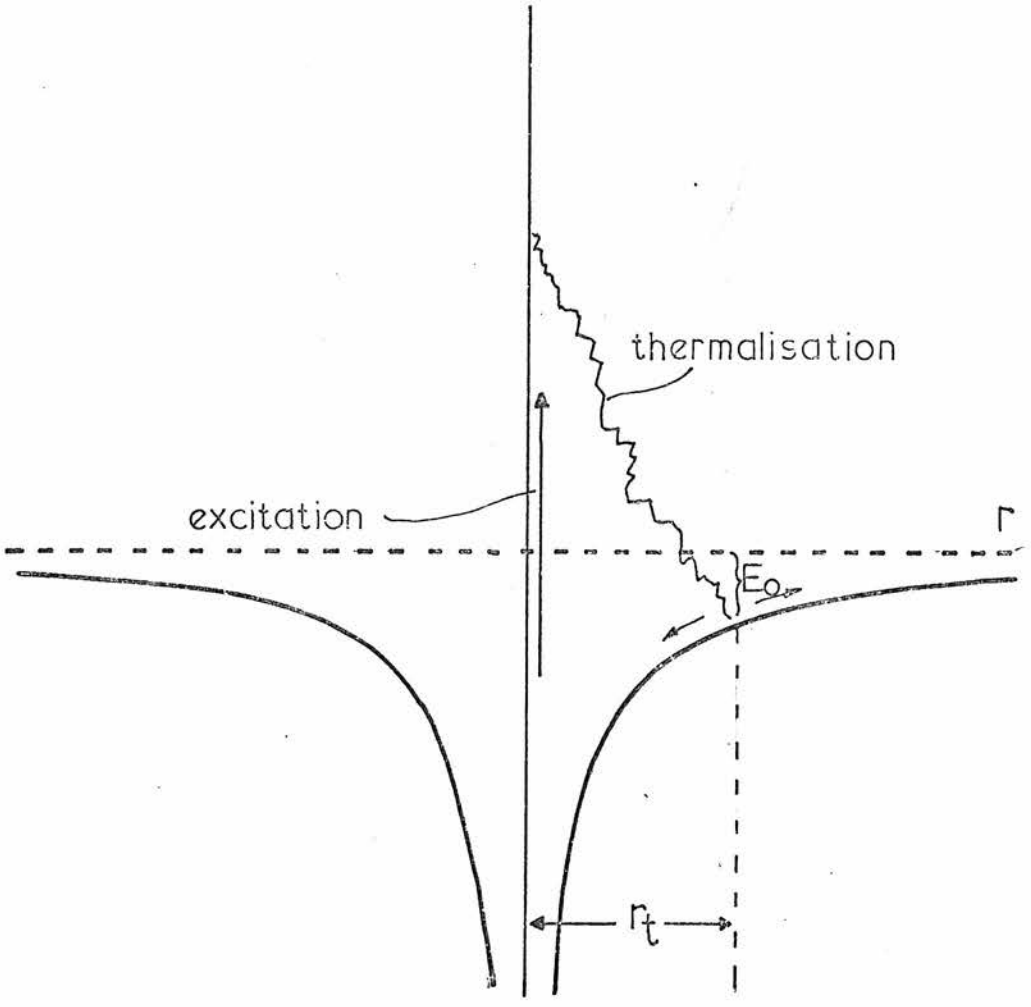

Fig 3.3 Photogeneration in Se
(ref 17)

The quantum efficiency is then found by considering the relative probabilities, at this point, for ionisation - which is activated, and 'geminate recombination', considered constant.

The treatment accounts for the gap of ~0.5 eV between absorption and quantum efficiency 'edges'. As E_o is dependent upon $h\nu$, the variation of activation energy for η, with photon energy, given in equation 3.2.3 is explained, while Poole-Frenkel barrier lowering as discussed in 2.2.5, accounts for the high field dependence. Various modifications to this treatment, e.g. for low fields, are discussed by Tabak and Warter[87], and Knights[98].

The model as presented allows a continuum of binding energies in a classical treatment, which may have limited validity, although a spreading of allowed 'discrete' binding energies, which may be close together at the top of the well, could occur in such materials. Selenium has been used as an example here, as there are few reports on quantum efficiencies in other chalcogenides. It is possible that the molecular nature of Se is responsible for its behaviour, and this must be borne in mind when considering other materials.

3.2.3 GENERAL FEATURES OF PHOTOCONDUCTIVITY IN AMORPHOUS CHALCOGENIDES

Photoconductivity experiments on a number of amorphous chalcogenides, using gap-cell geometry as described in 3.2.1, reveal several similar features.

Among the materials studied are $Ge_{15}Te_{81}Sb_2S_2$, $Si_{11}Ge_{11}As_{35}P_3Te_{40}$, $Ge_{16}As_{35}Te_{28}Si_{21}$[99], $2As_2Te_3.As_2Se_3$[100], As_2Se_3[101], and As_2Se_3 doped with Cu, Ag, In, Ga[102,103].

Figure 3.4 shows a sketch of the typical behaviour observed for ΔI vs $1/T$ at several excitation levels[99]. A maximum is observed in the temperature dependence, and on the high temperature side, the photoconductivity is smaller than the dark conductivity, increases exponentially with $1/T$, with 'activation energy' ΔE_m, and varies linearly with excitation F.

On the low temperature side, the photoconductivity is greater than the dark conductivity, decreases exponentially with $1/T$, with activation energy ΔE_b, and varies as $F^{\frac{1}{2}}$. At low temperatures, this slope may decrease, as shown.

Figure 3.5 shows explicitly the relation between ΔI and F (in photons m^{-2} s^{-1}) on a log-log scale, for two temperatures, as reported by Weiser et al[100] on $2As_2Te_3.As_2Se_3$. At low intensities, $\Delta I \propto F$, while at high intensities $\Delta I \propto F^{\frac{1}{2}}$, and the temperature dependence reverses, between those two regimes, in agreement with the observations on figure 3.4.

In general these features have been interpreted in terms of trapping and recombination kinetics. In the 'linear' regime, recombination is 'monomolecular', while in the square root regime, recombination is 'bimolecular'. The discussion which follows in this chapter examines the kinetic theory behind these descriptions.

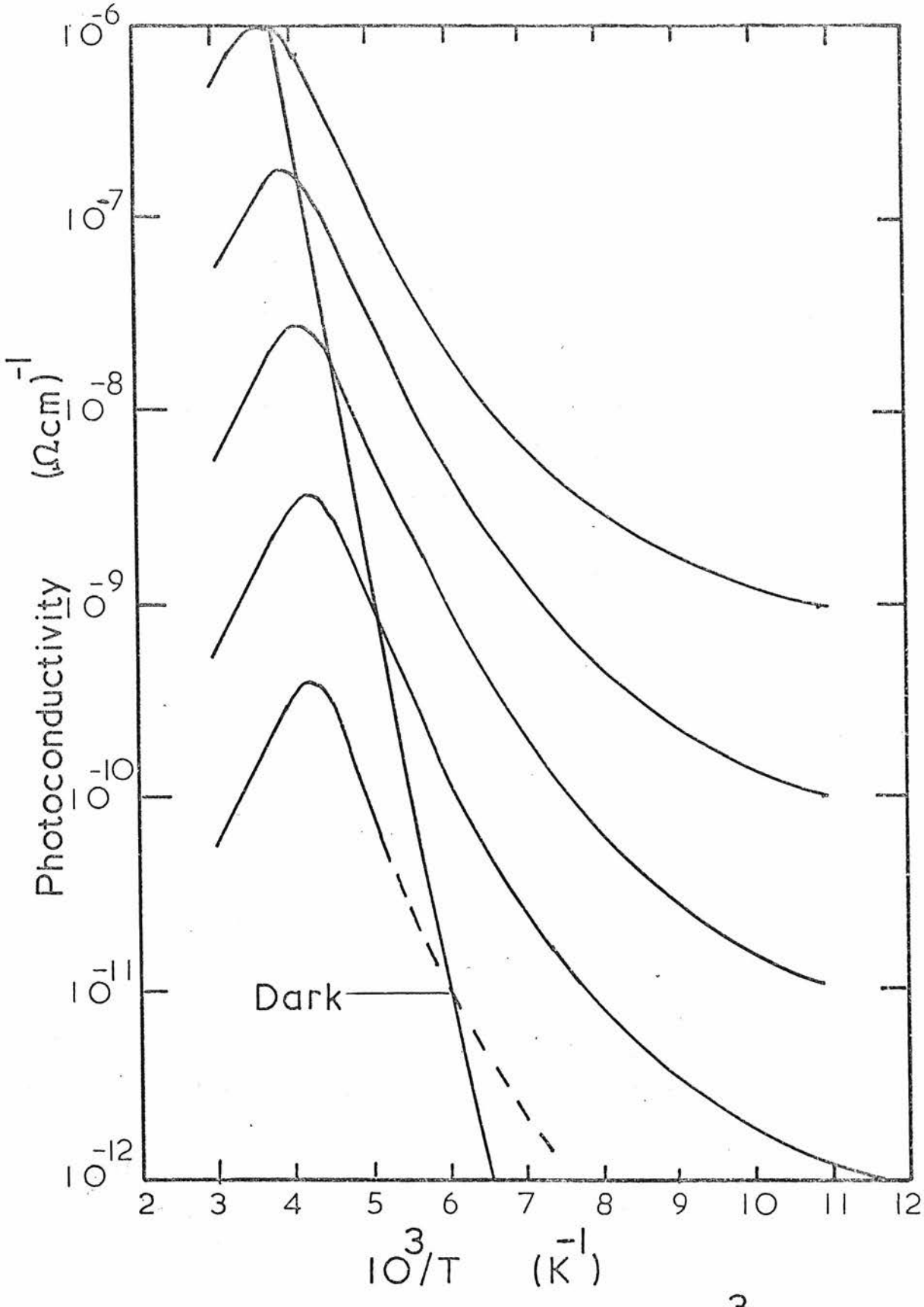

Fig 3.4 Photoconductivity vs $10^3/T$ at various excitations ($Ge_{15}Te_{81}S_2Sb_2$) (ref. 99)

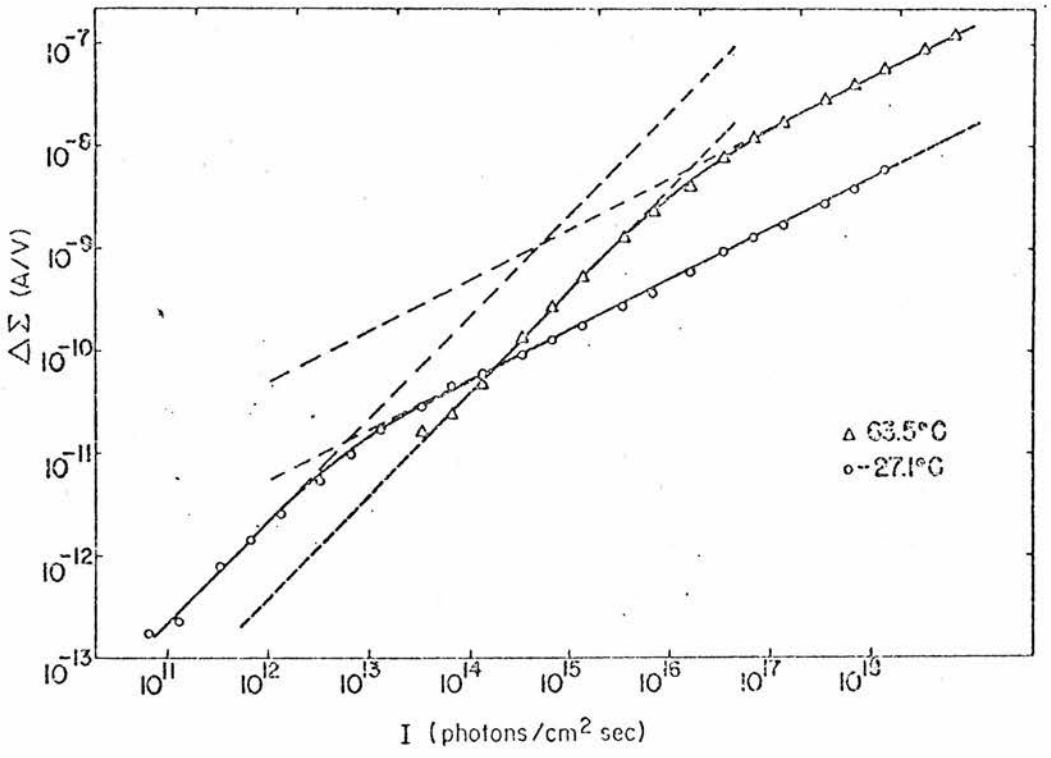

Fig 3.5 Photoconductance vs photon flux in $2.As_2Te_3.As_2Se_3$ (ref. 100)

The wavelength dependence of the steady state photocurrent has also been measured, using gap-geometry[59,89,101-105] in a number of chalcogenides. In such experiments, the generation, transport, and recombination effects cannot be effectively separated, as in the 'drift' technique described in 3.2.2. This may lead to widely different results, on the same material, if different measurements and normalisation procedures are used. Figure 3.6 illustrates this for the spectral response ΔI vs $h\nu$ in As_2Se_3, as reported by Kolomiets[103] and Rockstad[105]. To clarify this point - if spectral sources, such as monochromators, are used, which produce illumination whose intensity varies with wavelength, the photoresponse may be normalised to constant incident energy, or constant incident photon flux. Such a procedure is unreliable however, if the appropriate 'recombination regime' is not known, or unspecified. This probably accounts for the differences in the literature, and make it difficult to extract any information on quantum efficiencies, band gaps etc., from such data.

Two general types of behaviour emerge, however. In some materials[59,89], the photoresponse rises to a saturation value with increasing photon energy, near the optical gap energy E_{opt}, and remains constant to high photon energies. In other materials[103], a peak is observed, and the response drops at high photon energies above E_{opt}. While in crystalline semiconductors, such behaviour is often associated with surface recombination

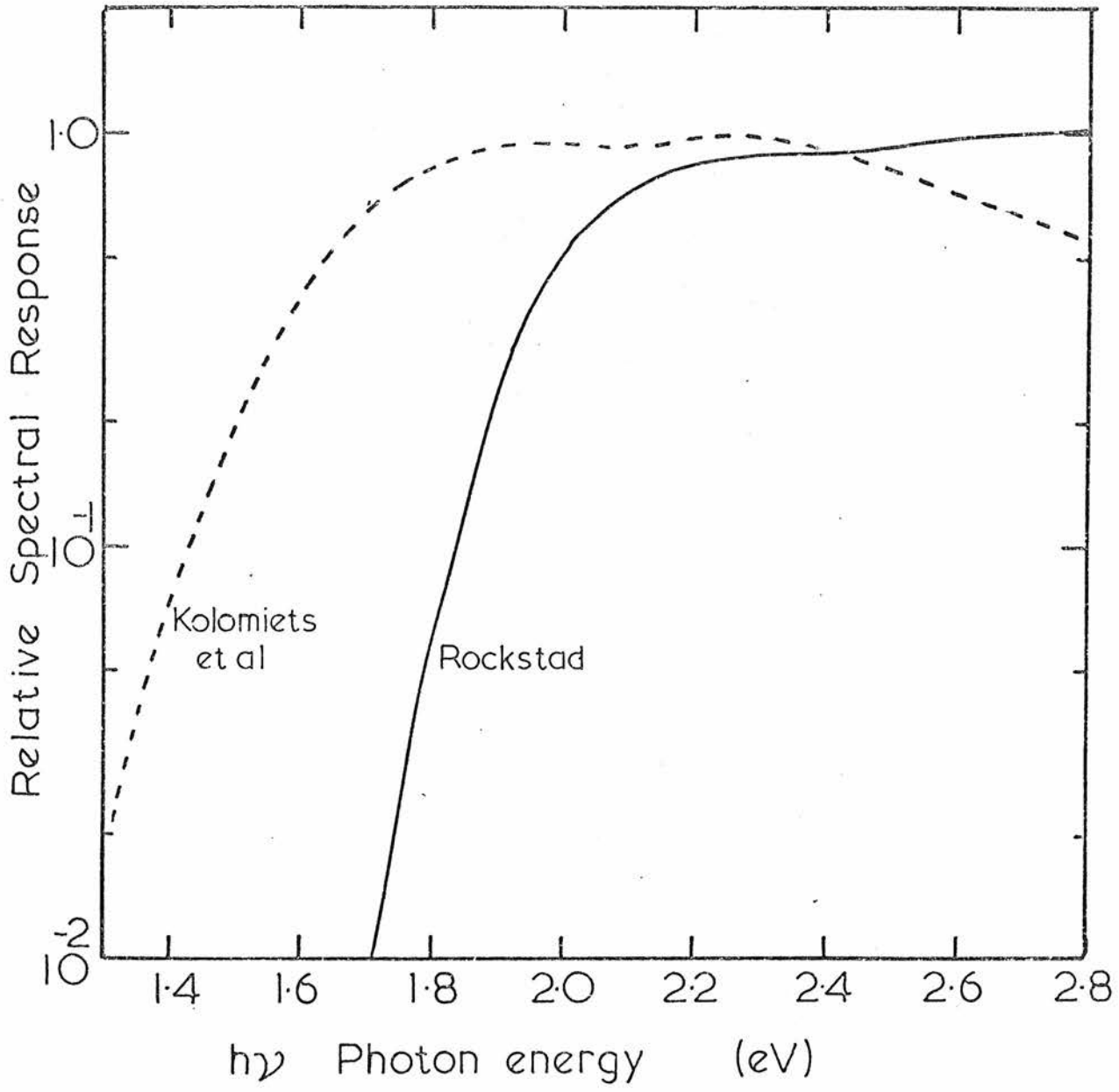

Fig 3.6 As_2Se_3 Spectral response (photocurrent) from two sources.

centres, it will be shown, in chapter 8, that the bulk recombination kinetics may explain this feature.

3.2.4 DENSITY OF STATES MODELS

A number of different models for the density of states in amorphous chalcogenides have been used in interpretations of the behaviour discussed in 3.2.3.

Distributed states. Treatments using distributed localised states have usually taken the C.F.O. model as a guide-line, in that the two 'tails' of states reflect their parentage in their charge-occupancy type. The conduction band tail states-distribution function $g_c(E)$ are negative when electron occupied while valence tail states-distribution $g_v(E)$ are neutral when electron occupied.

Weiser et al[100], Arnoldussen et al[99], and Simmons and Taylor[106-108], use wide exponential tails, shown in figure 3.7a. Weiser and Simmons have mainly treated a symmetric case, (single tailing constant E_o) while Arnoldussen et al have also treated asymmetric tails.

Mott and Davis[109] have used a more limited linear tail model, shown in figure 3.7b, where the distributions fall to zero at E_A and E_B.

Discrete levels. As mentioned in chapters 1 and 2, some of the simpler chalcogenide compounds (such as those studied in this work (As_2Te_3,As_2Se_3)) in the short range may be structurally well defined. Fairly discrete localised levels may therefore appear, associated with

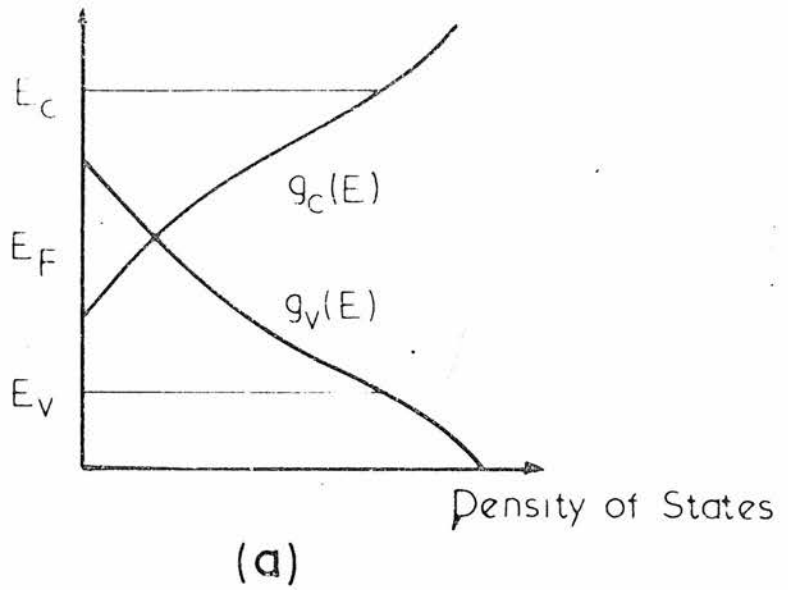

(a)

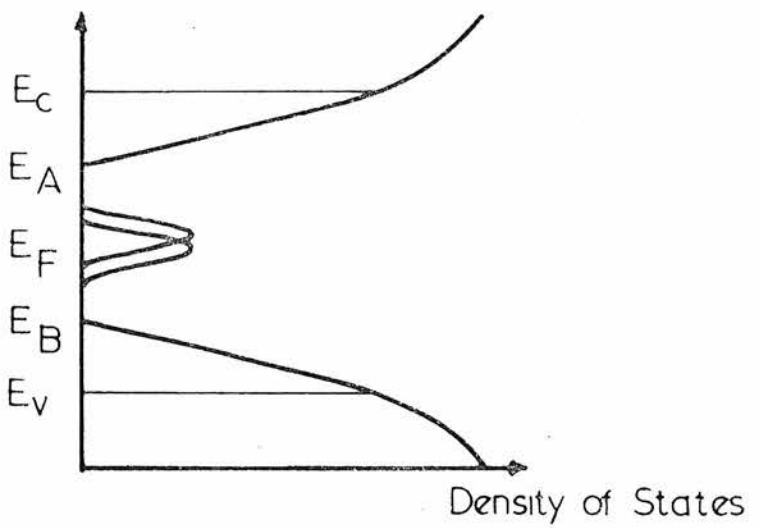

(b)

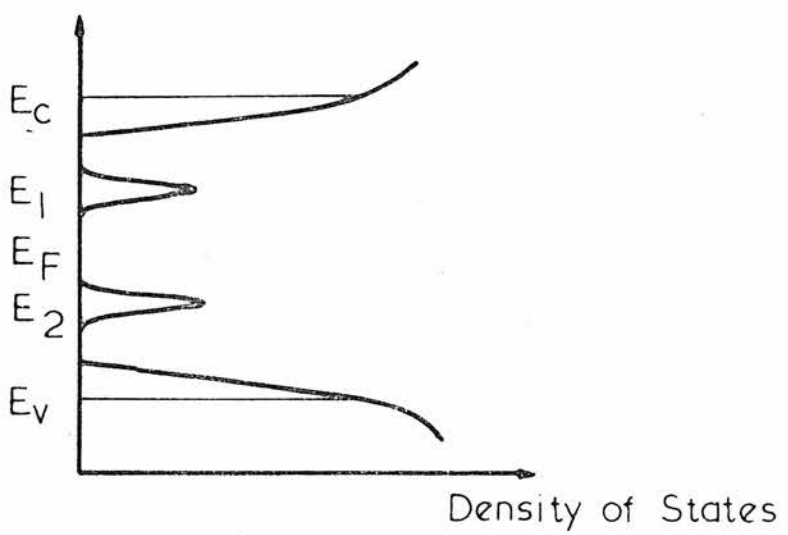

(c)

Fig 3.7 Density of States Models

(a) C.F.O.
(b) Mott-Davis
(c) 'Discrete' Levels

well defined structural defects, although limited band-tails may also be present. It is this 'conventional semiconductor' approach which has been used mainly in this work, as the simplest means of interpreting experimental data. In addition, it will be shown that, with the exception of Simmons and Taylor's work, the assumptions employed by the 'distributed states' authors reduce their analyses to a situation very similar to the discrete level case.

Figure 3.7c shows again the discrete level density of states diagram. For simplicity, set '1' above E_F is assumed to be of neutral centres as is the C.F.O. conduction band tail, and set '2' below E_{FO}, is of the same charge-type as the C.F.O. valence band tail, although reversing the charge-type to 'coulombic' centres would not seriously affect the results.

It should be noted that other localised state levels may exist within the mobility gap, and which are not revealed by the present experiments. To this extent this work presents an 'approach', and not a 'model'.

The following sections discuss the general theory for kinetics in semiconductors, before application is made to such models for amorphous materials.

3.2.5 ELECTRON TRANSITIONS

The following sections deal with the 'kinetic' terms in the continuity equations, which describe electron and hole transitions between the states in a semiconductor, in the absence of spatial effects. In thermal

equilibrium, the rates of the various transitions result in the Fermi-Dirac distribution, described in 2.1.2. When excess generation is present, the other rates alter, and a new steady state is reached. This process is discussed in the following sections.

Figure 3.8 shows on a simplified schematic band diagram, the transitions which will be considered. Band to band electron excitation (generation) labeled G and its inverse, the capture of a free electron by a free hole (recombination) labeled G'.

It will be assumed that the localised states normally encountered are monovalent, possessing only two occupancy states. A localised state - here at energy E_i, may capture a free electron-transition a, and can release such a trapped electron, back to the conduction band-transition a'.

Such a monovalent state, may, when occupied by an electron, capture a free hole by transition d', which can subsequently be re-excited-transition d.

The possibility of transitions between localised states has already been mentioned in connection with hopping conduction, where the initial and final states are in the same trap distribution, and have similar energies. Ryvkin[110], Weiser[59], and others have pointed out that transitions between localised states widely separated in energy may be possible, if there is sufficient overlap of the wave functions. This is included in figure 3.8 where electron transitions between states at E_j and E_i are shown (electron loss from

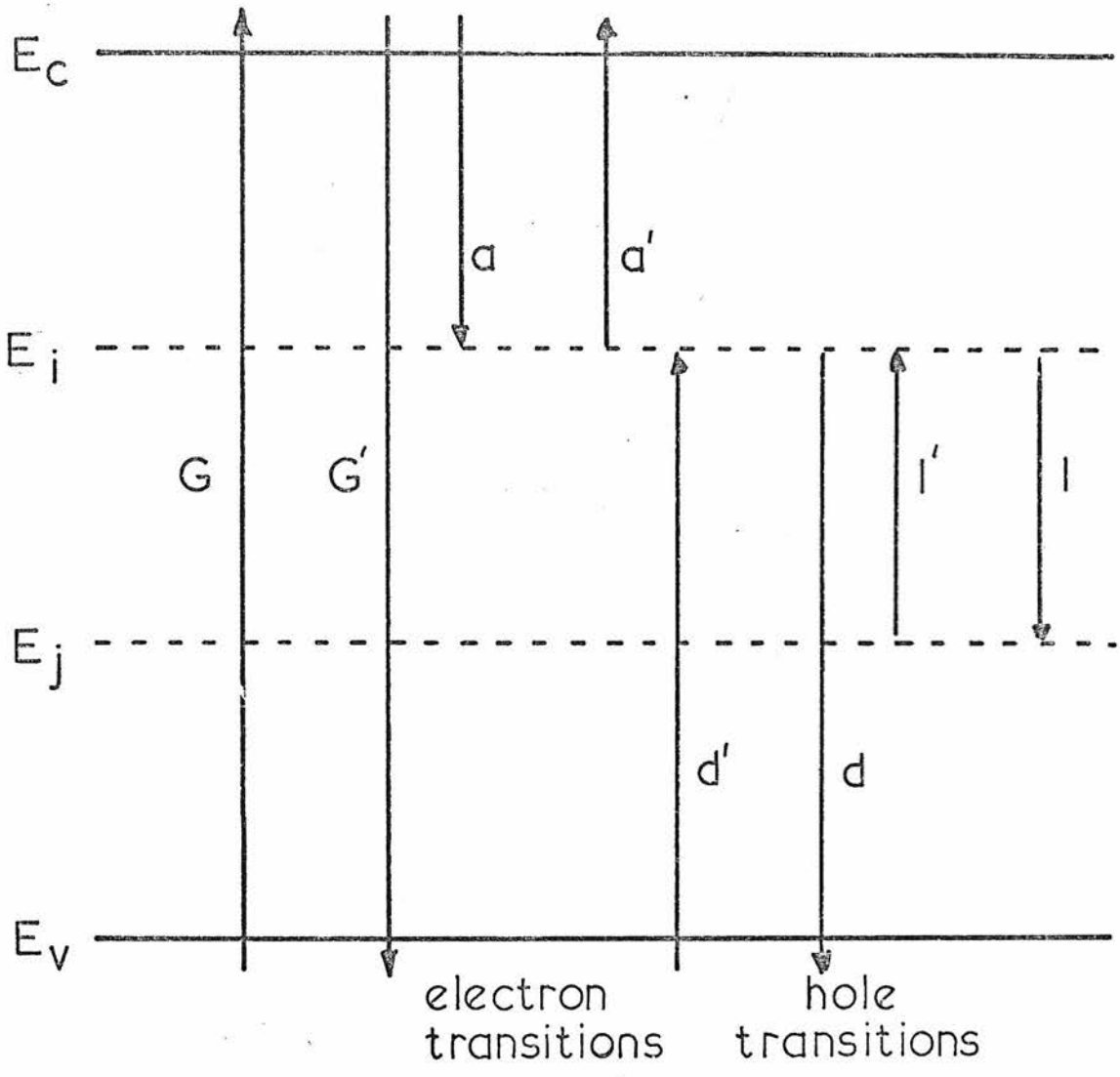

Fig 3.8 Carrier Transitions

and capture into E_i, denoted by $1'$ and 1 respectively)

Trapping and recombination. The process by which a carrier is captured by a localised state and re-released to the same band, is normally termed 'trapping', while the annihilation of an electron by a hole is termed 'recombination'. Recombination can occur by direct band to band transitions (G') or via localised states by a number of steps. A two step process occurs when the state captures first an electron (a) then a hole (d'), or vice versa. Localised-localised recombination also occurs in the model of figure 3.8, where a state at E_i captures an electron, at state at E_j captures a hole, and a localised-localised transition subsequently occurs.

A localised state can therefore act as a trapping centre, and a recombination centre, and the assignment of one or other of these names to the state depends only on its relative efficiency in those roles.

The nomenclature is for this reason, loose.

Types of transition. There are basically 3 ways in which energy can be absorbed or released in a transition. Blakemore[115] discusses the various processes. Radiative transitions, in which a photon is absorbed, or released may be direct or indirect if phonon participation occurs.

Radiationless transitions, in which only phonons participate. If the energy involved in the excitation or capture is high ($>> kT$) several phonons are required together.

Auger transitions, in which kinetic energy of a

third carrier (as well as the initial and final states of the carrier making the transition) is involved. The excitation process is impact ionisation.

In the analysis which follows, in this chapter, the spin degeneracy factor in the trap occupancy function will be absorbed into the exponential factor, by definition, for clarity. Mass action laws appropriate to 'radiative' and 'radiationless' transitions, described above, will be considered.

3.2.6 TRANSITION PROBABILITIES AND MASS ACTION LAWS

Quantum mechanical/phenomenological picture. In principle, transition probabilities for the various types of transition can be calculated using quantum mechanics, and in some crystalline semiconductors, where the band structure and form of the wave functions is well known, this has been done. In amorphous semiconductors, where there is little detailed knowledge of band structure and wave functions, transition probabilities can be expressed by phenomenological methods, in terms of mass action laws, involving such parameters as capture-cross sections. This method has been used successfully in the past in crystalline semiconductors to construct models for the materials in question, from experimental data. The full quantum mechanical picture cannot be constructed, but useful information on the types of transition and the distribution and types of state can be found.

Capture probability/time and rate. Radiative and radiationless (phonon) transition rates can be described by similar mass action laws. Consider firstly free electron capture by 'i' centres at E_i, density N_i cm^{-3}, and electron occupancy f_i, transition a in figure 3.8. The probability (per unit time) of such capture is

$$P(\text{capture}) = 1/\tau^{n}_{ti} = C^{n}_{i} N_i(1 - f_i) \qquad 3.2.8$$

where C^{n}_{i} is a 'capture coefficient', $N_i(1 - f_i)$ is the density of capturing centres, and τ^{n}_{ti} is the mean free electron capture time by unoccupied 'i' states.

The total electron capture rate (m^{-3} s^{-1}) for free electron density n, is

$$r^{n}_{i} = n/\tau^{n}_{ti} = C^{n}_{i}\, n\, N_i(1 - f_i)\ m^{-3} s^{-1} \qquad 3.2.9$$

For free hole capture transition d', now by occupied 'i' centres, similar expressions can be written - the rate r^{p}_{i} is

$$r^{p}_{i} = p/\tau^{p}_{ti} = C^{p}_{i}\, p\, N_i f_i \ \ m^{-3}\ s^{-1} \qquad 3.2.10$$

where C^{p}_{i} and τ^{p}_{ti} are the capture coefficient and mean capture time respectively for free hole capture by an 'i' state. These transitions may be called band-localised, or B-L.

Localised-localised 'hole capture' transition 1'. A localised-localised (L-L) capture transition occurs when a hole from an electron unoccupied 'j' state, is captured by an occupied 'i' state. If the density of

'j' states is N_j, and electron occupancy is f_j, then the rate is

$$r_{ij} = N_j(1 - f_j)/\tau_{ij} = K_{ij}\, N_i f_i\, N_j(1 - f_j) \qquad 3.2.11$$

where K_{ij}, and τ_{ij} are the transition coefficient and mean transition time respectively, for L-L hole transitions into 'i' states from 'j' states (or L-L electron transitions into 'j' states from 'i' states). Note that L-L 'electron transitions' could have been considered instead. The choice is arbitrary.

Free-free capture transition G'. The rate of free electron-hole capture is

$$r_{np} = C_{np}\, p\, n = p/\tau_n = n/\tau_p \qquad 3.2.12$$

where C_{np}, τ_n, τ_p, are the free-free capture coefficient, electron capture time, and hole capture time.

Detailed balance and release transitions. The rates of the inverse transitions (a', d, l) can be written in a similar way, regardless of the mechanisms involved, whether radiative or radiationless, by invoking the principle of detailed balance. This states that in a system in thermal equilibrium, the rates of a process and its inverse are equal, and balance in detail.

Consider electron release from 'i' states, to the conduction band. If this is a phonon-involved process, the rate e_i^n can be expressed in terms of an 'attempt to escape frequency' ν_e, related to the highest phonon frequency[111], and at thermal equilibrium

$$e_{io}^{n} = N_i f_{io} \nu_e \exp(-\frac{E_c - E_i}{kT}) \qquad 3.2.13$$

where the subscript 'o' refers to thermal equilibrium. By equating 3.2.13, and equation 3.2.8 at thermal equilibrium, ν_e may be eliminated, to give

$$\nu_e = N_c C_i^n \qquad 3.2.14$$

$$\text{and} \qquad e_i^n = N_i f_i C_i^n n_i = N_i f_i / \tau_{tri}^n \qquad 3.2.15$$

$$\text{where} \qquad n_i = N_c \exp(-\frac{E_c - E_i}{kT}) \qquad 3.2.16$$

n_i is an 'effective density' - the density of free electrons which would exist if the Fermi level were coincident with the traps, and is introduced to give the capture and release rates equations 3.2.15 and 3.2.8, the same form. τ_{tri}^n is the mean emission time of an electron in an 'i' state. Note that equation 3.2.15 for the release rate, would follow whatever the release mechanism.

Similarly, the rate of free hole release (transition d) can be written

$$e_i^p = N_i(1 - f_i) C_i^n p_i = N_i(1 - f_i)/\tau_{tri}^p \qquad 3.2.17$$

$$\text{where} \qquad p_i = N_v \exp(-\frac{E_i - E_v}{kT}) \qquad 3.2.18$$

Localised-localised 'hole release' transition l.

The rate of L-L release transitions - i.e. of holes from i to j states (or electrons from j to i states) is

$$e_{ji} = K'_{ji} N_i(1 - f_i) N_j f_j = N_i(1 - f_i)/\tau_{ji} \qquad 3.2.19$$

where $$K'_{ji} = K_{ij} \exp(-\frac{E_i - E_j}{kT}) \qquad 3.2.20$$

Lastly, the free-free spontaneous generation rate (transition G') is

$$e_{np} = C_{np} N_v N_c \exp(-\frac{E_c - E_v}{kT}) \qquad 3.2.21$$

in a wide band, non-degenerate semiconductor.

3.2.7 CAPTURE CROSS SECTIONS

In the case of capture of a free carrier, the capture coefficient of the centre involved can often be written

$$C = vs \qquad 3.2.22$$

where v is the mean thermal speed of the free carrier, and s is the 'capture cross section' of the centre for that carrier. Thus, the capture coefficients of 'i' states for electrons and holes can be expressed

$$C_i^n = v_n \, s_i^n \quad cm^3 \, s^{-1} \qquad 3.2.23$$

$$C_i^p = v_p \, s_i^p \qquad 3.2.24$$

where v_n and v_p are the free electron and hole thermal velocities, and s_i^n and s_i^p are the capture cross sections of unoccupied and occupied 'i' centres for free electrons and holes respectively. Similarly, for free-free capture,

$$C_{np} = v_n \, s_p = v_p \, s_n \qquad 3.2.25$$

where s_p and s_n are the capture cross sections of a free hole and electron, for the opposite carrier.

If the electron and hole effective masses are taken to be isotropic and equal to that of a completely free electron (m_o) then

$$v_n = v_p \approx 10^5 \text{ m s}^{-1}$$

Experimentally, values of s have been found between 10^{-16} m^2 and $< 10^{-24}$ m^2, in crystalline semiconductors.

Radiative capture by a free carrier or localised centre, usually gives a value of about 10^{-23} m^2. It is interesting to note that this can be calculated from the observed optical absorption spectra of a material, and the principle of detailed balance[112].

This result implies that the probability of interband radiative recombination (transition G') is very low in non-degenerate semiconductors with a band gap of >20 kT.

Radiationless or phonon involved capture can result in a wide range of capture cross-sections, depending on the type of centre involved. For such a process to have a high probability, the carrier must be strongly coupled to the lattice in its initial or final state - i.e. localised. Radiationless interband transitions are therefore also very unlikely.

If the binding energy or 'depth' of the localised state is >> kT, then a number of phonons are involved

in the transitions. Simultaneous emission of several phonons has a low probability ($s << 10^{-19}$ m^2). Lax[1] has proposed a model where a carrier is first captured into a highly excited state of the centre, followed by a 'cascade' process through the excited states, to the ground state, each step requiring one or two phonons only.

The cross-section for coulomb-attractive centres can thus be as high as 10^{-16} m^2. For neutral centres, as pointed out[1], the polarizability of the centre could give rise to an inverse fourth power potential of moderate range, (several Angstroms) and the possibility of a 'ladder' of excited states. Lax calculates that for neutral centres as deep as 0.5 eV, a capture cross section of 10^{-19} m^2 is possible, with emission of acoustic or optical phonons.

Capture cross-sections of $\lesssim 10^{-26}$ m^2 are normally associated with coulomb repulsive centres, - simultaneous multiphonon emission being a probable capture mechanism. Capture cross-sections, as defined, cannot be associated with localised-localised (L-L) transitions. L-L transitions over more than a few kT of energy are assumed to be radiative[100,113]. In this case, it is of interest to compare the L-L capture coefficients obtained (K) with the capture coefficient C of a centre of typical cross-section e.g. 10^{-21} m^{-2}, which gives $C \approx 10^{-16}$ m^3 s^{-1}. This is about the highest value for radiative recombination in crystalline semiconductors (GaAs), and is unlikely to be exceeded in L-L transitions.

3.2.8 RATE EQUATION FORMALISM

The steady state case. This section deals with the non-equilibrium steady state situation, for an arbitrary trap distribution. In this case, the rate of change of occupancy of the levels involved is zero. Having dealt with this case, introducing such important concepts as 'Quasi Fermi levels' and 'demarcation levels', and treating the various approaches in the literature, (including the discrete level) will enable transient effects to be considered, in section 3.3.

Arbitrary trap distribution. The discrete level used to introduce the various electron/hole transitions can now be assumed to be part of a distribution of 'traps' g(E) in the mobility gap, such that

$$N_i \equiv g(E_i)dE \qquad 3.2.26$$

In the following discussion, transition rates will therefore be integrated or summed over all possible initial and final states in the distribution and bands.

Using a single distribution function, rather than, say, one for each band tail, simplifies the general approach, while differences in charge/occupancy type can be introduced later in a 'charge neutrality' condition.

It is also necessary to introduce energy dependent capture coefficients for capture of a free electron $C_n(E)$, capture of a free hole $C_p(E)$, and for L-L 'hole capture' transitions $K(E_i, E_j)$.

As a centre probably has a greater capture cross section in its charged state (for the opposite sign carrier) than in its neutral state, this, to some extent, identifies the band tails.

$K(E_i,E_j)$, and $K'(E_i,E_j)$ may each be split into capture (energy releasing) and emission (energy absorbing) components.

i.e. $K(E_i,E_j)$ $E_j < E_i$ energy release - hole capture

$E_j > E_i$ energy absorbed - electron emission

$K'(E_i,E_j)$ $E_j < E_i$ energy absorbed - hole emission

$E_j > E_i$ energy release - electron capture

The occupation function for states in the distribution is $f(E)$, and its complement, the hole occupancy $(1 - f(E))$ is written $\overline{f}(E)$. The 'effective' densities for release purposes are written n_1 and p_1.

Free carrier rate equations. Neglecting free-free recombination, the occupancy of the conduction band is determined by the following rate equation

$$\frac{dn}{dt} = G - \int_{E_v}^{E_c} n\, C_n(E)\, g(E)(1 - f(E))dE + \int_{E_v}^{E_c} n_1(E)\, C_n(E)\, g(E)\, f(E)dE = 0 \qquad 3.2.27$$

Note that the densities and rates are total quantities, including both thermal equilibrium terms (denoted by subscript 'o') and excess terms (denoted by prefix Δ)

$$\text{e.g.} \quad G = G_o + \Delta G$$

$$n = n_o + \Delta n \quad \text{etc}$$

$$f(E) = f_o(E) + \Delta f(E)$$

The occupancy of the valence band can also be written, in a similar way

$$\frac{dp}{dt} = G - \int_{E_V}^{E_C} p\, C_p\,(E)\, g\,(E)\, f\,(E) dE + \int_{E_V}^{E_C} p_1\,(E)\, C_p\,(E)\, g\,(E)\,[1 - f(E)] dE = 0 \qquad 3.2.28$$

Expressing 3.2.28 in terms of the trap hole occupancy $\overline{f}(E)$ makes the equations symmetrical in form for n, and p.

To solve equations 3.2.27 and 3.2.28 for the free carrier densities, for a given trap distribution ($C_p(E)$, $g(E)$, $C_e(E)$ known), requires a knowledge of the trap occupation function $f(E)$, in the particular steady state case considered.

Trap occupancy function. In the steady state, the trap occupancy function must be calculated in terms of the 6 types of transition discussed in 3.2.5.

Shockley and Read[114] calculated the occupancy for a single trap level, for the conventional case - i.e. no L-L transitions, and Simmons[106] showed that their result also applied to distributed traps, also neglecting L-L transitions.

The general result including L-L transitions can be found as follows. The total rate of change of trap

occupancy, by all 6 mechanisms, integrated across the mobility gap must be zero

i.e.

$$\int_{E_V}^{E_C} n\, C_n(E)\, g(E)\, [1 - f(E)]dE \qquad - \int_{E_V}^{E_C} n_1\, C_n(E)\, g(E)\, f(E)dE$$
$$(a) \qquad\qquad (a')$$

$$- \int_{E_V}^{E_C} p\, C_p(E)\, g(E)\, f(E)dE \qquad + \int_{E_V}^{E_C} p_1\, C_p(E)\, g(E)\, [1 - f(E)]dE$$
$$(d) \qquad\qquad (d')$$

$$- \int_{E_V}^{E_C}\int_{E_V}^{E_C} K(E,E_j)\, g(E)\, f(E)\, g(E_j)\, [1 - f(E_j)]dE_j dE \qquad (1')$$

$$+ \int_{E_V}^{E_C}\int_{E_V}^{E_C} K'(E,E_j)\, g(E)\, [1 - f(E)]\, g(E_j)\, f(E_j)dE_j dE \qquad (1)$$

$$= \frac{d}{dt} \int_{E_V}^{E_C} g(E)\, f(E)dE = 0 \qquad 3.2.29$$

As Simmons[106] points out, if such an equation is valid for an arbitrary trap distribution, then the integrand (with respect to E) is also zero.

$$\therefore\ g(E)[1-f(E)]\{nC_n(E) + p_1C_p(E) + \int_{E_V}^{E_C} K'(E,E_j)g(E_j)f(E_j)dE_j\}$$
$$= g(E)[f(E)]\{n_1C_n(E) + pC_p(E) + \int_{E_V}^{E_C} K(E,E_j)g(E_j)[1-f(E_j)]dE_j\} \qquad 3.2.30$$

The terms within the braces on the L.H.S. represent the sum of 'electron <u>in-going</u>' transition probabilities (per unit time) for unoccupied traps at Energy E, (i.e. electron capture and hole release) while those on the

R.H.S. represent the sum of electron outgoing transition probabilities for occupied traps. .(i.e. electron release and hole capture). Replacing these probabilities with the appropriate transition labels used in 3.2.11, the occupancy function can be expressed,

$$f(E) = \frac{a + d + l}{a + a' + d + d' + l + l'}$$

$$= \frac{\Sigma \text{ electron 'in-going' transition probability}}{\Sigma \text{ all transitions probability}} \qquad 3.2.31$$

now l and l' refer to the integrals of L-L transitions - as in 3.2.30. This is equivalent to the expression derived by Arnoldussen et al[99], using two distribution functions, but it should be noted that in the steady state, B-L and L-L transitions balance independently, so from 3.2.27 and 3.2.28 and 3.2.29

$$f(E) = \frac{a + d}{a + a' + d + d'} = \frac{l}{l + l'} \qquad 3.2.32$$

Similarly, the hole occupancy is given by

$$\overline{f}(E) = \frac{a' + d' + l'}{a + a' + d + d' + l + l'} \qquad 3.2.33$$

The statistic derived from equation 3.2.29 is completely general, and covers all the cases reported in the literature. It allows for an arbitrary distribution of traps, B-L, and L-L transitions - including multiple L-L transitions within the trap distribution.

Note that although the occupation factor can be expressed in terms of probabilities of two 'types' of transition i.e conventional B-L, and L-L transitions

independently this does not imply that calculations based on each type separately (i.e. ignoring the other) yield identical solutions.

The trap occupancy factor, and hence the free carrier densities contained in equation 3.2.31 depend, under the given conditions on the most probable transition 'paths' leading to electron-hole recombination, as will be discussed in 3.2.12. Such 'dominant' mechanisms control the statistic, and the less important transition probabilities merely (adjust to) fit the established statistic.

The charge neutrality condition. In the absence of injected charge and diffusion effects, uniform excitation must result in charge neutrality, as excitation and recombination involve charge pairs. The statement of charge neutrality actually gives additional information to that contained in the rate equations discussed.

In thermal equilibrium, the Fermi function results in a trap occupation ensuring neutrality as mentioned in 2.2. The change in occupation resulting from excitation also involves zero net charge. A general neutrality condition can now be written

$$\int_{E_V}^{E_C} g(E)\{f(E) - f_o(E)\}dE + n - n_o + p - p_o = 0$$

or

$$\int_{E_V}^{E_C} g(E)\,\Delta f(E)dE + \Delta n - \Delta p = 0 \qquad 3.2.34$$

For total densities the neutrality equation must be broadened to give

$$n + \int_{E_V}^{E_C} q(E)\, g(E)\, f(E)dE = p + \int_{E_V}^{E_C} [1 - q(E)]\, g(E)\, \bar{f}(E)\, dE \quad 3.2.35$$

where $q(E) = 1(0)$ if the state of charge of an electron occupied state at E is negative (neutral).

3.2.9 APPROXIMATIONS AND ASSUMPTIONS : A LIST

To continue from this point to solve the free carrier rate equations is in principle possible, but in the general case considered so far, is very difficult. Most treatments of the problem make a number of simplifying assumptions or approximations to allow analytic solutions to be made which are not too cumbersome, physically meaningful, and which fit the experimental data (sic).

(a) The form of g(E). This has already been discussed in some detail. Discrete levels may be represented by delta functions.

(b) The form of $C_n(E)$, $C_p(E)$ and $K(E_i, E_j)$. For discrete levels, those values can be fixed, while for distributed states, several different forms have been used, by different authors. This will be discussed in the relevant review sections.

(c) Simplified forms of f(E) and $\bar{f}(E)$ for different energy ranges, in given steady state conditions. Related to this are some important concepts in photoconductivity - Quasi Fermi levels, and Demarcation levels.

(d) Related to (b) and (c), simplifying assumptions regarding the possible recombination paths of photoexcited electrons and holes, and the important concept of lifetime.

(e) Small signal and large signal approximations. The variables are expressed as sums of equilibrium ('0') and excess ('Δ') terms. In small signal (low excitation) case, equilibrium components are much larger than excess terms, while in the large signal case, the opposite is true. Appropriate approximations can then be made.

3.2.10 QUASI - FERMI LEVELS

Under optical excitation the increased free electron and hole densities may be expressed formally in terms of two Quasi Fermi levels or 'IMREFS', E_{Fn}, and E_{Fp}, respectively, closer to the relevant bands than the equilibrium Fermi level, E_F

$$\text{i.e. } n = N_c \exp\left(-\frac{E_c - E_{Fn}}{kT}\right) \quad E_{Fn} > E_F \qquad 3.2.36$$

$$p = N_v \exp\left(-\frac{E_{Fp} - E_v}{kT}\right) \quad E_{Fp} < E_F \qquad 3.2.37$$

These energies may also be used in a limited way to describe trap occupancies, but Simmons[106] 'trap Fermi levels' provide a more general description, as will be shown.

In the 'small signal' case (3.2.9e), $E_{Fn}, E_{Fp} \approx E_F$, and the trap occupancy function is approximated by the equilibrium function $f_o(E)$. The discussion which follows,

therefore deals with the large signal case.

3.2.11 TRAP OCCUPANCY FUNCTION FEATURES

The interesting result of equation 3.2.32 allows many of the features of the trap occupancy function f(E), to be obtained by a 'conventional' approach, even when L-L transitions occur. The occupancy function can be expressed in two ways

$$f(E) = \frac{n\left(C_n(E) + p_1(E)\, C_p(E)\right)}{C_n(E)(n + n_1(E)) + C_p(E)(p + p_1(E))} \qquad 3.2.38$$

$$\equiv f(E) = \frac{\int_{E_V}^{E_C} K(E,E_j)\exp(-\frac{E-E_j}{kT})g(E_j)f(E_j)dE_j}{\int_{E_V}^{E_C} K(E,E_j)g(E_j)[1-f(E_j)(1-\exp(\frac{E-E_j}{kT}))]dE_j} \qquad 3.2.39$$

Note that both forms, 3.2.38 and 3.2.39 contain factors which implicitly depend upon the generation rate, and the predominant recombination paths. - i.e. form 3.2.38 contains the steady state free densities n and p, while form 3.2.39 contains the occupancy function ($f(E_j)$) itself. Nevertheless, analysis of form 3.2.38 alone will reveal the features of f(E), even when n and p may ultimately depend upon L-L recombination paths. A study of the probable recombination paths will then complete the analysis.

Constant trap species (Conventional approach).

Consider first the case where C_n and C_p are either independent of energy, or the ratio $C_n(E)/C_p(E) = R$ for a trap, is constant. Simmons[106] uses this (perhaps arbitrarily chosen) property to define a single trap

'species', with a great simplification in the resulting analysis

$$\text{i.e. } f(E) = \frac{Rn + p_1(E)}{R(n + n_1(E)) + p + p_1(E)} \qquad 3.2.40$$

Some initial simplification can be effected by noting that the 'thermal release' probabilities remain unchanged, while n and p are increased, with excitation. In certain energy ranges, $n_1(E)$ and $p_1(E)$ can be neglected.

$$\begin{aligned} &\text{Above } E_F, \quad p_1(E) < p_o < p \\ &\text{Below } E_F, \quad n_1(E) < n_o < n \end{aligned} \qquad 3.2.41$$

Define an energy E_i, as follows

$$E_i = \tfrac{1}{2}(E_v + E_c) - \frac{kT}{2} \log_e \left(R\frac{N_c}{N_v}\right) \qquad 3.2.42$$

This energy is probably within a few kT of the 'mid-gap' position, even for a large (or small) R, and is therefore close to E_F, which appears to be roughly mid-gap in many amorphous semiconductors

$$\begin{aligned} \text{for } \quad E > E_i \ (E_F) \quad & p_1(E) < R\, n_1(E) \\ E < E_i \ (E_F) \quad & R\, n_1(E) < p_1(E) \end{aligned} \qquad 3.2.43$$

Therefore above $E_F(E_i)$, $p_1(E)$ can be neglected, while below $E_F(E_i)$, $n_1(E)$ can be neglected, in equation 3.2.40.

$$\text{i.e. above } E_F \quad f(E) \approx \frac{nC_n}{C_n(n + n_1(E)) + pC_p} \qquad 3.2.44$$

$$\text{below } E_F \quad f(E) \approx \frac{nC_n + p_1(E)\, C_p}{nC_n + C_p(p + p_1(E))} \qquad 3.2.45$$

Trap Quasi-Fermi levels, and free Q.F.L.s.

Above E_F

As Simmons has shown[106], writing equation 3.2.42 as

$$f(E) = \frac{nC_n}{nC_n + pC_p}\left(1 + \frac{C_n n_1(E)}{nC_n + pC_p}\right)^{-1} \qquad 3.2.46$$

and defining a trapped electron Quasi-Fermi level E_{Ft}^n by

$$C_n N_c \exp(-\frac{E_c - E_{Ft}^n}{kT}) = nC_n + pC_p \qquad 3.2.47$$

then above E_F, the occupancy can be written as a modulated Fermi-Dirac function

$$f(E) = \left(\frac{nC_n}{nC_n + pC_p}\right)\left(1 + \exp\left(\frac{E - E_{Ft}^n}{kT}\right)\right)^{-1} \qquad 3.2.48$$

Above E_{Ft}^n, as defined, $C_n n_1(E) > nC_n + pC_p$, and

$$f(E) \approx \left[\frac{nC_n}{nC_n + pC_p}\right] \exp(-\frac{E - E_{Ft}^n}{kT}) < 1 \qquad 3.2.49$$

i.e. the traps are filled in a Boltzmann-like distribution.

It is interesting to compare this result with the 'classical' approach, which does not define a trap-Quasi Fermi level. In the same energy region ($C_n n_1 > nC_n + pC_p$), equation 3.2.44 reduces to

$$f(E) \approx \frac{n}{n_1(E)} = \exp(-\frac{E - E_{Fn}}{kT}) \qquad 3.2.50$$

$$\text{i.e.} \quad \frac{nC_n}{nC_n + pC_p} = \exp(-\frac{E_{Ft}^n - E_{Fn}}{kT}) < 1 \qquad 3.2.51$$

Equation 3.2.50 shows that in the energy range where a Boltzmann distribution is appropriate, the trapped electron occupancy can be described by the free electron Quasi-Fermi level. Traps in this range are said to be in Quasi-thermal equilibrium or thermal contact with the conduction band, as the rates of trapping and release interchange with the conduction band are greater than the capture rate of free holes

$$\text{i.e. } g(E)(C_n n_1(E) f(E)) > g(E) C_p p f(E) \qquad 3.2.52$$

(release rate)

$$g(E)(C_n n(1 - f(E))) > g(E) C_p p f(E) \qquad 3.2.53$$

(trapping rate)

An important result of equation 3.2.50 is that for this energy range, the ratio of free electron density to trap occupancy remains approximately unchanged with excitation - i.e.

$$n/f(E) \approx n_o/f_o(E) = N_c \exp\left(-\frac{E_c - E}{kT}\right) \qquad 3.2.54$$

Below E_{Ft}^n the occupancy factor is constant

$$f = \frac{nC_n}{nC_n + pC_p} = \frac{Rn}{Rn + p} \qquad 3.2.55$$

The concept of a trap Quasi-Fermi level offers a more complete description of f(E), as, in the region between E_{Fn} and E_{Ft}^n, equation 3.2.50 is not valid.

If $nC_n > pC_p$, then the occupancy of traps below E is greater than $\frac{1}{2}$, and E_{Fn} is close to E_{Ft}^n, while if $pC_p > nC_n$, the occupancy above E_{Fo} is less than $\frac{1}{2}$, and

E_{Fn} lies well below E_{Ft}^{n}. Figures 3.9a and 3.9b illustrate these two situations.

Below E_F

It is convenient to consider the 'hole occupancy' $\overline{f}(E) = (1 - f(E))$ for states below E_F, as this results in expressions similar in form to those derived for $f(E)$ above E_F. Firstly,

$$\overline{f}(E) = \frac{pC_p}{nC_n + C_p(p + p_1(E))} \qquad 3.2.56$$

which also has a modulated Fermi-Dirac form about a trapped hole Quasi Fermi level E_{Ft}^{p}, defined by

$$C_p N_v \exp\left(\frac{E_{Ft}^{p} - E_v}{kT}\right) = nC_n + pC_p \qquad 3.2.57$$

$$\text{i.e.} \quad \overline{f}(E) = \frac{pC_p}{nC_n + pC_p}\left(1 + \exp(E - E_{Ft}^{p})\right)^{-1} \qquad 3.2.58$$

Below E_{Ft}^{p} the traps are filled with holes according to a Boltzmann distribution, as $p_1(E) > nC_n + pC_p$

$$\overline{f}(E) = \frac{pC_p}{nC_n + pC_p} \exp\left(-\frac{E_{Ft}^{p} - E}{kT}\right) \qquad 3.2.59$$

or, using the free hole Q.F.L., E_{Fp}, in this region,

$$\overline{f}(E) = \exp\left(-\frac{E_{Fp} - E}{kT}\right) \qquad 3.2.60$$

i.e. below E_{Ft}^{p}, the traps are in Quasi thermal equilibrium with the valence band, and the rates of free hole capture and release are much greater than the rate of free electron capture. In this region, then, the ratio

$$p/\overline{f}(E) \approx p_o/\overline{f}_o(E) = N_v \exp\left(-\frac{E - E_v}{kT}\right) \qquad 3.2.61$$

is unchanged with excitation.

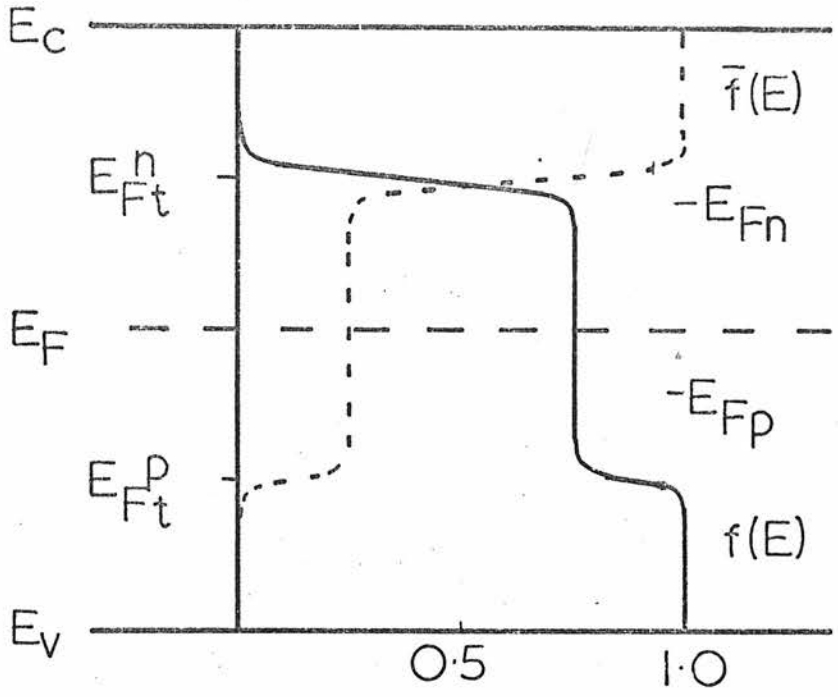

(a) $nC_n > pC_p$

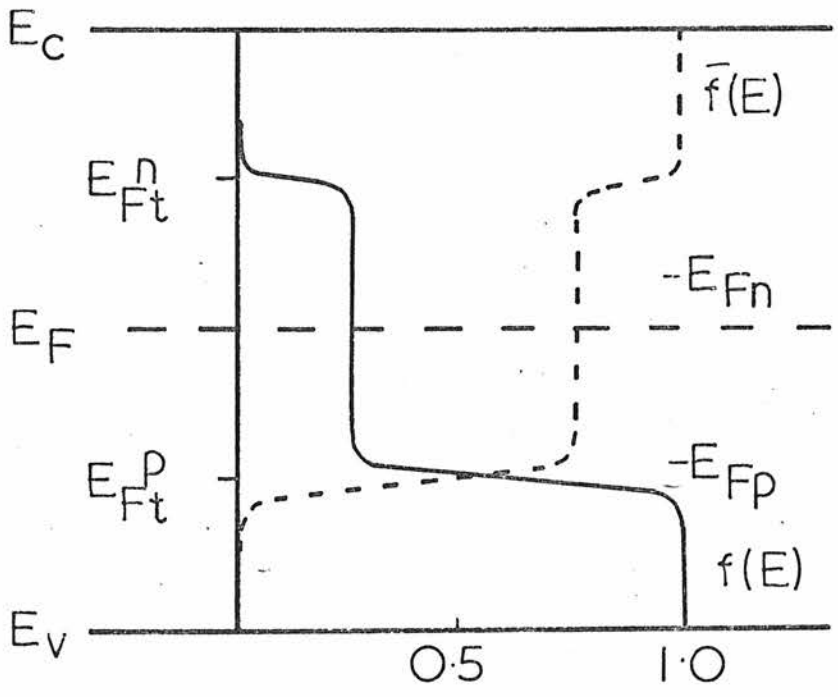

(b) $pC_p > nC_n$

Fig 3.9 Trap Occupancy (Constant Species) under Illumination.

Note that equation 3.2.60, using E_{Fp}, is not valid in the region $E_{Ft}^{p} < E < E_{Fp}$.

Above E_{Ft}^{p}, the trap hole occupancy is constant

$$\bar{f}(E) = \frac{pC_p}{nC_n + pC_p} \qquad (E_{Ft}^{p} < E < E_{Fo})$$

or

$$f(E) = \frac{nC_n}{nC_n + pC_p} \qquad 3.2.62$$

i.e. the trap occupancy is constant, given by equation 3.2.55, between the two trap Fermi levels E_{Ft}^{n} and E_{Ft}^{p}.

Figures 3.9a and 3.9b, illustrate the occupancy function and relative positions of E_{Fp} and E_{Ft}^{p}, for $pC_p > nC_n$ and $pC_p < nC_n$.

Different trap 'species'. The definition of a trap 'species' having a constant ratio $C_n/C_p = R$, allows convenient analysis of the occupation function. In practice, the coefficients may vary in different ways with energy (R not constant) or different species may exist at the same energy. (R multivalued). In these cases single trap Fermi levels cannot be defined, and f(E) may not be unique.

The relation between the capture coefficients and energy depends upon the variation of the nature of the state with energy, and the transition mechanisms involved. e.g. if band tail states become more localised with depth, C_n and C_p may reflect this, becoming smaller. The C.F.O. midgap 'crossover' states may have different values of R at the same energy.

As a pertinent example of what could happen where $R = C_n/C_p$ has some functional dependence on energy, consider a conduction band tail whose states are negative when occupied. Suppose that this results in $C_p > C_n$, C_p relatively depth insensitive, and C_n reducing with depth from E_c. Figure 3.10a illustrates schematically the form of R(E), while figure 3.10b, shows the equilibrium occupancy and steady state occupancy function under illumination. Notice that a 'peaking' in f(E) can occur, well above E_F, and that the states near E_F can be significantly depopulated under illumination. This is an important feature of some of the 'distributed states' models for photoconductivity.

With variable species, it is still possible to obtain, sufficiently near E_c and E_v

$$n_1(E) > nC_n(E) + pC_p(E) \quad E \text{ near } E_c$$

and 3.2.63

$$p_1(E) > nC_n(E) + pC_p(E) \quad E \text{ near } E_v$$

In these regions the Boltzmann distributions for trapped electrons and holes (equations 3.2.50 and 3.2.60), with respect to E_{Fn} and E_{Fp}, still apply.

Trap occupancy and L-L transitions. Analysis of equation 3.2.39 for the trap occupancy in terms of L-L transitions, in a general case of arbitrary g(E) and transition coefficients, is much more difficult than for form 3.2.38. A different approach may in fact be more productive along the lines of a random walk, or Markov process analysis.

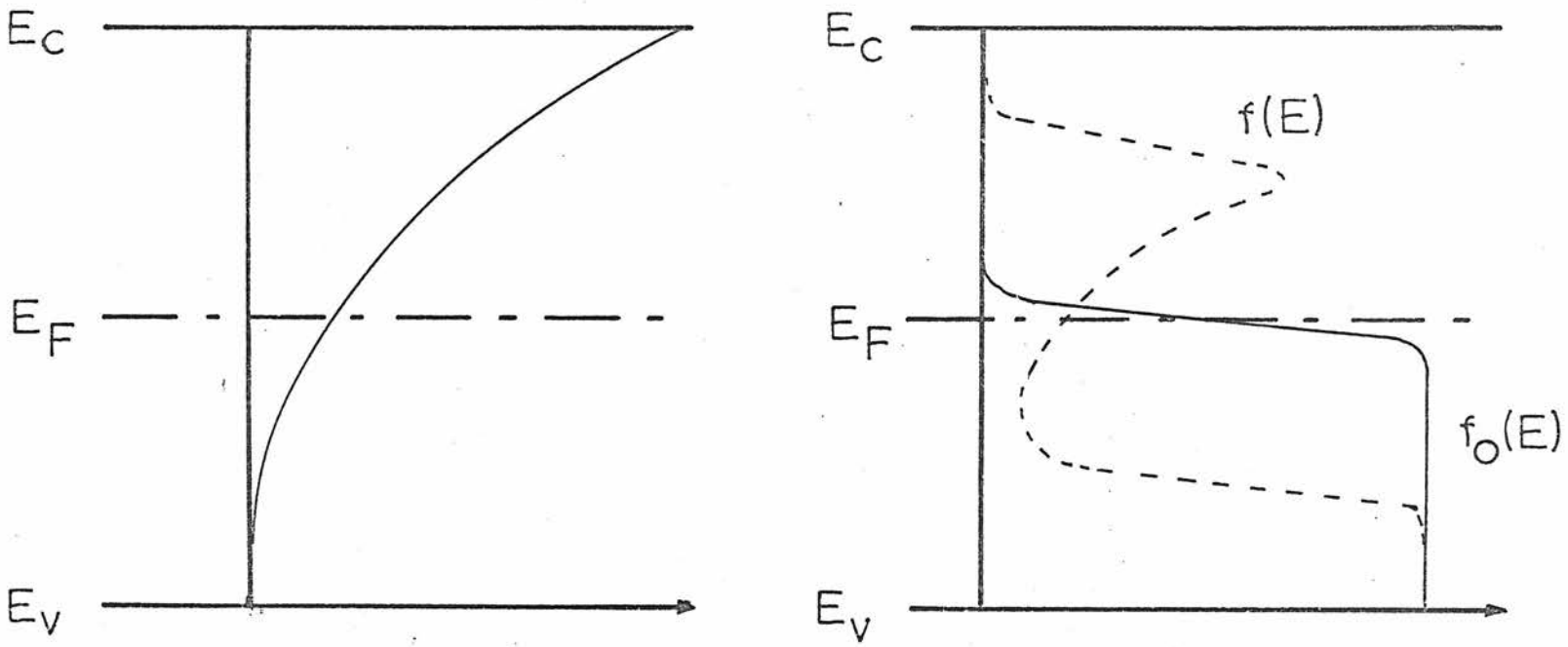

(a) Species function R(E) (b) Occupancy

Fig 3.10 Trap Occupancy (Variable species) under Illumination

In states near the band edges, L-L 'thermalising' transitions will occur, the probability of a recombination transition being small. For each such path by which a carrier reaches a given level, from the band, detailed balance holds for each step in thermal equilibrium, and in the hypothetical case mentioned. The only energy of interest is then the total difference, say $(E_c - E)$, and a Boltzmann distribution follows.

3.2.12 RECOMBINATION, LIFETIMES AND DEMARCATION LEVELS

Neglecting band-band recombination, photogenerated free electrons and holes will make a number of transitions by various 'paths' through the localised and extended states, before recombining at a localised centre. In the steady state, the total rate of such events equals the generation rate.

Substituting equation 3.2.31 for the trap occupancy into the free carrier rate equations gives a very general form of the equating of generation and recombination rates.

Using the transition labels again

$$\frac{dn}{dt} = 0 = G - \int_{E_V}^{E_C} g(E) \left\{ \frac{+ a(d' + 1') - a'(d + 1)}{a + a' + d + d' + 1 + 1'} \right\} dE \qquad 3.2.64$$

$$\frac{dp}{dt} = 0 = G - \int_{E_V}^{E_C} g(E) \left\{ \frac{d'(a + 1) - d(a' + 1')}{a + a' + d + d' + 1 + 1'} \right\} dE \qquad 3.2.65$$

Here the positive parts of the integrands represent recombination rates, while the negative parts re-emission

or generation rates. e.g.

$$\left\{ \frac{ad'}{a + a' + d + d' + l + l'} \right\}$$

represents the probability per unit time that a free electron is captured (a) and a free hole is captured, (d') by a state at energy E - i.e. B-L recombination

$$\left\{ \frac{al'}{a + a' + d + d' + l + l'} \right\}$$

is the probability/unit time that a free electron and a localised hole are captured - this will be termed L-L recombination.

The B-L recombination path involves 2 steps, while L-L recombination as defined above implies a minimum of 3 steps for a free electron and hole to ultimately recombine.

Recombination paths. Equations 3.2.64 and 3.2.65 illustrate how, when there are a number of 'parallel' recombination paths, that path with the highest probability will dominate, while the overall recombination rate is controlled by the slowest step in that path.

For example, consider a case where there are no states outwith the trap Q.F.L.s, and B-L hole capture (d') is the fastest step then $d' >> a$, $l' >> l$, d, a', follows, and

$$\Delta G = \Delta n \int_{E_V}^{E_C} g(E)\, C_n(E) dE = \Delta n / \tau_n \qquad 3.2.66$$

where τ_n is the free electron lifetime. The free hole lifetime is similarly defined.

Note that τ_n and τ_p are the average times that a

photoexcited electron or hole spends in the conduction and valence bands, between generation and recombination, excluding time spent in traps. The total 'photoexcited' lifetime of a photogenerated carrier can be much longer than its free lifetime.

A general analysis of equations 3.2.64 and 3.2.65 for free lifetimes, in terms of trapping parameters and generation rate, is extremely difficult. The approach taken in this work is essentially that illustrated in the simple case above - i.e. consideration of a dominant 'path', some suitable approximation for the occupancy factor for the localised states involved, and the charge neutrality condition.

Demarcation levels. Rose[111] introduced the concept of demarcation levels in a conventional photoconductor model, to describe the roles of localised states as temporary traps, or recombination centres. Above the electron demarcation level, E_{dn}, a trapped electron will have a greater probability of re-emission to the conduction band, than of recombining with a free hole. Thus at E_{dn}, the equality holds

$$C_n(E_{dn})\, n_1(E_{dn}) = pC_p(E_{dn}) \qquad 3.2.67$$

$$\therefore \quad E_{dn} = E_v + (E_c - E_{Fp}) + kT \log_e \left\{ \frac{C_p N_v}{C_n N_c} \right\} \qquad 3.2.68$$

A single species of trap will have unique electron and hole demarcation levels, (E_{dn} and E_{dp})

$$E_{dp} = E_c - (E_{Fn} - E_v) + kT \log_e \left(\frac{C_p N_v}{C_n N_c} \right) \qquad 3.2.69$$

Note that $E_{dn} < E_{Ft}^{n}$ and $E_{dp} > E_{Ft}^{p}$.

It is, of course, still possible to define a demarcation level by equation 3.2.67, if $R = C_n/C_p$ varies slowly, with E.

In this description states lying above E_{dn} are supposed to act mainly as temporary traps for free electrons and play relatively little part as recombination centres, while below E_{dn}, the reverse is true. The same argument applies to states below and above E_{dp}.

Still considering a single trap species distributed through the gap, it may seem now that the bulk of the recombination traffic passes through states between E_{dn} and E_{dp}, (Simmons[106] and Taylor include states between E_{Ft}^{n} and E_{Ft}^{p}) and in fact equitably through all these states. Simmons and Taylor perhaps misleadingly say that such states have a constant "recombination efficacy". This is true only in one special case - that of a constant density of states, and constant capture coefficients.

Referring to equation 3.2.64 it can be seen that if g(E) diminishes more slowly than the Boltzmann function toward the gap centre, then recombination will proceed mainly through states close to the two demarcation levels. If the capture coefficients diminish more slowly than the Boltzmann function toward the gap centre (with R(E) constant), then even with a constant g(E), the dominant recombination paths will again be through states near the demarcation levels. By invoking variations in g(E) or $C_p(E)$ and $C_n(E)$, more rapid than the Boltzmann function for a given temperature, situations

can arise where dominant recombination paths involve states outwith the demarcation levels, and normally classed as temporary traps.

Localised-Localised transitions can be formally included in the definitions of demarcation levels. For a constant species, the electron demarcation level may be defined in the following way

$$C_n(E_{dn})\, n_1(E_{dn}) + \int_{E_{dn}}^{E_c} K(E_{dn},E_j)\, g(E_j)(1 - f(E_j))dE_j = C_p(E_{dn})p + \int_{E_v}^{E_{dn}} K(E_{dn},E_j)\, g(E_j)(1 - f(E_j))dE_j \qquad 3.2.70$$

where the L.H.S. represents the total 'upward' electron emission probability/unit time, and the R.H.S., the total hole capture (from 'below') probability/unit time. A similar equation can be written for E_{dp} (using K').

3.2.13 DISCRETE TRAP MODEL

The general formalism of the preceding sections can now be used to explain the photoconductivity features discussed in 3.2.3. In this section, a discrete-trap model is used to illustrate the conditions and assumptions required to explain the behaviour, in the simplest possible way. In particular, it will be shown that for most models, recombination must proceed via states far from E_F, in contrast to the situation in many crystalline semiconductors. This implies, as does optical work, that $g(E_F)$ is small, or the matrix element

for transitions involving states at E_F is small - i.e. small capture cross sections.

The discrete trap model, shown in figure 3.11 represents the simplest of a number of models proposed in the literature to explain the experimental features in section 3.2.3. In all of those models (with the exception of Simmons and Taylor's) there is sufficient structure or variation in g(E) or in the transition coefficients $C_p(E)$, $C_n(E)$ and $K(E,E_j)$, so that the dominant recombination paths involve states away from the gap centre, and even outwith the demarcation and trap-Fermi levels, (if they can be defined). In this way, states in the 'Boltzmann distribution' regions, defined by equations 3.2.49 and 3.2.59 which would normally be classed as temporary traps, play a major (albeit inefficient) part in recombination.

Nomenclature

The following parameters are appropriate to figure 3.11

E_1, E_2	trap energies $E_1 > E_F$ $E_2 < E_F$
N_1, N_2	trap densities
f_1, $\bar{f}_2$	trap occupancies
n_1, n_2	electron emission - effective densities
p_1, p_2	hole emission - effective densities
C_{n1}, C_{n2}	electron capture coefficients
C_{p1}, C_{p2}	hole capture coefficients
K_{12}, K'_{12}	L-L transition coefficients

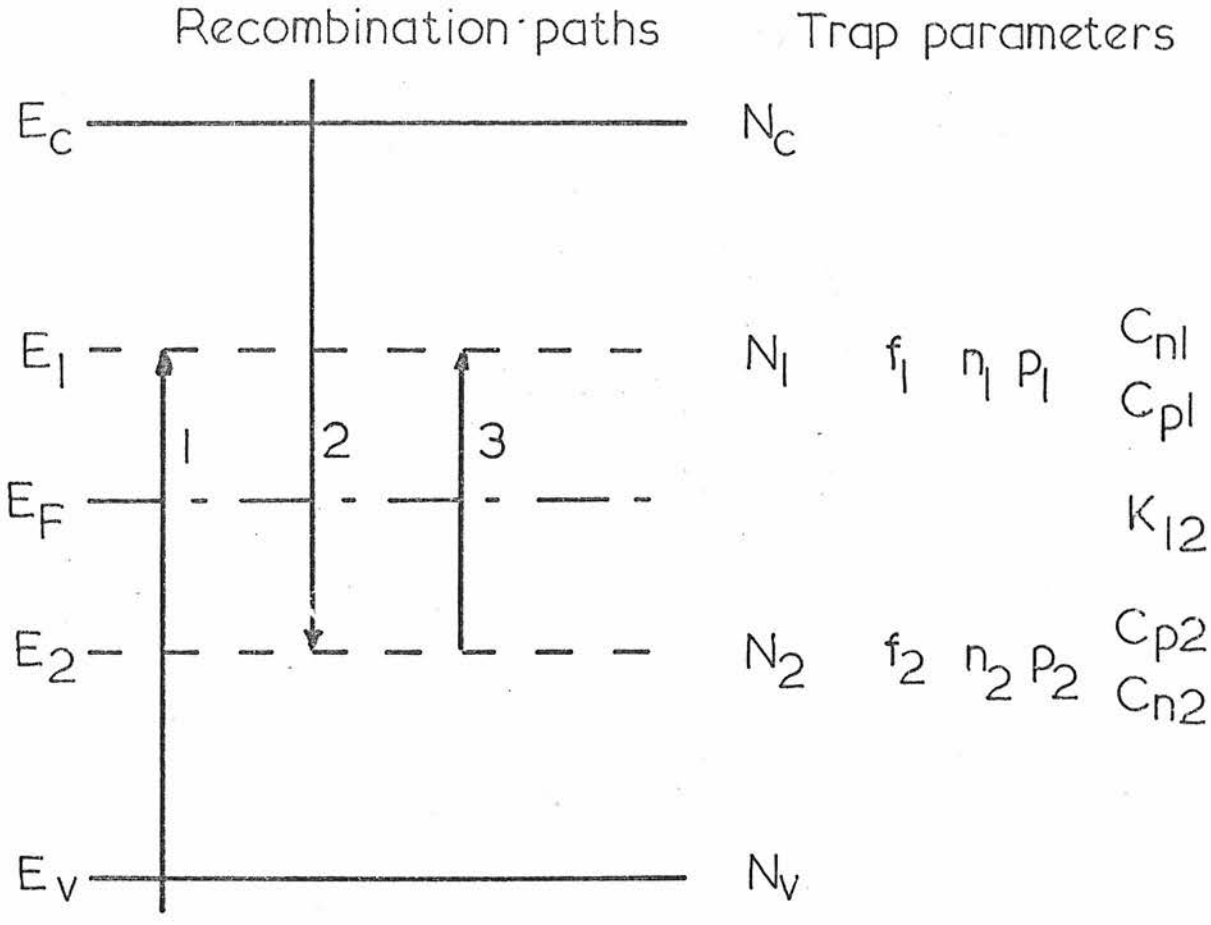

Fig 3.11 Discrete level model

The localised state distribution may be expressed, in equations 3.2.64 and 3.2.65

$$g(E) \equiv N_1 \, \delta(E - E_1) + N_2 \, \delta(E - E_2) \qquad 3.2.71$$

where δ is the Dirac-delta functional.

Approximations

It is assumed that both sets of traps lie outwith the appropriate trap Q.F.L.s under all experimental conditions, i.e. the following inequalities hold

$$\left.\begin{aligned} E_1 &> E_{Ft1}^{n} \\ E_2 &< E_{Ft2}^{p} \end{aligned}\right\} \quad \therefore \quad f_1, f_2 \ll 1 \qquad 3.2.72$$

$$\left.\begin{aligned} E_1 &> E_{Fn} \\ E_2 &< E_{Fp} \end{aligned}\right\} \quad \therefore \quad \begin{aligned} n_1 &\gg n \quad p_1 \ll p \\ n_2 &\ll n \quad p_2 \gg p \end{aligned} \qquad 3.2.73$$

$$\left.\begin{aligned} E_1 &> E_{dn} \\ E_2 &< E_{dp} \end{aligned}\right\} \quad \therefore \quad \begin{aligned} C_{n1} \, n_1 &\gg C_{p1} \, p + K_{12} \, N_2 \bar{f}_2 \\ C_{p2} \, p_2 &\gg C_{n2} \, n + K_{12} \, N_1 f_1 \end{aligned} \qquad 3.2.74$$

$$E_2 < E_F < E_1 \quad \therefore \quad \begin{aligned} K_{12} \, f_2 &\gg K_{12}' \, f_2 \\ K_{12} \, f_1 &\gg K_{12}' \, \bar{f}_1 \end{aligned} \qquad 3.2.75$$

The traps are in fact, in Quasi thermal equilibrium with the nearer band, so

$$f_1 = n/n_1 \quad \bar{f}_2 = p/p_2 \qquad 3.2.76$$

Charge neutrality

Assuming set 1 traps are negative when electron occupied, set 2 traps are positive when hole occupied, and the trapped charge density is much greater than the free charge density, as might be expected in amorphous semiconductors, equation 3.2.35 gives

$$N_1 f_1 \approx N_2 \bar{f}_2 \qquad 3.2.77$$

substituting 3.2.77 in 3.2.76 gives

$$n \approx p\left(\frac{n_1}{p_2} \cdot \frac{N_2}{N_1}\right) \qquad 3.2.78$$

Thermal equilibrium. The equilibrium Fermi level is, from equation 3.2.77.

$$E_F = \tfrac{1}{2} kT \log (N_2/N_1) + \tfrac{1}{2} (E_1 + E_2) \qquad 3.2.79$$

giving

$$p_o = N_v (N_1/N_2)^{\frac{1}{2}} \exp\left(- \frac{\frac{1}{2}(E_1 + E_2) - E_v}{kT}\right) \qquad 3.2.80$$

i.e. E_F is roughly midway between the two sets, even when there is some density asymmetry.

Steady state solution

Substitution of the delta functions distribution (3.2.71) into the free hole recombination equation, (3.2.65) gives, in the steady state

$$\frac{dp}{dt} = 0 = G - N_1 \left\{ \frac{pC_{p1}(nC_{n1}+K'_{12}N_2 f_2) - p_1 C_{p1}(n_1 C_{n1}+K_{12}N_2 \bar{f}_2)}{C_{n1}(n+n_1)+C_{p1}(p+p_1)+N_2(K'_{12}f_2+K_{12}\bar{f}_2)} \right\}$$

3.2.81

$$- N_2 \left\{ \frac{pC_{p2}(nC_{n2}+K_{12}N_1 f_1) - p_2 C_{p2}(n_2 C_{n2}+K'_{12}N_1 \bar{f}_1)}{C_{n2}(n+n_2)+C_{p2}(p+p_2)+N_1(K_{12}f_1+K'_{12}\bar{f}_1)} \right\}$$

With the approximations introduced above, this simplifies to

$$G \approx \frac{N_1 C_{p1}}{n_1}(np - n_1 p_1) + \frac{N_2 C_{n2}}{p_2}(np - n_2 p_2)$$

$$+ \frac{N_1 N_2}{p_2}(p\,K_{12}\,f_1 - p_2\,K'_{12}\,\bar{f}_1) \qquad 3.2.82$$

The negative terms within the brackets represent re-emission, which does not appreciably change in this model, on illumination. Therefore, substituting the charge neutrality equation 3.2.77 and solving for the excess free hole density gives a very simple solution

$$G-G_o = \Delta G = [\,2p_o\Delta p+\Delta p^2]\{C_p \frac{N_2}{p_2} + C_{n2} \frac{N_2^2}{p_2^2}\frac{n_1}{N_1} + K_{12}\frac{N_2^2}{p_2^2}\} \qquad 3.2.83$$

Small signal ($p_o >> p$) and large signal ($\Delta p >> p_o$) cases clearly present themselves here. The three terms in the braces represent the three possible recombination paths - i.e. the first term (path 1) B-L recombination via set 1, with hole capture the slower step; the second term (path 2), B-L recombination via set 2, with electron capture the slower step; while the third term (path 3) represents L-L recombination. The factor N_2/p_2 which appears in all three terms may be interpreted as the partitioning of holes between the set 2 traps and the valence band.

It will usually be the case that <u>one</u> of the above paths dominates under given conditions. Solutions for each path may be found separately and checked against experimental data.

The results for small and large excitation for each path are given below

Small signal. $\Delta G \ll G_o$, $\Delta p \ll p_o$

Path 1 (B-L)

$$\Delta p = \frac{\Delta G}{2C_{p1}(N_1N_2)^{\frac{1}{2}}} \exp\left[+\frac{\frac{1}{2}(E_1 - E_2)}{kT}\right] \qquad 3.2.85$$

Path 2 (B-L)

$$\Delta p = \frac{\Delta G N_v}{2C_{n2}N_2N_c}\left(\frac{N_1}{N_2}\right)^{\frac{1}{2}} \exp\left[+\frac{\frac{1}{2}(E_1-E_2)+(E_c-E_1)-(E_2-E_v)}{kT}\right] \qquad 3.2.86$$

Path 3 (L-L)

$$\Delta p = \frac{\Delta G N_v}{K_{12}N_2(N_1N_2)^{\frac{1}{2}}} \exp\left[+\frac{\frac{1}{2}(E_1 - E_2) - (E_2 - E_v)}{kT}\right] \qquad 3.2.87$$

Large signal. $\Delta G \gg G_o$ $\Delta p \gg p_o$

Path 1 (B-L)

$$\Delta p = \left(\frac{\Delta G N_v}{C_{p1}N_2}\right)^{\frac{1}{2}} \exp\left[-\frac{\frac{1}{2}(E_2 - E_v)}{kT}\right] \qquad 3.2.88$$

Path 2 (B-L)

$$\Delta p = \left(\frac{\Delta G N_1}{C_{n2}N_c}\right)^{\frac{1}{2}} \exp\left[-\frac{(E_2 - E_v) - \frac{1}{2}(E_c - E_1)}{kT}\right] \qquad 3.2.89$$

Path 3 (L-L)

$$\Delta p = \left(\frac{\Delta G}{K_{12}}\right)^{\frac{1}{2}} \frac{N_v}{N_2} \exp\left[-\frac{E_2 - E_v}{kT}\right] \qquad 3.2.90$$

In the small signal case, the free excess hole density can be written, for suitable values of E_1, E_2,

$$\Delta p \alpha \Delta G \exp(+ \frac{\Delta E_m}{kT}) \qquad 3.2.91$$

i.e. linear dependence on excitation, and positive exponential dependence upon 1/T. The excess carriers recombine into a virtually fixed 'pool' of the thermal population of the recombination centres, the free hole lifetime τ_{pm} is independent of excitation and the process may be termed monomolecular.

e.g. for path 1

$$\tau_{pm} = (2C_{p1}N_1 f_{10})^{-1} \qquad 3.2.92$$

In the large signal case, the behaviour can be written

$$\Delta P \alpha \Delta G^{\frac{1}{2}} \exp(- \frac{\Delta E_b}{kT}) \qquad 3.2.93$$

i.e. square root dependence on excitation and negative exponential dependence upon 1/T. The photo-generated densities are greater than thermal populations, and the recombining species are either proportional, for B-L paths 1 and 2, or equal, for L-L path 3, so the recombination can therefore be termed bimolecular. The free hole lifetime τ_{pb} now depends upon excitation, e.g. for path 1

$$\tau_{pb} = \left(\frac{\Delta G C_{p1} N_2}{P_2} \right)^{-\frac{1}{2}} \qquad 3.2.94$$

B-L vs L-L recombination. It can be seen that the steady state features predicted for the free hole density, agree in form with the experimental data for photocurrent, for all three recombination paths. To determine which path dominates under given conditions requires careful analysis of the data and comparison with other electrical properties, e.g. conductivity, transient photoconductivity etc. It may not be possible to distinguish paths 1 and 2, but there are significant differences in the results for B-L and L-L recombination.

For example, in the large signal case, comparing path 1 (B-L) and path 3 (L-L), ΔE_b is half the depth of set 2, and equal to the depth of set 2, respectively. Also, the hole occupancy of set 2 for B-L recombination (path 1) has an opposite temperature dependence to the free hole density - i.e. increasing with decreasing temperature, while for L-L recombination, the occupancy is temperature independent.

3.2.14 PHOTOCURRENT

For homogeneous excitation, the photocurrent density ΔJ may now be calculated

$$\Delta J = \mathcal{E} \int \mu(E)\, g(E)\, \Delta f(E).\ dE \qquad 3.2.95$$

where $\mathcal{E}$ is the applied (y-direction) field. If free hole transport dominates

$$\Delta J = \mathcal{E} e\, \mu_{po}\, \Delta p. \qquad 3.2.96$$

and as μ_{po} is relatively temperature insensitive, the photocurrent has the same temperature and intensity dependence as Δp, discussed in 3.2.13.

If hopping transport - say in a limited valence band tail, extending from E_v to E_3 ($E_3 \leq E_2$) dominates and the quasi thermal equilibrium condition holds for its occupancy, then

$$\Delta J \text{ (hopping)} \propto \mathcal{E}_e \Delta p \exp\left(\frac{(E_3 - E_v) - \Delta W}{kT}\right) \quad 3.2.97$$

Now extra activation energies are introduced into the solutions, and interpretation of the results becomes more difficult.

3.2.15 SPATIAL EFFECTS

Inhomogeneous excitation. The generation rate in the sample shown in figure 3.1 at depth x, is

$$\Delta G(x) = \eta A(x) \quad 3.2.98$$

where A(x) is the volume absorption at depth x. If multiple reflection effects are included, (but not interference) then

$$A(x) = (1-R_1) F \alpha \exp(-\alpha x)\left(\frac{1+R_2\exp[-2\alpha(d-x)]}{1-R_1R_2\exp[-2\alpha d]}\right) \quad 3.2.99$$

where R_1 is the air-film reflectance, and R_2 is the film-substrate reflectance. If the film is sufficiently thick, so that reflection from the back surface can be ignored, then

$$A(x) = (1 - R_1) F \alpha \exp(-\alpha x) \quad 3.2.100$$

Ignoring diffusion effects, the excess density may be obtained as a function of depth (x), knowing the depth dependent generation rate. The photocurrent is obtained by integration through the sample thickness

$$\Delta I = w\, e\, \mu_{po}\, \mathcal{E} \int_{o}^{d} \Delta p\,(x)\, dx \qquad 3.2.101$$

for the case of free hole conduction.

Diffusion effects and space charge. It is not intended to analyse completely the effects of diffusion in the continuity equations. A piece-meal approach of internal consistency can be adopted to ascertain if the spatial distribution of excess carriers calculated from equation 3.2.98 above introduces significant diffusion in the x-direction.

3.2.16 REVIEW OF DISTRIBUTED STATES MODELS

Discrete levels vs distributed states. Two important points emerge from the analysis of 3.2.13. Firstly, to explain the 'activated' high and low temperature behaviour of Δp (and ΔI) recombination must proceed via states significantly removed from the gap centre and E_F, and in fact, in the 'Boltzmann occupation' regions. Secondly, bimolecular behaviour requires that these states control the charge neutrality condition (at least in the bimolecular regime).

The simple discrete level model easily satisfies these conditions, by effectively introducing delta functions in the trap distribution g(E), at energies E_1 and E_2 in recombination equations 3.2.64 and 3.2.65.

Most of the distributed states models[99,100,109] introduce a rapid decrease or discontinuity (faster than the Boltzmann function) in g(E) or in the transition coefficients (C,K) at equivalent energies to satisfy the first condition. The second condition requires that excitation depopulates states near E_F (or reduces the charge density). As pointed out in section 3.2.11 (figures 3.10a, 3.10b) a suitable variation in trap species with energy, will ensure this. Most of these models therefore require two types of localised state, with very asymmetric cross section ratios, and values of E_i quite far from E_F. This does not affect the analysis of 3.2.11. The only model which does not make the above assumptions is that of Taylor and Simmons[108] which gives slightly different results - to be discussed later.

As will be shown, with the exception of Taylor and Simmons, these analyses give results so similar to the discrete level case that it is difficult to distinguish between the models by experiment.

Model of Weiser et al. Photoconductivity (Weiser et al[100]) and photoluminescence[116] in $2As_2Te_3$, As_2Se_3 were interpreted using a C.F.O. model with L-L transitions. Figure 3.5. showed the intensity dependence of photoconductance, demonstrating the linear and square root regions. The photoluminescence spectrum peaked at 0.65 eV, which the authors associate with radiative L-L transitions.

The interpretation is as follows[100,117].

Photogenerated free carriers lose energy by being captured by a shallow localised state, and proceeding by a series of one-phonon thermalisation transitions to drop deeper in the band tails. As g(E) and the localisation parameter fall off with reducing energy, the steps become more difficult. The thermalising carrier may also recombine (by L-L transitions) with carriers in the other band-tail, over a range of energies, a process which also becomes more difficult as the carrier becomes more localised, although not so rapidly as the thermalising transitions, as the final state may be less localised.

Stern[113] approximates one tail's g(E) by a ladder of energy levels separated by a phonon energy E_{ph}, and down which carriers thermalise. The other tail, into which recombination occurs, is also considered as a ladder of levels.

The occupancy $f(E_i)$ of conduction band tail level E_i density N_i can be written, in terms of L-L transitions. (valence band tails states denoted by subscript j).

$$f_i = \left(N_{i+1}K'_{i,i+1}f_{i+1}+N_{i-1}K'_{i,i-1}f_{i-1}+\sum_j N_j K'_{ij} f_j\right)$$

$$\left(\frac{N_{i+1}K'_{i,i+1}f_{i+1}+N_{i-1}K'_{i,i-1}f_{i-1}+\sum_j N_j K'_{ij}f_j}{+\,N_{i+1}K_{i,i+1}(1-f_{i+1})+N_{i-1}K_{i,i-1}(1-f_{i-1})+\sum_j N_j K_{ij}(1-f_j)}\right)^{-1}$$

(P_{th}) (P_r) 3.2.102

The occupancy and role of a given level are examined by considering the relative magnitudes of the important terms labeled P_{th} (thermalising probability) and P_r (recombination probability), involving electron loss, and which are related to the other terms (i.e. they are not an arbitrary choice).

Figure 3.12a shows the exponential conduction band tail, and figure 3.12b shows how P_{th} and P_r are expected to vary with energy in say the conduction band tail, in the dark, and with increasing illumination. P_{th} is assumed to vary more rapidly with energy than P_r, and the two are equal at energy E_{RC} called the recombination edge. It follows that even in the dark, states above E_{RC} are effectively in thermal contact with the conduction band, while those below E_{RC} are in contact with the valence band tail. This situation is a L-L equivalent of a variable trap species with cross-sections and R decreasing with depth, fulfilling the requirements mentioned above.

With increasing illumination, (ΔG_1 and ΔG_2) P_r increase as shown schematically in 3.12b, while P_{th} does not change significantly if the occupation is low. The 'recombination edge' therefore shifts upwards, but not far, if P_{th} varies rapidly with energy. Figure 3.12c shows the equilibrium occupancy function, and the occupancy under ΔG_1 and ΔG_2. It is assumed here that part of the tail lies below E_F, for completeness, but Weiser does not mention this explicitly.

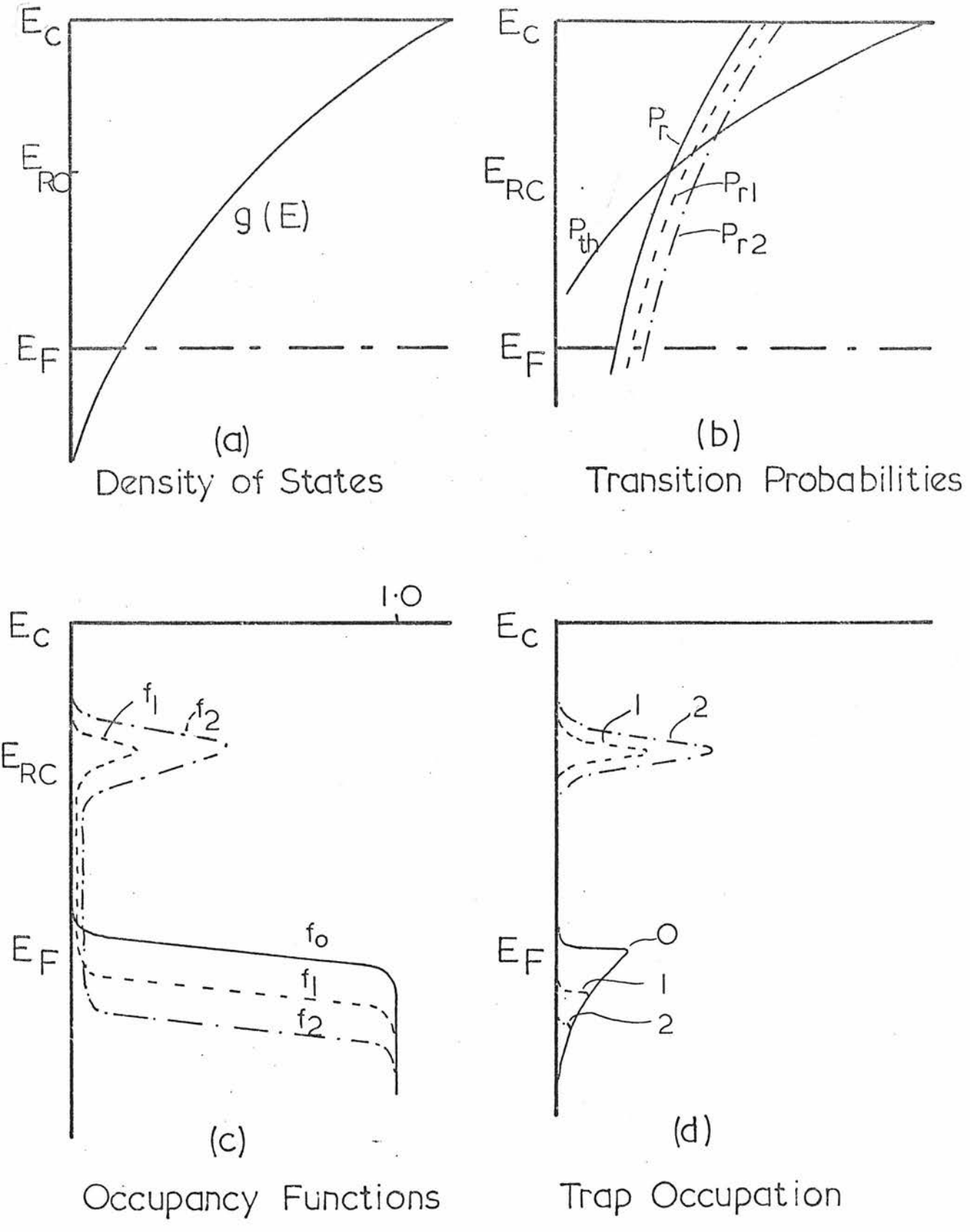

Fig 3.12 Model of Weiser et al. for Photoconductivity
Two Excitation levels $\Delta G_1 < \Delta G_2$

If P_{th} varies sufficiently rapidly with energy below E_{RC}, then as ΔG increases, a bump in the occupancy will appear at E_{RC}, while the previously full states below E_F become depopulated, and the states between E_F and E_{RC} remain relatively empty - i.e. the thermalising excess electrons do not penetrate deeper than E_{RC}, as they recombine upon doing so. If $P_{th} \gg P_r$ above E_{RC}, then the occupancy is Boltzmann-like.

Figure 3.12d shows the actual occupation vs ΔG, and the resemblance to the 'discrete trap' case is marked, in terms of the occupancy x recombination product, which peaks at E_{RC}. Using a relatively shallow exponential tail, the Boltzmann occupancy ensures that most of the trapped excess carriers lie within kT of E_{RC}. Thus, comparing models, $E_1 \equiv E_{RC}$, and $N_1 \equiv kT\ g(E_{RC})$. A similar argument can be applied to the valence band tail (recombination edge E_{RV}). Furthermore, if K_{ij} does not vary appreciably through the population peaks, then these equivalent parameters may be substituted in equation 3.2.82 for discrete levels.

Charge neutrality at low excitation will be controlled by states near E_F, rather than at E_{RC} and E_{RV}. The behaviour will be qualitatively similar however, to the discrete trap case, and at high intensities, virtually indistinguishable from it, when the peaks at E_{RC} and E_{RV} control neutrality. This will be discussed in the next section, and in the experimental chapter.

Some features of this model require further examination. Firstly, the rapid decrease of P_{th} with energy. According to Stern[113],

$$P_{th,i} \propto N_{i-1} \alpha_i \alpha_{i-1}$$

where α is the localisation decay constant, which in another paper[118] is shown not to decrease very rapidly with depth (certainly not as rapidly as required), although a more rapid variation of P_{th} is suggested, due to spatial correlations in the random potential present.

Secondly, the assumption that L-L recombination dominates B-L recombination (this applies to all L-L models). Spatial separation of the states involved could make this process difficult.

Taking typical figures for the parameters in this model, for $2As_2Te_3$ As_2Se_3 from Weisers papers[100,119] i.e. $g(E_c) \sim 10^{27} - 10^{28}$, E_o (band tailing constant) ~ 0.1 eV and $E_c - E_{RC} \sim 0.13$ eV gives an effective density of recombination centres $kTg(E_{RC}) \sim 10^{25} - 10^{26}$, with average separation 20 - 40 Å. Now the average separation of 'active' centres-occupied by electrons and holes is greater than this, as $f(E_{RC}) \ll 1$. In fact, as $(E_{RC} - E_F) \approx 0.34$ eV, $f_o(E_{RC}) \sim 10^{-6}$ at room temperature, and assuming a 100 fold increase in population under excitation, $\Delta f\ (E_{RC}) \leq 10^{-4}$, gives an average separation for recombining carriers of > 500 - 1000 Å which seems inconsistent with the value for K obtained $\sim 1.8 \times 10^{-16}$ m^3 s^{-1}.

A possible explanation by Weiser[117] is that thermalising electrons and holes approach favourable sites for recombination by coulomb attraction, though this has yet to be treated quantitatively. It is relevant to note that in calculating optical absorption, many authors, e.g. Davis and Mott[17] assume that the matrix element for such tail-tail L-L transitions is very small.

Model of Arnoldussen et al. Arnoldussen et al[99] present a detailed analysis of photoconductivity in chalcogenides, mainly multicomponent switching alloys say $Ge_{15}Te_{81}S_2Sb_2$, $Si_{11}Ge_{11}As_{35}P_3Te_{40}$. The experimental features are similar to those observed elsewhere but, there are some additional points, illustrated at the start of this chapter, in figure 3.4. At very low temperatures, the photoconductance vs 1/T slope reduces, tending to zero slope, while in the 'intermediate' temperature region, at low intensities, the activation energy is still ΔE_b, but the intensity dependence is linear.

A band tail model in the spirit of the C.F.O. model is used, with conduction and valence band tails represented by $g_c(E)$ and $g_v(E)$. Figure 3.13a shows the assumed energy variation of the "effective recombination centre density". The rapid fall at E_1 and E_2 is associated with the density-transition coefficient product, rather than with unambiguous structure in g(E). This approach effectively inserts a step-function into the recombination equations 3.2.64 and 3.2.65, without

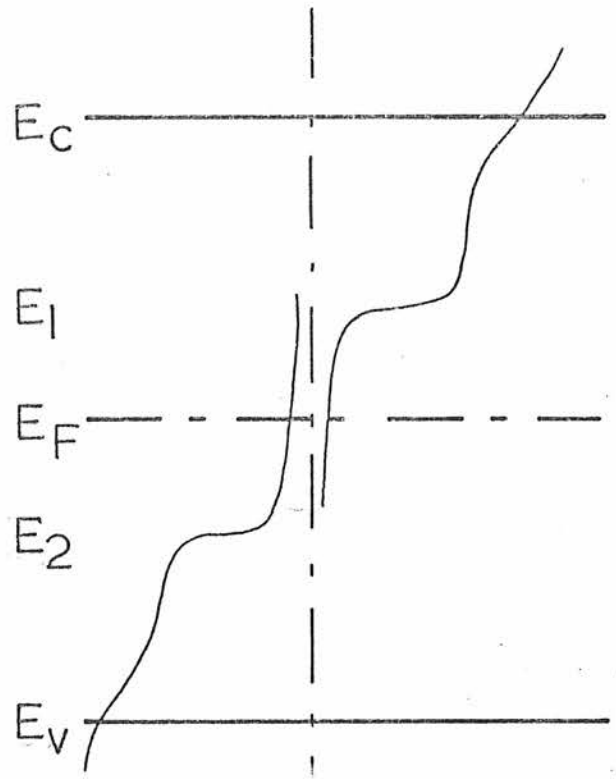

(a) Density of effective recombination centres

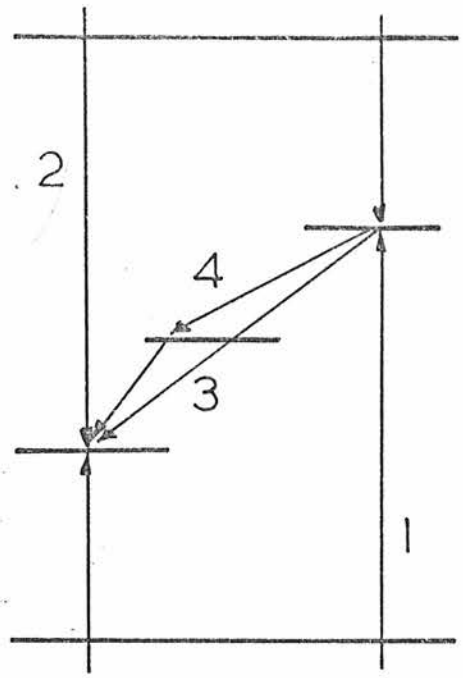

(b) Recombination paths

		eV	g(E)	capture coefficient	
E_c					
E_1	- - - - - - -	0·60	1.5×10^{25}	C_{p1}	9×10^{-14}
E_F	— - — - — -	0·34		K_{12}	2.1×10^{-13}
E_2	- - - - - - -	0·08	1.5×10^{25}	C_{n2}	9×10^{-14}
E_v		0			

(c) Typical parameters $Ge_{15}Te_{81}S_2Sb_2$

Fig 3.13 Model of Arnoldussen et al.

associating it with any particular parameter, although variation in the transition coefficients is implied.

Figure 3.13b shows the transitions considered. Paths 1, 2, and 3 are similar to those analysed in 3.2.13, while path 4 involves L-L transitions via mid gap states. Thermalisation by multiple L-L transitions is not considered so trapping is a single step B-L process.

The charge-occupation nature of the tail states is assumed to give for conduction and valence band tails respectively, $R_c(E) << 1$ and $R_v(E) >> 1$, as the cross section is assumed larger for charged states. This ensures depopulation of the overlap states on illumination. Another point, not mentioned, is that R_c and R_v must also change rapidly at E_1 and E_2, to ensure that the 'non-overlap' states between E_1 and E_2 are always relatively empty, so that the occupation at E_1 and E_2 controls neutrality, at high illumination.

Thus, whether B-L or L-L recombination predominates, the occupation varies with excitation in a way similar to Weiser's model, as the states at E_1 and E_2 are always outwith their relevant demarcation energies - i.e. in the Boltzmann occupation region. The situation reduces again to effectively discrete levels (densities $\sim kT\, g_c(E_1)$ and $kT\, g_v(E_2)$).

Additional features of the model involve the charged 'overlap' states at E_F. They effectively 'pin' E_F and control the charge neutrality condition, at low excitation. The results obtained for this situation are

qualitatively very similar to those obtained for the discrete level case, except that E_F need not lie roughly mid-way between E_1 and E_2. Secondly, the linear low excitation intermediate temperature behaviour is explained by an extra L-L recombination path via states at E_F, (path 4 say).

As an example of this analysis, consider the data on $Ge_{15}Te_{81}S_2Sb_2$ shown in figure 3.4. A comparison of the respective paths is made, and it is concluded that in the high temperature (monomolecular) regime, B-L (1 or 2) or L-L (path 3) recombination could dominate, while at lower temperatures, L-L recombination dominates.

The 'flattening out' at low temperature is explained by wide splitting of the demarcation levels, to include E_1 and E_2, a feature which could occur in the discrete level case also. In this range, relatively temperature insensitive capture terms control the occupancies and recombination rates.

It was found necessary to include an activated mobility (typically ~ 0.1 eV) for free carriers (see equation 3.2.95) to obtain agreement with experimental data, in particular the difference between conductivity and thermopower activation energies. This seems unlikely, for carriers above the mobility edges, as are assumed in the analysis, but may be compatible with hopping conduction. This activation energy must also fall at low temperatures.

Some of the typical parameter values for $Ge_{18}Te_{81}S_2Sb_2$

for a symmetric tails analysis are shown in figure 3.13. The values for transition coefficients are very high - in particular, the L-L coefficient $K_{12} \sim 2 \times 10^{13}$ m^3 s^{-1} which is surprisingly higher than the B-L coefficients, and 3 orders of magnitude higher than the value quoted for B-L recombination in GaAs.

The same criticisms regarding the probability of L-L recombination apply to this model as to Weiser's model, especially since thermalisation and motion in the band tails is excluded. Using the values quoted in the paper, the effective total density of recombination states is $\sim 3 \times 10^{24}$ m^{-3}, while the density of active (occupied) states at room temperature assuming $f = 100\ f_o \sim 10^{-4}$ is, $\sim 3 \times 10^{21}$ m^{-3}, giving an average separation of ~ 2000 Å ! L-L recombination must be unlikely under these circumstances.

Model of Mott and Davis. Mott and Davis[120] discuss photoconductivity kinetics using the limited tail model of figure 2.4b, reproduced again as figure 3.14. The assumption that g(E) falls to zero at the tails' extremities (at E_1 and E_2) gets rid of the need for variation in transition coefficients with energy.

Under excitation, the tail states are assumed to lie outwith their respective trap Fermi levels, and are therefore filled according to Boltzmann statistics. L-L recombination proceeds via those states rather than the 'bump' which pins E_F. These midgap states must again have low cross-sections or low density. To

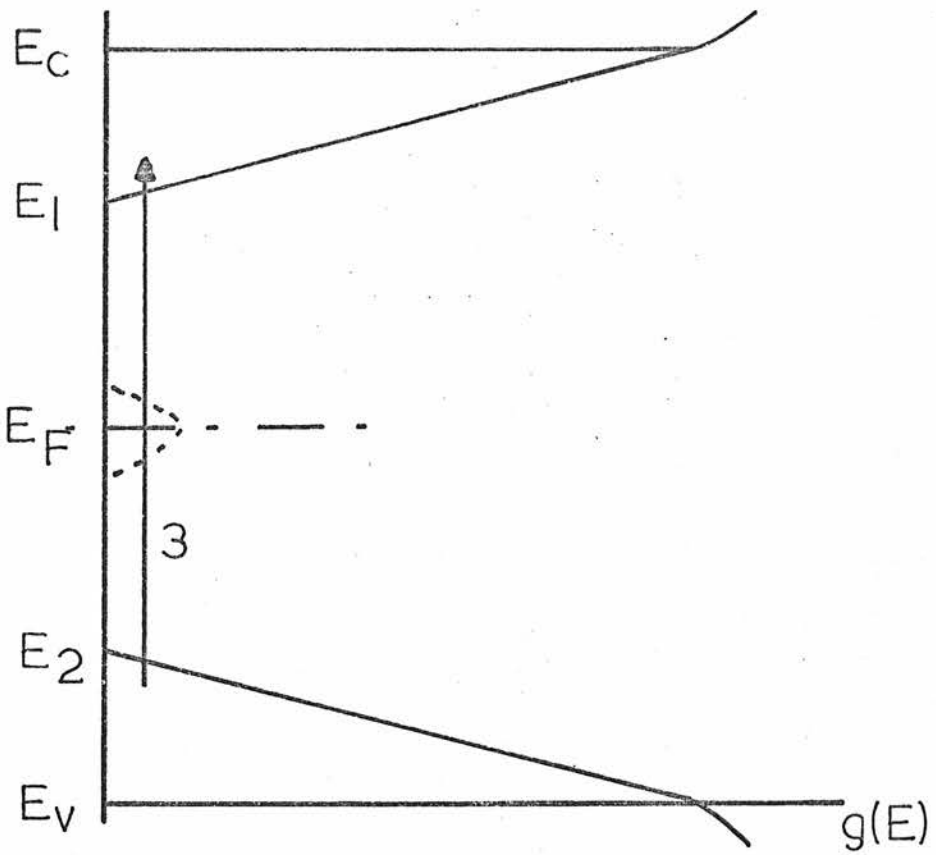

Fig 3.14 Model of Mott and Davis

ensure that charge neutrality at high excitation is controlled by the tail states, the species of the midgap states must be such that they are depopulated upon illumination.

The analysis now becomes similar to the discrete level case. 'Effective discrete' densities may be substituted in recombination equation 3.2.83 e.g. for a linear conduction band tail

$$'N_1' \approx N_c \frac{(E_c - E_1)}{kT} \qquad 3.2.103$$

Model of Simmons and Taylor. Simmons and Taylor[106-108] have discussed steady state photoconductivity in a number of papers - some general and some with reference to amorphous semiconductors. The formulation of the problem used in this thesis is based in part on their work, although there are several major differences.

Simmons and Taylors' general analysis uses only 'conventional' B-L transitions, and the particular density of states model employed is one of symmetrical exponential band tails, of the C.F.O. type. Another major point of difference from all the other analyses is that there is no 'recombination edge'. i.e. the transition coefficients do not vary rapidly with energy, at any point. This in turn means that (for a constant trap species) recombination occurs via states within the trap Q.F.L.s. How does this give agreement with such experimental results as well defined activation energies ΔE_m and ΔE_b, and square root (bimolecular)

intensity behaviour?

Consider the high excitation situation, with constant trap species, and equal electron and hole capture coefficients. Figures 3.15a,b,c, show the density of states, occupancy, and trap occupation for two excitation levels. Electron occupancy (f) is implied above E_F, and hole occupancy ($\bar{f}$) below E_F. States between E_{Ft}^n and E_{Ft}^p have constant occupancy and are all equally effective in recombination. Contrast this with (i) the peaked occupancy functions of other analyses of distributed states, caused by changes in species, and (ii) peaked recombination effectiveness caused by changes in the absolute magnitude of the transition coefficients, at the recombination edges.

The trap occupation is, however, peaked at the trap Q.F.L.s, due to the exponential tailing in g(E). Consequently, charge neutrality and recombination may be dominated by states near the trap Q.F.L.s if the tails are reasonably steep. This situation is similar to that obtained in other models, but as can be seen in figure 3.15c, the positions of the trapped charge peaks will vary with illumination or with temperature. As a result, a plot of Δp vs $1/T$ is curved, and the intensity relation is somewhere between square root and linear behaviour.

The curvature in Δp vs $1/T$ is ironed out somewhat in the photocurrent vs $1/T$ plot, by invoking a temperature dependence of free mobility controlled by phonon scattering at high temperatures, changing to charged centre

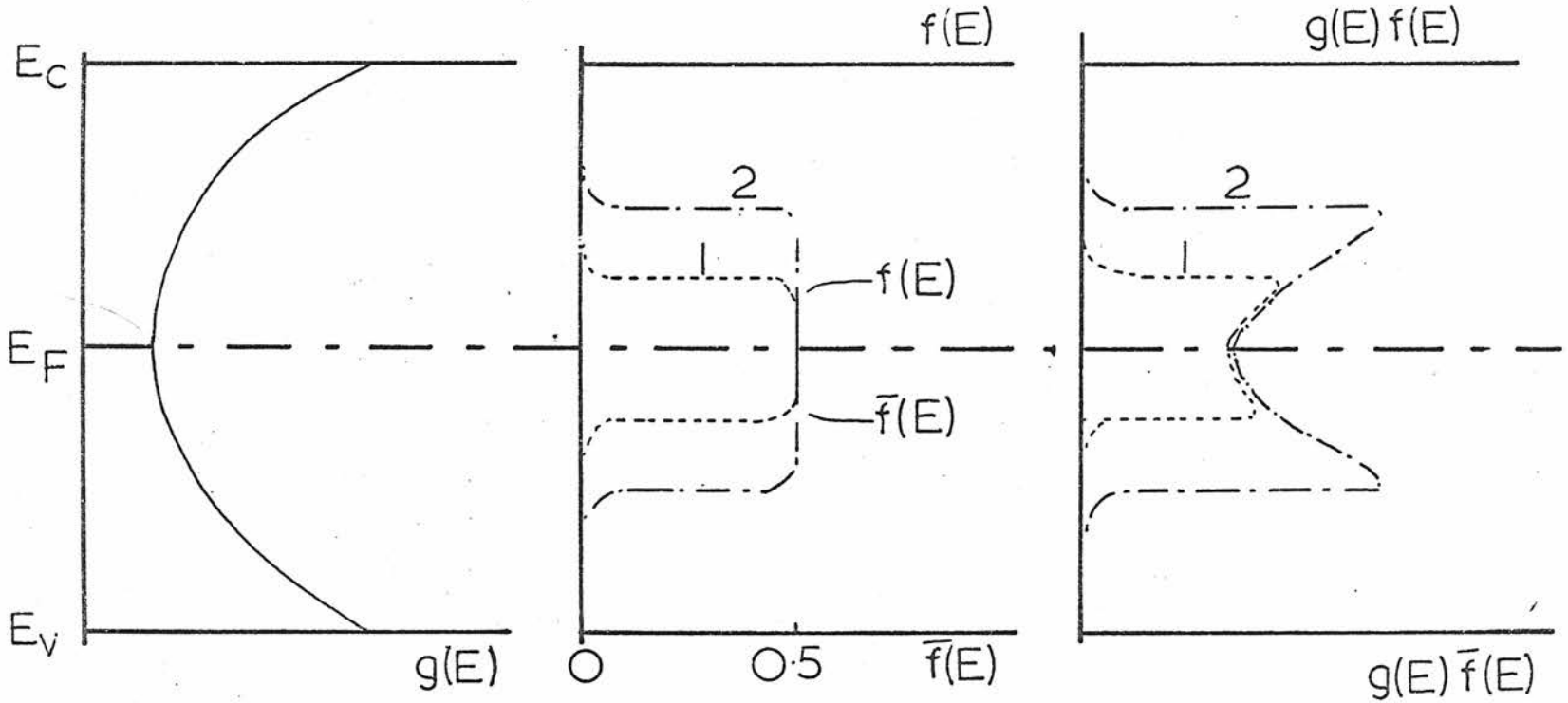

Fig 3.15 Model of Simmons and Taylor Two excitation levels $\Delta G_2 > \Delta G_1$

scattering (density N_s) at lower temperatures and high excitation.

$$\mu_o \propto T^{-3/2} \quad \text{high temperature}$$
$$\mu_o \propto \frac{T^{+3/2}}{N_s} \quad \text{low temperature} \qquad 3.2.104$$

3.3 TRANSIENT PHOTOCONDUCTIVITY

This section deals with simple solutions for the growth and decay of photoconductivity upon the application and removal of constant excitation, in the discrete-trap case.

3.3.1 THE QUASI-THERMAL EQUILIBRIUM APPROXIMATION

Expressions for the free hole lifetime under different excitation and recombination conditions were given in 3.2.13. In general, however, the observed transient behaviour exhibits very different time constants. Formally, the rate equation for the total excess population must be considered - i.e. (c.f. equation 3.2.29)

$$\frac{d}{dt}\left\{\int_{E_V}^{E_C} g(E)\,\Delta f(E)\,dE + \Delta n + \Delta p\right\} = \Delta G(t) \qquad 3.3.1$$

A general solution is impossible, but for the model of 3.2.13, the situation is simplified.

Consider the set of traps at E_2, and the valence band as a 'reservoir' for excess holes, and similarly, the system of conduction band and traps at E_1, as an electron reservoir. In the steady state, equation 3.2.61

holds, and the ratio of free/trapped holes is independent of illumination - i.e. the 'Quasi-thermal equilibrium' (Q.T.E.) approximation

$$\text{i.e.} \quad \frac{\Delta p}{N_2 \Delta \bar{f}_2} = \frac{p_2}{N_2} \qquad 3.3.2$$

It is now assumed that this relation holds during the growth to, and decay from, the steady state. The limits of the validity of this assumption are examined in 3.3.3.

To appreciate the consequences in physical terms, consider the decay of free hole density after excitation has ceased, via path 1. During the decay, rapid trapping interchange with hole traps maintains the Q.T.E. partitioning of free/trapped holes. The observed decay is therefore that of the total reservoir of trapped and free holes. In general, if the free hole lifetime is τ_p, then the observed decay time is τ_c.

$$\tau_c \approx \tau_p \times \frac{N_2}{p_2} \gg \tau_p \qquad 3.3.3$$

A rate equation must be written for the hole reservoir, for all paths, i.e. eliminating intra reservoir transitions.

$$\frac{d}{dt}\left(\Delta p + N_2 \Delta \bar{f}_2\right)$$

$$\approx \frac{d}{dt}\left(\frac{N_2}{p_2}\Delta p\right) = \Delta G - \left[2p_o \Delta p + \Delta p^2\right] \frac{N_2}{p_2}\left\{C_{p1} + C_{n2}\frac{N_2}{p_2}\frac{n_1}{N_1} + K_{12}\frac{N_2}{p_2}\right\}$$

3.3.4

i.e. in terms of Δp

$$\frac{d}{dt}(\Delta p) \approx \Delta G \left(\frac{P_2}{N_2}\right) - \{2p_o\Delta_p + \Delta_p^2\}\left[C_{p1} + C_{n2}\frac{N_2}{p_2}\frac{n_1}{N_1} + K_{12}\frac{N_2}{P_2}\right] \qquad 3.3.5$$

solutions of which are given in 3.3.2. Let the last factor in brackets be θ.

3.3.2 BASIC DECAY SOLUTIONS

i) Small signal case

Solution of equation 3.3.5 gives exponential decay

$$\Delta p(t) = \Delta p_{ss} \exp(-t/\tau_{cm}) \qquad 3.3.6$$

where Δp_{ss} is the steady state solution of section 3.2.13 and

$$1/\tau_{cm} = 2p_o\left(C_{p1} + C_{n2}\frac{N_2}{p_2}\frac{n_1}{N_1} + K_{12}\frac{N_2}{p_2}\right) = 2p_o\theta \qquad 3.3.7$$

All the paths are included here.

The temperature dependence of the decay time is an important means of distinguishing B-L and L-L recombination.

$$\text{Path 1} \quad \tau_{cm}(1) \alpha \exp\left(\frac{(E_2 - E_v) + \frac{1}{2}(E_1 - E_2)}{kT}\right) \qquad 3.3.8$$

$$\text{Path 2} \quad \tau_{cm}(2) \alpha \exp\left(\frac{(E_c - E_1) + \frac{1}{2}(E_1 - E_2)}{kT}\right) \qquad 3.3.9$$

$$\text{Path 3 L-L} \quad \tau_{cm}(3) \alpha \exp\left(\frac{\frac{1}{2}(E_1 - E_2)}{kT}\right) \qquad 3.3.10$$

All exponents are positive, but the L-L path gives a smaller temperature dependence. The greater temperature dependence in the B-L cases arises from the fact that a small temperature dependent fraction of one of the reservoirs is active in recombination, (hence the $(E_2 - E_v)$ and $(E_c - E_1)$ terms) while almost the whole reservoir is involved in L-L recombination. The term $\frac{1}{2}(E_1 - E_2)/kT$ can be interpreted as the equilibrium temperature dependence of recombination centre density.

ii) Large signal case

The decay in the large signal case is 'quasi-hyperbolic' - typical of a bimolecular process

$$\text{i.e. } \Delta p(t) = \frac{\Delta p_{ss}}{1 + \Delta p_{ss}\ \theta\ t} \qquad 3.3.7$$

A bimolecular decay time τ_{cb} may be defined as the time for the excess density to decay to half the steady state value

$$\tau_{cb} = \left(\frac{\theta\ \Delta G\ P_2}{N_2}\right)^{-\frac{1}{2}} \qquad 3.3.8$$

The decay time is now dependent upon light intensity, and again, B-L and L-L paths give rather different temperature dependences.

$$\text{Path 1.} \quad \tau_{cb}(1) \propto \exp\left\{\frac{\frac{1}{2}(E_2 - E_v)}{kT}\right\} \qquad 3.3.9$$

$$\text{Path 2.} \quad \tau_{cb}(2) \propto \exp\left\{\frac{\frac{1}{2}E_c - E_1}{kT}\right\} \qquad 3.3.10$$

$$\text{Path 3.} \quad \tau_{cb}(3) \quad \text{Temperature independent}$$

It was found that the simple solutions obtained above, for bimolecular decay could not adequately explain

some of the results on As_2Se_3 and As_2Te_3. Transient features seem to indicate the presence of other localised states within the mobility gap, which are not sufficiently numerous to affect the steady state results. More detailed analyses are therefore included, in chapter 8.

3.3.3 VALIDITY OF THE Q.T.E. APPROXIMATION

The validity of the Q.T.E. partitioning approximation for transient conditions can be checked by solving the complete rate equations for free and trapped densities, after the onset of illumination, in the discrete trap case, including intra-reservoir transitions.
e.g. for free and trapped holes

$$\frac{dp}{dt} = G - \underline{N_2 C_{p2}\{p(1-\bar{f}_2) - p_2\bar{f}_2\}} - N_1 C_{p1}\{pf_1 - p_1(1-f_1)\} \qquad 3.3.11$$

$$\frac{d}{dt}(N_2\bar{f}_2) = \underline{N_2 C_{p2}\{p(1-\bar{f}_2) - p_2\bar{f}_2\}} - N_2 C_{n2}\{n\bar{f}_2 - n_2(1-\bar{f}_2)\}$$

$$- N_1 N_2\{f_1\bar{f}_2 K_{12} - K'_{12}(1-f_1)(1-\bar{f}_2)\} \qquad 3.3.12$$

For short times, only the underlined terms - corresponding to intra reservoir transitions - need be considered. This follows from the discussion of 3.2.11 and the major assumption is that the hole trapping time is shorter than the free recombination time. (At longer times, the recombination terms increase, and eventually lead to the steady state condition). The further assumption, that $\bar{f}_2 \ll 1$, makes the equations linear.

Solving these simultaneous differential equations gives

$$\Delta p(t) = \Delta G[\tau_{t2}(1 - \exp(- t/\tau_{t2}) + t\ p_2/N_2] \qquad 3.3.13$$

$$N_2\Delta\bar{f}_2(t) = \Delta G[t - \tau_{t2}(1 - \exp(- t/\tau_{t2}))] \qquad 3.3.14$$

These functions are plotted schematically in figure 3.16a and the ratio $\Delta p(t)/N_2\Delta\bar{f}_2(t)$ in figure 3.16b. The growth can be seen to be the sum of an exponential 'equilibration' term, and a linear term. The equilibration time can be seen to be the hole trapping time $\tau_{t2} \approx 1/N_2C_{p2}$, and at times greater than τ_{t2}, the ratio of free/trapped holes is p_2/N_2.

This is in contrast to the view that several capture and release times must elapse before equilibration is achieved. The Q.T.E. approximation is thus valid at times greater than τ_t after changes in excitation, and τ_t can be very short ($< 10^{-9}$ sec) in some chalcogenides. It should also be emphasised that the recombination terms become significant after a time τ_c and not after the free lifetime τ_p. The linear region of figure 3.16a is therefore accessible experimentally.

3.3.4 PHOTO-MOBILITY

The linear region of excess carrier growth depicted in figure 3.16a allows the mobility of excess carriers to be measured. If the photocurrent is carried by free holes, then

$$\frac{d\Delta I}{dt} \alpha\ \mu_{po}\ \frac{d\Delta p}{dt} \alpha\ (\mu_{po}\ \frac{p_2}{N_2})\ \Delta G \qquad 3.3.15$$

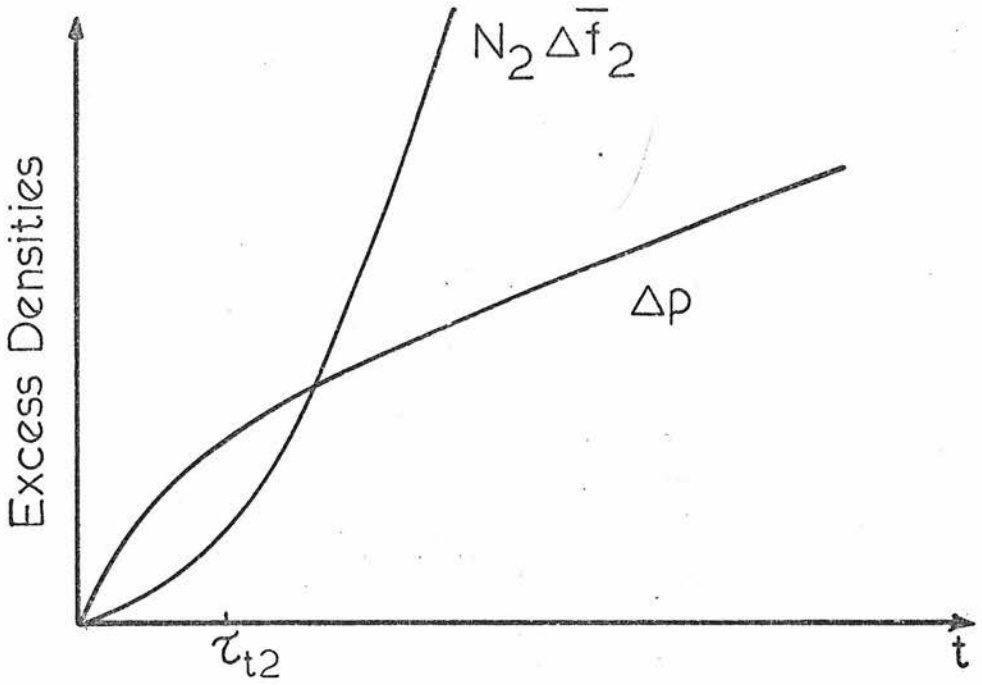

Fig 3 16a Step response Photogrowth of free and trapped hole densities

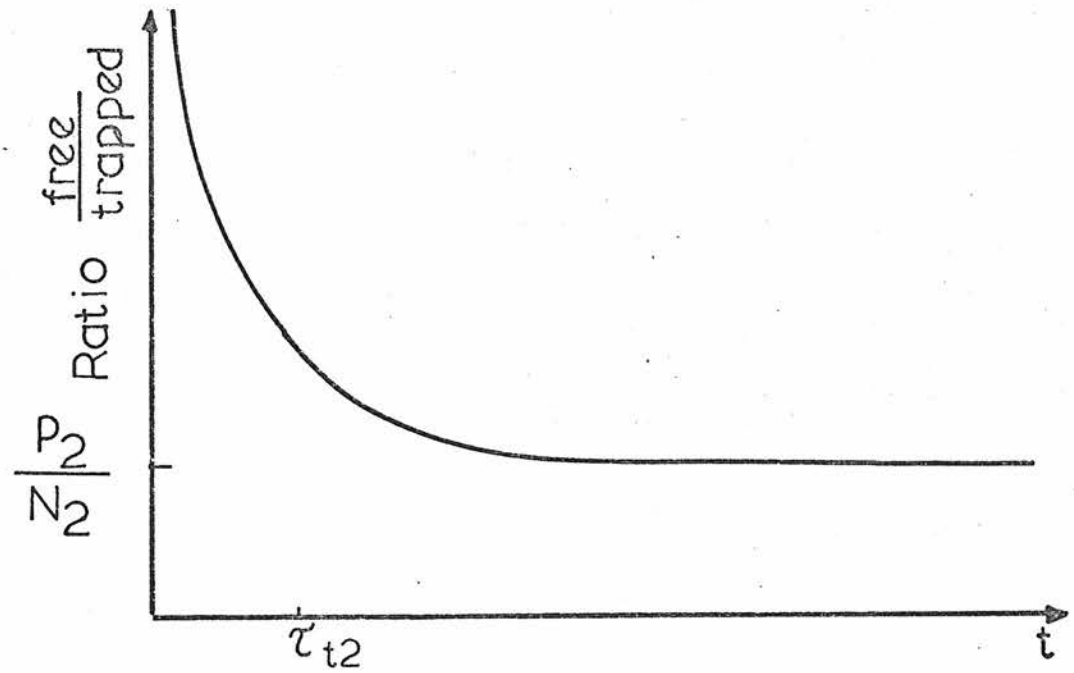

Fig 3 16b Ratio $\frac{\text{free}}{\text{trapped}}$ excess densities

in the linear slope region. Now the factor in brackets is approximately the trap-limited drift mobility μ_d

$$\mu_d \approx (\mu_{po} \frac{p_2}{N_2}) \qquad 3.3.16$$

In general, whatever the conduction mechanism, the effective mobility of the total excess population may be ascertained.

The results of sections 3.3.3 and 3.3.4 apply to transient response, with only one discrete trapping level. It is again possible that a number of levels are present which may influence the transient response and yet not control the steady state condition. This in fact appears to be the case experimentally, and a short time 'photocurrent slope' measurement may reveal the trap-limited drift mobility corresponding to a faster trapping, yet less dense, set of traps than that revealed in steady state measurements. A fuller analysis shows that a number of linear regions may appear in the growth curve, each corresponding to a particular trap level.

Analysis for distributed states is correspondingly more difficult, and has not been attempted.

CHAPTER 4

EXPERIMENTAL METHODS FOR OPTICAL AND PHOTOCONDUCTIVE PROPERTIES

4.1 INTRODUCTION

A number of techniques, many of which are standard in principle were used to determine the optical and photoconductive properties of the amorphous chalcogenide thin film samples. The optical measurements, in most cases, duplicated work by others in the field, as reported in Chapter 7 .

This was felt to be essential for quantitative interpretation of the photoelectric measurements as accurate knowledge of the optical parameters of identical films was required. In view of the slight differences between various authors' reported values for these parameters, in particular, the optical absorption coefficient, α, optical measurements were carried out on films prepared simultaneously with those used for photoconductive work. It will be evident that small errors in the value taken for α, which appears as an exponent in many of the expressions developed, can introduce large relative errors.

The photoconductivity measurements had a relatively novel feature in that recently developed semiconductor light emitting devices (l.e.d.'s) were used extensively. These devices provide an easily calibrated and controlled source of light, with a fairly narrow spread of photon energy. The light intensity can be accurately varied over 10 orders of magnitude, and, when used with suitable fast pulse generators, they enable a time resolution of 10^{-8} s

to be achieved. This performance equals (or betters) previously used flash techniques such as spinning mirrors[121] and pressurised spark discharges[122].

Straight-forward electrical characteristics were also determined for the films in the dark, as these gave information essential for the interpretation of the photoconductivity data.

4.2 SAMPLE PREPARATION AND CHEMICAL ANALYSIS

The preparation of the specimens used in this work is straightforward. Thin film samples for optical, electrical, and photoconductive use were prepared simultaneously by evaporation of the material from a heated quartz capsule, on to glass substrates 8" - 9" above the source through appropriate cut-outs and masks, at a pressure of about 10^{-5} torr. The materials were '5N' (99.999%) purity As_2Te_3 and As_2Se_3 lumps (Koch-Lite Laboratories Ltd). The substrates used throughout were of Corning 7059 (Barium aluminosilicate) glass, and a fast evaporation rate of about 300 Å s^{-1}, together with a moveable radiation shield, ensured that the substrate temperature did not rise appreciably above 20°C.

In this way, thin films of thicknesses from 0.3 μm to 2.5 μm were deposited, the lower limit being set by a desire to avoid pinholes. An upper limit was set because it has been reported that crystallisation can occur during evaporation of As_2Te_3 films, on the surface furthest from the substrate, if the film thickness exceeds about 1 μm[59]. Furthermore, absorption measurements were required for high values of α, from 10^5 to 10^7 m^{-1}, in order to cover the region of the fundamental absorption edge, in which region

the photoconductivity and its associated parameters, such as quantum efficiency, were being investigated.

On completion of the evaporation, the film thickness was determined, using a 'Talysurf' model 4 thickness monitor. This instrument operates by drawing a needle across the surface under investigation, registering the 'step' at the edge of the evaporated film, by a zero drift a.c. technique. As its resolution is about 0.01 μm, typical errors in sample thickness determination were about ± 1%. Occasionally, the films were slightly 'wedge'-shaped, with a thickness variation of up to 2% from one side to another, but as optical and electrical measurements were made over a very limited region of the deposited film, this introduced no significant error. A good clean 'step' from substrate to film was obtained by scraping the film back with a sharp scalpel blade, and this was repeated at several points round the sample.

No detailed investigation on sample composition was carried out, but some representative films were checked by X-ray fluorescence analysis and others by spectrophotometer colorimetry techniques. The x.r.f. work was carried out in the Geology Department of this University, and the x.r.f. sample was deposited at the same time as the optical and electrical samples, on a glass disc, $1\frac{1}{4}$" diameter. As the sensitivity of the x.r.f. method is dependent on film thickness, the accuracy of this analysis was estimated at no better than ± 5 at.% while the colorimetry methods give an accuracy of $\lesssim$ 2 at.%. for a sample mass of ~ 10 mg.

The geometry of the samples is shown in figure 4.1. Apart from the x.r.f. discs, all samples were deposited on 1" x $\frac{1}{2}$" substrates, 0.02" thick. Metal electrodes, for the electrical and photoconductive samples had previously been evaporated on to some slides. For this part of the work, a co-planar geometry was used, the interelectrode gap being obtained by using fine nickel wire as a mask. The metal evaporation was carried out in another vacuum system, using electron beam evaporation at a pressure of 10^{-5} Torr. Semi-transparent electrodes of gold were used, about 200 Å thick, as it was found that gold made satisfactory low resistance contacts to all the films used. Fine gauge copper wires were attached to the ends of the electrodes by means of silver 'dag' suspension providing a good mechanical and electrical joint.

4.3 ENVIRONMENTAL CHAMBER

Most of the measurements reported here were carried out in vacuo, in a chamber fitted with a 'cold-finger' temperature control assembly and various optical and electrical parts. The complete system is shown in figure 4.2.

The temperature control assembly with sample clamp is shown in figure 4.3 and schematically in figure 4.4. A copper reservoir, insulated with polystyrene foam is filled with liquid nitrogen which flows into a $\frac{1}{4}$" blind hole in a $\frac{1}{2}$" copper rod brazed into the reservoir's side. Surrounding this rod, but not touching it is a $\frac{3}{4}$" stainless

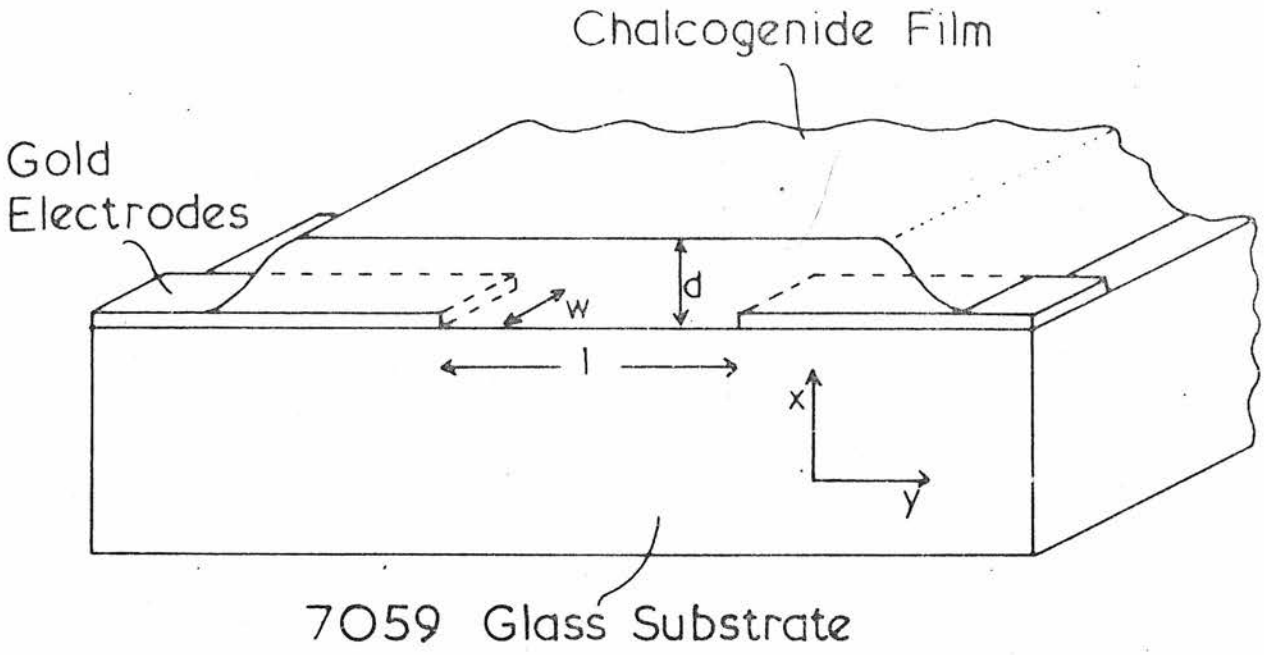

Fig 4.1 Sample Geometry.

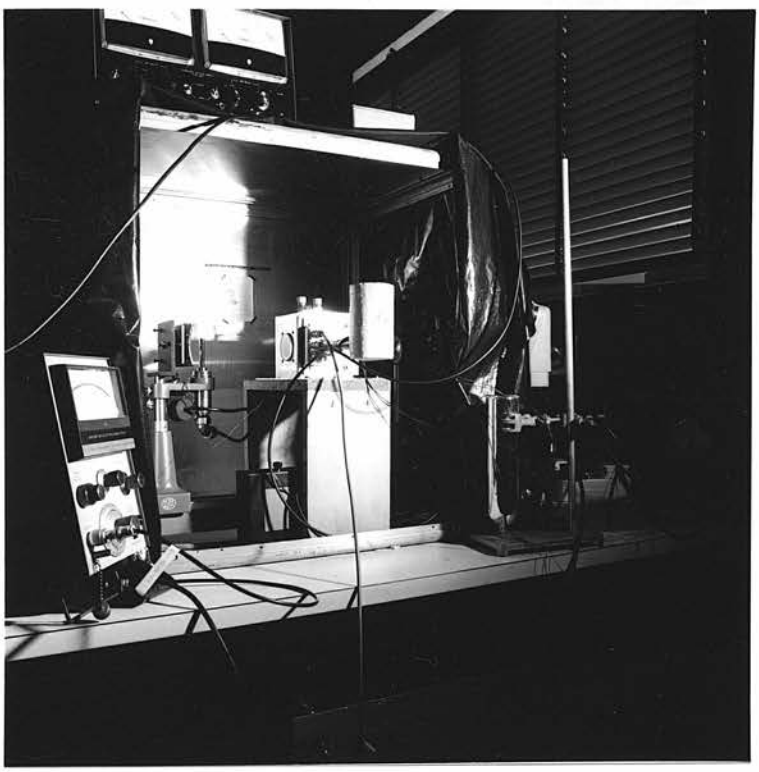

Fig 4.2 Measurement System.

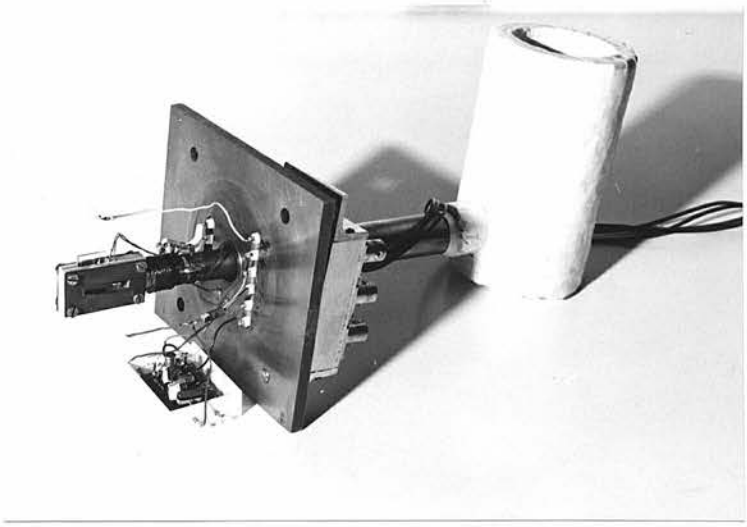

Fig 4.3 Cold finger Temperature controller

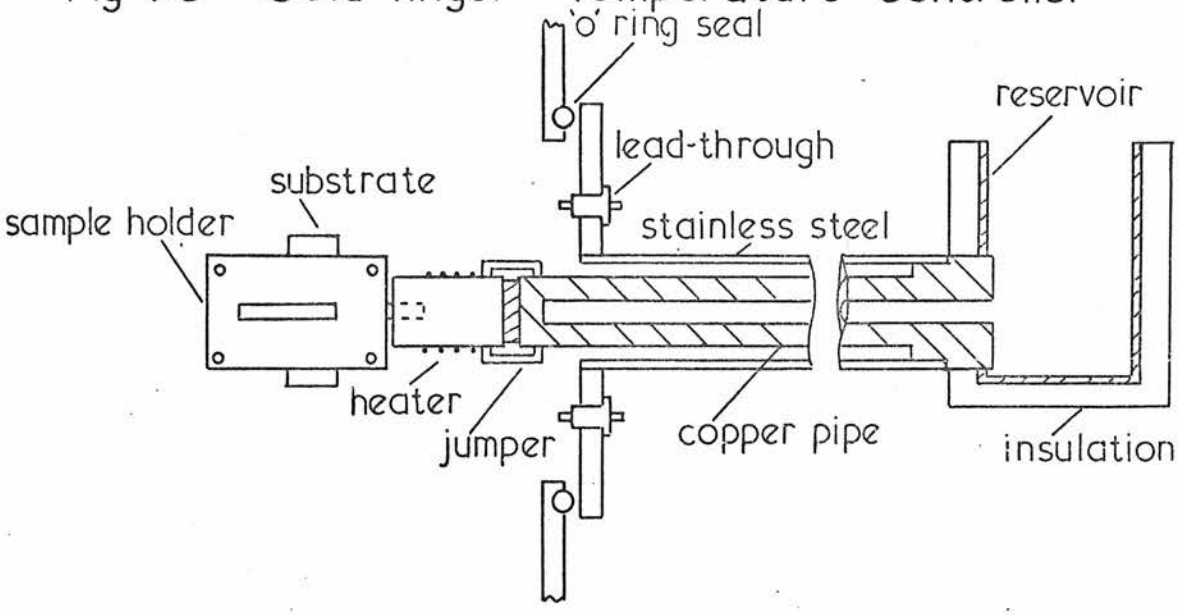

Fig 4.4 Cold finger Temperature controller (schematic)

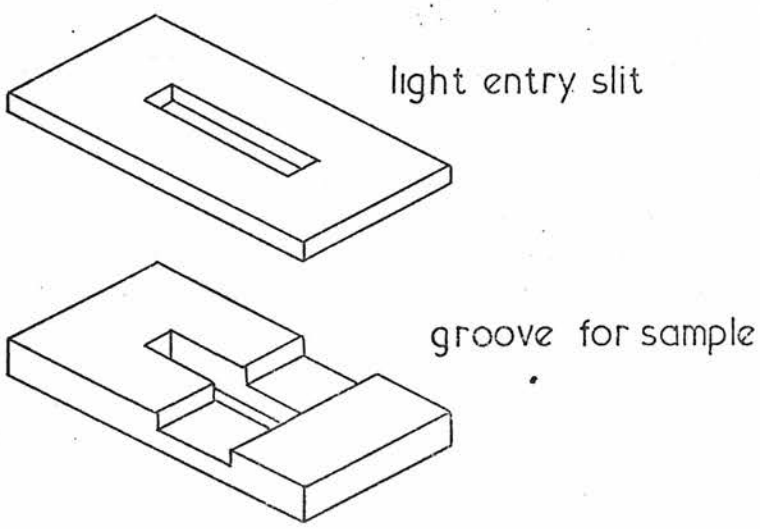

Fig 4.5 Sample holder

steel tube welded to the rod and reservoir at one end, and to a brass flange at the other. The low thermal conductance of this tube enables the use of an ordinary rubber 'O' ring vacuum seal between the brass flange and the vacuum chamber. Although the other end of this tube is at 77 K, the brass flange remains at room temperature, keeping the 'O' ring flexible. Conduction and convection of heat across the gap between the copper rod and stainless tube is small, as this gap is evacuated along with the vacuum chamber, when in use.

The cold copper rod thus projects into the vacuum chamber, and an $\frac{1}{8}$" thick ceramic disc insulator separates it from a further length of copper rod, upon which a heater coil is wound. This heater coil consists of 30 turns of thin nichrome wire, wound non-inductively in two layers upon asbestos tape. Eight removable 'jumper' bars connect the heater and cold rod thermally (and electrically) across the ceramic disc.

Temperature control of the sample clamp is effected by heat flow balancing. Heat input to the heater coil is balanced against heat flow across the jumper bars to the cold finger, and by varying the heater current, or removing jumpers, a very fine control can be achieved.

Figure 4.5. shows the sample clamp construction. The 1" x $\frac{1}{2}$" slide is held "face-up" in a groove in one side of the clamp by two pads of P.T.F.E. tape stuck to the other side of the clamp. A rectangular hole 1" x $\frac{1}{8}$" is cut in both sides of the clamp, to allow optical work to be done

on the sample, and two copper 'radiation baffles' can be bolted on either side to minimise radiative heat loss from the exposed part of the sample. The clamp screws tightly into the heater section of the temperature control assembly, with a $\frac{1}{4}$" diameter copper bolt. Chromel-alumel thermocouples were also held in the sample clamp, for temperature monitoring.

Several 'dry runs' were carried out to check the operation of this temperature control system. Continuous variation of the temperature of the clamp between 95 K and 500 K was possible, with a cool-down time to 95 K of about 30 minutes. Radiation losses were responsible for the inability to cool below 95 K.

The possibility of a temperature difference between the sample clamp and the upper surface of a sample was checked by using a small thermistor bead element stuck to a glass substrate. It was found that this temperature difference was 5 K when the clamp thermocouple read 100 K. Subsequent measurements were thus corrected, using a linear interpolation of this difference, between 100 K and 290 K. Substrate temperatures could normally be held to within $\pm$ 0.25 K for indefinite periods, a stability judged to be satisfactory for the present work.

Electrical connections to the sample and other gear inside the vacuum chamber were made via 10 P.T.F.E. 'barb' lead throughs, of very high insulation resistance, through the flange of the cold finger assembly. Many of these leads required screening from electrical interference, pickup etc., and were connected to co-axial (BNC) sockets

screwed into a small box covering the lead throughs.

A small preamplifier, its power supplied via lead throughs could be placed within the vacuum chamber, very close to the sample. The performance and design of this amplifier will be discussed later, and also the reasons for its proximity to the sample.

The vacuum chamber itself is a $4\frac{1}{2}$" x $4\frac{1}{2}$" x 4" box constructed from $\frac{3}{8}$" dural alloy, with welded vacuum-tight seams. It has 3 circular holes all with grooves for 'O' rings. Two of these, on opposite faces are the optical ports, and the third is for the cold finger flange. On the top of the box are two miniature gas-valves (manufacturer "Drallim").

Quartz windows are held in place at the optical ports by flanges, bolted into tapped blind holes in the chamber wall. An alternative means of introducing light to the sample is by means of a 'light-pipe', and the type used here was a $\frac{1}{4}$" diameter polished perspex rod passing through a $\frac{1}{4}$" vacuum lead through in an aluminium flange. The flange replaces one of the quartz windows at an optical port, with the light pipe protruding inward to within $\frac{1}{8}$" of the sample. Perspex is easily polished, and the end faces of the pipe were machined flat and polished to give a fairly undistorted transmission. This light input method also screens the sample electrically, from the light source.

4.4 OPTICAL MEASUREMENTS

Measurements of optical transmission and reflection using thin film samples, were carried out, allowing the determination of the optical absorption constant and the refractive index of the material in question. The photon energy dependence of those properties was plotted, and interpreted using current models for amorphous materials. The equipment mainly used in this part of the work consisted of a Hilger D285 monochromator, with a tungsten ribbon light source, a Hilger-Schwartz fast vacuum thermopile model FT20, and Grubb-Parsons a.c. thermopile amplifier type TA. A chopping frequency of $16\frac{2}{3}$ Hz was used, the amplifier being tuned to this. For most of the measurements, the monochromator was fitted with a glass prism, giving a useful wavelength range of 0.4 μm to 2.0 μm.

Alternatively a Zeiss spectrometer model MM12D, with PbS detector and amplifier unit PMQII was used, with Quartz prisms, for some transmission and reflection measurements at room temperature.

Transmission measurements were done on thin film samples held in the sample clamp and vacuum enclosure already described. The enclosure was placed on rails, with two end-stops to register its position for the two measurements required. In one position, the sample interrupted the light beam, and in the other position, the light passed through the rectangular hole in the sample holder uninterrupted. The transmission T_r was measured at 2 temperatures, 100 K and 290 K and the optical absorption

constant α, at each photon energy was calculated using the following expression to relate α to T_r [59]

$$T_r = \frac{(1 - R_1)(1 - R_2)(1 - R_3)e^{-\alpha d}}{(1 - R_2R_3)\{1 - [R_1R_2 + R_1R_3(1 - R_2)^2]e^{-2\alpha d}\}} \quad 4.4.1$$

This equation applies to the case of an absorbing film on a non-absorbing substrate. The effects of multiple reflections are included, but interference and coherence effects are not. R_1, R_2, R_3 are the reflectances at the air-film, film-substrate, and substrate air interfaces, respectively. R_3 is calculated from the known index of refraction of the glass substrate $n_g = 1.5$, with the relation

$$R_3 = \left(\frac{n_g - 1}{n_g + 1}\right)^2 = 0.04 \quad 4.4.2$$

To calculate the reflectances R_1 and R_2, the refractive index n_s of the thin film material was determined by examining the interference fringes which appeared in the high transmission region. The condition for maximum transmission is given by

$$2 n_s d = m \lambda \quad 4.4.3$$

and for minimum transmission

$$2 n_s d = (m + \tfrac{1}{2}) \lambda \quad 4.4.4$$

where d is the film thickness, m is an integer, and λ the

free space wavelength of the incident light. Although the value of the refractive index was found to vary with wavelength, the expression 4.4.1 for α is relatively insensitive to the values of R_1 and R_2 in the low transmission region ($T_r \ll 1$) so the value taken for n_s was that determined at the onset of the interference fringes, as close to the absorption edge as possible.

Attempts were also made to measure the reflectance of the sample directly. Light from the monochromator exit slit is focussed on the detector, which swings on an arm at the axis of which the sample can be placed. In the first position, the incident intensity is measured, and in the second position the intensity of reflected light at a small angle ($< 10^{\circ}$) to the normal, with identical light path length is measured.

An accuracy of no better than $\pm 10\%$ in reflectance was estimated, due to variations in path length, image size and detector positioning. Within these limits, reasonable agreement was obtained with values estimated from interference effects in transmission.

4.5 DARK CONDUCTIVITY MEASUREMENTS

Prior to the photoconductivity work, straightforward electrical measurements were carried out, with the same samples, in the dark. The dependence of the 'dark' conductivity on temperature, at low and high fields, was studied, and current-voltage measurements were carried out at different temperatures. These measurements, as well as providing information required in the interpretation of

photoconductivity results, such as the position of the thermal equilibrium Fermi level gave useful additional information on electronic structure and conduction mechanisms.

An aluminium box 25" x 25" x 20" surrcunded the sample chamber, screening it from external light and electrical interference during these and subsequent measurements. Light from the monochromator exit was allowed to enter, and the Liquid nitrogen reservoir protruded through opaque plastic sheet, to allow 'topping up'.

A d.c. voltage was applied to the sample by a Bradley model 123 d.c. source, with stepped output (mV steps) from 0 - 500 V. An R-C filter was placed at the output of this source to reduce further the level of mains hum on the applied voltage, and to avoid voltage spikes' which occurred on switching the output voltage. A Keithley model 610B electrometer was used for all the current measurements, with special 'low-noise' input cable to minimise tribo-electric effects.

4.6 OPTICAL SOURCES AND DETECTORS

4.6.1 DETECTORS

The Hilger-Schwartz fast vacuum thermopile was used as a standard to calibrate the light sources and other detectors. This device is a power detector, measuring the power in the incident radiation over its surface area, independent of the wavelength of the radiation. The wavelength was limited by the CaF_2 window of the device to the range 0.2 μm to 10 μm, satisfactory coverage for the

present measurements. Sensitivity was quoted by the manufacturer as 23 $\mu V.\mu W^{-1}$ of incident radiation, and as the detector surface area was 0.2 mm x 4 mm (8×10^{-7} m^2) this is a power density sensitivity of 1.84×10^{-2} V W^{-1} m^2. Translating this into terms of photon flux density F(photons m^{-2} s^{-1}), the relationship between photon wavelength λ and energy E is used

$$E = h\ c/\lambda \qquad 4.6.1$$

This gives, using appropriate units

$$E = \frac{1.240}{\lambda(\mu m)} \quad \text{electron volts} \qquad 4.6.2$$

and leads to the relation

$$= \frac{\text{Power density (W } m^{-2})}{1.98} \times \lambda\ (\mu m) \times 10^{19} \qquad 4.6.3$$

(photons m^{-2} s^{-1})

Because of the low sensitivity and slow response time of the thermopile a second detector was required for low light intensity and high speed measurements. A silicon p-i-n photodiode, Monsanto type MD2, was chosen for this application, but this device has the disadvantage, when compared with the thermopile, of having a peaked spectral response, and is essentially a quantum (not power) detector. This was not important as it was to be used with sources of specified wavelength (l.e.d.'s) and was calibrated against the thermopile using those sources. Table 4.1 lists the sensitivities of the diode at the 3 wavelengths of interest.

Wavelength (μm)	Sensitivity	
	A W^{-1} m^2	μA/10^{19} photons m^{-2} s^{-1}
0.655	11.9 x 10^{-4}	3.64
0.905	9.1 x 10^{-4}	2.00
0.845	8.7 x 10^{-4}	2.04

Table 4.1. MD2 p-i-n photodiode sensitivity

One of the main advantages of the MD2 p-i-n photodiode is its fast response time, which has been measured as less than 1.0 ns in the circuit shown in figure 4.6. This circuit, with a 15 V battery, was built in a small screened can with optical access through a $\frac{1}{4}$" light pipe, see figure 4.7.

4.6.2 SOURCES

The monochromator used as a source of variable wavelength light has been described above. For steady-state photoconductivity work, the same configuration is used, light from the exit slit being focussed on the sample with a short focal length achromatic lens. Typical photon flux densities available from this source ranged between 10^{17} and 10^{20} photons m^{-2} s^{-1}, depending on wavelength. The combination of Tungsten light source and glass prism gives a spectral distribution of photon flux, which, uncorrected, peaks at 1.2 μm.

Two light emitting diodes were used extensively for the pulsed photoconductivity measurements and also for some steady-state measurements. Figure 4.8 shows some of

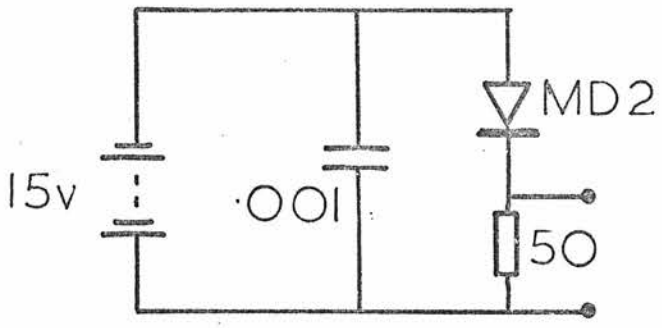

Fig 4.6 p-i-n diode photodetector circuit

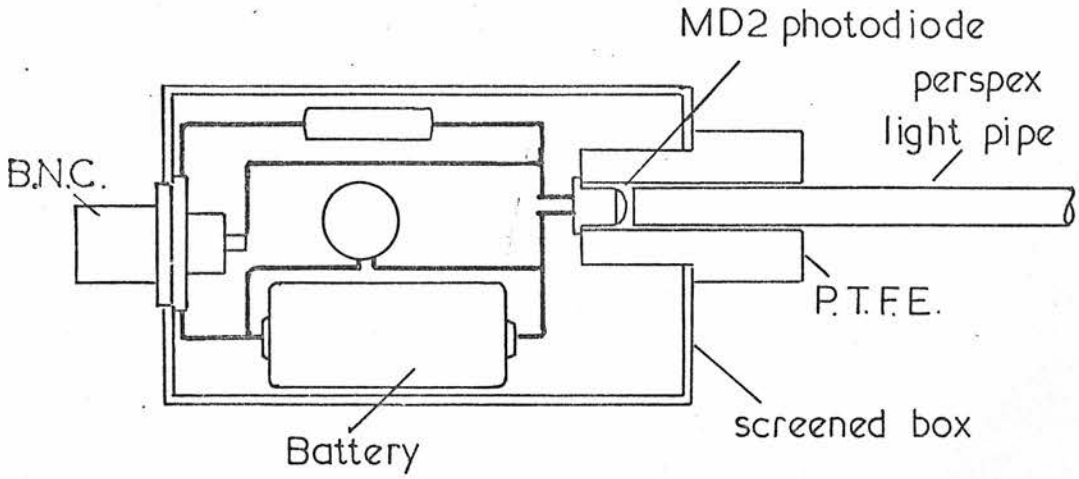

Fig 4.7 Photodetector construction

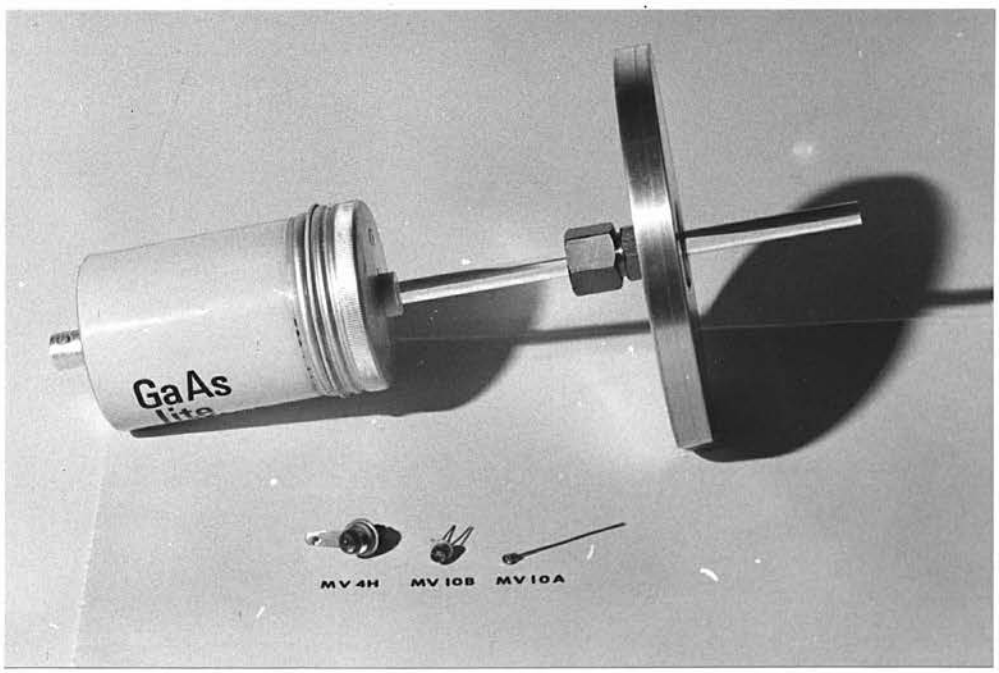

Fig 4.8 Typical light emitting diodes

the devices available. These devices are diffused planar diodes which emit light incoherently, when forward biased, over a narrow band of 400 Å half width. The first device, type MV4H was a GaAsP diode, emitting in the visible region at a wavelength of 0.655 μm peak. The second device, type ME5A was a GaAs diode emitting in the infra-red at 0.905 μm peak. Details of the devices are given in the Monsanto Directory of GaAs lite Products (Cupertino California, 1971).

For As_2Se_3, with an optical gap of 1.86 eV at room temperature, the GaAsP l.e.d., emitting at 1.89 eV was employed, while for the narrower gap material As_2Te_3, (optical gap 0.86 eV at room temperature), the GaAs l.e.d. and laser emitting at 1.37 eV were suitable.

Each diode was calibrated for photon flux density output versus steady d.c. current input, using a d.c. power supply, rheostat, and MD2 photodetector. At all times, during calibration and subsequent use, the diodes were fitted with $\frac{1}{4}$" diameter Perspex light pipes, and the calibration curves of figure 4.9 refer to the photon output from the light pipe. It can be seen that a wide range (10^{13} to 10^{20} photons m^{-2} s^{-1}) of photon flux density was available, and easily controlled and monitored, using a sensitive multimeter (Solartron type 1240), with current range 1 μAmp to 2 Amps.

For the production of light pulses of known width and amplitude, the simple circuit shown in figure 4.10 was used. A BFX 38 high current transistor in emitter-follower configuration is fed from a 50 ohm output pulse generator ('Intercontinental' type PG1). Connected in

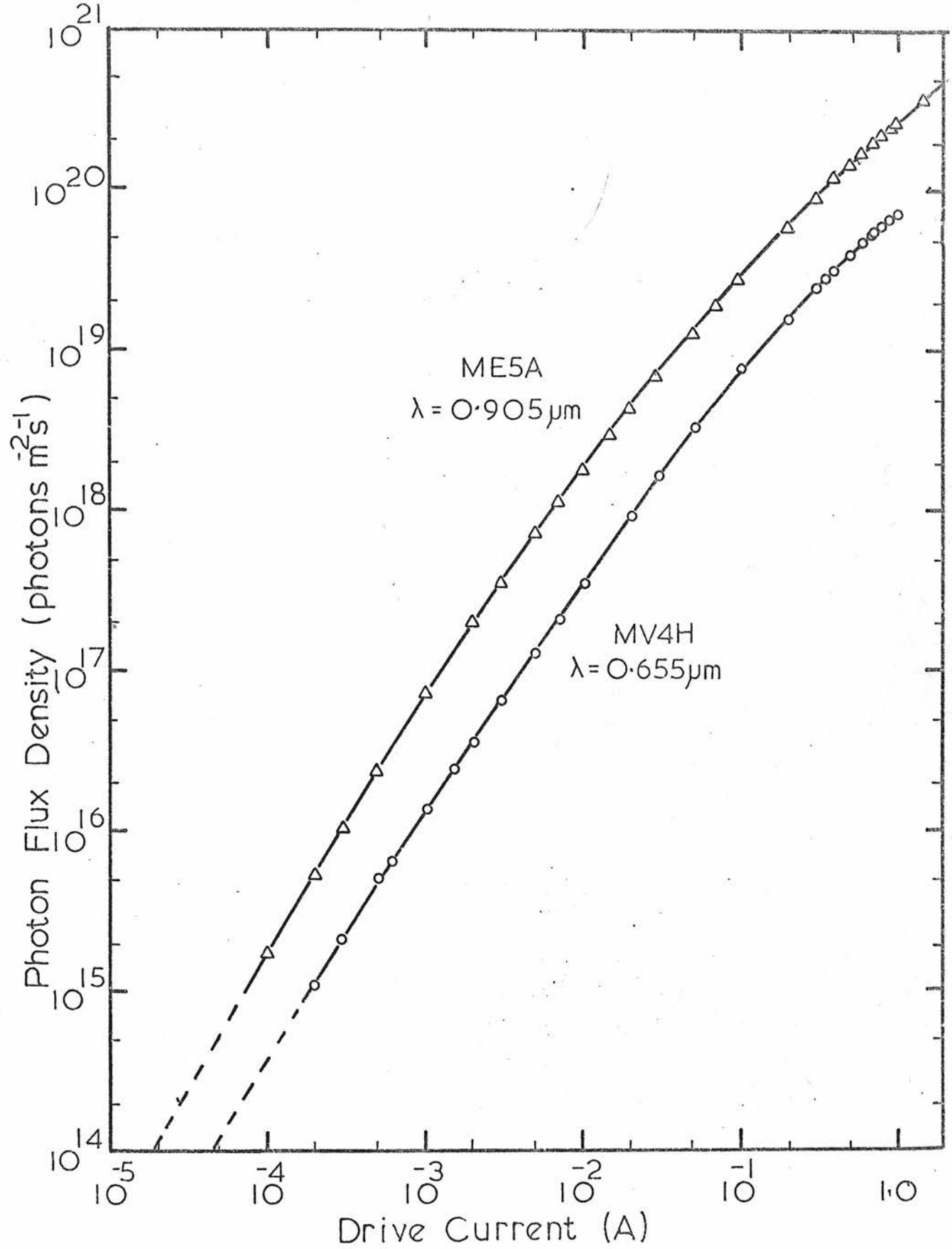

Fig 4.9 Light Emitting Diodes Calibration

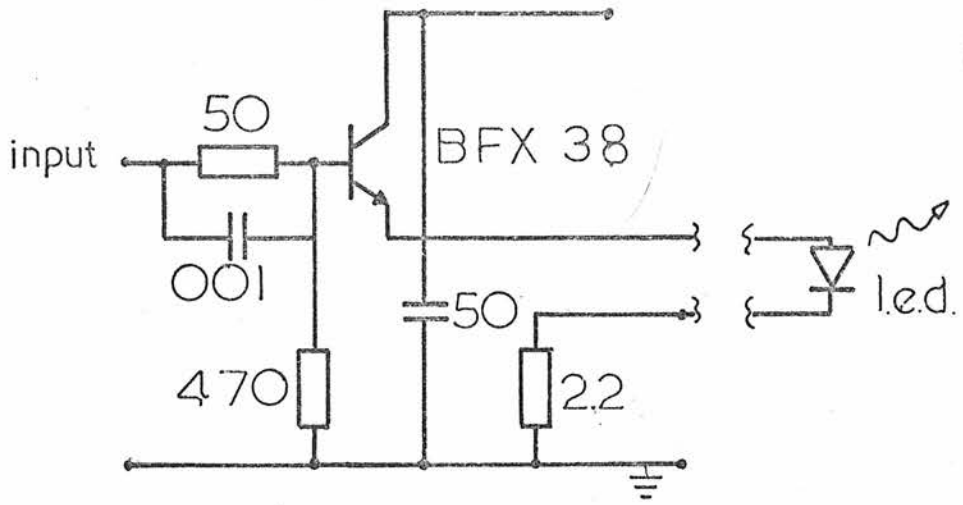

Fig 4.10 L.E.D. Pulsing circuit

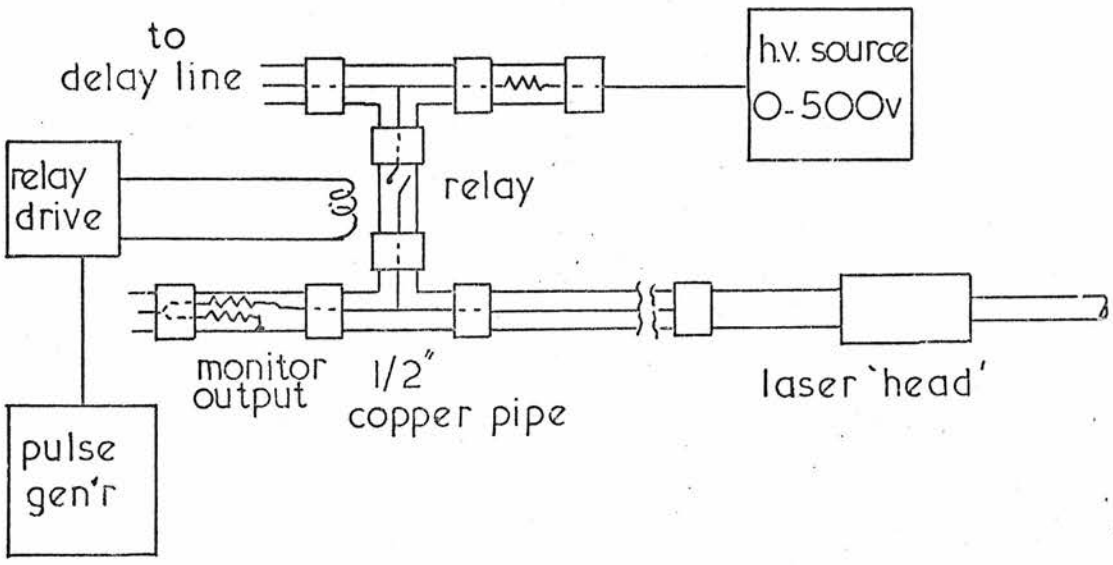

Fig 4.11 Laser pulse generator schematic.

series with the emitter are the l.e.d. and a 2.2 ohm resistor for current monitoring. Current pulses of up to 5 A could be obtained, with rise and fall times (10% to 90%) of 100 to 200 ns. To avoid over heating of the transistor, the supply voltage V_{CC} is varied to keep the transistor just out of saturation, a condition which results in low power dissipation and relatively fast response.

The light output pulses from the l.e.d.'s were monitored with a fast photodetector (MD2) and a Hewlett Packard 140 A oscilloscope, and were found to have rise and fall times very similar to the current pulses. This is not surprising, as, using suitable circuitry, the diodes are capable of 10 ns response times. (20 ns was the shortest optical rise/fall time achieved in this laboratory with the l.e.d.'s).

A GaAs laser, RCA type TA7606 was used to give fast rising high output light pulses of up to 10^{23} photons m^{-2} s^{-1}. This device is also a semiconductor diode, which emits light when forward biased. The construction of the diode is such, that when a sufficiently high density of carriers is injected into the junction region, lasing by light stimulated radiative recombination occurs, and light is emitted from the thin junction region (about 1 μm across). Unlike most other lasers, the beam is not parallel, as it diffracts on leaving the narrow emission region, giving a spread of about 15^{o} half width, a disadvantage obviated by the use of light pipe in close contact with the laser and the sample.

Rather different circuitry shown schematically in figure 4.11 was used to produce the fast rising high current pulses required to drive the laser (up to 5 A). A 50 ohm co-axial line is charged through a 100 kilohm resistor from a Bradley 123 voltage source, and then discharged by the mercury wetted reed relay (Elliot type 226D) in to a 50 ohm matched line, terminated by the laser in series with a 47 ohm resistor.

The reed relay contacts, normally held off by a bias magnet, were closed by applying a coil current of 1 A, supplied by a high power transistor circuit shown in the figure. The transistor circuit was fed with 2 ms pulses at a repetition rate of 1 - 100 Hz, from a pulse generator (Intercontinental type PG1) and was found to give satisfactory bounce-free operation in the reed relay.

Careful design of the system, which involved placing the relay, charging resistor and monitoring potential divider within $\frac{1}{2}$" copper tubing,minimised unwanted reflections due to mismatches. Satisfactory matching of the output was achieved using a 47 ohm resistor in series with the laser, as the forward dynamic resistance of the laser is low (< 10 ohms at high current). Two additional components were included in the laser "head"; a silicon diode back to back with the laser diode, to prevent excessive reverse voltages causing damage to the laser (3 V reverse is the maximum allowed back voltage) and a 100 ohm resistor to ensure proper turn off in the period between the end of the current pulse and the re-opening

of the relay contacts. As mentioned, these components are included in a matched laser "head" which is shown in cross-section in figure 4.12.

At room temperature, power dissipation limits the maximum pulse width to 200 ns, at a peak current of 10 A, while operation at liquid nitrogen temperature allows pulse widths of up to 2 μs. Calibration was carried out using an MD2 photodiode and Hewlett-Packard type 140 A oscilloscope. Figure 4.13 shows the photon flux density output versus drive current for room temperature operation with 200 ns pulses, and for liquid nitrogen temperature operation with 2 μs pulses. For operation at liquid nitrogen temperatures, a simple heat-sink clamp was attached to the laser head, and immersed in liquid nitrogen. Again, as with the l.e.d.'s, a $\frac{1}{4}$" Perspex light pipe was used with the laser during calibration and operation.

Rise and fall times of the current pulse and light pulse were also checked, using a Bradley type 158 sampling adaptor with the Hewlett-Packard oscilloscope, to reduce the instrumental rise time to <1 ns. The light 'turn-on' was satisfactory, rising to 50% in 1.6 ns, and 100% in < 10 ns. The radiation decay, after a rapid initial fall to 50% in 1.6 ns, exhibited a longer 'tail', of low level (< 10%) lasting a further 30 ns. This was attributed to poor quality delay line cable, as the current pulse was of similar shape, but did not appreciably affect decay time measurements in the materials studied.

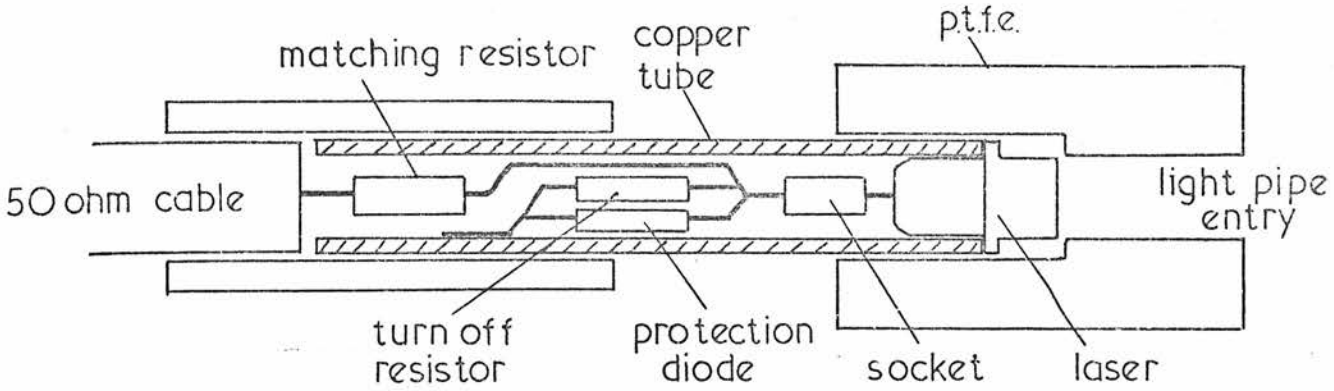

Fig 4.12 Laser head assembly

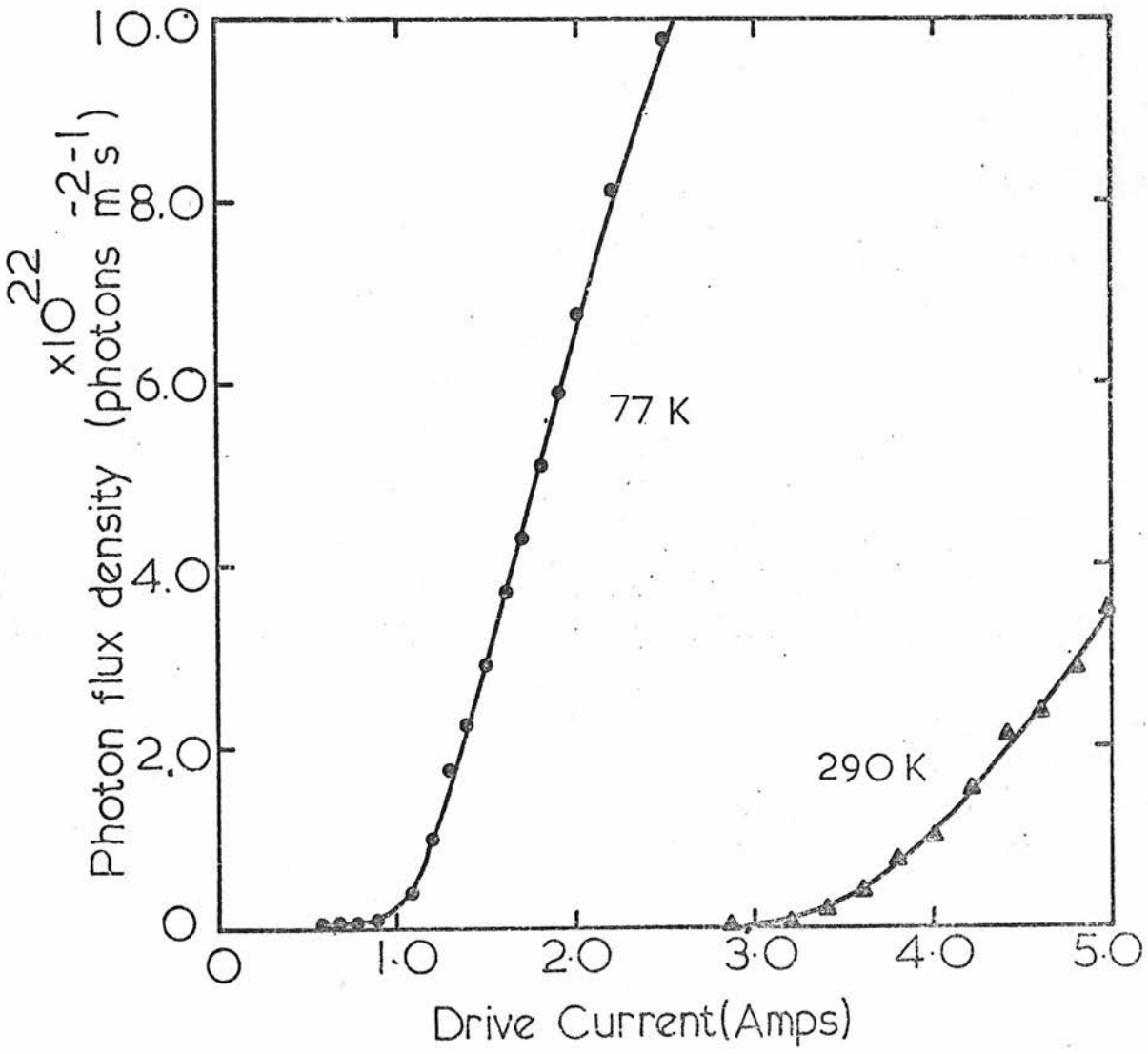

Fig 4.13 GaAs Laser calibration

4.7 LIST OF PHOTOCONDUCTIVITY MEASUREMENTS

Steady state photoconductivity

Spectral dependence

Temperature dependence

Intensity dependence

Transient photoconductivity

Photocurrent growth

Photocurrent decay

4.8 STEADY STATE PHOTOCONDUCTIVITY TECHNIQUES

4.8.1 PHOTOCURRENT DETECTION

Two methods d.c. and a.c. were used to measure the photocurrent, depending on the 'background' dark current. In the d.c. method used when the dark current was relatively small compared with the photocurrent, a d.c. voltage source supplied a constant field and the total current under steady illumination was measured with a Keithley 610B electrometer, making small corrections for the known dark current. The other method employs chopped illumination and a.c. detection, eliminating the dark current from the measurement. A constant voltage was applied to the sample in series with a small resistor, and the illumination was chopped at a rate of $16\frac{2}{3}$ Hz, producing an a.c. photo signal in the series resistor. This signal after amplification by a small f.e.t. preamplifier was detected

using a lock-in amplifier (Princeton Applied Research model HR-8). The a.c. method becomes unusable, however, when the photocurrent response time approaches the reciprocal of the chopping rate, a condition under which no measurements were made.

Bearing the above limitations in mind, the d.c. method was capable of detecting photocurrents of 10^{-13} A in a background of 10^{-13} A dark current, while the a.c. method enabled the detection of 2×10^{-12} A photocurrents in a background of 10^{-6} A dark current.

4.8.2 SPECTRAL RESPONSE

As already mentioned, a Hilger D285 monochromator, with tungsten ribbon lamp, was employed as a source of variable wavelength illumination, while the incident intensity was measured with the fast thermopile. To achieve as high an intensity as possible, the monochromator entrance and exit slits were opened to a wide setting of about 1 mm, resulting in a low, but satisfactory resolution. Care was taken to illuminate the samples with equal photon flux density at all wavelengths, an important precaution where the photoconductivity is not linearly dependent on intensity. Where this procedure was not possible, the (measured) intensity dependence of photoconductivity was included in a normalisation of photocurrent vs. photon energy at constant flux density.

The dependence of photocurrent on photon energy was determined for several values of applied field at various temperatures.

4.8.3 TEMPERATURE DEPENDENCE

Under a constant photon flux of fixed wavelength, at constant applied field, the dependence of photocurrent on temperature was measured, using the above-mentioned detection techniques. The light source in this case was normally an l.e.d., operated with constant drive current for d.c. photocurrent detection, or with a low frequency square wave drive current for a.c. detection (observing the limitation on repetition rate). Low fields of $< 10^5$ V m^{-1} were used to avoid non ohmic effects.

4.8.4 INTENSITY DEPENDENCE

Again using an l.e.d. calibrated source, the photocurrent-photon flux dependence was measured over a wide range of incident photon flux, at several fixed temperatures. The same criteria concerning the light/dark current ratio applied to the choice of d.c. (steady light) or a.c. (chopped light) detection. For very high intensities, the pulsed GaAs laser was used, provided the photocurrent response time was shorter than the light pulse width. With these methods, the range of photon flux densities used was from 10^{13} to 10^{23} photons m^{-2} s^{-1}. The applied field was also kept low in this stage of the work.

4.9 TRANSIENT PHOTOCONDUCTIVITY TECHNIQUES

4.9.1 OPTICAL SOURCES

The l.e.d.'s and laser diode light sources were used exclusively for the transient measurements, and a description of their attendant circuitry and operation was given earlier in this chapter.

4.9.2 PHOTOCURRENT DETECTION SYSTEM

Figure 4.14 shows schematically the light pulser and photocurrent detection system; it is the same as that described above for chopped light measurements. The changing photocurrent develops a voltage across the series resistor R_s, which is amplified, processed and displayed on an oscilloscope screen, or X-Y recorder.

The three (conflicting) requirements for the detection - system are - wide bandwidth, high gain, and low noise, to enable measurements of fast, low level voltage signals. The response speed in such a system is severely limited by the presence of stray capacitance to earth across the input resistor R_s, which is mainly the sum of sample capacitance and preamplifier input capacitance. This latter capacitance was reduced by using a f.e.t. source follower preamplifier with a.c. 'boot strapping', shown in figure 4.15.

An input capacitance of about 1.5 pF was achieved with this method, and an input resistance of about 10^7 ohms. The voltage gain of this preamp is almost unity, and its output impedance is less than 50 ohms. By placing the preamplifier inside the sample vacuum chamber, close to the series resistor R_s, the overall stray capacitance was reduced to about 2 to 3 pF, allowing the use of large series resistance (R_s) values, and therefore improving the system's sensitivity.

The ultimate speed of response, with low values of R_s, is set by the amplifier system itself, and rise/fall times

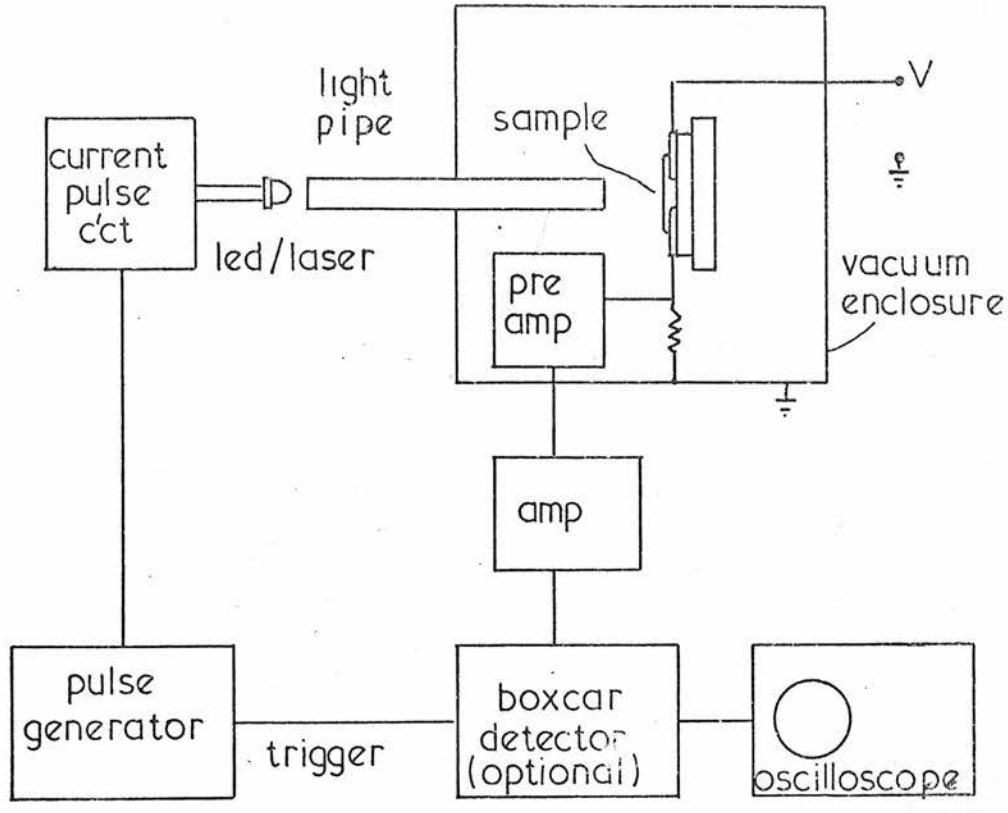

Fig 4.14 A.C. and pulsed photocurrent system

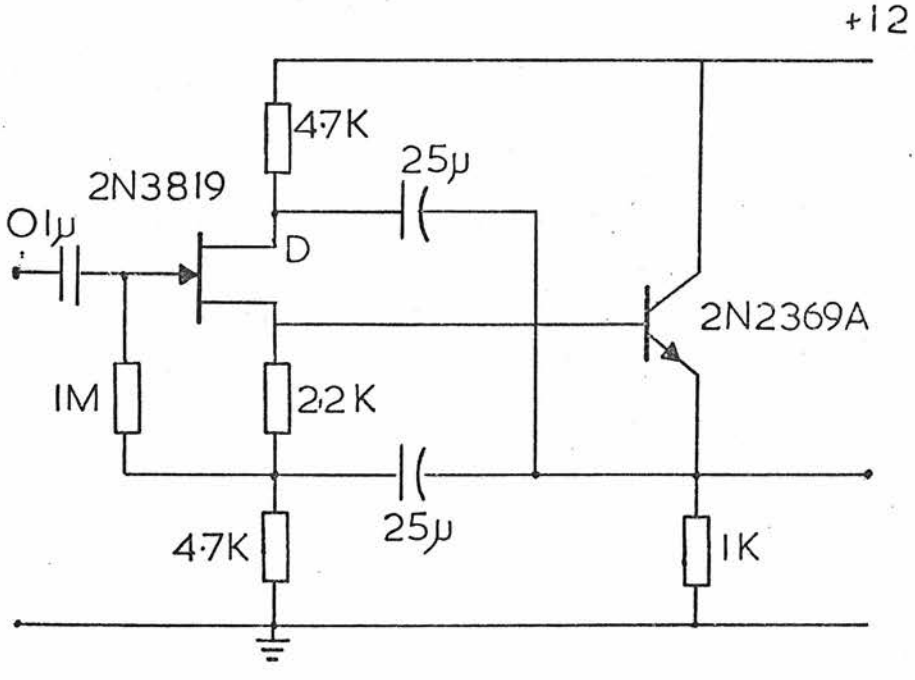

Fig 4.15 Wideband f.e.t. preamplifier.

(10% - 90%) for the system are as follows : preamp alone, 10 ns with no overshoot, preamp and x10 transistor stage, 30 ns, with a single short 10% overshoot. In use, the most common series resistor values were 10 k ohm 300 k ohm 1 M ohm, giving response times (10 - 90%) (for x10 gain) of 30 ns, 1 μs and 3 μs respectively.

As the amplifiers used were a.c. coupled to minimise temperature drift problems, large coupling capacitors extended the low frequency response, minimising the error on long pulses to < 1.5% "droop" in 10 ms, in the worst case, when R_s = 1 M ohm.

The ultimate sensitivity of the detection system is limited by noise and interference, primarily originating at the sample and amplifier input. Thermal noise associated with the sample and series resistor is inevitably present and could be reduced by cooling the resistor, a measure which was not taken, however. Amplifier noise was minimised by using low noise transistors throughout the design, paying particular attention to the input stage, where a low noise f.e.t. type 2N3819 (Texas Instruments) was selected. In this way, the amplifier noise figure, F_n, defined as

$$F_n = 20 \log \left(1 + \frac{\text{amplifier noise, referred to input}}{\text{thermal noise of source, } R_s}\right) \text{dB} \quad 4.6.4$$

was reduced to ≲ 1 dB over a wide frequency range (1 kHz - 10 MHz), and a wide range of source resistor R_s (10^4 ohm - 10^7 ohm). This means that the amplifier

contributed less than 10% of the total system noise at all times, a close approach to the ultimate limit set by thermal noise.

For rapidly varying photocurrents, the response time of the detection equipment can be reduced by making the series resistor, R_s, smaller. Unfortunately, as can easily be shown, thus results in a degradation of photosignal/noise ratio, and a loss in sensitivity of the system. Consider the case where the sample resistance is much greater than the series resistor R_s; the voltage applied to the sample is V, the photo induced conductance change is δG, and the stray capacitance at the amplifier input is C_s.

The signal to noise voltage ratio is then, at best

$$S/N = \frac{V \delta G R_s}{(kT/C_s)} \qquad 4.6.5$$

which is proportional to R_s (T is the temperature of the resistor R_s). If the required system response time is τ, then it follows that the signal to noise ratio

$$S/N \propto \frac{\tau}{C_s^{\frac{1}{2}}} \qquad 4.6.6$$

which again argues for a minimisation of amplifier input stray capacitance.

In some cases, e.g. measurement of the transient photo response of As_2Te_3 to low level excitation, it was necessary, for the sake of a short system response time ($\tau < 1$ μs) to reduce R_s to such an extent that the signal to noise ratio became much less than unity. Signal retrieval by means of a Brookdeal "Boxcar detector"

model 415/425, was then employed. This is a single-channel analogue instrument which uses correlation techniques to improve the signal/noise ratio of a repetitive waveform. The noisy waveform is 'scanned' slowly, over a large number of repetitions by a sampling gate circuit, allowing the signal, with a correlation of unity between samples to be extracted from the noise, whose correlation between samples is low because of its random nature. For display, the output of the Boxcar detector was fed to an X-Y recorder (Hewlett-Packard model 7035A) or to a storage oscilloscope (Tektronix type 549).

4.9.3 PHOTOCURRENT GROWTH

As explained in 3.3.4, in the initial region of photocurrent growth, recombination effects can be ignored, and information obtained on trapping and trap-limited mobilities from the initial slope $d\,\Delta I/dt$.

Measurements of this initial slope were made at several temperatures for samples of As_2Se_3 (273 K - 373 K) and As_2Te_3 (120 K - 295 K), and the applied field varied (up to 1.6×10^7 V m^{-1}).

As_2Se_3 also exhibited a second growth region and extensive measurements and photographs were made of this feature.

4.9.4 PHOTOCURRENT DECAY

The decay of the excess photocarrier density when excitation stops, gives important information on trapping and recombination processes.

The photo decay of amorphous As_2Se_3 and As_2Te_3 was recorded photographically, and the decay time - usually defined as the time for the photocurrent to fall to half its steady state value - was investigated, for a range of temperatures and excitation.

CHAPTER 5

NOISE IN SEMICONDUCTORS

5.1 INTRODUCTION

Noise in semiconductors appears as spontaneous fluctuations in the current passing through, or the voltage across a device or sample. These fluctuations reflect the particulate nature of the current carriers in semiconductors and their essentially statistical behaviour.

A study of these effects is a useful adjunct to other investigations - e.g. photoconductivity, and may be used to determine such parameters as lifetimes and trap densities. In devices, noise sets limits on the usefulness of a device - e.g. in low level amplification. Here a knowledge of the factors responsible for noise will allow optimum operation or improvement.

Semiconductor noise can be divided roughly into four categories; Diffusion noise, normally identified with thermal or 'Johnson'[123] noise; Drift noise - normally associated with current flow in the 'shot effect'; generation-recombination (g-r) noise associated with conductivity fluctuations and carrier kinetics; and 1/f noise, which often originates at contacts.

It is the category of generation-recombination (g-r) noise with which this work is concerned, as its origins, and mathematical formalism, involve the same processes and concepts as photoconductivity. Bearing in mind the

difficulty of the measurements, and the relatively few results which were obtained, only a brief description of the theory will be given.

For an elegant and detailed exposition of fluctuations in semiconductors, the review by van Vliet and Fasset[124] should be referred to.

5.2 MATHEMATICAL BACKGROUND

As the analysis given in 5.4 on g-r noise treats the carrier density (more precisely, number) as a random variable, some of the important terms and relations in random variable theory are listed for reference.

The random variable may be denoted by the stochastic function $y(t)$ which can be characterised by a probability distribution function, and has certain well defined statistical properties, such as average values. In this context, the random process described by $y(t)$ is assumed to be stationary and ergodic. Some of the important averages are listed below.

Averages

$$\text{Mean value} \quad \bar{y} = \lim_{T \to \infty} \frac{1}{T} \int_0^{\infty} y(t)dt \qquad 5.2.1$$

$$\text{Variance} \quad \overline{\Delta y^2} \text{ where } \Delta y(t) = y(t) - \bar{y} \qquad 5.2.2$$

$$\text{The Autocorrelation function} \quad C(s) = \overline{y(t)\, y(t+s)} \qquad 5.2.3$$

This is an important average indicating how future values of the fluctuating variable (e.g. carrier density) are affected by present values.

Spectral resolution

The fluctuations may be resolved into a frequency spectrum according to

$$\overline{\Delta y^2} = \int_0^\infty S_y(f)df \qquad 5.2.4$$

where $S_y(f)$ is the spectral density, the quantity most often measured in noise studies. A more explicit connection between the time and frequency domains is given by the Weiner-Khintchine relation[125]

$$S_y(f) = 4\int_0^\infty C(s)\cos \omega s \, ds \qquad 5.2.5$$

In practice the autocorrelation function is usually calculated first, from a knowledge of the physics of the processes occurring, and then the spectral density calculated.

Classification of random processes

A purely random process can be characterised by a single probability distribution, has a delta function autocorrelation, and a flat, or white spectral density.

A Markov random process is characterised by the second (joint) probability distribution, and in general, has a 'memory' or exponential autocorrelation function. Many of the random processes occurring in nature are Markov-type, including g-r noise.

If the autocorrelation function is then

$$C(s) = \overline{y^2} \exp(- s/\tau) \qquad 5.2.6$$

then (5.2.5) gives

$$S_y(f) = \frac{4\,\overline{y^2}\,\tau}{1 + \omega^2\,\tau^2} \qquad 5.2.7$$

5.3 GENERAL FEATURES OF SEMICONDUCTOR NOISE

Diffusion noise in a homogeneous semiconductor sample is connected with the random motion of charge carriers resulting from scattering events, and results in voltage fluctuations across a sample, or current fluctuations, if external circuitry is connected. This type of noise is therefore observable under 'zero field' conditions, and does not require a net d.c. current to allow its observation. Under zero or low field conditions diffusion noise is merely thermal or 'Johnson' noise with a 'white' spectral density - i.e. in a sample of resistance R, at temperature T, the open-circuit thermal noise voltage spectral density is

$$S_v(f) = 4kTR \qquad 5.3.1$$

This noise source, which appears in all resistors and semiconductors is a convenient standard of noise spectral density.

At high frequencies (in the infra red region), this falls off as quantum effects become significant[126]. At high fields, where the carrier energy distribution may be altered, its characteristics may also change.

Noise associated with the drift of injected carriers, specifically their random departure and arrival

times at electrodes is familiar in the 'shot' effect observed in valves. The discrete nature of the current carriers gives rise to this effect. Current flow is therefore essential for the generation and observation of this noise. In valves, a white spectrum is exhibited, which falls off at high frequencies, due to transit time effects.

At low frequencies, the noise current spectral density is

$$S_i(f) = 2eI \qquad 5.3.2$$

and again, noise generated in this way, e.g. in vacuum diodes, is used as a standard of spectral density.

In semiconductors, similar ideas apply, but there are additional parameters, such as trapping, recombination, and ambipolar effects. In particular, van Vliet[127] points out that if trapping times are shorter than transit times, then only current carriers very near the electrodes are involved and the resulting noise can be neglected.

Generation-recombination noise is associated with fluctuations in the mean transition rates of electrons and holes between the different energy states in a semiconductor.

Those fluctuations give rise to a fluctuating conductivity (even in zero field conditions) which, in the presence of an external source gives rise to current and voltage fluctuations at the samples electrodes. The

spectrum of g-r noise can exhibit many relaxation modes or 'bumps', (see equation 5.5.4) associated with trapping and recombination times, and can be a rich source of information on the electronic structure of the material in question.

The distinctive feature of 1/f noise, also known as flicker noise is that its spectral density increases as the frequency decreases. The range of frequency over which this dependence is followed can be very wide - e.g. as low as 6×10^{-5} Hz[128] and up to 4 MHz[129]. Such noise arises in a wide range of situations including valves, resistors, semiconductors etc, and thus has prompted researchers e.g. Bell[130] to look for a common cause.

At present there is no unanimity between experimental and theoretical workers, as to its origin. In semiconductors, 1/f noise has been associated with current carrying contacts, and in granular materials at grain boundaries[131]. The effect has also been observed, however, in single crystals e.g. Montgomery[132], and Maple et al[133] who associated it with surface effects.

A single time constant process will give a spectrum of the form of equation 5.2.7. However, a super position[134] of a number of those processes, or a distribution of time constants, say $g(\tau)$ can give an approximation to a 1/f spectrum, formally

$$S(f) = \int_{\tau_1}^{\tau_2} g(\tau) \frac{\tau}{1 + \omega^2 \tau^2} \, d\tau \qquad 5.3.3$$

and with $g(\tau) = A/\tau$, this results in a 1/f spectrum.

Brophy[135] suggested that distributed traps might give such a time constant distribution, while McWhorter[136] suggested slow modulation of the Fermi level at the semiconductor surface, by 'slow' surface states.

Other theories have been proposed by Petritz[137], Bess[138], Hooge[139] and others.

5.4 GENERATION–RECOMBINATION NOISE

Conductivity fluctuations. As mentioned above, this type of noise arises from carrier density fluctuations. Consider a p-type semiconductor specimen of length l and cross-sectional area A. The stochastic variable of interest is the total number of carriers, say P, in the sample:- $P = A\ l\ p$. The resistance of the sample is $R = l^2/e\ \mu_{po}\ P$. Consider now the fluctuation ΔP in the carrier number, (a dimensionless quantity) about the mean value P_o and, hence fluctuations in resistance ΔR, about R_o

$$\Delta R/R_o = \Delta P/P_o \qquad 5.4.1$$

If the applied voltage V is constant, then the current will fluctuate about its mean value I_o, so that

$$\overline{\Delta I^2} = I_o^2 \frac{\overline{\Delta P^2}}{P_o^2} \qquad 5.4.2$$

The Langevin equations

The Langevin[140] method treats the spontaneous fluctuations of parameters in a system - here the energy level occupancies - as departures from the steady state,

or equilibrium, caused by some 'random source function'. This allows the system's behaviour i.e. response to the source, to be calculated, using the macroscopic differential equation, linearised for small fluctuations.

In the case of a semiconductor, the macroscopic kinetic equations are essentially the same as those used in chapter 3, for photoconductivity. The significance of the random source function in this case is that it represents the very rapid changes in carrier densities due to the random events of generation and capture - e.g. by absorption of black body radiation quanta, or phonon energy.

Consider firstly, a two level system, where transitions occur between the valence band and some other level - e.g. the conduction band, or a localised level. Charge neutrality reduces this to a single variable problem. The Langevin equation can be written

$$d(\Delta P)/dt = \Delta P/\tau + \epsilon(t) \qquad 5.4.3$$

where τ is the free recombination time.

Now, it is assumed that $\epsilon(t)$, the random source function is purely random, as defined in 5.2 - i.e. it has delta function auto correlation. The solution of 5.4.3 gives an exponential autocorrelation function for ΔP - i.e. it is a Markovian random variable.

$$\overline{\Delta P(t)\,\Delta P(t+s)} = \overline{\Delta P^2}\,\exp(-s/\tau) \qquad 5.4.4$$

and applying the Weiner-Khintchine relation (5.2.5) the spectral density of the hole number fluctuation is

$$S_{\Delta P}(f) = 4\,\overline{\Delta P^2}\,\frac{\tau}{1 + \omega^2\,\tau^2} \qquad 5.4.5$$

so the current noise spectral density is

$$S_i(f) = 4\,I_o^{\,2}\,\frac{\overline{\Delta P^2}}{P_o^{\,2}}\,\frac{\tau}{1 + \omega^2\,\tau^2} \qquad 5.4.6$$

The noise spectrum will thus be small if $\overline{\Delta P^2}$, or τ, is small. Thus a two level, single variable process results in a single 'relaxation mode' in the noise spectrum.

The variance $\overline{\Delta P^2}$ can be obtained by statistical considerations. For example in the case where the density of trapped carriers is much greater than the density of free carriers, and the trap occupancy is low, individual generation and capture events are independent, Poisson statistics apply, and $\overline{\Delta P^2} = P_o$, which is in fact the largest value that the variance can take in thermal equilibrium. This situation is of relevance in amorphous semiconductors.

For other cases - e.g. a doped semiconductor with almost fully ionised dopant atoms, van der Ziel showed that binomial statistics would apply, and the variance could be very small,which seems physically reasonable.

Van Vliet and Fasset[124] calculated the variance in the general case by statistical means, using the 'Master' equation - a differential equation for the probability distribution of the level occupancy, while Burgess[141] used thermodynamic arguments. The result, known as the generation-recombination theorem, gives in the univariate case,

$$\overline{\Delta P^2} = G(P_o)\tau \qquad 5.4.7$$

Multilevel semiconductors

The more important case of multilevel semiconductors can be treated by extensions of both the Langevin and Master equation methods.

Consider an m-level system, in which the occupation of level i is n_i, and fluctuation $\Delta n_i = n_i - n_{io}$. Assembling the fluctuations in vector form, $\underset{\sim}{\Delta n}$, the linearised kinetic equations can be written in a form analogous with the single variable case. Charge neutrality considerations reduce the number of variables to (m-1).

i.e. the Langevin equation is

$$d/dt\ (\underset{\sim}{\Delta n}) = -\ \underset{\sim}{M}\ \underset{\sim}{\Delta n} + \underset{\sim}{\varepsilon}(t) \qquad 5.4.8$$

where $\underset{\sim}{M}$, analogous to $1/\tau$, is the phenomenological relaxation matrix, whose elements may be calculated from the transition rates between levels in the system. The m-1 characteristic roots of the secular equation

$$|\ \underset{\sim}{M} - \underset{\sim}{I}/\tau\ | = 0 \qquad 5.4.9$$

are the reciprocal time constants $1/\tau_k$, of the g-r process, describing the decay of small disturbances in the system.

The auto, and cross correlation functions can be found, giving

$$\overline{\Delta n_i(t)\ \Delta n_j(t+s)} = \overline{\Delta n_i\ \Delta n_j} \sum_{k=1}^{m-1} C_k^{ij} \exp(-\ s/\tau_k) \qquad 5.4.10$$

and spectral densities, using the Wiener Khintchine theorem

$$S_{ij}(f) = \overline{\Delta n_i \, \Delta n_j} \; 4 \sum_{k=1}^{m-1} C_k^{ij} \frac{\tau_k}{1 + \omega^2 \tau_k^{\,2}} \qquad 5.4.11$$

i.e. there are m-1 relaxation modes, or bumps in the spectrum. Again the variances and cross-variances may be found by statistical means[142].

In semiconductor noise investigation, only the spectra $S_{nn}(f)$ $S_{np}(f)$ and $S_{pp}(f)$ of the density fluctuations of free electrons and holes are required, and in the present work, only the spectrum for free holes (if extended state conduction dominates).

5.5 NOISE IN AMORPHOUS CHALCOGENIDES

There are very few reports of noise measurements in amorphous chalcogenides, the main reason being the very low levels of noise spectra observed. Kornfel'd and Sochova report that in liquid Sb_2S_3[143] and vitreous $As_2Te_3Tl_2Se$ and $As_2Te_3Tl_2Te$[144], the noise level at d.c. currents of up to 3 mA, was below the resolution of their detection equipment. In the last two materials, spectral density studies led them to conclude that the noise spectral density at 1.4 KHz was less than the thermal noise of their samples.

Main and Owen[144a] reported noise spectra in bulk vitreous samples of $As_2Te_3Tl_2Se$, and As_2SeTe_2 using a number of electrode materials - e.g. Ag, In-Ga (Au also, in subsequent work) and different sample geometries, e.g. 2-electrode disc shape, and 4-electrode 'bridge'

samples. In all cases, the spectra were of 1/f in form of very low level, falling below the thermal noise of the samples at a few kHz.

Those spectra were interpreted empirically in terms of a distribution of time constants of the type mentioned in equation 5.3.3, and free carrier mobility of the order 10^{-3} to 10^{-2} m^2 V^{-1} s^{-1} estimated, although there were a number of disposable parameters.

The very low level of the noise, at first sight seems puzzling, since it is to be expected that in such semiconductors with high trap densities, the fluctuation in free carrier density will be high - as mentioned in 5.4. The existence of some structure, - relaxation modes in the noise spectra for thin film evaporated As_2Te_3 samples, used in photoconductivity work, led to a simple analysis based on the photoconductivity model, which explained this apparent discrepancy.

Simplified g-r noise analysis

Again, the analysis will be presented before the results. Referring to the model for photoconductivity presented in 3.2.13, and figure 3.11, the number of levels taking part will be at least 4 i.e. valence band, localised states at E_1 and E_2, and the conduction band, and could be as many as 7 if band tails and states at the Fermi level contribute. The analysis will be restricted to this discrete level model, but results for a distributed state model will be similar under the conditions mentioned in 3.2.16.

A number of drastic simplifications must be introduced to reduce the analysis to workable proportions. The assumptions made in 3.2.13 concerning trap occupancies will be held to be valid. If transitions to states near E_F can be neglected and the other traps are in thermal contact with the nearest band, then equation 3.2.78 reduces the problem effectively to a '2-level' situation, where each level consists of a reservoir of band and relevant traps.

The noise spectra do indeed only reveal one major relaxation mode, which as expected, corresponds to the decay time for a small excess reservoir population - i.e. the observed monomolecular photo decay time τ_{cm}. To gain an insight into the reasons for the low spectral density, however, the analysis which follows considers a 3-level situation.

As photoconductivity results indicate that B-L recombination dominates, at least near room temperature, the noise analysis will, for clarity assume only recombination by path 1 (see figure 3.11).

Next, it will be assumed that as the densities of trapped carriers are large compared with free carriers, and that as the trap levels communicate with each other via the small free density, the relative fluctuations in trapped carrier density are small. As holes dominate the conductivity, fluctuations in electron density will be ignored. Transitions into possible localised valence band tail states will, for the present be ignored, as the occupation of these states is assumed to be less

than that of states at E_2.

It will be shown later that in addition to introducing another 'trapping mode' into the noise spectrum at high frequencies, the presence of tail states may modify the trapping mode associated with states at E_2.

The general 3-level analysis, involving the expressions 5.4.8 - 5.4.11 was tried, and although solutions were obtained, the method was cumbersome. The simple analysis given below gives satisfactory solutions with the approximations introduced.

The kinetic equations 3.3.11 and 3.3.12 used to describe the growth of photocarrier density, may be reduced to two <u>linear</u> equations in Δp and $N_2 \Delta f_2$, for small fluctuations. The Langevin equation for ΔP is then easily obtained

$$d^2/dt^2\ (\Delta P) + (1/\tau_{pm} + 1/\tau_{t2} + 1/\tau_{tr2})\ d/dt\ (\Delta P) + \Delta P/\tau_{pm}\ \tau_{tr2} = \epsilon(t) \qquad 5.5.1$$

where as before $1/\tau_{pm} \approx C_{p1}\ N_1\ f_{1o}$, $1/\tau_{t2} \approx C_{p2}\ N_2$ and $1/\tau_{tr2} \approx C_{p2}\ p_2$. Now assuming multiple trapping, so $\tau_{t2} << \tau_{pm} < \tau_{tr2}$, a simple approximate expression for the autocorrelation function may be found

$$C(s) \approx \overline{\Delta P^2}/\tau_{cm}\ (\tau_{pm} \exp(-s/\tau_{cm}) + \tau_{cm} \exp(-s/\tau_{t2})) \qquad 5.5.2$$

where $\tau_{cm} = \tau_{pm}\ \tau_{tr2}/\tau_{t2} \approx \tau_{pm} \times N_2/p_2$ is just the observed monomolecular photodecay time. Applying the Wiener-Khintchine theorem gives a spectral density

$$S_{\Delta P}(f) = 4\,\overline{\Delta P^2}\left(\frac{\tau_{pm}}{1+\omega^2\tau_{cm}^2} + \frac{\tau_{t2}}{1+\omega^2\tau_{t2}^2}\right) \qquad 5.5.3$$

Furthermore, as mentioned in 5.4, assuming independent generation and trapping events, and Poisson statistics, gives $\overline{\Delta P^2} = P_o$. The current noise spectral density is then

$$S_i(f) = 4\,I_o^2/P_o\left(\frac{\tau_{pm}}{1+\omega^2\tau_{cm}^2} + \frac{\tau_{t2}}{1+\omega^2\tau_{t2}^2}\right) \qquad 5.5.4$$

The first relaxation mode in equation 5.5.4 may be associated with the relatively slow interchange between the (valence band + set '2' traps) reservoir, and the set '1' centres - i.e. the recombination component, while the second mode is related to the rapid trapping in set '2' traps - the trapping component.

The experimental results from the present work are described and discussed in chapter 8, but it is worth pointing out here that equation 5.5.4 reveals why the noise spectra in amorphous semiconductors are so low. The only mode which has so far been resolved experimentally (in this work) is the recombination mode, as its low frequency plateau value is perhaps 10 to 10^3 higher than the trapping mode plateau. (τ_{pm}/τ_{t2}).

Integration of 5.5.3 over all frequencies reveals that the recombination mode only contributes a small fraction of the total variance - i.e. $(\tau_{pm}/\tau_{cm})\,\overline{\Delta P^2}$ and τ_{pm}/τ_{cm} could be $<10^{-2}$. Thus, most of the variance is associated with trapping noise, which extends to high frequencies, as τ_{t2} could be $<10^{-9}$ s, and consequently has a low plateau value.

The 1/f component which appears in the noise spectra of previous work could be a mixture of contact effects, and several smeared out recombination modes, due to deeper, or slower traps.

CHAPTER 6

NOISE MEASUREMENT

6.1 INTRODUCTION

The parameter of interest in this study is the current noise spectral density $S_i(f)$ due to conductivity fluctuations in a semiconductor sample (also called current noise).

Figure 6.1 shows in schematic form, how this is measured. A noise free voltage source supplies d.c. current to the sample, so that conductivity fluctuations appear as voltage fluctuations, across a series resistor R_s, to which the input of a low noise wide band preamplifier is connected. (The configuration is identical to that used in photoconductivity). Following wide band amplification, the noise is selectively amplified by a tuned filter, and the emerging narrow band noise is detected quadratically by a meter with a slow response time.

A second measurement, with no d.c. current reveals the 'background' of thermal noise in the sample and associated circuitry, and the system noise, mainly in the preamplifier first stage.

6.2 EXPERIMENTAL SAMPLES

The noise spectra discussed in chapter 8, were measured using the same thin film As_2Te_3 samples as were used in photoconductivity studies, and a description was given in 4.1.

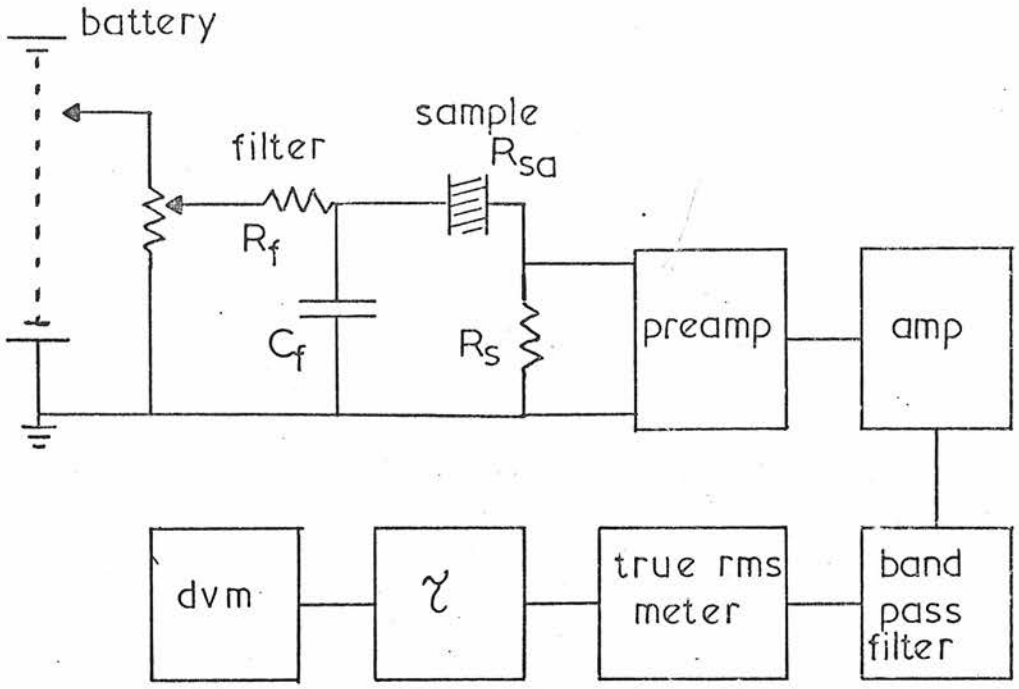

Fig 6.1 Noise measurement system

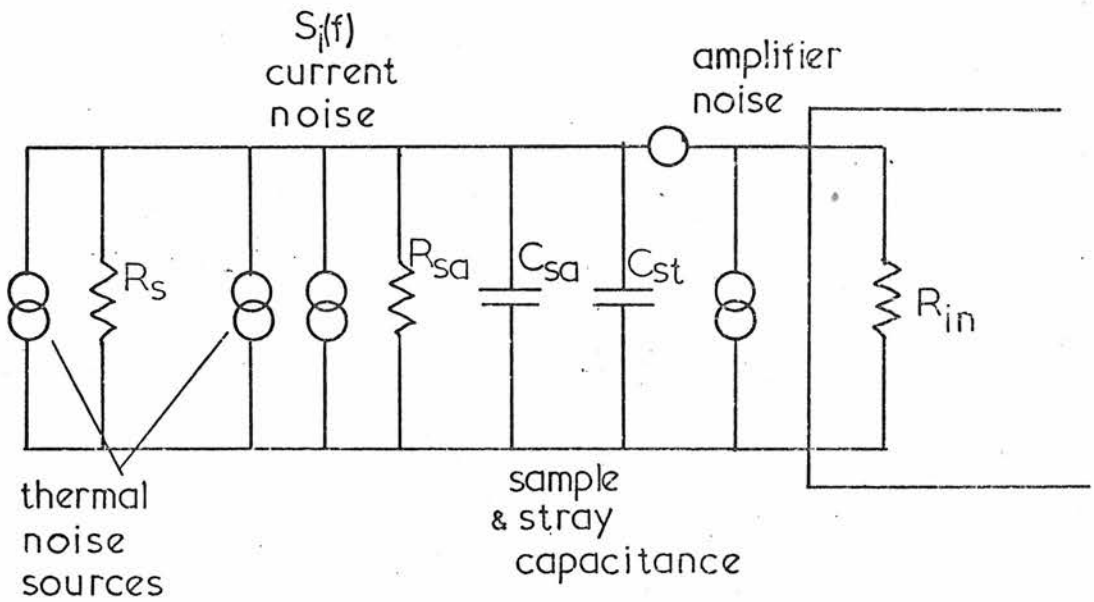

Fig 6.2 Input circuitry & equivalent noise generators

Some preliminary work was also carried out on bulk samples of $As_2Te_3Tl_2Se$, the results of which were reported elsewhere[144a]. The material was prepared in evacuated silica tubes, heated to 800°C, and air quenched. The simplest samples were discs, cut from the (boule' with electrodes evaporated on opposite faces. Another geometry employed was a 'bridge' - i.e. a bar with two side arms. A number of electrode materials were investigated (Au, Ag, In-Ga) and it was found that gold electrodes resulted in the lowest levels of contact noise. It was hoped that the use of gold electrodes on the thin film samples would thus allow the bulk generated noise to be observed. Low contact noise levels are also an indication of good 'ohmic' contacts.

6.3 NOISE MEASUREMENT SYSTEM

6.3.1 VOLTAGE SUPPLY

Figure 6.1 shows the typical voltage source used. The battery, an Ever Ready B1702 (tapped, up to 60 V) was connected to a wire-wound potentiometer to provide a variable voltage, which was then filtered by the low pass combination R_f and C_f. The very low cut-off frequency of this filter ($\lesssim$ 1Hz) minimised the effects of internally generated battery noise. The battery and associated circuitry were placed in a screened aluminium box, and its output leads were also screened, to minimise 50 Hz mains pickup at the system input.

All resistors used were wire-wound, or metal film, as those give zero, or very low excess noise

respectively over their thermal level, when d.c. current is passed. Although the sampling resistor R_s should ideally be wire-wound, for low noise, a metal film resistor was normally used, as wire wound resistors can have an appreciable reactance at high frequencies. It was ascertained, by using a metal film resistor as a dummy sample, that the excess or current noise in this type of resistor was below the limits of the measurement system, so effectively, only thermal noise was present.

6.3.2 STANDARD NOISE SOURCES

The noise generated in the sample may be compared with a standard noise source, the most commonly used type being a saturated vacuum diode. This generates shot noise, as mentioned in 5.3 , with flat current noise spectral density

$$S_{id} = 2\, e\, I_d \quad A^2\, Hz^{-1} \qquad 6.3.1$$

where I_d is the d.c. diode current. The noise is injected by capacitively coupling the anode to the sample top electrode.

Although this method is convenient in that the system gain and bandwidth need not be known accurately, it is only useful for relatively high levels of sample noise - i.e. the sample current noise must be much greater than the background thermal noise, while the levels to be measured were very low. Secondly, the anode slope resistance of the diode, which is effectively

in parallel with the sample, may shunt the sample noise if the sample resistance R_{sa} is greater than ~1 MΩ. In such a case, the diode is of course no longer a true current noise source and hence was discarded.

If the preamplifier and system noise were zero, then the thermal noise of the sample and associated resistors would be a convenient standard source. As the amplifier noise could not be eliminated, the measurement method was reduced to that described in 6.1 - i.e. an absolute measurement of sample noise. This required an accurate calibration of the system gain and bandwidth, however.

6.3.3 WIDE BAND AMPLIFIERS

The requirements for the amplification system in noise measurements are essentially the same as in photoconductivity measurements - outlined in 4.9.2. - i.e. low noise, high input impedance, wide bandwidth, and high dynamic range. This last requirement applys more to the output stages which may have to accommodate high noise 'peaks'.

It can easily be shown that the noise generated in the first stage of the amplification, dominates the overall system noise-figure, defined in 4.9.2, so care was taken in the first stage preamplifier design. A number of designs were tried, but it was found that the two amplifiers described in 4.9.2 for photoconductivity work were quite adequate, see figure 4.15. To minimise amplifier noise, metal film and metal oxide resistors

were used in the input stages, and selected low noise transistors, (2N3819 and BC154) used throughout.

The f.e.t. preamplifier was generally used as the first stage, with unity voltage gain, followed by cascaded x10 gain bipolar stages, to give a total voltage gain (A), of 10^2 - 10^4. An ingenious method, suggested by Baxandall[144b], was used to measure the low noise figures of these amplifiers. A source resistor, roughly of the value of the sample network resistance, was connected to the amplifier input, and dipped in liquid nitrogen, while the drop in output noise was monitored. Noise figures of ~ 1 dB were obtained over a range of source resistance and frequency.

6.3.4 BAND-PASS FILTER

The band-pass filter in figure 6.1 allows the spectral density of the sample noise to be computed. If the voltage transfer function of the filter is H(f), and the input noise voltage spectral density is $S_{in}(f)$, then the total mean square output voltage $\overline{V_{out}^2}$, is

$$\overline{V_{out}^2} = \int_o^\infty S_{in}(f)\, H^2(f)\, df \approx H_o^2\, S_{in}(f_o) \int_o^\infty \frac{H^2(f)}{H_o}\, df$$

$$= H_o^2\, S_{in}(f)\, B_{eq} \qquad 6.3.2$$

where H_o is the centre frequency (f_o) voltage gain and the pass-band is so narrow that $S_{in}(f)$ can be approximated by $S_{in}(f_o)$. Equation 6.3.2 also defines the noise equivalent bandwidth B_{eq}, which is not, in general, equal to the usual '3 dB' bandwidth B.

The filters used in this work were the input section of a P.A.R. lock-in amplifier, type HR-8, useful up to 180 kHz, and some L-C filters made in the department. The 'two-pole' characteristics of such filters leads to the following relationship

$$B_{eq} = 1.22\ B$$

This was verified experimentally, by graphical integration, for several frequencies. Typical Q values for the filters, ranged between 10 and 20.

6.3.5 TRUE R.M.S. INDICATION

As noise voltages from uncorrelated sources add quadratically, a quadratic detector, whose output is proportional to the square of the input voltage is required. In this work, a Hewlett-Packard 3400 A true-r.m.s. voltmeter was used. This instrument was ideal, in that it had a frequency range of 10 Hz - 10 MHz, and a wide dynamic range for noise measurements.

Normally, the voltmeter reading fluctuated about the mean value. To improve the accuracy of the measurement, a d.c. output proportional to the scale reading, available at the rear of the instrument, was put through a low pass filter of time constant τ, into a digital voltmeter. It can be shown that when the noise equivalent bandwidth of the system is B_{eq}, the probable error of a single noise reading is [145]

$$\text{Error} = 100\ (2\ B_{eq}\ \tau)^{-\frac{1}{2}}\ \%$$

By varying τ, from 1 s to 100 s, this error was kept below 5 %.

6.3.6 INTERFERENCE PRECAUTIONS

As with all low level systems, many precautions must be taken to avoid pick-up of unwanted signals, especially at the input stages.

All of the input circuitry, the voltage supply, and preamplifier, were placed in a screened metal box, to avoid mains pick-up at the high impedance input. Only one earthing point was used, to avoid inductive mains pick-up. Cable noise was minimised by using short lengths of 'low noise' cable, rigidly fixed to the bench top if necessary.

6.4 NOISE SPECTRA COMPUTATION

Figure 6.2 shows the input circuitry and equivalent noise generators, associated with each noise source. The sample capacitance, and stray capacitances associate with wiring and amplifier input are also indicated.

The noise voltage spectral density $S_{vin}(f)$ appearing at the amplifier input is composed of several components.

$S_{vT}(f)$ - thermal noise originating from the resistive components of the sample and series resistor.

$S_{vi}(f)$ - noise arising from conductivity fluctuations and contact noise in the sample

$S_{va}(f)$ - amplifier noise, referred to the input.

The measurement procedure outlined in 6.1 yields the following readings, at a given filter centre frequency f_o.

i) No current through sample. The output mean square voltage $\overline{v_{o1}^2}$ is

$$\overline{v_{o1}^2} \approx (S_{vT}(f_o) + S_{va}(f_o))\, A^2\, H_o^2\, B_{eq}(f_o) \qquad 6.4.1$$

ii) Current passing through sample. The output mean square voltage $\overline{v_{o2}^2}$ is

$$\overline{v_{o2}^2} \approx [S_{vT}(f_o) + S_{va}(f_o) + S_{vi}(f_o)]\, A^2\, H_o^2\, B_{eq}(f_o) \qquad 6.4.2$$

The voltage noise spectral density at the preamp input, associated with sample current noise, is then obtained

$$S_{vi}(f_o) = \frac{\overline{v_{o2}^2} - \overline{v_{o1}^2}}{A^2\, H_o^2\, B_{eq}(f_o)} \qquad 6.4.3$$

Straightforward circuit analysis gives the noise current spectral density $S_i(f_o)$

$$S_i(f_o) = \frac{(\overline{v_{o2}^2} - \overline{v_{o1}^2})}{A^2\, H_o^2\, B_{eq}(f_o)} \; \frac{1 + (\omega C_T R_T)^2}{R_T^2} \qquad 6.4.4$$

where $R_T = R_s R_{sa}/(R_s + R_{sa})$ and C_T is the sum of sample and stray capacitance. The amplifier input resistance is usually much greater than R_T, and has a negligible effect.

For optimum sensitivity to the sample noise, R_s should be much greater than R_{sa}, - i.e. current source

operation, but as R_{sa} was normally ~1 MΩ or greater, and C_T ~ 2 pF, this limited the system bandwidth. In practice, sensitivity was sacrificed for bandwidth, and R_s was chosen to be less than R_{sa}, typically ~10 kΩ.

A bandwidth of ~3 MHz was achieved, allowing measurement of spectra with relaxation mode time greater than ~100 ns.

CHAPTER 7

PREVIOUS WORK ON As_2Te_3 AND As_2Se_3

7.1 INTRODUCTION

It is useful at this point to summarise some of the recent measurements of optical and electrical properties of bulk and thin film As_2Te_3 and As_2Se_3 for comparison with the present work. The band structure, distribution of localised states, lifetimes and carrier mobilities are of particular interest.

7.2 As_2Te_3

Optical absorption measurements carried out by Weiser and Brodsky[119] and Rockstad[105] on evaporated films, interpreted by the relation

$$\alpha(\nu) = B(h\nu - E_{opt})^2/h\nu$$

give

E_{opt}(300 K) = 0.86 eV Weiser and Brodsky

0.83 eV Rockstad

E_{opt}(0K) = 0.95 - 0.98 eV Weiser and Brodsky

Temperature coefficient $\gamma = -5 \times 10^{-4}$ eVK^{-1} Weiser and Brodsky

D.C. conductivity measurements give

σ (Room temperature) $1 - 7 \times 10^{-4}$ Rockstad

$1 - 2 \times 10^{-4}$ Weiser and Brodsky

conductivity activation energy E_σ 0.40 ± .02 eV Weiser and Brodsky

0.46 eV Croitoru et al[146]

pre-exponential factor $C = 6 \times 10^4$ Ω^{-1} m^{-1} Weiser and Brodsky

A.C. conductivity measurements, by Rockstad[56,105] giving an ω^1 dependence around 10^6 Hz are interpreted by Mott and Davis[147] in terms of a high density of states at the Fermi level, of $g(E_F) \sim 5 \times 10^{25}$ m^{-3} eV^{-1}.

Photoconductivity. Spectral response : Weiser and Brodsky[119] report a relative spectral response which rises from about 0.1 at 0.85 eV photon energy, to unity at about 1.2 eV. The response above 1.2 eV was not measured.

Transient response. Photocurrent rise and decay times of ~50 ns and 150 ns respectively were obtained at room temperature by Weiser and Brodsky, with GaAs laser excitation. The free hole lifetime was estimated as < 50 ns.

Mobility. Weiser and Brodsky estimated values for N_v, of 2.4×10^{25} - 3×10^{26} m^{-3}, and μ_{po} between 10^{-4} - 4×10^{-4} m^2 V^{-1} s^{-1} from dark conductivity, and a minimum value for μ_{po}, of 3×10^{-5} m^2 V^{-1} s^{-1} from photoconductivity. Trapping effects were noted, but no detailed information on trapping levels and cross-sections were given.

Hall effect measurements on $As_{50}Te_{50}$ by Emin et al[33] reveal a room temperature Hall mobility of 4×10^{-6} m^2 V^{-1} s^{-1} and a small activation energy of ~0.06 eV, interpreted as due to polaron conduction.

Thermopower measurements on $As_{50}Te_{50}$ by Emin et al[33] give a thermoelectric power energy $\dot{E}_s \approx 0.25$ eV the discrepancy between this and the 0.44 eV activation energy being associated with polaron hopping energy

7.3 As_2Se_3

Optical absorption. There are many reports of optical absorption in bulk vitreous and thin film As_2Se_3[40,148,149,150]. Interpreting the high absorption data in the same way as in As_2Te_3 gives typical results.

E_{opt}(300 K) 1.80 eV Owen[150]

1.73 Zallen et al[149]

E_{opt}(0K)

Temperature coefficient γ - 7 x 10^{-4} eV K^{-1} Edmond[40]

D.C. Conductivity in bulk and thin film As_2Se_3 has been measured often[40,41,65,152].

Typical values for bulk material at low fields, are

σ(295 K) 5 - 6 x 10^{-11} Ω^{-1} m^{-1} De Wit and Crevecoeur[65]

Pre-exponential factor C 2-5 x 10^5 Ω^{-1} m^{-1} Davis and Mott[153]

E_σ 0.905 eV Edmond[40]

0.95 eV Marshall and Owen[20]

Thin films exhibit a wider range of values, e.g. room temperature conductivities in the range 3 x 10^{-10} - 3 x 10^{-9} Ω^{-1} m^{-1}, and an activation energy which is not temperature independent, in the range 100 to 400 K. Davis and Shaw[92] report a variation in E_σ from 0.1 eV to 1.5 eV in this range.

High field conductivity behaviour has been reported by De Wit and Crevecoeur[65] Marshall and Owen[20] and Marshall and Miller[66]. Marshall and Miller fit the data to a single exponential form

$$\sigma(\mathcal{E}) = \sigma(0) \exp [e\, a(T)\, \mathcal{E}/kT]$$

which gives value for a (295 K) of ~35 Å, for Marshall's data, and ~18 Å for De Wit and Crevecoeur.

A.C. conductivity in bulk As_2Se_3 has been measured extensively[42,148,154-156], and an ω^1 dependence obtained in the range 10^2 - 10^7 Hz at least. Interpretation in terms of Fermi level hopping gives $g(E_F) \approx 10^{24}$ m^{-3} eV^{-1}.

Thermoelectric power measurements in the liquid state (Edmond[40]) and glassy state (Uphoff and Healy[41]) give a positive thermopower, indicating hole conduction.

Photoconductivity. Photoconductivity in bulk and thin film As_2Se_3 has been investigated in some detail[101-105,148,151].

The spectral response reported by Rockstad[105] and Kolomiets et al[103] differs in shape, probably due to ~~different geometric factors and normalising due to~~ different geometric factors and normalising procedures (as mentioned in 3.2.3). According to Rockstad, the response rises uniformly with the absorption edge, and levels out above ~2.2. eV in a thin film, while in a bulk sample, Kolomiets et al report a peak at ~2 eV, with response falling at higher photon energies. Neither author mentions whether normalising included a knowledge of the photocurrent-intensity behaviour.

The temperature dependence of the steady state photoconductivity in the low temperature, high intensity region using non-monochromatic illumination, (presumably in the bimolecular regime) is reported by Kolomiets et al[102,103] as ~0.4 eV although values of 0.25 eV[101] and 0.35 eV[158] have also been obtained by Kolomiet's group.

Photocurrent decay behaviour has been reported in a number of papers by Kolomiet's group[102,103,159] and normally interpreted as consisting of fast ($\sim 10^{-3}$ s) and slow (> 1 s) exponential components, associated with slow (β) and fast (α) trapping centres. Above 120°C, the photodecay time (fast component) is intensity independent and decreases with increasing temperature, with activation energy ~ 0.4 eV[102].

Quantum efficiency measurements, made by Xerographic discharge methods[160] reveal a field dependence of $\sim \mathcal{E}^{\frac{1}{2}}$, for fields greater than 4×10^6 V m^{-1}.

Drift mobility μ_d. Hole drift mobilities have been measured in sandwich samples of vitreous and evaporated As_2Se_3 by transit time techniques[20,160,161]. In all cases the transit pulses were rounded, due to deep trapping effects, and the mobility was field dependent. Typical values for μ_d at $\sim 10^7$ V m^{-1} are $2 - 4 \times 10^{-9}$ m^2 V^{-1} s^{-1}. The mobility appears to be trap limited, and Marshall and Owen[20] find a Poole-Frenkel field dependence, giving a zero field room temperature value, of $\sim 5 \times 10^{-10}$ m^2 V^{-1} s^{-1}, a trap depth of 0.43 eV and density $N_t \sim 10^{26}$ m^{-3}.

Localised states. Kolomiets[162] and Kolomiets and Mazets[163] have summarized the distribution of localised states in crystalline and amorphous As_2Se_3, obtained by a number of methods, including thermally stimulated currents (TSC) space charge limited currents (SCLC), induced photoconductivity (IPC). In the crystal

there appear to be a number of discrete levels at 0.49, 0.58 and 0.72 eV above E_v, while in the glass, states are distributed between 0.35 and 0.75 eV, although there may be some maximum around 0.6 eV. Street and Yoffe[164] find a level at 0.40 ± 0.03 eV from T.S.C. results.

Photoluminescence measurements[165] at 77 K give a broad emission spectrum which peaks at 0.88 eV, indicating radiative transitions to gap centre states. Photoluminescence quenching spectra at 6 K[166] indicate a localised level about 0.6 eV deep.

All of these measurements indicate some definite structure in the distribution of localised states, much of which is corroborated in the present work.

CHAPTER 8

AMORPHOUS As_2Te_3

8.1 SAMPLES

A number of thin film samples were produced by the methods outlined in 4.1, for optical and electrical work. Detailed measurements were carried out on only a few of these. The thickness range was as follows :

Sample		Sample	
C-15	0.35 μm	C-19	0.67 μm
C-16	0.35 μm	C-20	0.67 μm
C-17	1.50 μm	C-27	0.54 μm
		C-28	0.24 μm

Chemical analysis, by spectrophotometer colorimetric techniques was carried out some months after the sample preparation. Due to the small amounts of film material (< 1 mg) and possible surface oxidation, the accuracy was not high, and the films were estimated to be within 5-10 at.% of the stoichiometric composition, perhaps slightly rich in As. The electrical properties were so similar to those reported elsewhere, that the other properties are taken to be typical of As_2Te_3.

8.2 OPTICAL PROPERTIES

Figure 8.1 shows typical optical transmission data for a 0.67 μm thick sample, at 293 K and 99 K, and room temperature reflection data. The refractive index of the

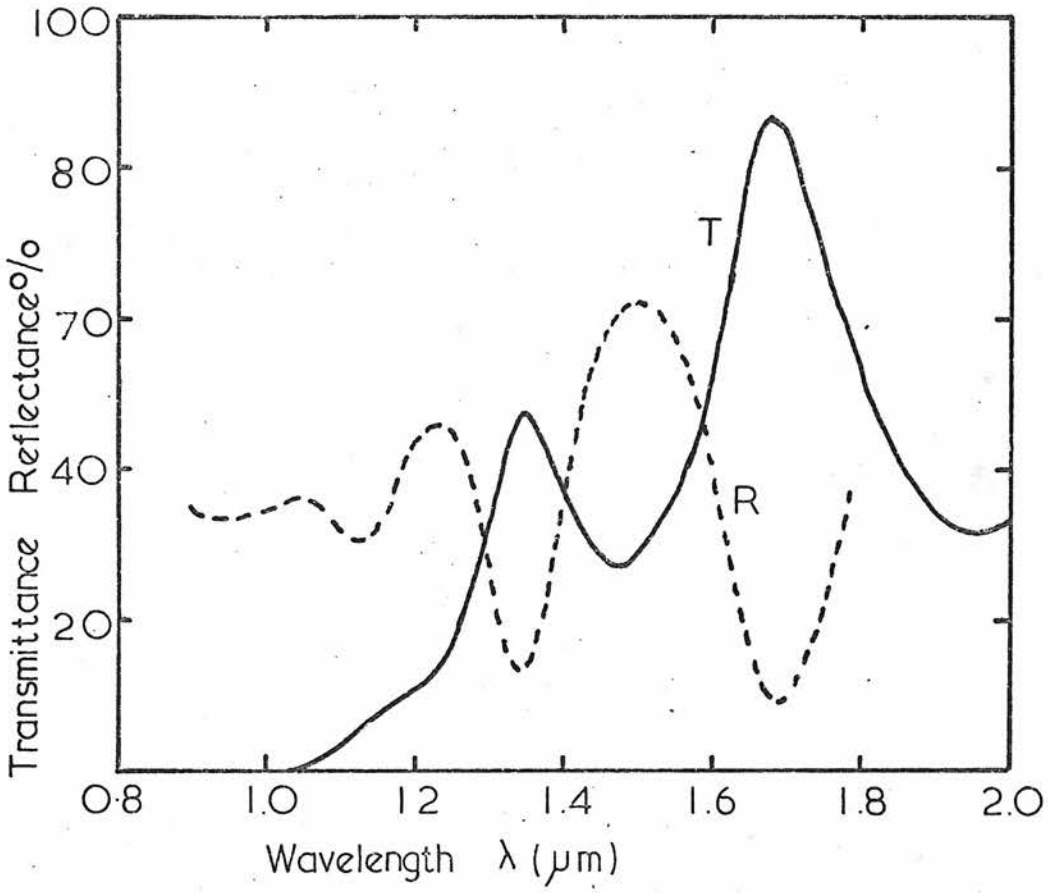

Fig 8.1 As_2Te_3 Transmittance reflectance vs Wavelength

film n_s, at room temperature was obtained from the interference fringes, using equation 4.4.3. This was found to vary slightly with wavelength, being 3.75 at ~ 1.9 μm, and 3.9 near the onset of absorption, although this latter figure may be high as absorption affects the accuracy of the calculation. These figures compare well with Weiser and Brodsky's figure[119] of 3.76.

Assuming $n_s \approx 3.8$, gives an air-film reflectance R_1, from equation 4.4.2 of 0.34, in good agreement with the value measured in the high absorption region. As the calculations for α, made from the low transmission data are not sensitive to the value of R_1, this figure was used throughout, giving a film-substrate reflectance R_2, of 0.188, and giving an equation for transmission

$$T_r = \frac{0.519 \exp(-\alpha d)}{1 - 0.073 \exp(-2\alpha d)} \qquad 8.2.1$$

Figure 8.2 shows the absorption coefficient α, vs photon energy $h\nu$, at 293 K and 99 K, for two samples of thickness 0.67 μm and 1.5 μm. Also shown is Rockstad's room temperature curve[105], which is in reasonable agreement.

The data of figure 8.2 fit well to the quadratic relation of equation 3.1.9, i.e.

$$\alpha(\nu) = B(h\nu - E_{opt})^2/h\nu \qquad 8.2.2$$

with $B \approx 8.6 \times 10^7$ m^{-1} eV^{-1}, and figure 8.3 plots $(\alpha h\nu)^{\frac{1}{2}}$ vs $h\nu$ for the two temperatures. Extrapolated values of E_{opt} are

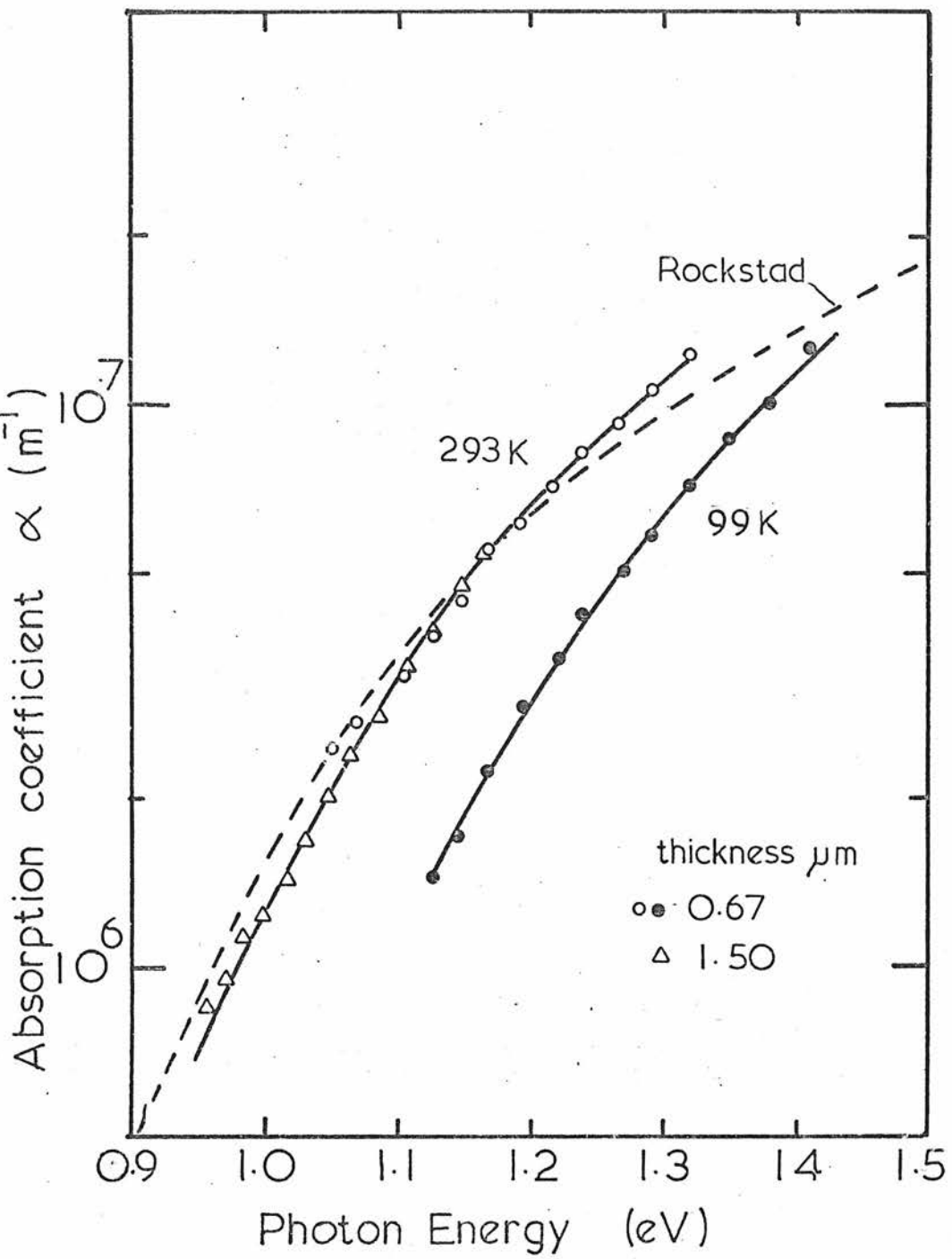

Fig 8.2 As_2Te_3 Optical absorption coefficient vs Photon energy

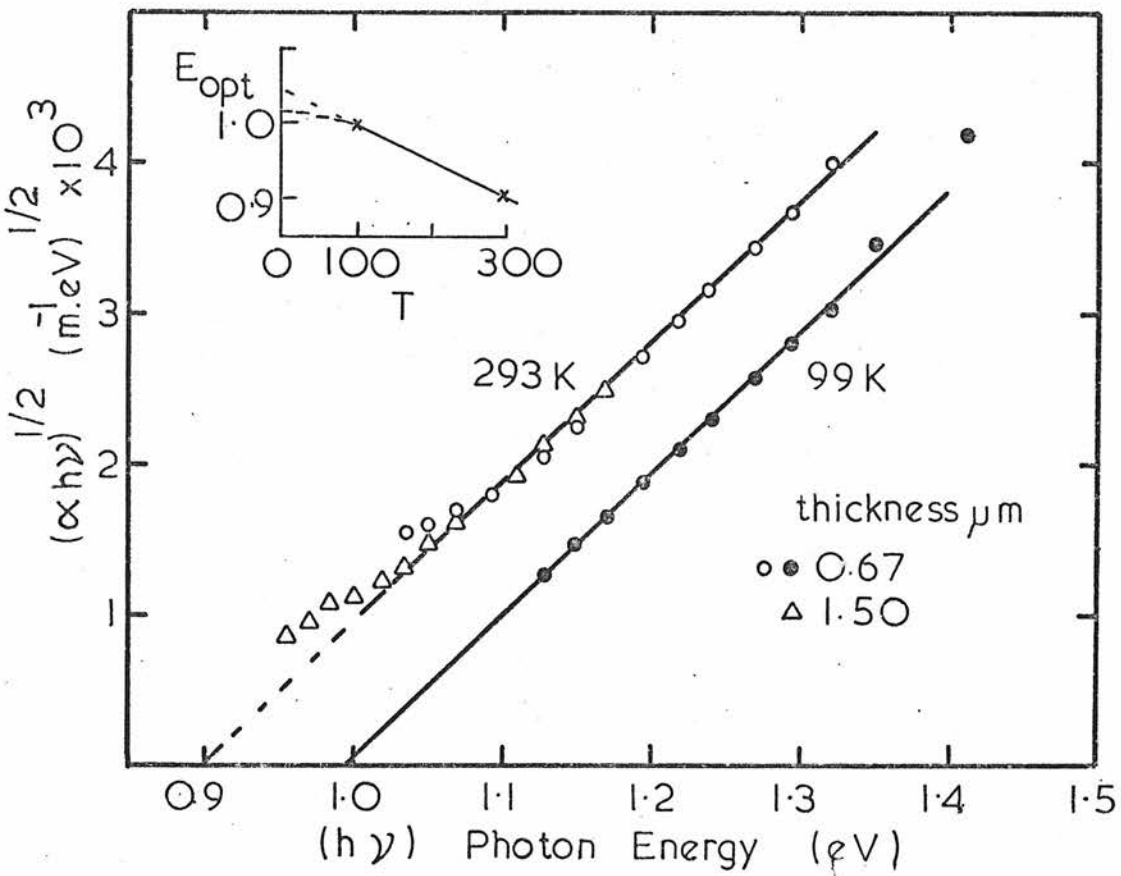

Fig 8.3 As_2Te_3 $(\alpha h\nu)^{1/2}$ vs $h\nu$

$$293\ K \quad E_{opt} \approx 0.90\ eV$$

$$99\ K \quad E_{opt} \approx 1.00\ eV$$

Assuming a linear optical gap temperature dependence, gives a gap coefficient $\gamma \approx -4.7 \times 10^{-4}$ eV K^{-1}, in good agreement with Weiser and Brodsky's value of -5×10^{-4} [119]. The inset of figure 8.3 illustrates this temperature dependence and the estimated value of E_{opt} at OK, assuming some flattening out at low temperatures, is ~1.01 eV, somewhat higher than Weiser and Brodsky's value of ~0.98 eV.

Davis and Mott[17] give an expression for the coefficient B - i.e.

$$B \approx \left(\frac{\sigma_o}{n_s\ c\ \epsilon_o\ \Delta E}\right) m^{-1}\ eV^{-1} \qquad 8.2.3$$

For a case with linear band tails of depth ΔE. Anticipating the results of later sections and putting $\Delta E \approx 0.2$ eV and $\sigma_o \sim 1.1 \times 10^4\ \Omega^{-1}\ m^{-1}$, gives $B \approx 5 \times 10^6\ m^{-1}\ eV^{-1}$, rather lower than the experimental value, and Weiser and Brodsky's[119] value of 4.7×10^7. Davis and Mott[17] point out that the value of σ_o in the absorption expression, may not equal the d.c. conductivity value, as the interband transition matrix element need not equal that for states in one band. Equation 8.2.3 is in any case, only a rough estimate.

It cannot be assumed that the optical gap is the gap between extended states or mobility edges, or that it corresponds to the onset of B-L transitions in a limited tail model as discussed by Davis and Mott[17].

The value will be used, however, as a rough guide to the mobility gap.

8.3 DARK CONDUCTIVITY

D.C. dark conductivity measurements were made on the coplanar thin film samples listed in 8.1. The gap width l was 25 μm and typical electrode width w was 4-5 mm. Room temperature conductivities (σ) vary by less than a factor of 3, around a value of $\sim 10^{-2}\ \Omega^{-1}\ m^{-1}$ agreeing well with Weiser and Brodsky's value.

	σ		σ
C-15 0.35 μm	1.6×10^{-2}	C-19 0.67 μm	1.0×10^{-2}
C-16 0.35 μm	1.6×10^{-2}	C-20 0.67 μm	1.0×10^{-2}
C-17 1.50 μm	8.6×10^{-3}	C-27 0.54 μm	1.56×10^{-2}
		C-28 0.24 μm	6.0×10^{-3}

Figure 8.4 shows a plot of log (conductivity) vs 1/T at low applied field ($\mathcal{E} = 4 \times 10^4$ V m^{-1}), for C-19, C-27 and C-28. Over a wide range the plots are linear - i.e. of the form :

$$\sigma = C\exp(-E_\sigma/kT)$$

with the values :

C-19 $C = 1.7 \times 10^3$ $E_\sigma = 0.42$ eV

C-27 $C = 1.0 \times 10^3$ $E_\sigma = 0.40$ eV

C-28 $C = 2.3 \times 10^3$ $E_\sigma = 0.43$ eV

also in reasonable agreement with those reported before[105,119].

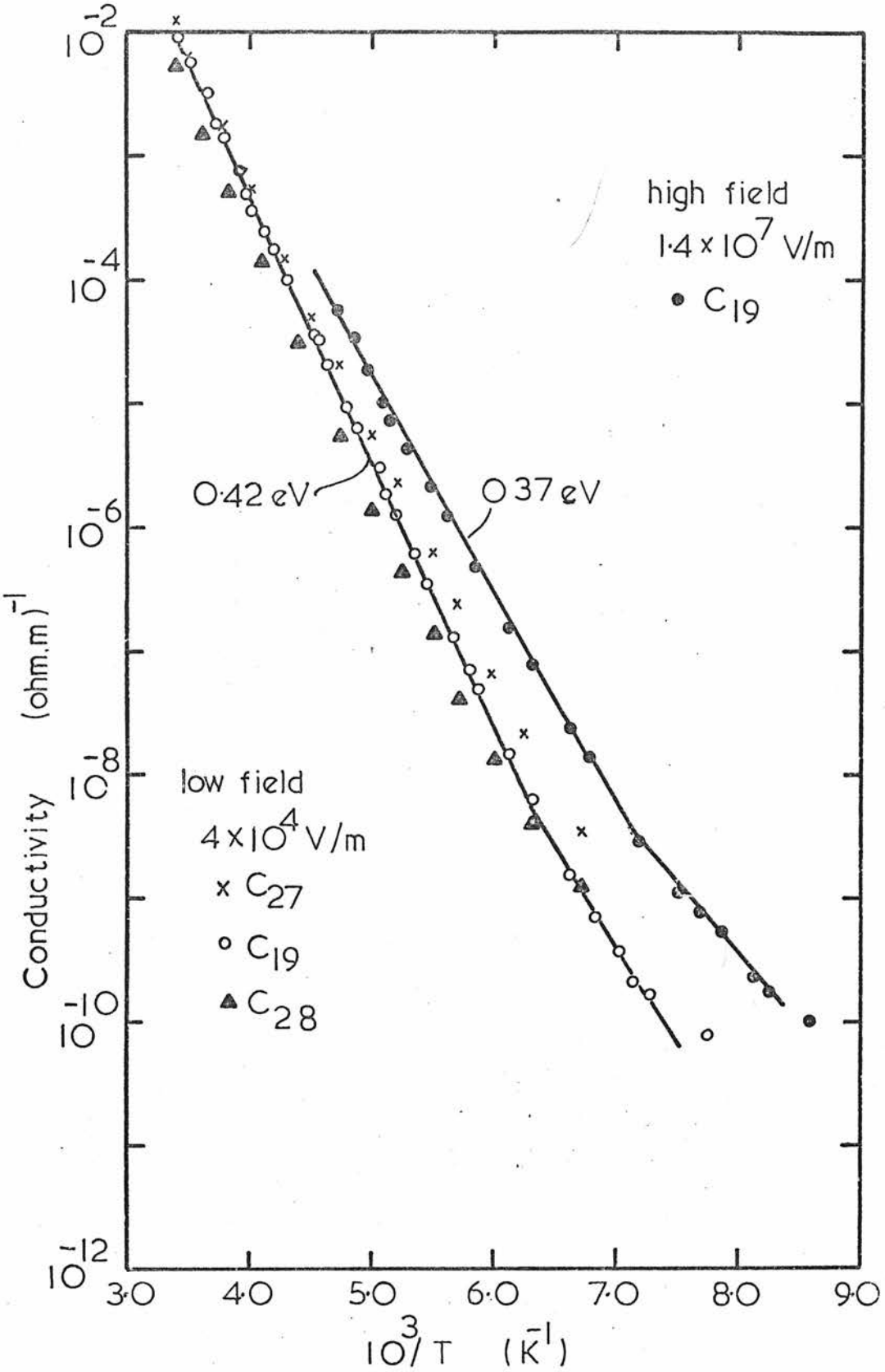

Fig 8.4 As_2Te_3 Conductivity vs $10^3/T$ at low & high fields

If conduction is by free holes, then $C \approx \sigma_o \exp(\gamma/2\ k)$, where γ is the optical gap temperature coefficient. The factor $\exp(\gamma/2\ k) \approx 15$, is only an estimate, as there may not be a direct relationship between the optical gap and mobility gap. This gives values for σ_o of 1.1×10^4, 7×10^3, $1.5 \times 10^4\ \Omega^{-1}\ m^{-1}$ respectively, for C-19, C-27 and C-28, which is what would be expected for transport in barely delocalised states near the mobility edge - i.e. in the diffusive transport region.

Below ~140 K, the conductivity data for C-19, show a slight change in slope. Although the range for this region is small, it could be fitted by band-tail hopping conduction in a tail of width $E_3 - E_v$, with hopping energy ΔW_3

$$\text{i.e. } \sigma = \sigma_1 \exp(-((E_F - E_3) + \Delta W_3)/kT)$$

The measured activation energy is ~0.3 eV, and substituting a band-tail depth of 0.2 eV indicated by transient photo-growth measurements (see 8.11) gives ΔW_3 of ~0.1 eV, a reasonable value, and σ_1, neglecting gap temperature effects, of between 10 and 100 $\Omega^{-1}\ m^{-1}$, a reasonable range for hopping conduction. The dearth of data in this region make this interpretation only tentative, but it must be borne in mind for later work.

8.4 HIGH FIELD EFFECTS

The d.c. conductivity was observed to increase with applied field, and possible mechanisms have been considered :

Poole Frenkel effect, field assisted hopping, and a hypothetical "mobility edge" effect.

8.4.1 POOLE FRENKEL EFFECT

If extended state conduction predominates, then some field produced redistribution of free and trapped charge may account for the high field behaviour. In general both the emission and capture probabilities for a given centre may be field dependent.

Using the simple 4-level model discussed in chapter 3, the distribution of free and trapped holes may be expressed as a function of field .

$$\frac{p(\mathcal{E})}{N_2 \bar{f}_2(\mathcal{E})} \approx \frac{C_{p2}(0) p_2(\mathcal{E})}{N_2 C_{p2}(\mathcal{E})} \qquad 8.4.1$$

if interchange with the valence band predominates, and lattice coupling is field independent.

For Coulombic centres, with C_{p2} field independent, this results in the Poole-Frenkel effect, and $p_2(\mathcal{E})$ can be written

$$p_2(\mathcal{E}) = N_v \exp\left(- \frac{(E_2 - E_v) - \beta\mathcal{E}^{\frac{1}{2}}}{kT}\right) \qquad 8.4.2$$

where $\beta\mathcal{E}^{\frac{1}{2}}$ is the barrier reduction for thermal ionisation on a simple one-dimensional analysis.

Taking the measured refractive index $n_s \approx 3.8$ for As_2Te_3 gives a high frequency dielectric constant $\epsilon \approx 14.4$

$$\text{and} \quad \beta = \left(\frac{e^3}{\pi\epsilon\epsilon_o}\right)^{\frac{1}{2}} \approx 2.0 \times 10^{-5} \text{ eV } V^{-\frac{1}{2}} \text{ m}^{\frac{1}{2}}$$

As mentioned in chapter 2 a full 3-dimensional analysis (Hartke[73], Ieda[74]) could give a lower theoretical value for β and, at sufficiently low fields, estimated by Marshall and Miller to be $\sim 2 \times 10^6$ V m^{-1}, a transition to hyperbolic sine and then ohmic behaviour, should occur.

It should be noted that such a trap-band redistribution can only be measured directly by such techniques as drift mobility measurements, where on the time-scale of the experiment, recombination equilibrium is not reached. Conductivity measurements are, however, made under steady state conditions, where the redistribution of equation 8.4.1 alters the equilibrium recombination rate. For example, the simple 4-level analysis of 3.2.13, gives, for B-L path 1 recombination, a free hole density

$$p(\mathcal{E}) = \left(\frac{C_{p2}(0)p_2(\mathcal{E})}{C_{p2}(\mathcal{E})} \; \frac{C_{p1}(0)p_1(\mathcal{E})}{C_{p1}(\mathcal{E})} \; \frac{N_1}{N_2} \right)^{\frac{1}{2}} \qquad 8.4.3$$

Hence, if C_{p2} and the recombination parameters are field insensitive, the conductivity will have the form (for coulombic centres)

$$\sigma(\mathcal{E}) = \sigma(0) \exp(-\tfrac{1}{2} \beta \mathcal{E}^{\frac{1}{2}}/kT) \qquad 8.4.4$$

i.e. <u>conductivity</u> measurements could give a value for β of <u>half</u> the theoretical value. Possible field dependences of the other factors could mask this lowering (or even alter the form of the field dependence), but are not incorporated in this simple form of the theory.

Note that equation 8.4.3 may be inappropriate if the Fermi level is pinned by other states, but it does serve to show that recombination should be considered in the analysis, a point which will be returned to in 8.8 and 8.10, on high field photoconductivity.

Figure 8.5 is a plot of $\log \sigma$ vs $\mathcal{E}^{\frac{1}{2}}$ for several temperatures, for sample C-19. Straight lines cannot be fitted to the data over the whole range of applied field, and even at fields $> 2 \times 10^6$ V m^{-1} where equation 8.4.2 could apply, there is still some curvature. Sufficiently high fields could not be applied to give enough variation in σ, above 2×10^6 V m^{-1} to determine whether the behaviour tended to linearity. If a 'slope' is taken from the nearly linear part at high fields, as shown in figure 8.5, then a value for β of $\sim 1.5 \times 10^{-5}$ eV V$^{-\frac{1}{2}}$ m$^{\frac{1}{2}}$ is obtained, over most of the temperature range covered. This is in reasonably good agreement with the 1-dimensional theoretical value. On the other hand it is somewhat high for agreement with the 3-dimensional analysis, especially if recombination has a further lowering effect, and this might be taken to imply some field dependence of the other factors in equation 8.4.3.

8.4.2 EXPONENTIAL FIT OF DATA

The Poole-Frenkel effect is therefore a possible candidate for the high field conductivity behaviour. It was found, however, that the data gave a much better fit over the whole field range, to an expression of the

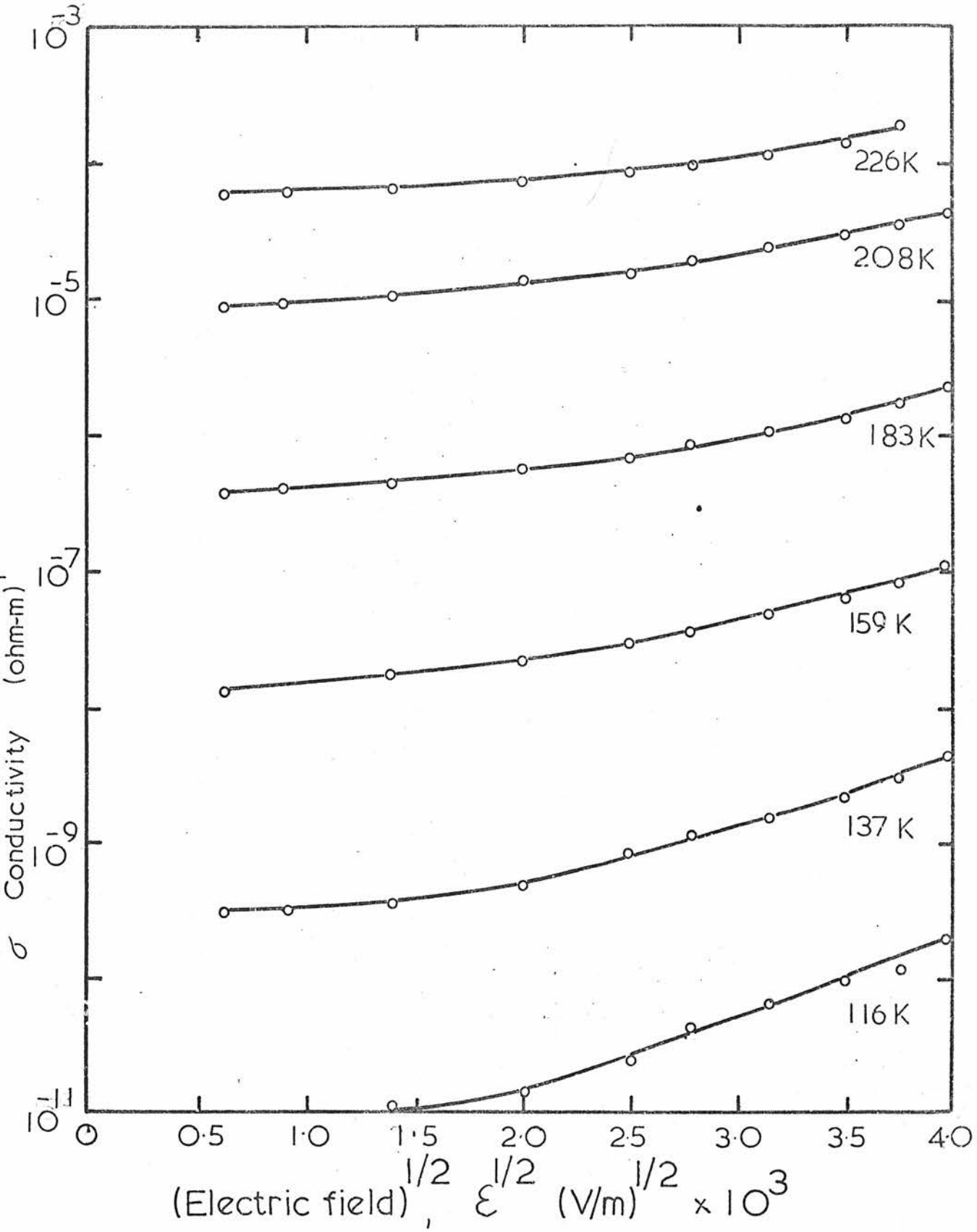

Fig 8.5 As_2Te_3 Conductivity vs $\mathcal{E}^{1/2}$

form discussed in 2.2.5 - i.e.

$$\sigma(\mathcal{E}) = \sigma_o \exp[-\{E_\sigma - e\, a(T)\mathcal{E}\}/kT] \qquad 8.4.5$$

(including the gap temperature coefficient factor in σ_o) where E_σ is the low field (strictly speaking, zero field) activation energy. Figure 8.6 illustrates this for the data of figure 8.5.

The temperature dependence of the activation length parameter a(T) is shown in figure 8.7, and can be seen to have a roughly linear dependence

$$a(T) = a(0) - dT \qquad 8.4.6$$

where $a(0) = 31$ Å (extrapolated)

$$d \approx 7 \times 10^{-2} \text{ Å K}^{-1}$$

As mentioned in 2.2.5, this behaviour is typical of many chalcogenides, and similar data are included in figure 8.7, for $Ge_{18}Te_{81}S_2Sb_2$ and $As_{10}Te_{50}Ge_{40}$. These measurements were carried out by the author, and Mr. A.W. Wallace, respectively in this Department.

When a(T) is of the form of equation 8.4.6, then the change in conductivity activation energy depends on the 'zero temperature' value a(0), while the intercept at $1/T = 0$ is reduced. For example, a field of 1.2×10^7 V m^{-1} should result in a change of activation energy, from 0.42 eV, to about 0.37 eV, and a depression of σ_o by a factor of ~ 0.38. High field data for $\mathcal{E} = 1.2 \times 10^7$ V m^{-1} are included in figure 8.4, showing the reduction in activation energy (above 140 K) to ~ 0.37 eV.

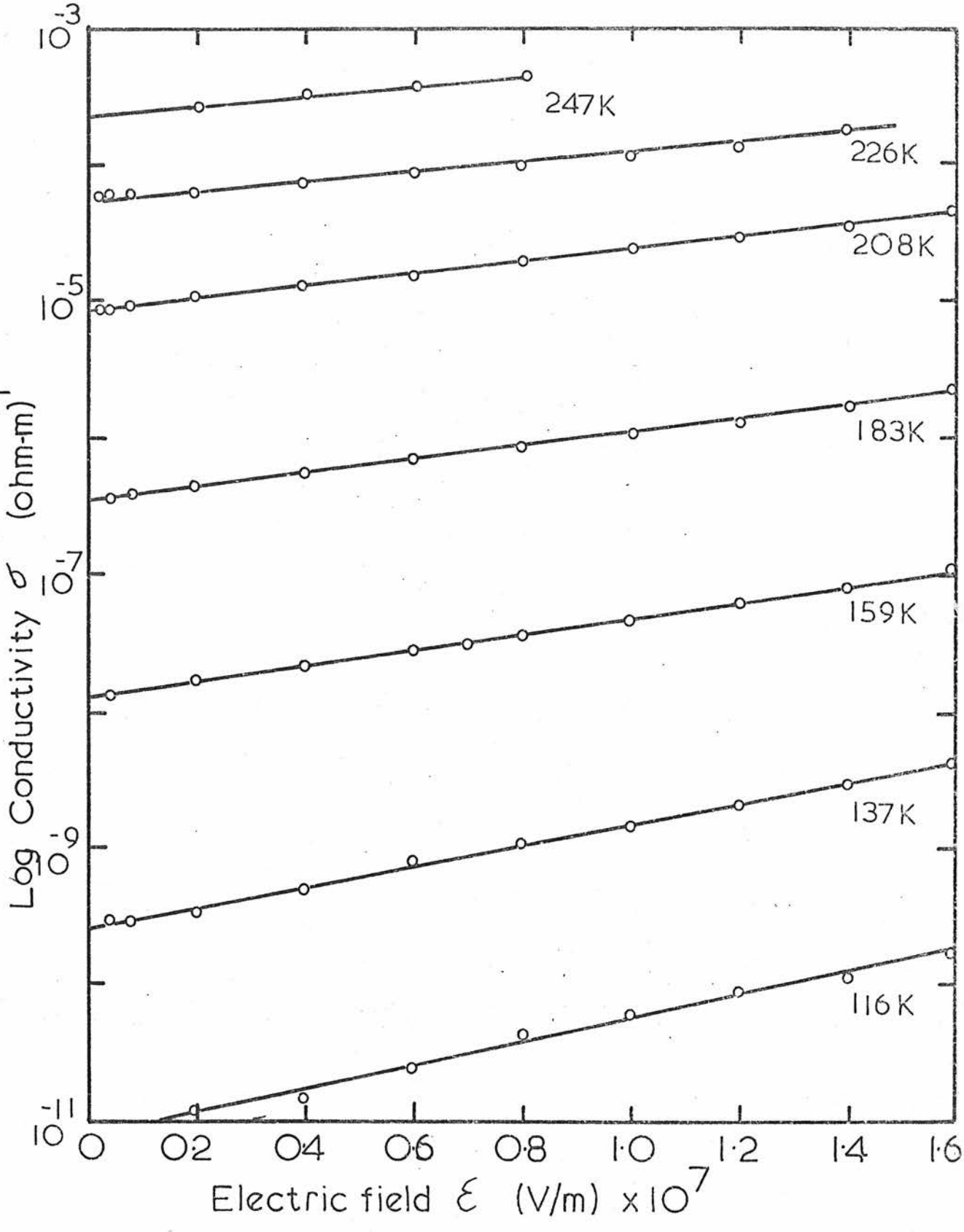

Fig 8·6 As_2Te_3 Log Conductivity vs Electric field

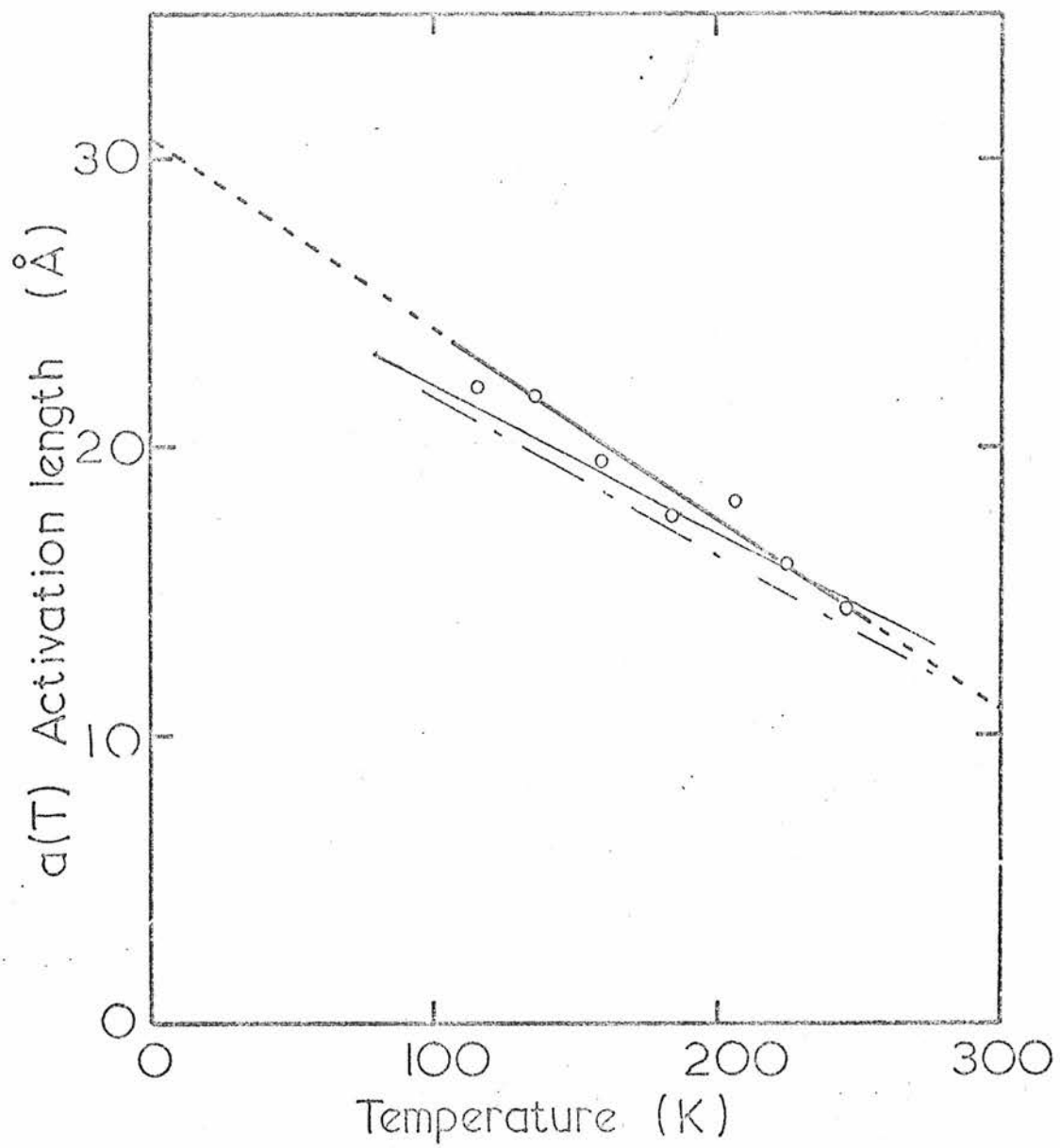

Fig 8.7 As_2Te_3 Activation length vs Temperature (dark)

$Ge_{15}Te_{81}S_2Sb_2$

$As_{40}Te_{50}Ge_{10}$

It is worth noting that the behaviour described by equation 8.4.5 has been observed in $Ge_{15}Te_{81}S_2Sb_2$ and As-Te-Ge, to fields $\geq 3 \times 10^7$ V m^{-1}. If this were also true for As_2Te_3, then the data of figure 8.5 would continue to curve, at higher fields, invalidating a Poole-Frenkel explanation.

8.4.3 FIELD ENHANCED HOPPING

Field enhanced hopping conduction in a band tail was considered, as the hyperbolic sine relation of equation 2.2.13 will result in the observed exponential field dependence at high fields.

This explanation does not seem likely for several reasons. Firstly, the value of σ_o (1.1×10^4 Ω^{-1} m^{-1}) is probably not compatible with this mechanism, which should give a pre-exponential factor of $\leq 10^2$ Ω^{-1} m^{-1}. The value of the hop distance must be ~ 20 Å in the temperature range studied, which seems somewhat large although not impossible. Perhaps the main objection however, is that a hyperbolic sine dependence should be observed, at fields below $\sim 5 \times 10^6$ V m^{-1}. This is not observed in As_2Te_3, nor in many other chalcogenides, as mentioned in chapter 2, where the exponential dependence is followed at fields as low as 10^5 V m^{-1} (Marshall[67]).

8.4.4 'MOBILITY EDGE' EFFECT

The proposal of Marshall and Miller[66], that this ubiquitous behaviour is caused by the effect of a field on carriers near the mobility edge, seems very plausible, although at the time of writing, detailed calculations have not been carried out. Whether the mechanism is understood as 'field stripping' of shallow localised states, or 'unblocking' of percolation bonds, it can be interpreted as a progressive lowering of the mobility edge. The depths or activation energies, of deeper lying traps both neutral and coulombic, are therefore also effectively reduced, even at fields too low to significantly alter the trap parameters, as in the Poole-Frenkel effect, a point which will be discussed in section 8.10 and 9.9 . on photoconductivity.

The 4-level steady state analysis which gave equation 8.4.3 is applicable when band tails are also present, if the total occupation of the tail states below the mobility edge is small compared with that of the 'discrete' states at E_2 and E_1. If the effective release terms may now be written

$$C_{p1}\, p_1(\mathcal{E}) = C_{p1}\, p_1(0)\, \exp(+\, a(T)\, \mathcal{E}/kT)$$
$$C_{p2}\, p_2(\mathcal{E}) = C_{p2}\, p_2(0)\, \exp(+\, a(T)\, \mathcal{E}/kT)$$

where $a(T)$ is the effective mobility edge shift, the capture parameters are field insensitive, and recombination path 1 dominates, then equation 8.4.3 naturally gives the required field dependence. (The same observed effect

would occur if E_F were pinned, in contrast to the Poole-Frenkel analysis).

8.5 PHOTOCONDUCTIVITY : SPECTRAL RESPONSE

The spectral response of a sample with coplanar electrodes is defined here as the relative steady state photocurrent per incident photon, vs photon energy - (the measurement technique was discussed in chapter 4). This procedure does not directly allow the separate investigation of the photogeneration process and the subsequent transport and recombination, but with a knowledge of the likely recombination behaviour from other measurements, information can be extracted on photogeneration efficiency (η) and surface effects (or the lack of surface effects).

Figure 8.8 shows the normalised spectral response at room temperature and at 143 K for sample C-19. The behaviour at these two temperatures is quite different. At room temperature, the response falls fairly steeply at photon energies below 1 eV, and has a constant value at energies above ~ 1.1 eV, to at least 2.4 eV. At 143 K however, the low energy fall off is less steep, and the response peaks at ~ 1.2 eV, falling again at high energies, to level off above ~ 2.2 eV.

This behaviour can be explained in terms of the prevailing bulk recombination kinetics, a photogeneration efficiency which is constant (probably unity) at high photon energies, and which falls off at low photon

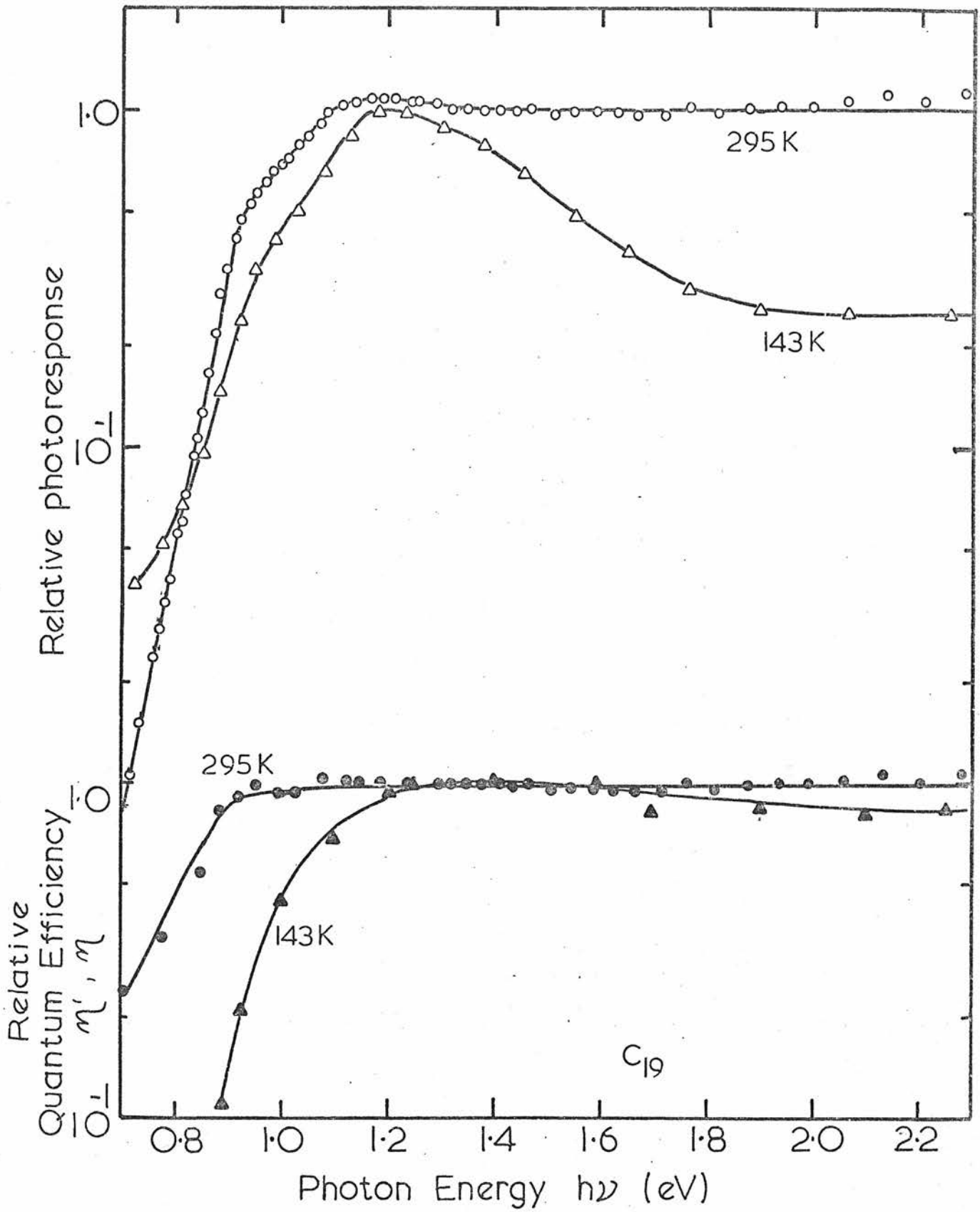

Fig 8.8 As_2Te_3 Spectral photoresponse & Quantum Efficiency vs Photon Energy

energies ($h\nu \leqq E_{opt}$). In this low energy region, the quantum efficiency may be activated. No recourse has to be made to additional spatial variation of recombination kinetics such as may be caused by surface states.

It was ascertained that with the excitation levels employed, (from the Hilger monochromator), at 295 K, small signal, or monomolecular recombination conditions prevailed in the bulk, while at 143 K, square root bimolecular recombination prevailed as will be discussed in 8.6. If diffusion effects are ignored, then the excess free hole density at depth x from the sample surface can be written

$$\text{linear case } \Delta p(x) = \Delta G(x)\tau_{pm}(x) \qquad 8.5.1$$

$$\text{Bimolecular case } \Delta p(x) = [\Delta G(x)/\theta(x)]^{\frac{1}{2}} \qquad 8.5.2$$

where τ_{pm} and θ are recombination constants defined in 3.3.1, but which may vary spatially, e.g. if surface states are present. The depth dependent generation rate was derived in equation 3.2.99, as

$$\Delta G(x) = \frac{\eta(h\nu,x)F\alpha(1-R_1)\exp(-\alpha x)\{1+R_2\exp[-2\alpha(d-x)]\}}{1-R_1R_2\exp(-2\alpha d)} \qquad 8.5.3$$

where F is the incident photon flux density, and spatial variation of η is included. Multiple reflection, but not interference is included. The total photocurrent can be obtained by integrating equations 8.5.1 and 8.5.2 through the sample thickness - i.e.

$$\Delta I = w\, e\, \mu_{po}\, \mathcal{E} \int_0^d \Delta p(x)\, dx \qquad 8.5.4$$

This is obviously impossible if the spatial variations of η, τ_{pm} and θ are not known. The following argument demonstrates, however, that these parameters probably do not vary with x.

The relative photocurrent per absorbed photon (η') at room temperature can be calculated from the photo-response data, and the total absorbance A, obtained from figure 8.1.

$$\text{i.e. } A = 1 - (T + R) \qquad 8.5.5$$

$$\therefore \eta' \alpha \Delta I/FA \qquad 8.5.6$$

and this is plotted in figure 8.8, vs photon energy. It can be seen that η' is virtually constant for energies above 1.0 eV to at least 2.4 eV. For this to be so, either the 'competing' photogeneration and recombination processes have energy and spatial dependences which cancel out exactly over a wide range of photon energy and absorption depth, or as seems more likely, both η and τ_{pm} are independent of photon energy and position (i.e. $\eta = \eta'$). Furthermore, if η is independent of photon energy over such a wide range, it has probably 'saturated' to a value of unity.

Integration of equation 8.5.4 now gives

$$\Delta I = \frac{w\, e\, \mu_{po}\, \mathcal{E}\, (\eta \tau_{pm}) F (1-R_1)[1-\exp(-\alpha d))(1+R_2 \exp(-\alpha d)]}{1-R_1 R_2 \exp(-2\alpha d)}$$

which gives almost identical results for η as equation 8.5.6

In the bimolecular case, the integration may be carried out by expanding the integrand as a power series, to give

$$\Delta I = w\, e\, \mu_{po}\, \mathcal{E} \left(\frac{4\,\eta F(1 - R_1)}{c\alpha\{1 - R_1 R_2 \exp(-2\alpha d\} } \right)^{\frac{1}{2}}$$

$$x(1 - (1 - R_2/6 + R_2^2/56 - \cdots\cdots) \exp(-\frac{\alpha d}{2})$$

$$- R_2/6 \exp(-2\alpha d) + R_2^2/56 \exp(-4\alpha d) + \cdots\cdot) \qquad 8.5.7$$

The terms beyond the second ($R_2/6$ coefficient) contribute less than 1%, over the range of α covered, and were ignored. Again, it is assumed that η and θ are spatially invariant.

Figure 8.8 also shows the energy dependence of η obtained from equation 8.5.7 and the spectral response at 143 K. Values for α at 143 K were obtained by linear interpolation (on the photon energy axis) of the results of figure 8.2. It can be seen that η is again constant at high photon energies, but the low energy fall off occurs at higher photon energy (1.2 eV) than at room temperature.

The high energy spectral response fall-off, at 143 K, is thus simply a result of the bimolecular bulk recombination kinetics - i.e. the bulk lifetime decreases when the carriers are produced in a smaller volume near the surface, as the absorption depth reduces. Surface

recombination states, which are often invoked to explain peaking of photoresponse in crystalline semiconductors, do not appear to be present in sufficient density to affect the response.

The low energy data for η, seem to fit qualitatively to the 'one-process' models of Tabak and Warter (exciton) or Davis and Mott (classical) it should be noted however, that there is no large gap between the absorption edge and the quantum efficiency fall off or 'edge', as in selenium.

The shift of this edge with temperature, ~0.2 eV between 143 K and 295 K is somewhat larger than would be explained by a shift in the absorption edge only and this would indicate that the generation is an activated process. Whether dissociation of an exciton is involved, or separation of a 'free' electron-hole pair, such a thermal activation is to be expected. Unfortunately the data available do not allow any detailed analysis.

8.6 PHOTOCURRENT INTENSITY DEPENDENCE

The relation between photocurrent in a coplanar sample, and incident photon flux density F, was measured at a sufficiently low field to avoid appreciable non-ohmic effects (8×10^4 V m^{-1}). A Monsanto type ME5A infrared GaAs l.e.d. was mainly used, with average photon energy of 1.37 eV. This ensured that the photogeneration efficiency was always saturated, over the temperature range covered.

Low level photocurrent signals ($\Delta I < I$ dark) were detected by an a.c. technique, modulating the source at frequencies between 15 and 100 Hz. High level signals ($\Delta I \geq I$ dark) were detected by a.c. and d.c. methods. At room temperature, the photoresponse time was fast enough to also allow the use of 2 μs light pulses of high intensity, from a GaAs laser operated at 77 K ($\lambda = 0.845$ μ, $h\nu \approx 1.47$ eV).

Figure 8.9 illustrates log photocurrent vs log incident photon flux F for several temperatures. The curve for 226 K shows most clearly the transition from a linear dependence to a square root dependence with increasing photon flux, a transition which occurs at other temperatures but is less accessible, experimentally. It is also clear that there is a reversal of temperature dependence between those two regimes.

At 143 K, at high intensities, there is a slight increase in slope, and at 115 K the photocurrent-intensity index is also slightly higher than square root ($\sim F^{0.57}$).

An estimate was made of the dark current flowing in the region of photoexcitation - i.e. in the absorption region, which is ~ 0.1 μm in this case, and this is marked in the figure, on some of the curves. It can be seen that the linear-square root transition occurs roughly at the point where $\Delta I \approx I$ dark.

Most of these data seem reasonably consistent with the analysis of chapter 3, where the transition discussed

Fig 8.9 As_2Te_3 Photocurrent vs Photon flux

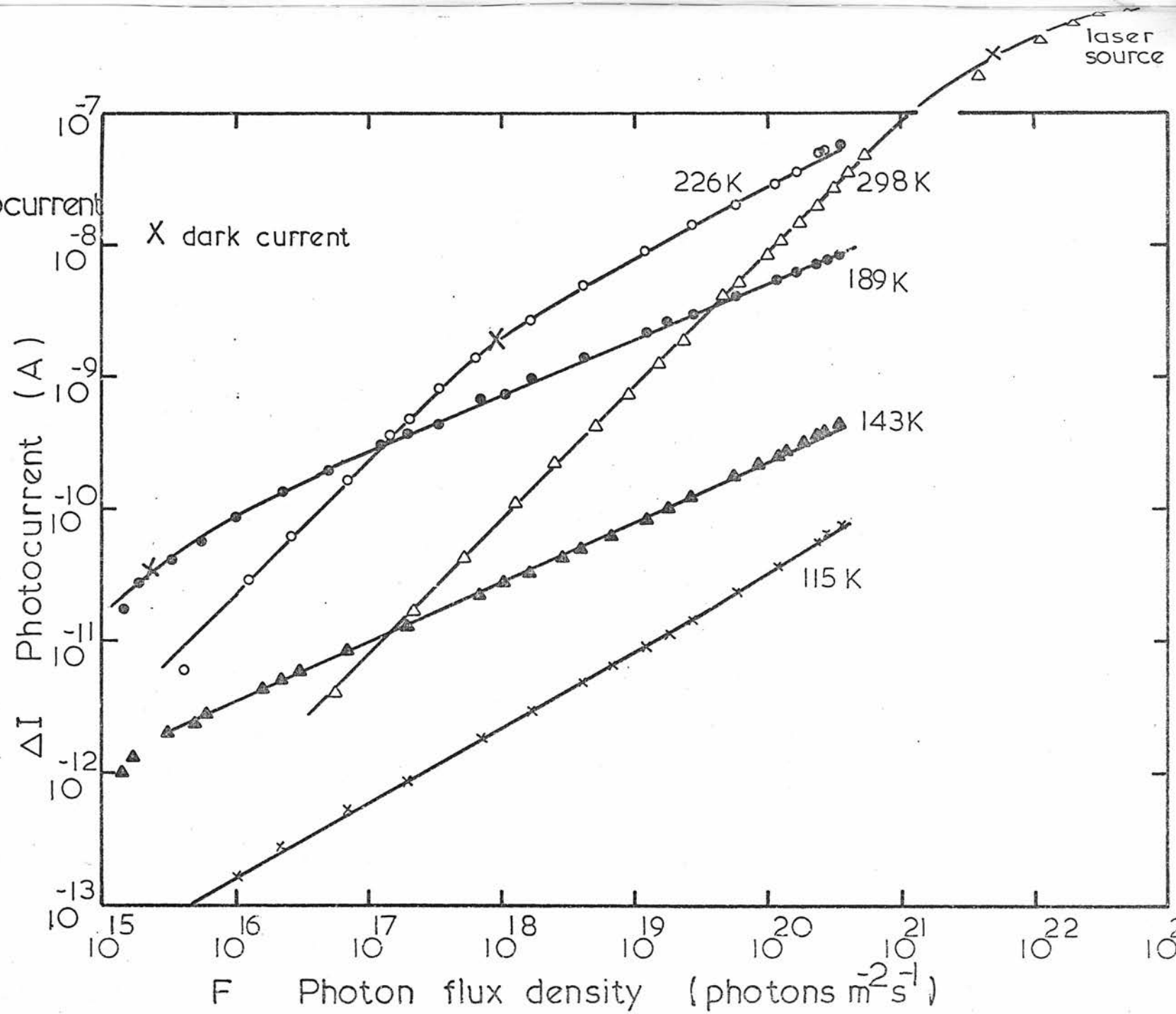

above, is between the small signal monomolecular recombination regime, and the high signal bimolecular regime. The reversal of temperature dependence is also predicted, whether recombination is by B-L or L-L transitions. The discrepancies at low temperature may be associated with wide splitting of the trap-Fermi levels, and this will be discussed in 8.10.

8.7 PHOTOCURRENT TEMPERATURE DEPENDENCE

The temperature dependence of the steady state photocurrent at constant photon flux density was measured at low electric field ($< 10^6$ V m^{-1}), using the ME5A l.e.d. and the TA7606 laser. Again modulation and d.c. techniques were used with the l.e.d., for low and high level signals respectively, although there was some overlap. The GaAs laser was operated at 77 K, with 2 A pulses of 2 μs duration, which allowed the photocurrent to reach its final value over most of the temperature range.

Figure 8.10 shows log (ΔI) vs $10^3/T$ for samples C-19 and C-27, for four photon flux densities ranging from 2.4×10^{19} to 6.5×10^{22} photons m^{-2} s^{-1}. This clearly illustrates the reversal of temperature dependence mentioned in 8.6 and the consequent maximum. Also shown in figure 8.10 is the estimated dark current flowing in the photoexcited region - only a rough estimate as the excess carrier distribution should alter between the two regimes, and this intersects each photocurrent plot near its maximum.

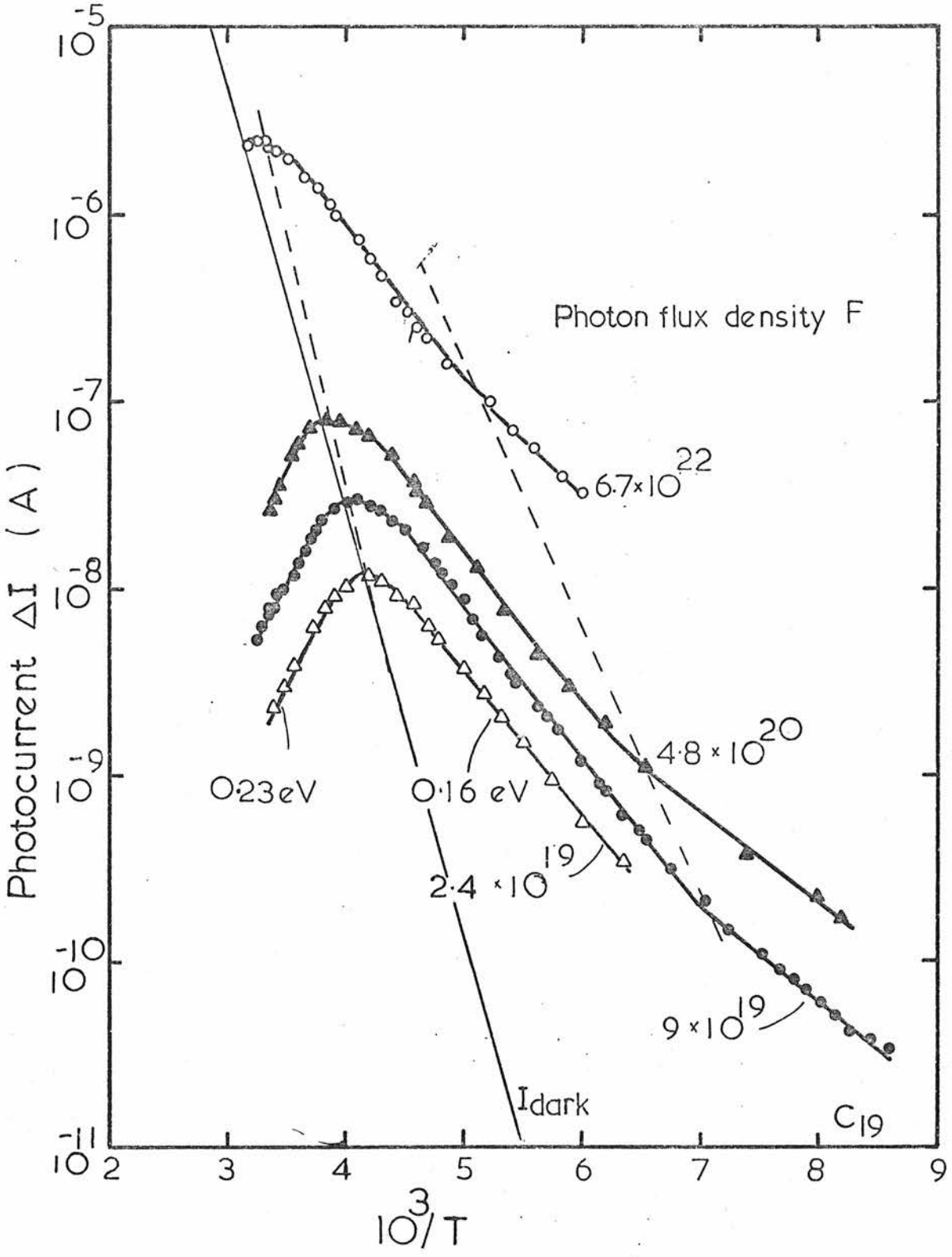

Fig 8.10 Photocurrent vs $10^3/T$ at different excitations

As_2Te_3

On the high and low temperature sides of the maximum, the intensity behaviour is linear and square root respectively, so the characteristic energies for mono and bi-molecular recombination can be assigned to the slopes - i.e.

$$\text{High temperature} + \Delta E_m = + 0.23 \text{ eV} \pm 0.2 \text{ eV}$$

$$\text{Intermediate temperature} - \Delta E_b = - 0.16 \text{ eV} \pm 0.1 \text{ eV}$$

There are however, two points of apparent discrepancy from the results of the simple theory of chapter 3.

Firstly, a line drawn through the maxima has a slope corresponding to E_{max} of about 0.5 eV, which is rather higher than the expected value of $E_\sigma \approx 0.42$ eV. This means that the small signal/large signal criterion is not followed exactly.

Secondly, there is a break to a lower slope at lower temperatures, with a tendency to flatten out at very low temperatures. Just below the break, the activation energy may be about 0.1 eV. A line drawn through the break points has a slope of ~ 0.3 eV.

Both of these features will be discussed in 8.10, but at this point it can be stated that the data do not invalidate the bulk of the analysis of section 3.2.13 and are in fact phenomenologically self consistent.

It can be shown by simple geometry that with a linear-square root transition, $E_{max} = \Delta E_m + 2\Delta E_b$ (~ 0.55 eV) which agrees roughly with the data. Similarly, the shift of the low temperature break point

with intensity is consistent with the slightly 'super-root' behaviour at low temperatures, in figure 8.9.

Note that if absorption effects are included, the temperature dependence of the photocurrent is unaffected in the monomolecular case, and only slightly so, in the bimolecular case. For complete absorption, as applies to the l.e.d. and laser outputs, equations 8.5.6 and 8.5.7 reduce to

$$\Delta I \;\alpha\; \eta\, \mu_{po}\, \tau_{pm}\, F \quad \text{(monomolecular)}$$

$$\Delta I \;\alpha\; \mu_{po} \left(\frac{\eta F}{\theta \alpha}\right)^{\frac{1}{2}} \quad \text{(bimolecular)}$$

Including the (interpolated) temperature dependence of α has a negligible effect on the data.

The data for the 'high' and 'intermediate' temperature range seem consistent with the analysis of chapter 3, although it is not possible to distinguish whether B-L or L-L recombination is occurring, as both predict the form observed. Photodecay time measurements help resolve this ambiguity.

8.8 PHOTOCURRENT FIELD DEPENDENCE

Photocurrent-voltage measurements were carried out in the high illumination region, to ensure that, for the other measurements, the field was kept low enough to avoid significant non-ohmic effects. The 1.37 eV GaAs source was used, to ensure that the photogeneration efficiency was saturated.

It was found, however, that these photocurrent data also fitted the exponential behaviour of equation 8.4.5. Figure 8.11 shows log (photoconductance) vs field, for several temperatures. Although the field dependence is exponential, it is much less than in the dark. Figure 8.12 plots the "activation length" obtained from the data, as well as the dark data, and gives

$$\text{Photocurrent } a(0) \approx 18 \text{ Å}$$
$$d \approx 3.5 \times 10^{-2} \text{ Å K}^{-1}$$

The interpretation of such results is uncertain, as photogeneration, kinetics, and transport may all be field dependent. In the discussion of 8.10, it will be shown that the 'mobility edge' field effect discussed in 8.3 and applied to the bimolecular kinetics case, could account for the difference between dark and photocurrent field dependences.

8.9 PHOTODECAY TIME

As was mentioned in 8.7, steady state photocurrent data could be interpreted in terms of B-L or L-L recombination paths. The photodecay results give further information on carrier kinetics and show that B-L recombination is the most likely mechanism.

The experimental method used, was described in 4.9. Care was taken to ensure that the illumination rise and fall times t_r and t_f and detection response time were

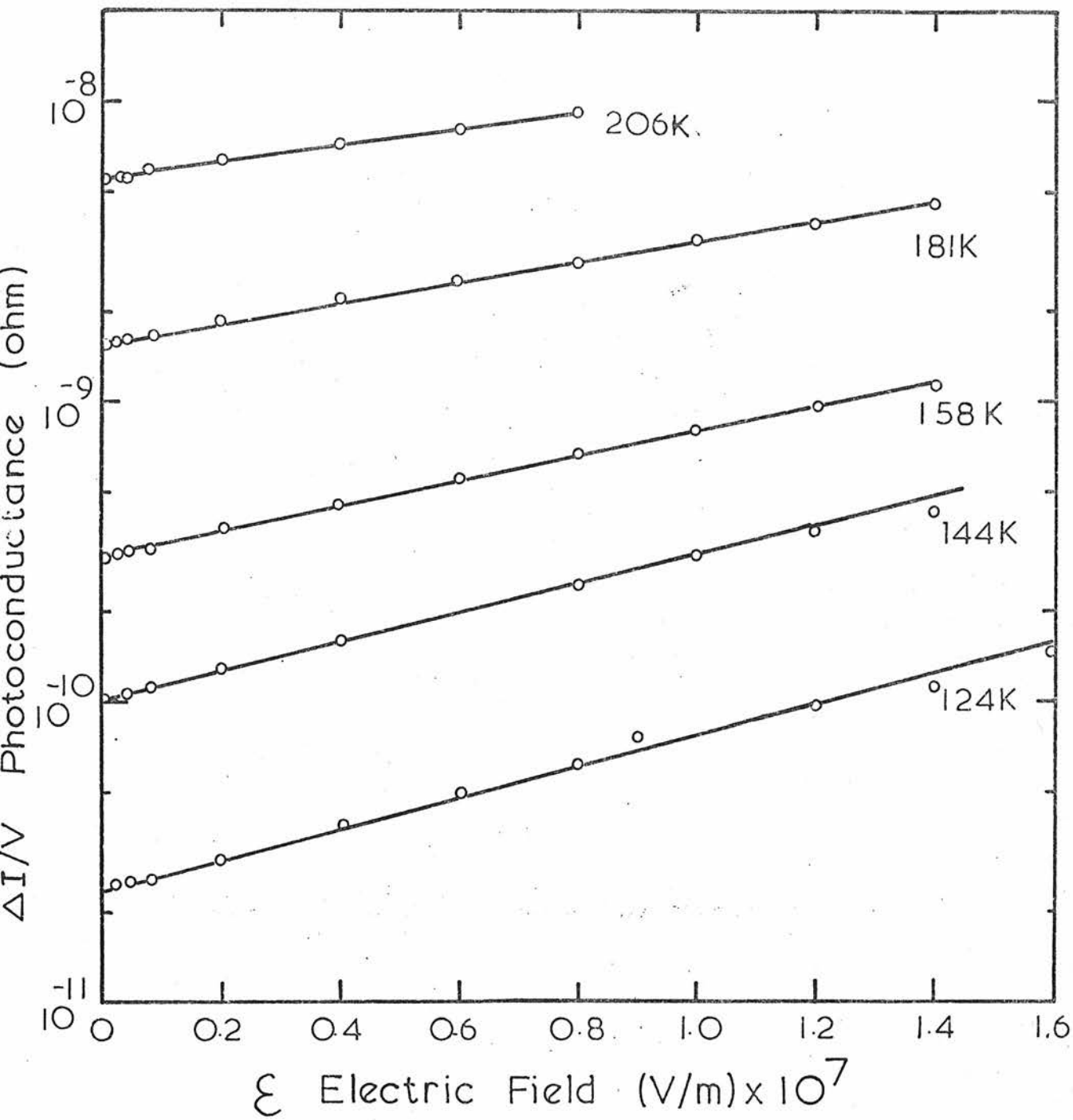

Fig 8.11 As_2Te_3 log photoconductance vs Field (bimolecular) at different Temperatures

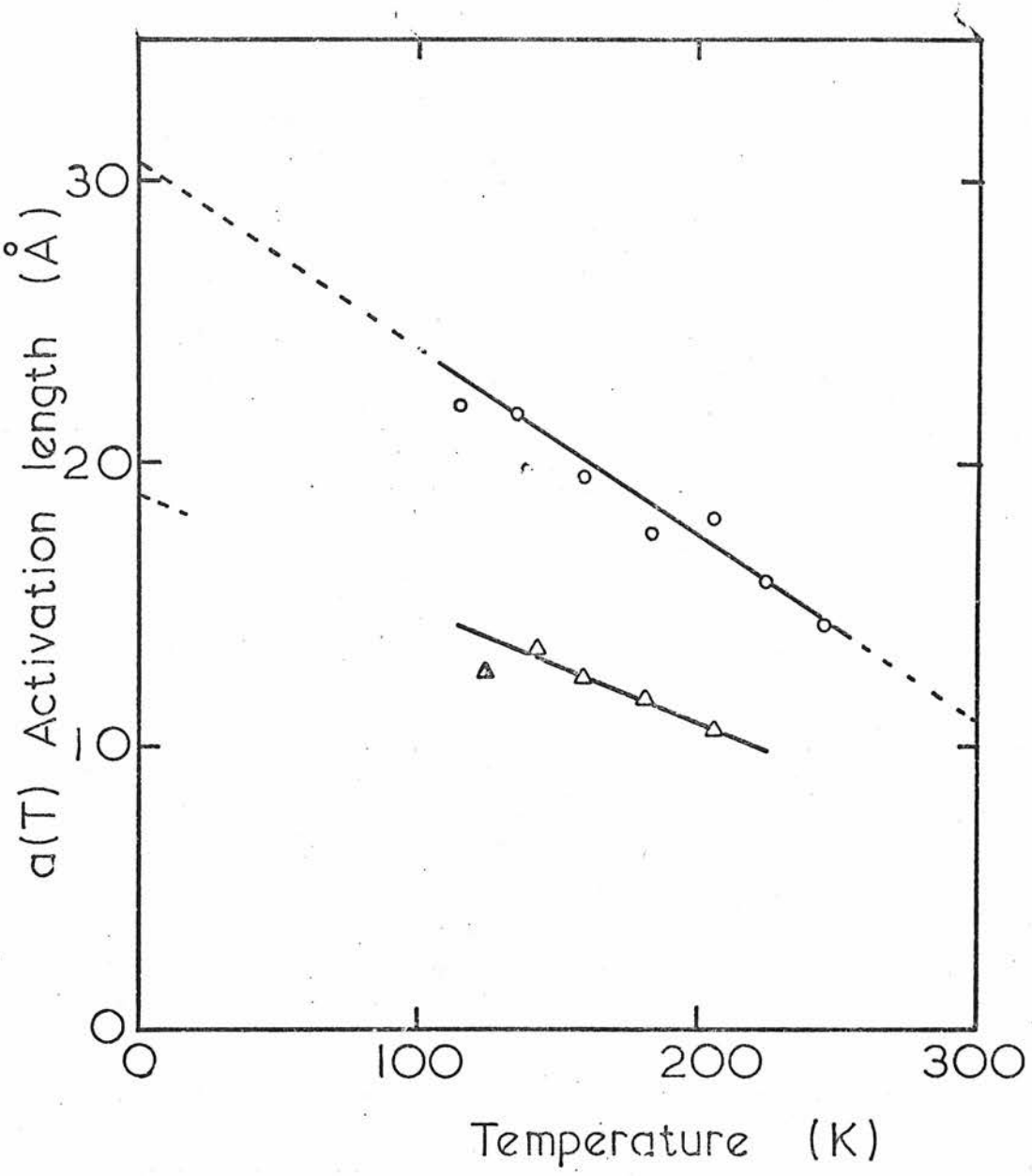

Fig 8.12 Field activation length a(T) vs Temperature

- ○ dark conductivity
- △ photoconductivity (bimolecular)

As_2Te_3

shorter than the photodecay time τ_c measured as the time for the photocurrent to decay to half its steady state value after the illumination was turned off. In this respect, both the ME5A l.e.d. ($t_r \leqq 0.2$ μs) and the TA7606 laser ($t_r < 10$ ns) were satisfactory, and the instrumental rise time was kept always $\leqq 0.3\ \tau_c$. This was done by reducing the series current sampling resistor, and hence the input R-C time constant of the preamplifier, as discussed in 4.9.2. In some cases, this resulted in a very poor photosignal/noise ratio, and synchronous 'Boxcar' detection was used to clean up the signal, as described in 4.9.2. Figure 8.13 shows such a photodecay trace, displayed by a storage oscilloscope (Tektronix type 549).

The variation of photodecay time τ_c with temperature is shown in figure 8.14, for four illumination levels. Superimposed upon these is the steady state photocurrent dependence of figure 8.10 for $F = 9 \times 10^{19}$ photons $m^{-2}\ s^{-1}$. It can be seen that in the high temperature 'linear' regime, τ_c is independent of illumination level, and has a marked temperature dependence which can be described by

$$\tau_{cm} \propto \exp(+\Delta E_{\tau m}/kT)$$

where $\Delta E_{\tau m} \sim 0.55 \pm 0.03$ eV.

The room temperature value of the monomolecular decay time is ~1 μs. Contrast this with the value obtained from Weiser and Brodsky's[119] results, of 100 ns, using GaAs laser excitation, and the value obtained here

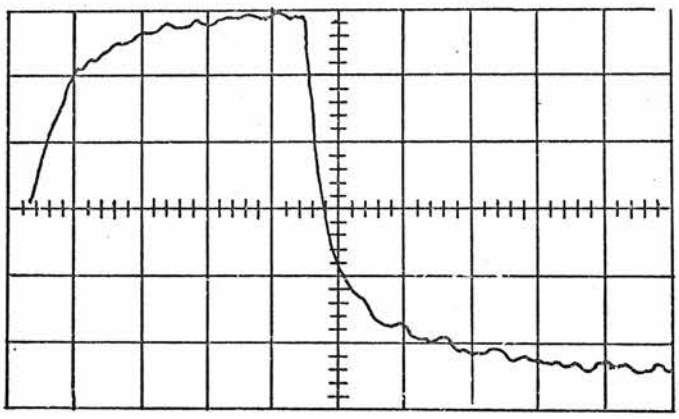

Fig 8.13 As_2Te_3 Photocurrent decay obtained by boxcar signal retrieval

vertical scale 5nA/cm
horizontal scale 20μs/cm
90μs light pulse $F = 9 \times 10^{19}$ photons $m^{-2}s^{-1}$
T = 281K.

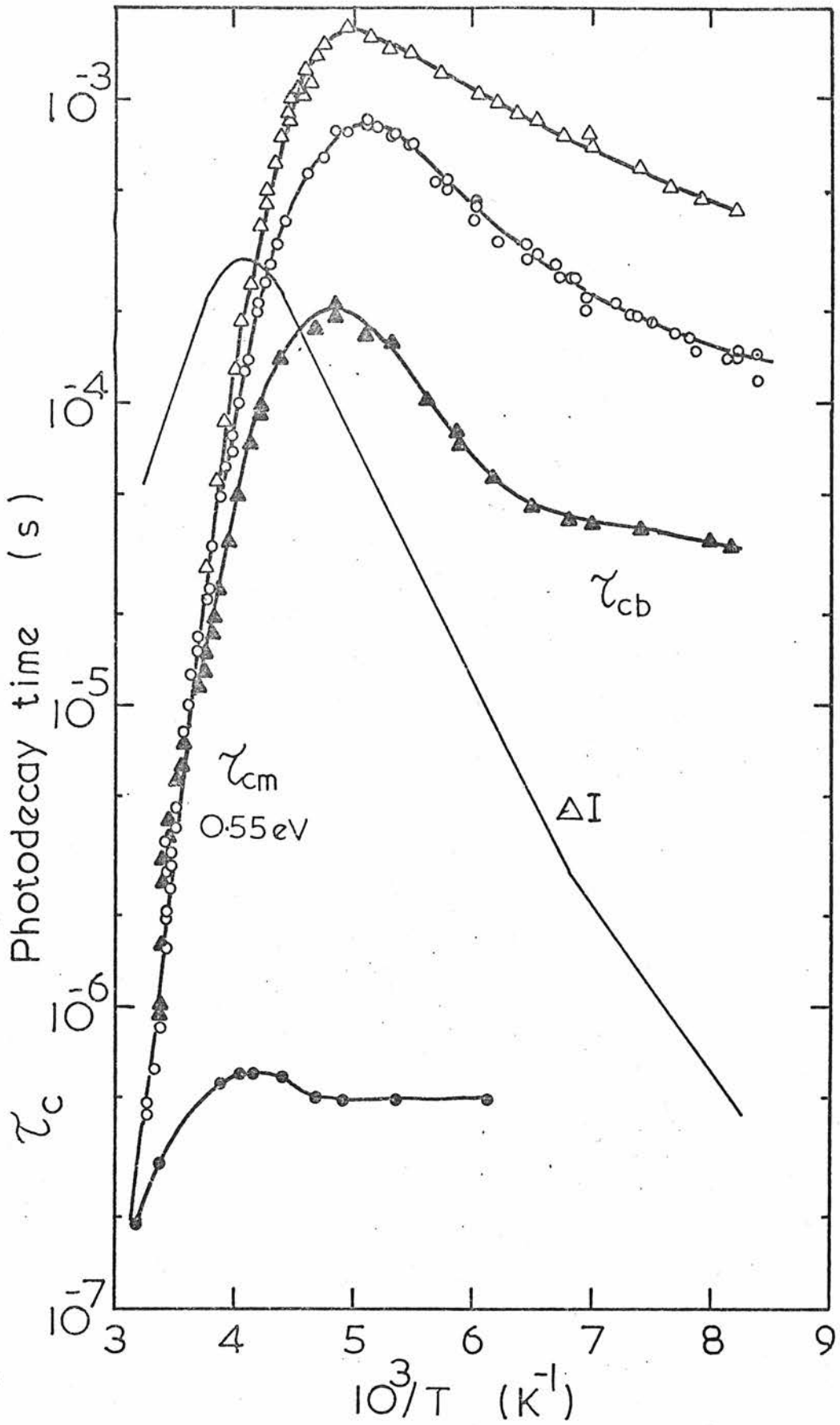

Fig 8.14 Photodecay time τ_c vs $10^3/T$ at different intensities. for As_2Te_3

Flux density photons $m^{-2}s^{-1}$

△ 2.4×10^{19} ▲ 4.8×10^{20}

○ 9.0×10^{19} ● 6.7×10^{22}

with laser excitation, of 200 ns. It is evident that in these cases, the recombination kinetics are bimolecular at room temperature see figure 8.1 and hence the decay time is reduced.

Figure 8.13 shows the time dependence of the decay at room temperature, for 'low' excitation, which fits well to the exponential curve predicted for monomolecular recombination. Figure 8.15 shows τ_c vs F for three temperatures. At 250 K, τ_c is nearly independent of F, while at 202 K, τ_c is proportional to $F^{-\frac{1}{2}}$ over a wide range. At 143 K, however, there is a steeper, unexplained, dependence.

In the square root regime, τ_c, now τ_{cb}, first continues to rise, to a maximum, then falls off slowly with reducing temperature, and diminishes with increasing illumination. The data for the highest illumination - 6.7×10^{22} photons m^{-2} s^{-1} may be slightly low at low temperatures as the available laser light pulse width was limited to 2 μsec, (77 K operation) and the steady state may not have been reached during this time.

8.10 PRELIMINARY MODEL FOR As_2Te_3

The data presented so far enable a preliminary model to be set up for the distribution of localised states, and carrier kinetics in As_2Te_3. Further data, presented in 8.11 - 8.12 corroborate this model, and also indicate the presence of additional states, not fully revealed by the measurements already described.

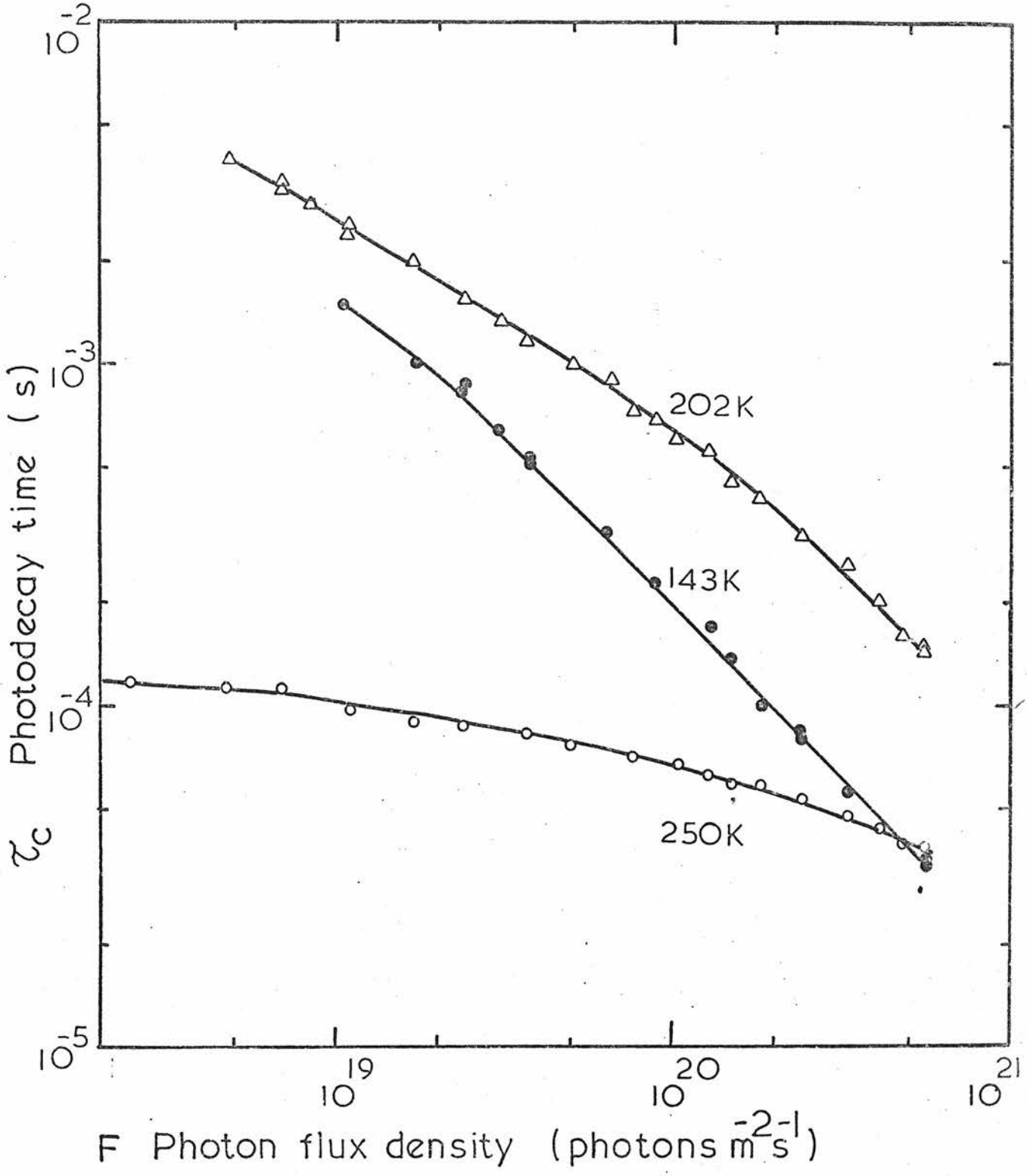

Fig 8.15 As_2Te_3 Photodecay time τ_c vs Photon flux density F

The model chosen, has to be consistent, as far as possible, with the following experimental data.

Optical gap (0K)	E_{opt}	1.01 eV
Dark conductivity activation energy	E_{σ}	0.42 eV
Steady state monomolecular 'activation'	ΔE_m	0.23 eV
Steady state bimolecular 'activation'	ΔE_b	0.16 eV
Monomolecular decay time 'activation'	$\Delta E\tau(m)$	0.55 eV

The preliminary model is based on these data and the analysis of chapter 3. Other features, such as the bimolecular decay time behaviour and low temperature photocurrent break cannot be described so simply, and will be discussed later.

In selecting the model, a number of possible situations had to be considered depending upong the choice of recombination paths (B-L or L-L) and transport mechanisms (in extended states, or hopping). If the possibility of a change with temperature, from B-L to L-L recombination and/or of transport mechanism, is included, the number of possible situations is large.

These analyses were carried out in the light of the 4-level model of chapter 3 and the most consistent model (a) was the relatively simple one of B-L recombination at all temperatures and extended state transport, with the proviso that the equilibrium Fermi level is 'pinned' by another set of states 0.42 eV above the valence band edge (density N_F, say).

The only other 'contender' was a model (b) in which B-L recombination in the monomolecular regime gives way to L-L recombination in the bimolecular regime. Although this requires no pinning of E_F, analysis shows that it does not give a very good fit to the high temperature photodecay data. Furthermore, if the transition from B-L to L-L recombination does not coincide in temperature with the transition from monomolecular to bimolecular kinetics, an intermediate region can occur in the photocurrent temperature dependence, with slope between ΔE_m and ΔE_b. It can be shown that the B-L to L-L transition temperature is independent of excitation, while the mono to bimolecular transition temperature is excitation dependent. The absence of an intermediate slope region therefore argues against model (b).

The recombination analysis of chapter 3 requires little modification in the presence of 'pinning' states, if they behave in a similar way to the 'gap-centre' states in the treatments of Weiser et al[100] and Arnoldussen et al[99]. Firstly, they play an insignificant role in recombination at all temperatures. The possibility of this occurring is related to the density and capture coefficients of the states and was discussed in 3.2.12. Secondly, the 'species' must be such that under high illumination, the charge density in these states is less than that in states at E_1 and E_2. The type and density of these states depends upon the

charge type and density of the states at E_1 and E_2. This will be discussed later.

The 'pinning' thus affects only the charge neutrality condition in the dark and low signal (monomolecular) regime. Referring to the equations for the monomolecular analysis, (3.2.85-3.2.87, and 3.3.8-3.3.10) the energy $\frac{1}{2}(E_1 - E_2)$ may now be replaced by $(E_1 - E_F)$, for B-L recombination path 1, using subscript 'm' for monomolecular values, giving

$$\Delta P_m = \frac{\Delta G}{N_1 C p_1} \exp(+\frac{E_1 - E_F}{kT}) = \Delta G \, \tau_{pm} \qquad 8.10.1$$

$$\tau_{cm} = \frac{N_2}{p_2 N_1 C_{p1}} \exp(+\frac{E_1 - E_F}{kT}) = \frac{N_2}{p_2} \, \tau_{pm} \qquad 8.10.2$$

As an illustration of the tests for a consistent model, table 8.10.1 lists the characteristic energies obtained for three cases. (a) B-L recombination at all temperatures (b) B-L in the monomolecular regime and L-L in the bimolecular regime and (c) L-L recombination at all temperatures. Transport is in extended states. Note that (a) and (c) require pinning of E_{Fo}, while (b) does not.

	(a) B-L	(b) B-L ⟶ L-L	(c) L-L
ΔE_m	$E_1 - E_F$	$E_1 - E_F$	$(E_1-E_F)-(E_2-E_v)$
ΔE_b	$\frac{1}{2}(E_2 - E_v)$	$E_2 - E_v$	$E_2 - E_v$
ΔE_τ	$(E_1-E_F)+(E_2-E_v)$	$(E_1-E_F)+(E_2-E_v)$	$E_1 - E_F$
E_σ	$E_F - E_v$	$E_F - E_v$	$E_F - E_v$

Table 8.10.1. comparison of different models for photoconductivity in As_2Te_3

Now, E_1 and E_2 can be found from the dark and steady state data, and the values used as a test of consistency to predict $\Delta E_{\tau m}$. The values so obtained are listed in table 8.10.2.

	(a) B-L	(b) B-L $\longrightarrow$ L-L	(c) L-L
$E_2 - E_v$	0.32 eV	0.16 eV	0.16 eV
$E_1 - E_v$	0.65	0.65	0.81
$E_F - E_v$	0.42	0.42	0.42
$\Delta E_{\tau m}$ (predicted)	0.55	0.39	0.39
$\Delta E_{\tau m}$ (measured)		0.55	

Table 8.10.2 comparison of energy values obtained from different photoconductivity models

Both (b) and (c) give a much smaller value for $\Delta E_{\tau m}$ than (a), and the measured value. The reason that B-L recombination can give $E_{\tau m} > E_{\sigma}$, is that only a small temperature dependent fraction of the total photo hole density - i.e. free holes, is involved in recombination into the temperature dependent recombination centre density.

It can also be shown that case (b) would result in an intermediate steady state region of slope + 0.07 eV or - 0.08 eV if the B-L $\longrightarrow$ L-L transition occurs at higher, or lower temperatures than that between mono and bimolecular conditions. Since the temperature of the latter transition is intensity

dependent, and that of the former is not, the absence of such a region argues against model (b).

Knowing $(E_2 - E_v)$ from model (a), some important parameters can be estimated from the data - i.e. N_v, N_2, μ_{po}, τ_{pm}, and lower limits for C_{p2}, using

$$\sigma_o = e\,\mu_{po}\,N_v = 1.1 \times 10^4\ \Omega^{-1}\ m^{-1} \qquad 8.10.3$$

$$\tau_{cm} = \left(\frac{N_2}{p_2}\right)\tau_{pm} = 1.0\ \mu s \qquad 8.10.4$$

$$\Delta I = we\mu_{po}\mathcal{E}\{\eta\tau_{pm}F(1-R_1)\} = 10^{-8}\ A \qquad 8.10.5$$

The room temperature data for ΔI and τ_{cm} are from figures 8.10 and 8.14, and equation 8.10.5 is for complete absorption.

From equation 8.10.3 the product $\mu_{po}N_v \approx 10^{23}\ m^{-1}\ V^{-1}\ s^{-1}$. According to Weiser and Brodsky[119] a value of $10^{26}\ m^{-3}$ is appropriate for N_v.

Substituting $N_v \sim 10^{26}$, gives the results

$$N_v \sim 10^{26}\ m^{-3}$$

$$N_2 \sim 3 \times 10^{24}\ m^{-3}$$

$$\mu_{po} \sim 10^{-3}\ m^2\ V^{-1}\ s^{-1}$$

$$\tau_{pm} \sim 10^{-9}\ s\ (295\ K)$$

and at room temperature

$$p_o \approx 6 \times 10^{19}\ m^{-3}$$

$$N_2\bar{f}_{20} \approx 6 \times 10^{22}\ m^{-3}$$

i.e. the ratio of free/trapped carriers, p_2/N_2 is $\sim 10^{-3}$. Note that in those calculations, p_2 was written as

$$p_2 \approx N_v \exp\left(\frac{\gamma}{3k}\right) \exp\left(-\frac{E_2 - E_v}{kT}\right)$$

including, as far as possible, the likely effects of gap dilation with temperature.

In section 8.13 room temperature noise spectra give an independent value for $N_2\bar{f}_{20}$ of $\sim 6 \times 10^{24}$ m^{-3}, so the above values are no longer merely estimates.

Estimates can be made for C_{p2} (σ_{p2}) if $\tau_{t2} < 10^{-9}$ sec giving

$$\sigma_{p2} > 10^{-21} \text{ m}^2$$

Again, this is a reasonable value for coulombic capture, and is also possible for capture by neutral centres, so it is not possible to check the type and density of any states near E_{Fo}, except that for pinning to occur, the density of charged states at E_F must be $> 6 \times 10^{22}$ m^{-3} or $> 3 \times 10^{24}$ m^{-3} if the states at E_2 are donor-like or acceptor like, respectively.

The low temperature 'break' in the steady state photocurrent could occur for one of three reasons; a change in transport mechanism; a change in recombination path; a change in the occupancy function for holetraps.

If hopping transport were to take over at low temperatures, then the break point temperature would be intensity independent assuming the Q.T.E. approximation

held, and this is clearly not so. Furthermore, the characteristic slope would be $+\frac{1}{2}(E_2 - E_v) - \Delta W_2$, or $-\frac{1}{2}(E_2 - E_v) + (E_3 - E_v) - \Delta W_3$ for hopping in states at E_2, or in a tail of depth $E_3 - E_v$, respectively. If ΔW_2 or $\Delta W_3 \sim 0.1$ eV, and $E_3 - E_v \sim 0.2$ eV, then the slopes would be + 0.06 eV or - 0.06 eV respectively, values which were not observed.

A change to L-L recombination would also occur at a fixed temperature, and would give a photocurrent vs $10^3/T$ slope of - 0.32 eV, neither of which was observed.

The last possibility seemed the most plausible - i.e. the hole trap quasi Fermi level E_{Ft}^p approaches E_2 as the temperature is reduced, and the quasi-thermal equilibrium statistic of equation 3.2.76 no longer holds. The position of the free hole Q.F.L. was calculated from the estimated ratio $\Delta p/p_o$ for each break point, and in each case

$$E_{Fp} \text{ (break)} - E_v \approx 0.3 \text{ eV}$$

As pointed out, a line drawn through the break points in figure 8.10 also has a slope of ~ 0.3 eV, in agreement with the above observation. Therefore this explanation seems plausible, if E_{Ft}^p and E_{Fp} are fairly close together.

A transition to linear intensity behaviour below the break temperature might be expected, if the trap quasi Fermi levels lie outwith the traps, but this was not observed in the temperature range covered. At the lowest temperature reached in this part of the investigation

(115 K), $\Delta I \propto F^{0.6}$ (approx). There are two possible explanations for this

(i) The trap level at 'E_2' is not discrete, but spread over some energy range

(ii) The trapped electron Q.F.L. E_{Ft}^{n} for the traps at E_1 is still <u>below</u> E_1 while the trapped hole Q.F.L. for traps at E_2 has 'passed through' the traps.

This latter situation is probably unlikely, as N_1 has to be rather greater than N_2, but can give a solution for Δp

$$\Delta p \propto \Delta G^{2/3} \exp(-\frac{E_c - E_1}{3kT}) \qquad 8.10.6$$

which is in reasonable agreement with the data, if $E_c - E_v \approx 1.0$ eV.

In either case, linear intensity behaviour would occur at still lower temperatures when the occupancies f_1 and $\bar{f}_2$ are controlled by recombination kinetics, and the photocurrent would become temperature independent.

The solution to the 4-level model, in this range, is (assuming B-L recombination)

$$\Delta p \approx \Delta G \left[\frac{N_1+N_2 + \{(N_1-N_2)^2 + 4N_1N_2C_{n2}C_{p1}/C_{p2}C_{n1}\}^{\frac{1}{2}}}{2N_1N_2C_{p1}}\right] \qquad 8.10.7$$

Unfortunately, this could not be verified experimentally.

The model, as developed, also allows a tentative explanation of the photocurrent field dependence being smaller than that of the dark current (Figures 8.6 and 8.11). Writing the bimolecular regime steady state photo hole density (equation 3.2.88) as

$$\Delta P_b \alpha \left(\frac{\Delta G \; p_2 \; (\mathcal{E})}{C_{p1} N_2} \right)^{\frac{1}{2}} \qquad 8.10.8$$

and noting that $p_2(\mathcal{E}) = p_2(0) \exp(a(T)\,\mathcal{E}/kT)$ 8.10.9

$$\text{or} \quad p_2(\mathcal{E}) = p_2(0) \exp(\beta \mathcal{E}^{\frac{1}{2}}/kT) \qquad 8.10.10$$

for a 'mobility edge shift' or Poole-Frenkel effect, respectively, the expected photocurrent field parameters are now $\frac{1}{2}$ a(T) or $\frac{1}{2}\beta$. The values appropriate to the dark conductivity are a(T) or β (possibly $\frac{1}{2}\beta$, if E_F is not pinned, and $N_1 \approx N_2$).

The measured values of a(T) (photo) are slightly greater than $\frac{1}{2}$ a(T) (dark), but the general behaviour does seem to be in agreement with the mobility edge shift hypothesis and the kinetic analysis. Note that L-L recombination would not give this result.

In physical terms, the field increases the free hole density - automatically increasing the recombination rate, and thus halving the effect (a kind of field "quenching"). In the dark, the generation rate is effectively increased also, so the full effect is observed.

8.11 'PHOTO-MOBILITY'

As pointed out in 3.3.3, 3.3.4, and 4.9.3, measurements of the growth of photocurrent at sufficiently short times can enable recombination effects to be ignored, allowing investigation of trapping effects. It was mentioned that such measurements may also reveal fast trapping states other than those controlling the steady state photo-

conductivity, and this was infact observed experimentally.

The experimental set up was the same as that used for photodecay measurements, with the same limitations on excitation and instrumental rise times. The excitation source was the GaAs laser, driven with 5 A, 200 ns pulses, at room temperature (photon flux density 3.5×10^{22} photons m^{-2} s^{-1}, rise time < 5 ns). Instrumental rise time was measured as 30 ns (10 - 90%). As the photocurrent rise time was typically greater than 200 ns, recombination can be neglected at shorter times. In practice, the 'initial slope' was obtained for 80 ns < t < 100 ns, a reasonable compromise. Figure 8.16 is the pulse photoresponse for a 0.1 μs laser pulse, showing the near-linearity of the rise at these short times.

Using equation 3.3.15, the trap limited drift mobility, under these experimental conditions, is

$$\mu_d = \frac{\frac{d}{dt}(\Delta I)_{t\approx 0}}{e\mathcal{E}w\eta F(1 - R_1)} \qquad 8.11.1$$

Figure 8.17 shows $\log(\mu_d)$ vs $10^3/T$ at different applied fields from 4×10^6 V m^{-1} to 1.4×10^7 V m^{-1}.

At low fields, above 200 K, the mobility is clearly activated, with activation energy $E_\mu = 0.20$ eV, and a room temperature value of $\sim 3.5 \times 10^{-6}$ m^2 V^{-1} s^{-1}. The figure also shows a reduction of activation energy with field, to ~0.1 eV at 1.4×10^7 V m^{-1}, and curvature to lower slope, at all fields, below about 160 K.

The low field data could be interpreted as band-transport with trapping in a discrete trap level at

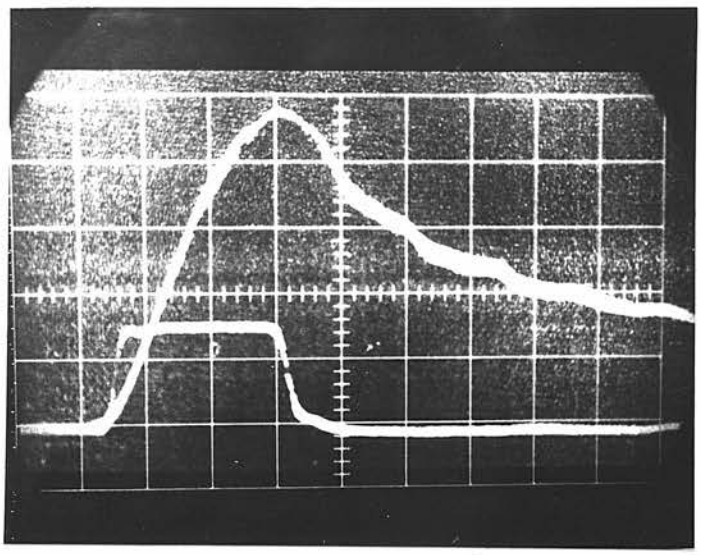

Fig 8.16 As_2Te_3 Photorise: response to 100 ns laser excitation pulse

vertical scale 2 μA/cm
horizontal scale 40 ns/cm

laser drive pulse 5A/cm

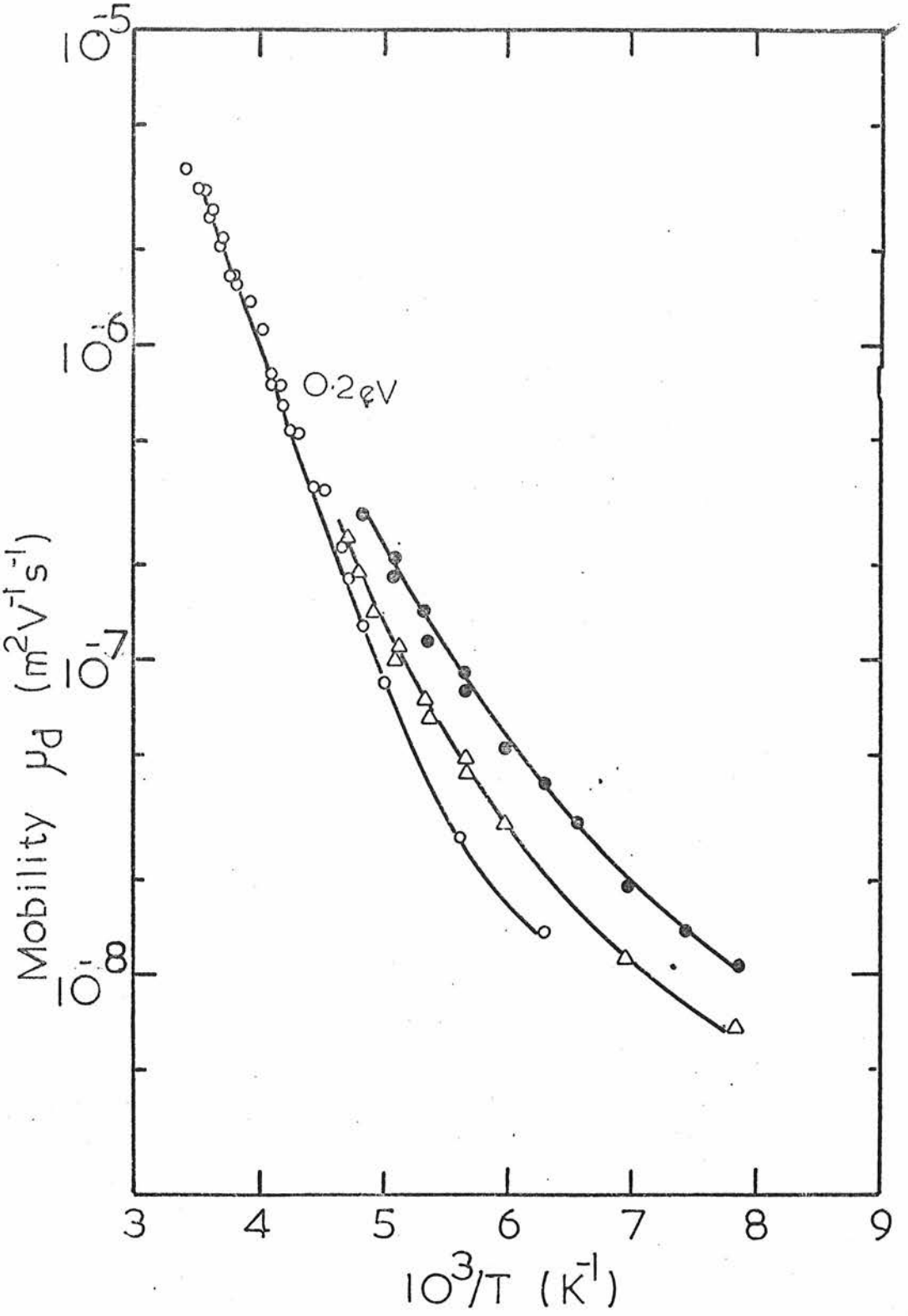

Fig 8.17 As_2Te_3 Photoderived mobility μ_d vs $10^3/T$

Electric field V/m ∘ 4.0 10^5 • 1.4 10^7 △ 4.0 10^6

energy E_3, 0.2 eV above the valence band edge. Its density is obtained from equation 2.1.6, including an estimate of gap dilation - i.e.

$$\mu_d = \mu_{po}(N_v/N_3) \exp[-(E_3 - E_v)/kT] \exp(\gamma/5\ k)$$

giving

$$N_3 \approx 3.2 \times 10^{24}\ m^{-3}$$

Alternatively, the low field data agree very well with trapping in a linear tail of localised states, extending $(E_3 - E_v) \approx 0.20$ eV into the gap, giving a drift mobility

$$\mu_d = \mu_{po}[(E_3 - E_v)/kT] \exp(\gamma/5\ k) \exp[-(E_3 - E_v)/kT]$$

i.e. $\mu_{po} = 4 \times 10^{-4}\ m^2\ V^{-1}\ s^{-1}$ in good agreement with the estimate of 8.10.

Although the high field data above 160 K show a reduction in activation energy, apparently in rough agreement with that predicted by Poole-Frenkel or mobility edge effects, from <u>conductivity</u> data, the field dependence of μ_d at fixed temperature, is less than that of the conductivity. At present, this is unexplained, as is the curvature in the $\log(\mu_d)$ vs $10^3/T$ dependence at low temperatures. It is possible, that even for such shallow states, the quasi thermal equilibrium approximation breaks down, at high laser excitation levels, and low temperatures.

The mobility results are interpreted, then, in terms of trapping in a band tail, extending 0.2 eV into the

forbidden gap. The trapping time must be extremely short, probably less than 10^{-10} s, but it cannot be ascertained whether this corresponds to a single capture by states at the tail extremity, or multi-step thermalisation.

Several points can be made about the method employed to measure mobility. It is comparable with transit-time techniques in that the motion of carriers is monitored at times short enough to avoid recombination effects. The excitation is applied uniformly between the electrodes, so diffusion effects (in the y-direction) are also avoided.

Perhaps the most significant feature of the method is that mobilities can be measured in high conductivity chalcogenides with short dielectric relaxation times. Such materials are not amenable to the conventional Haynes-Shockley method[169] because of the low mobilities involved, nor to the "Spear' transit time technique[54] because of the very short recombination times.

The limitations of the method are that a direct transit time is not measured, and the absolute generation rate ΔG, must be known. This requires the additional knowledge of optical absorption and quantum efficiencies of the material, and also, absolute calibration of the source intensity.

It should be pointed out that although the analysis carried out here is in terms of trap-limited band motion, the technique applies equally to other mechanisms, such as hopping.

8.12 LOW TEMPERATURE PHOTODECAY

The analysis of section 3.3 for the decay of excess hole density in the high excitation (bimolecular) regime assumed that the hole traps at E_2 remained in 'contact' with the valence band throughout the decay, and predicted a hyperbolic decay - i.e.

$$\Delta p(t) = \Delta p_{ss}/(1 + \Delta p_{ss}\,\theta\, t) \qquad 8.12.1$$

The decay time (to half-value) is

$$\tau_{cb} = (\Delta G\ \theta\ p_2/N_2)^{-\frac{1}{2}} \qquad 8.12.2$$

for B-L recombination (path 1) τ_{cb} should <u>increase</u> with 1/T, with activation energy $\frac{1}{2}(E_2 - E_v)$ (i.e. 0.16 eV), while for L-L recombination, τ_{cb} should be temperature independent. The <u>observed</u> behaviour, on figure 8.14 - i.e. τ_{cb} <u>decreasing</u> with 1/T, does not agree with either mechanism, for this simple analysis, but is somewhat closer to the L-L prediction. It is therefore necessary to show how B-L mechanisms can give rise to this behaviour, as L-L recombination has been discounted.

The first improvement to the analysis of 3.3 is to include spatial effects associated with absorption, as was done for the steady state case. Thus, by expressing

the terms in 8.12.1 as functions of depth x, and integrating through the sample thickness, (assuming complete absorption) the decay of the excess hole density per unit area $\Delta P_A(t)$, is

$$\Delta P_A(t) = \frac{2}{\alpha\theta t} \log \left[1 + (\theta \Delta G(0) p_2/N_2)^{\frac{1}{2}} t \right] \qquad 8.12.3$$

where $\Delta G(0) = \eta \alpha F(1 - R)$

This gives a decay time $\approx 3 \, (N_2/p_2 \, \theta \, \Delta G(0))^{\frac{1}{2}}$

i.e. three times longer than the time obtained assuming homogeneous excitation, but with the same temperature dependence.

The proposed explanation for the 'anomalous' temperature dependence of τ_{cb}, is shown in figure 8.18. The simple analysis of 3.3, implies that, as emptying of traps at E_2 keeps pace with recombination, the trapping time τ_{t2} is shorter than the free hole lifetime τ_p. At low temperatures, τ_p decreases as is evidenced by the decrease in photocurrent ($\Delta I = \Delta G \, \tau_p$). This is due to the increasing occupation of recombination centres at E_1. On the other hand, unless the traps at E_2 become appreciably occupied, τ_{t2} remains roughly constant.

Thus, below some temperature T_x, the free recombination time τ_{pb}, becomes shorter than τ_{t2}, and much of the excess free hole density can decay before the traps at E_2 begin to empty. Shallower traps, such as the tail states, with short trapping time (τ_{t3}, say) may keep pace with the decay, so that the effective decay time is still much longer than the true free lifetime.

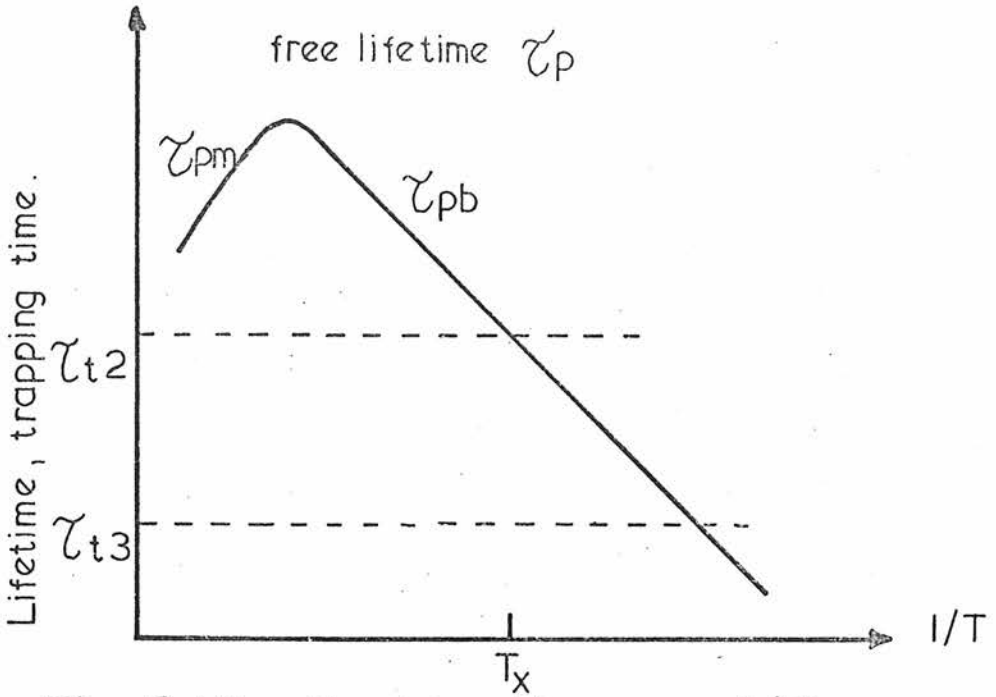

Fig 8.18 Capture times vs 1/T

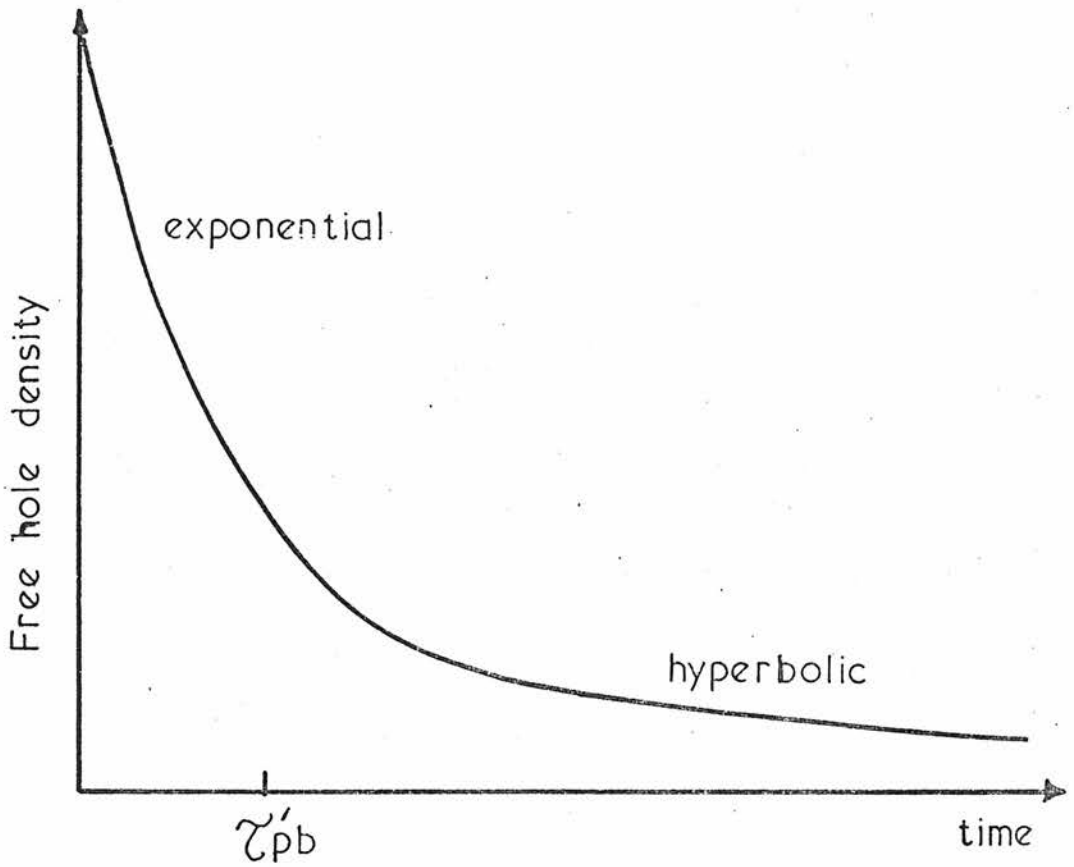

Fig 8.18a Photodecay $\tau_{t3} < \tau_{pb} < \tau_{t2}$

Figure 8.18a shows the expected form of the decay, when $\tau_{t3} \ll \tau_{pb} \ll \tau_{t2}$. The initial rapid fall is exponential, if the occupation of the recombination centres $N_1 \ \Delta f_1$ ($\approx N_2 \ \Delta \bar{f}_2$) is much greater than the excess density in the valence band and band-tail. The time constant τ'_{cb} is

$$\tau'_{cb} \approx N_3 (N_v N_2 C_{p1} \Delta G)^{\frac{1}{2}} \exp[\{(E_3 - E_v) - \tfrac{1}{2}(E_2 - E_v)\}/kT] \quad 8.12.4$$

where N_3 is the effective 'discrete' density of the tail states. In this rapid decay, the free hole density drops to a value $\Delta p'$, when the release rate from traps at E_2, not much altered from its steady state value, matches the recombination rate.

$$\text{i.e. } \Delta p' \approx p_2 \ C_{p2}/C_{p1}$$

and the subsequent decay is a long hyperbolic tail.

Although equation 8.12.4 predicts a small <u>positive</u> activation energy (~ 0.04 eV), the absolute value of τ'_{cb} is much smaller than the decay time predicted by the simple theory, τ_{cb}. Hence in the temperature region near T_x, the decay time will fall with reducing temperature as the ratio of the amplitudes of the fast/slow portions of the decay increases.

The ratios of the three time τ_p, τ'_{cb} and τ_{cb} for $F = 9 \times 10^{19}$, are, at say 150 K, using the energy and density values already obtained

$$\tau_{cb}/\tau'_{cb} \approx (N_2/N_3) \exp[+(E_2 - E_3)/kT] \approx 2 \times 10^2$$

$$\tau'_{cb}/\tau_{pb} \approx (N_3/N_v) \exp[+(E_3 - E_v)/kT] \approx 2 \times 10^6$$

Values estimated from figure 8.14, are, at 150 K, $\tau_{cb} \approx 4 \times 10^{-2}$ s, τ'_{cb} (measured) $= 2 \times 10^{-4}$ s, $\tau_{pb} \approx 2 \times 10^{-11}$s, in rough agreement with the above argument.

8.13 CONDUCTIVITY FLUCTUATIONS

The 3-level analysis for conductivity fluctuations, carried out in chapter 5, predicted two relaxation modes or 'bumps' in the current noise spectra. The slower mode, associated with recombination, accounts for only a small fraction of the free carrier variance, and has a characteristic 'turnover' time equal to the small signal photodecay time τ_{cm}.

Figure 8.19 shows typical current noise spectra, at three temperatures, for sample C-20 at an applied voltage of 10 V ($\mathcal{E} = 4 \times 10^5$ V m^{-1}). The diffuse bump which can be seen in each spectrum is the recombination mode, superimposed on a featureless background noise, probably due to contact effects.

Figure 8.20 compares the temperature dependence of the 'turnover' time constant, with the photodecay time τ_c, (at $F = 2.4 \times 10^{19}$ photons m^{-2} s^{-1}). There is good agreement for the small-signal case as expected, but the photodecay time at 242 K is shorter than the 'turnover' time, as the small signal approximation no longer applies.

Before making any quantitative estimates, the effect of an additional participating 'level' - the proposed band tail, must be assessed. An analysis may be carried out, along the lines of the 3-level analysis, but

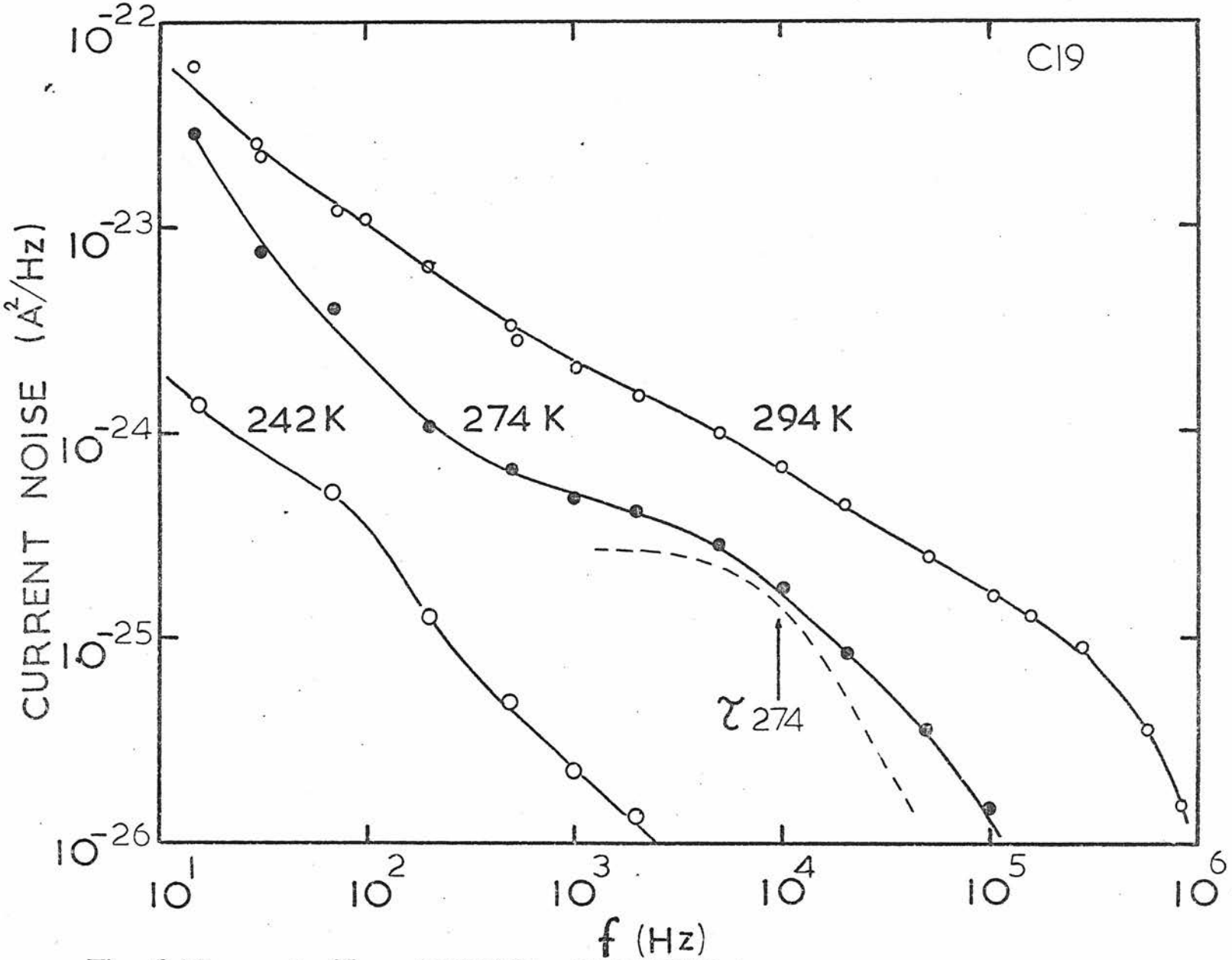

Fig 8.19 As_2Te_3 NOISE SPECTRA

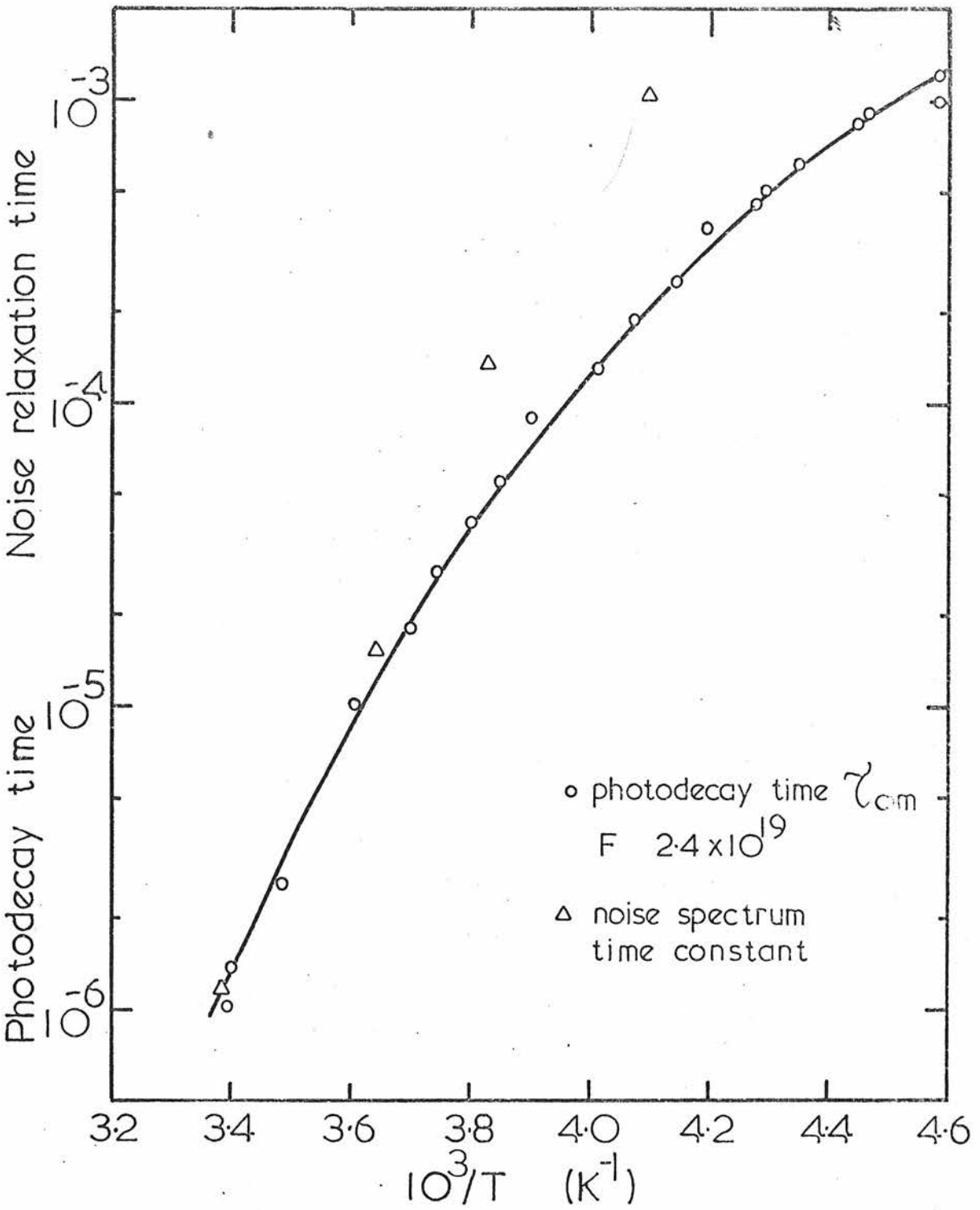

Fig 8.20 As_2Te_3 Comparison of low intensity photodecay time with noise spectra turnover times.

assuming that the (band + band tail) constitute one reservoir. (i.e. using the Q.T.E. approximation).

Most of the variance is due to band tail trapping and release, while the result of 5.5 is slightly modified, to

$$S_i(f) = \frac{4I_o^2}{P_o}\left(\frac{\tau_{pm}}{1+\omega^2\tau_{cm}^2} + \frac{\tau_{t2}}{1+\omega^2\tau_{t2}'^2} + \text{band tail term} \right) \quad 8.13.1$$

i.e. the recombination mode is unaffected, (if the occupation of the tail is less than the occupation of traps at E_2) but the turnover time for the trapping mode is increased to $\tau_{t2}' = \tau_{t2} \times \tau_{tr3}/\tau_{t3}$, where the subscript 3 refers to band tail trapping and release.

The plateau value of the recombination mode may be written as

$$\frac{4I_o^2\tau_{pm}}{P_o} = \frac{4I_o^2\tau_{cm}p_2}{p_o\ wld.N_2} = \frac{4I_o^2\tau_{cm}}{N_2 f_{20}.wld} \quad 8.13.2$$

which for the room temperature plateau value of $\approx 2 \times 10^{-25}$ A^2 Hz^{-1}, and $\tau_{cm} \approx 10^{-6}$ s, gives for the trap occupation at 294 K,

$$N_2 f_{20} = 6 \times 10^{22}\ m^{-3}$$

in excellent agreement with the estimate from photoconductivity results. Note that this result is <u>independent</u> of an estimate for N_v, so it supplies the required additional information (a fourth equation) to <u>verify</u> the estimates of trap parameters made earlier.

8.14 MODEL FOR As_2Te_3

The band model of figure 8.21 shows the distribution of localised states identified in this work, and some of the estimated parameters are listed below.

Energy (eV)		Density (m^{-3})	Capture coefficient ($m^{-3}\ s^{-1}$)
E_v	0	$N_v = 10^{26}$	
E_3	0.2	$N_3' = 3 \times 10^{25}$	
E_2	0.32	$N_2 = 3 \times 10^{24}$	$C_{p2} \geqq 10^{-16}$
E_f	0.42	$N_F \geqq 6 \times 10^{22}$	
E_1	0.65	$N_1 \lesssim 3 \times 10^{24}$	$C_{p1} \approx 10^{-14}$
E_c	1.0		

Free hole mobility $\mu_{po} \approx 10^{-3}\ m^2\ V^{-1}\ s^{-1}$

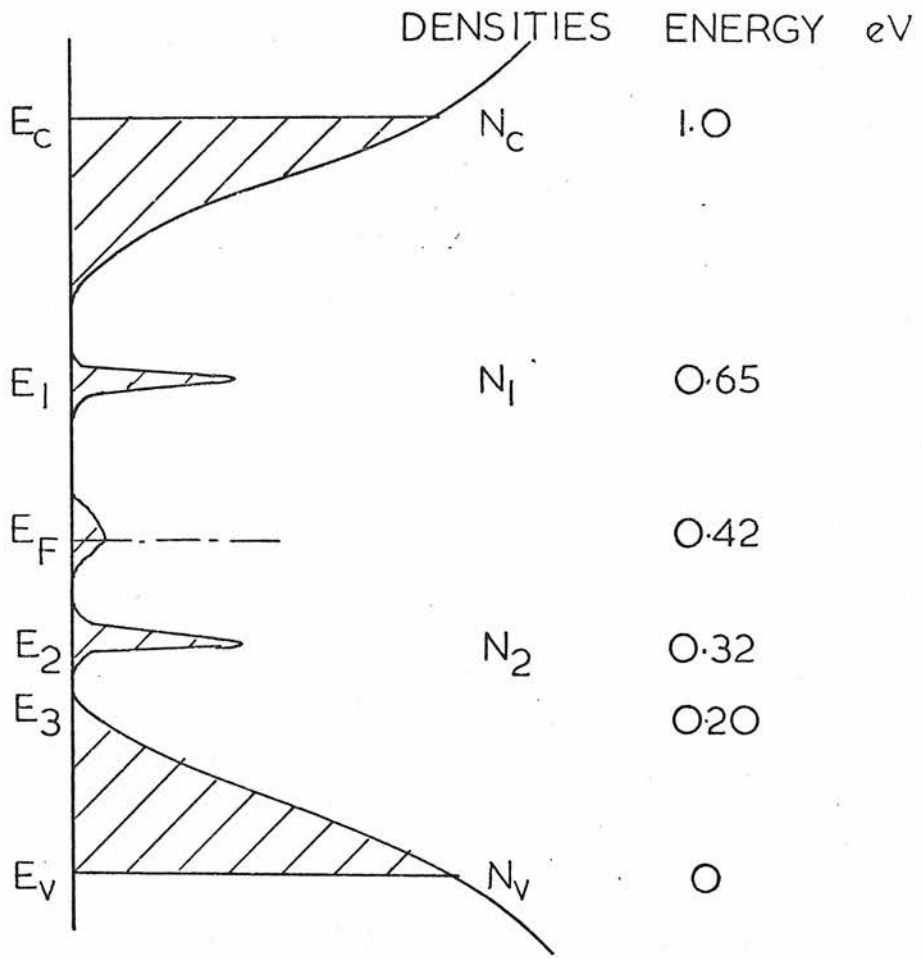

Fig 8.21 As_2Te_3 Schematic band diagram

CHAPTER 9

AMORPHOUS As_2Se_3 : EXPERIMENTAL RESULTS AND DISCUSSION

9.1 INTRODUCTION

In many respects the behaviour of As_2Se_3, and its interpretation are formally very similar to that of As_2Te_3, although there are differences of scale, e.g. in energies, and decay times. This may seem surprising, but it can only be stated that the experimental results obtained argue for such similar interpretations.

9.2 SAMPLES

Thin film samples were produced in the same way as the As_2Te_3 samples, for electrical and optical work. The thickness range was

Sample	
C-2	2.10 μm
C-7, C-8	0.87 μm
C-21, C-22	2.56 μm
C-23, C-24	1.35 μm

X-ray fluorescence measurements on films deposited in the same evaporation as C-7 and C-8 revealed a composition very close to As_2Se_3 - i.e. $As_{39}\ Se_{61}$. Again, the electrical properties of the other films were very similar to those of C-7 so that the results were taken to be typical of As_2Se_3.

9.3 OPTICAL PROPERTIES

Optical transmission measurements were made on thin films of As_2Se_3 at 298 K and 104 K. Figure 9.1 shows the optical absorption constant vs photon energy, obtained for samples made in the same evaporation as C-7 (0.87 μm) and C-22 (2.56 μm).

Again there was a reasonable fit to the quadratic relation of equation 3.1.9 demonstrated by figure 9.2, which shows $(\alpha h\nu)^{\frac{1}{2}}$ vs $h\nu$. The value of E_{opt} at 298 K and 104 K, is 1.86 eV and 1.97 eV respectively, and assuming a linear temperature dependence the temperature coefficient is $\gamma = -5.8 \times 10^{-4}$ eV K^{-1}, in reasonable agreement with Edmonds' value of -7×10^{-4}. The extrapolated value for E_{opt} (0K) is 2.03 eV, but 2.0 eV is probably closer to the actual zero temperature gap. This is somewhat higher (by about 0.1 eV) than values previously obtained[149,150].

The refractive index obtained from interference fringes near the absorption edge varied between 3.3 to 3.4, for different samples. This gives a calculated air-film reflectance $R_1 \sim 0.28$, in reasonable agreement with the measured value of 0.26.

9.4 DARK CONDUCTIVITY

D.C. dark conductivity measurements were made on thin film samples with coplanar gold electrodes, of similar geometry to the As_2Te_3 samples - i.e. gap width $l = 25$ μm, electrode width $w \approx 4.5$ mm. Room temperature conductivities were much lower than for As_2Te_3, and slow

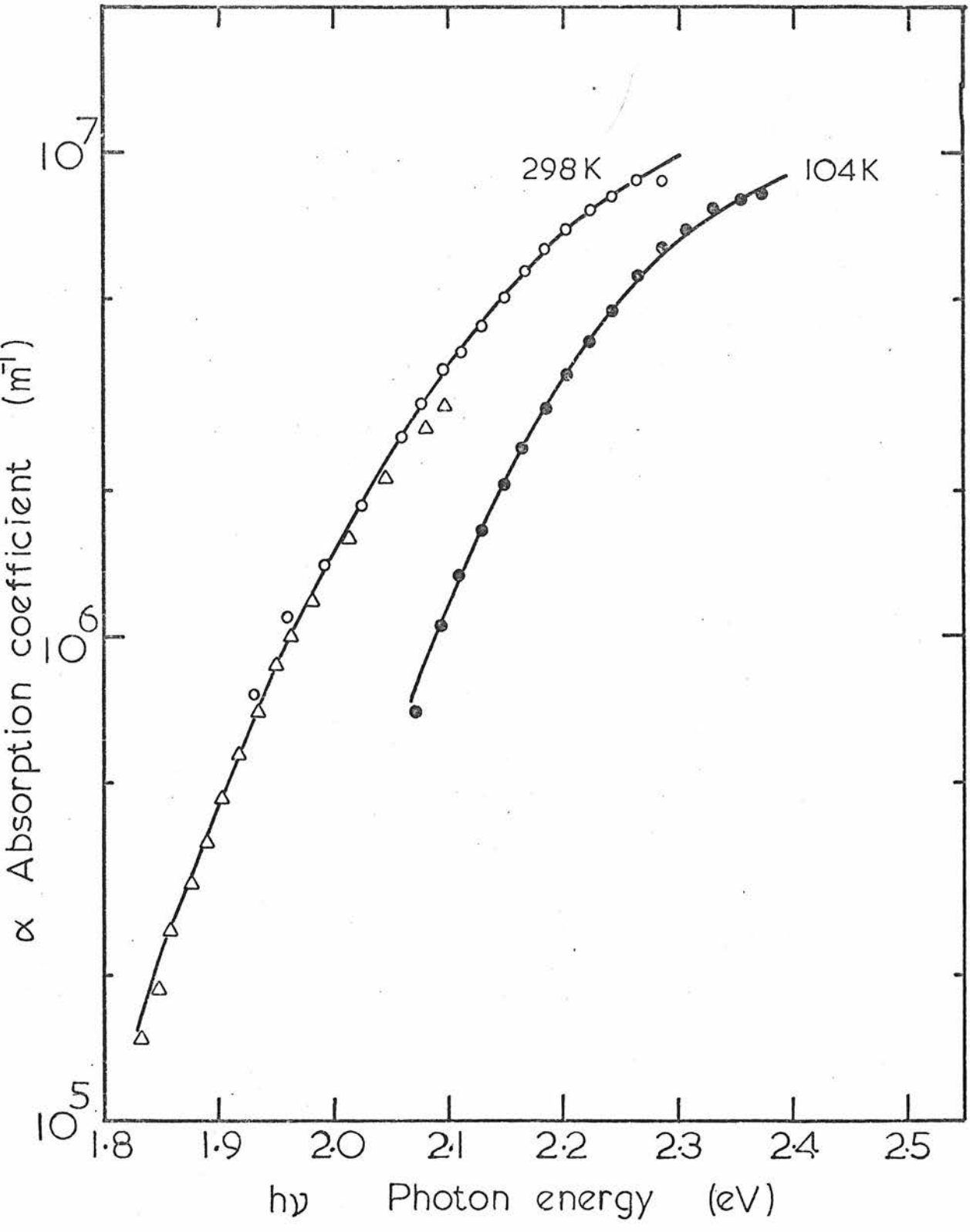

Fig 91 As_2Se_3 Absorption coefficient α vs Photon energy at two Temperatures

thickness : 0·87μm △ 2·56μm

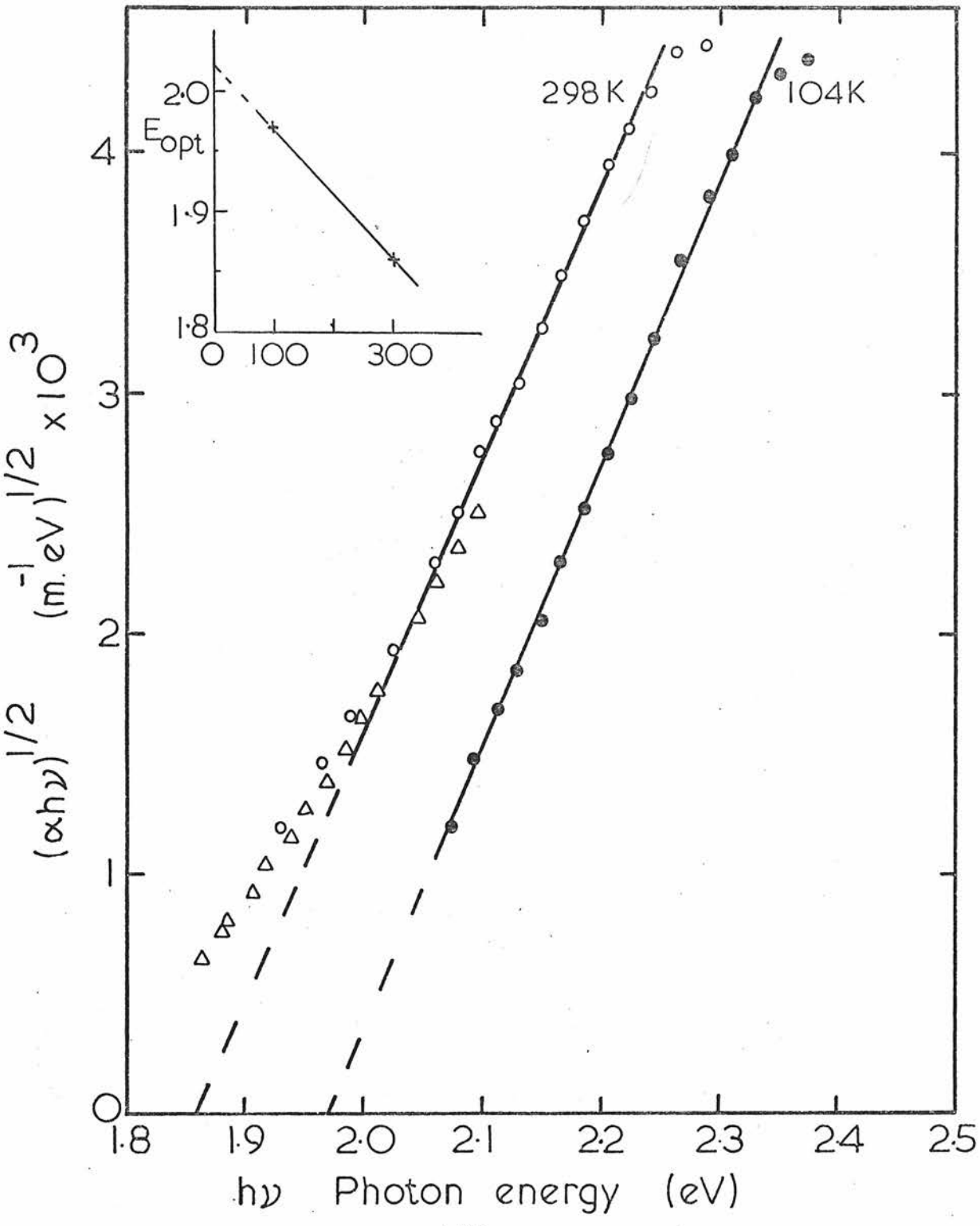

Fig 9.2 As_2Se_3 $(\alpha h\nu)^{1/2}$ vs Photon energy

thickness ○ 0·87 μm △ 2·56 μm

relaxation effects made measurements difficult. In addition, after exposure to light, a residual excess conductivity could persist for many hours, at room temperature. This is a typical problem in wide gap semiconductors probably associated with carrier release from very deep traps. Samples therefore had to be 'rested' in darkness, for some hours, prior to measurement.

Room temperature conductivities measured at low field, $\mathcal{E} < 4 \times 10^5$ V m^{-1}, nevertheless agreed very well with values reported for bulk As_2Se_3 [65] i.e.

Sample	d	σ (Ω^{-1} m^{-1})
C-2	2.1 μm	9.6×10^{-11}
C-7	0.87 μm	6.5×10^{-11}
C-8	0.87 μm	7×10^{-11}
C-22	2.56 μm	7×10^{-11}
C-23	1.35 μm	1×10^{-10}

Figure 9.3 shows a plot of $\log \sigma$ vs $10^3/T$ at low applied field (4×10^4 V m^{-1}), for samples C-7, C-8 and C-22. The relation is again of the form

$$\sigma = C \exp(- E_\sigma/kT)$$

with E_σ = 0.92 eV, in good agreement with Edmond's and Marshall's results [40,20], and $C \approx 3.8 \times 10^5$ Ω^{-1} m^{-1}, also a typical value. If conduction is by free holes, then $C \approx \sigma_o \exp(\gamma/2\ k)$ giving $\sigma_o \approx 1.3 \times 10^4$ Ω^{-1} m^{-1}, a value indicative of transport by a diffusive mechanism in states near the mobility edge.

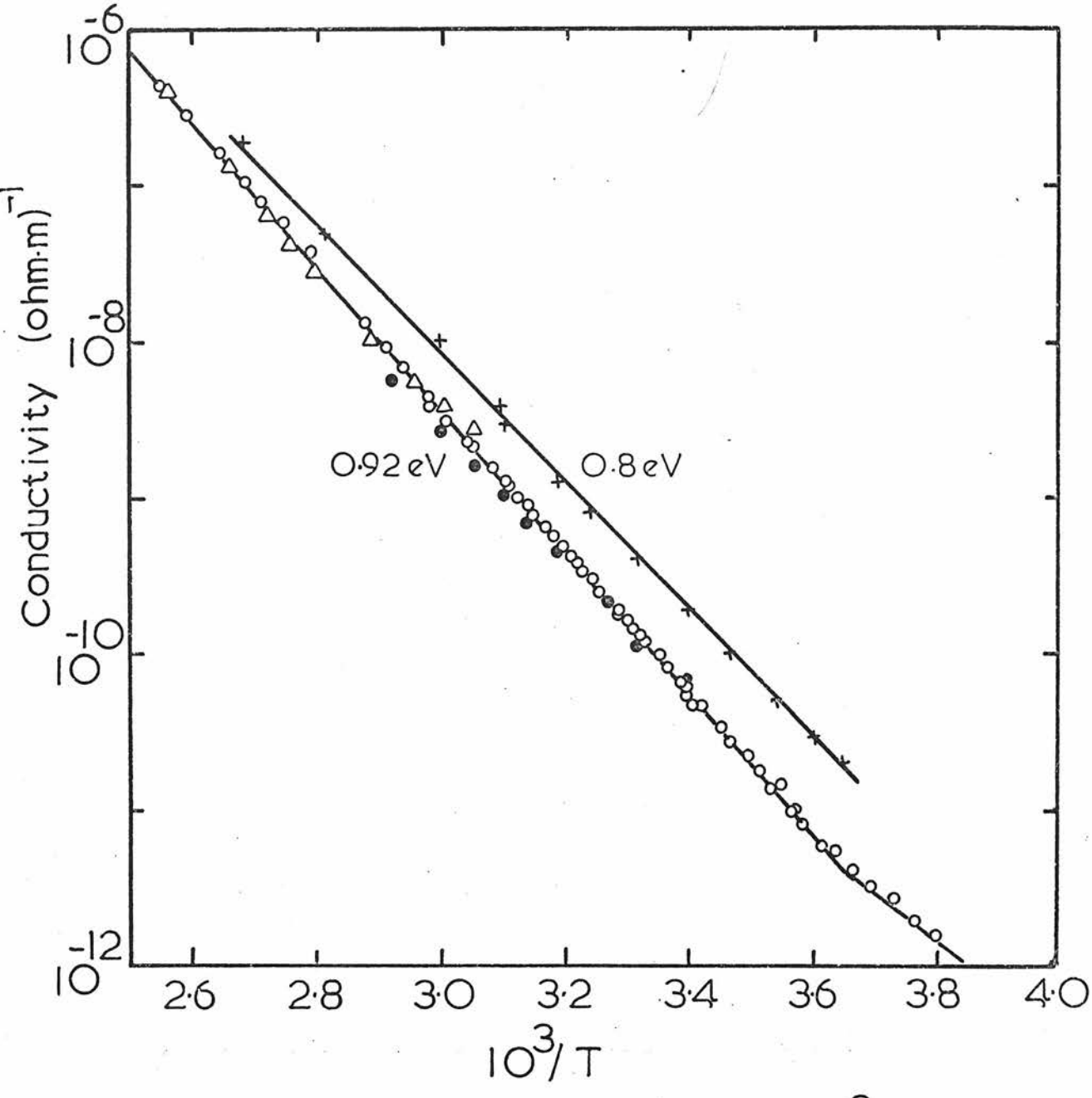

Fig 9 3 As_2Se_3 log conductivity vs $10^3/T$ at low and high fields

low field
4×10^4 V/m
∘ C_7
△ C_8
• C_{22}

high field
$1{\cdot}2 \times 10^7$ V/m
× C_7

9.5 HIGH FIELD CONDUCTIVITY

Only very cursory measurements were made at high fields, initially to determine the range of field over which the samples were 'ohmic'. Again, a number of mechanisms were considered, to account for the increase in conductivity at high fields.

Figure 9.4 is a plot of $\log \sigma$ vs $\mathcal{E}^{\frac{1}{2}}$, for several temperatures, to determine whether the Poole-Frenkel effect is responsible. Although there are very few data points, some curvature to lower slope is evident at most temperatures, below $\sim 10^{7}$ V m^{-1}, at least. This is predicted by the 3-dimensional treatments of the problem[73,74].

If a slope is taken from the high field portion ($\mathcal{E} > 8 \times 10^{6}$ V m^{-1}), a value of 1.3 - 1.5 eV V$^{-\frac{1}{2}}$ m$^{\frac{1}{2}}$ is obtained over the temperature range 298 - 373 K.

The measured refractive index of 3.3 gives a high frequency dielectric constant of ~ 11, and a theoretical value for β, on a one dimensional analysis, of $\sim 2.3 \times 10^{-5}$ eV V$^{-\frac{1}{2}}$ m$^{\frac{1}{2}}$. The experimental value is thus somewhat lower than that predicted by the one-dimensional theory, but in rather better agreement with a full three-dimensional treatment.

It was found again, however that a $\log \sigma$ vs $\mathcal{E}^{1}$ plot gave a much better straight-line fit of the data over the whole field range used in agreement with the observation of de Wit and Crevecoeur[65]. Figure 9.5 illustrates this for the data of figure 9.4. The form is

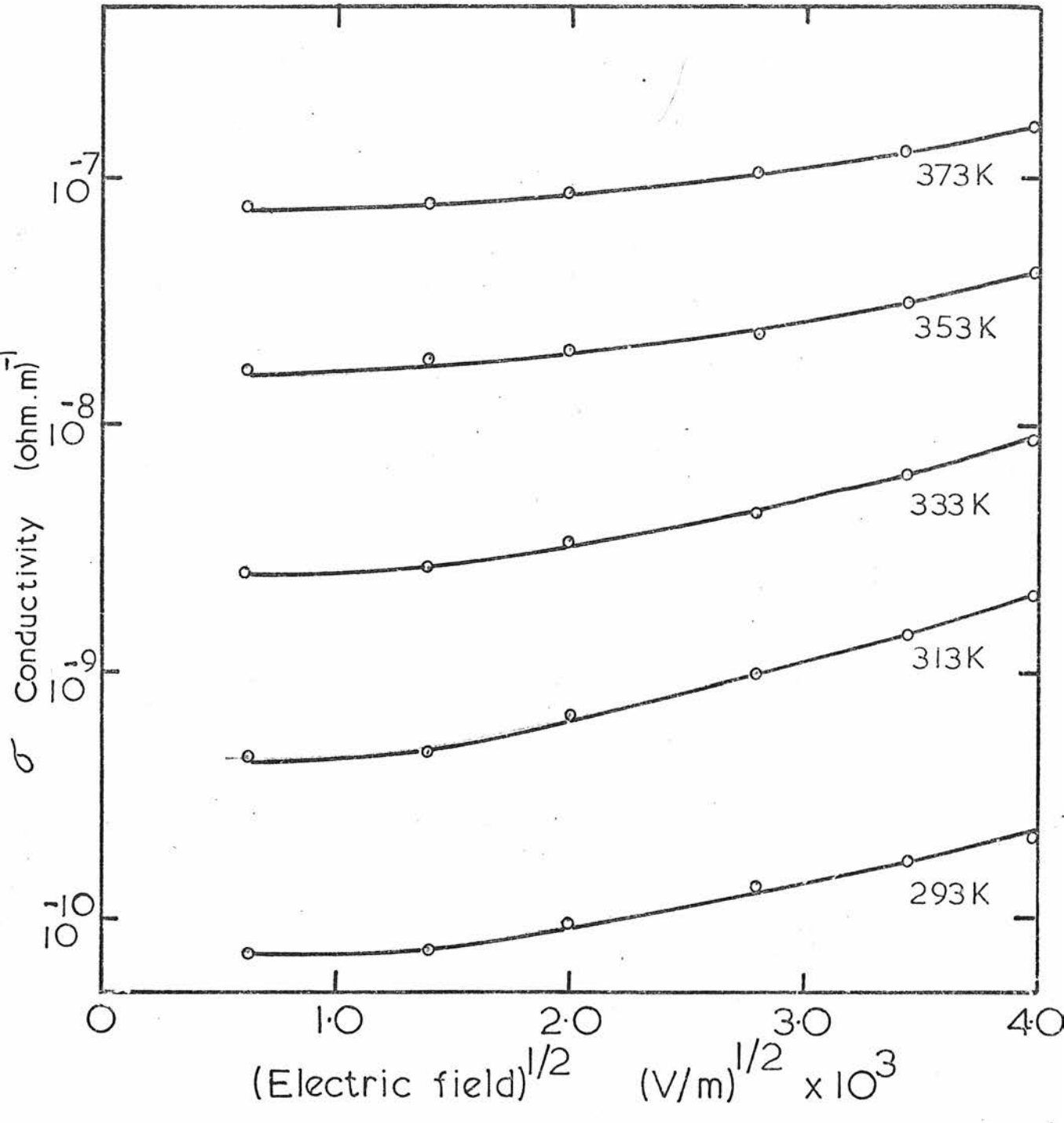

Fig 9.4 As_2Se_3 log conductivity vs (electric field)$^{1/2}$ at different Temperatures

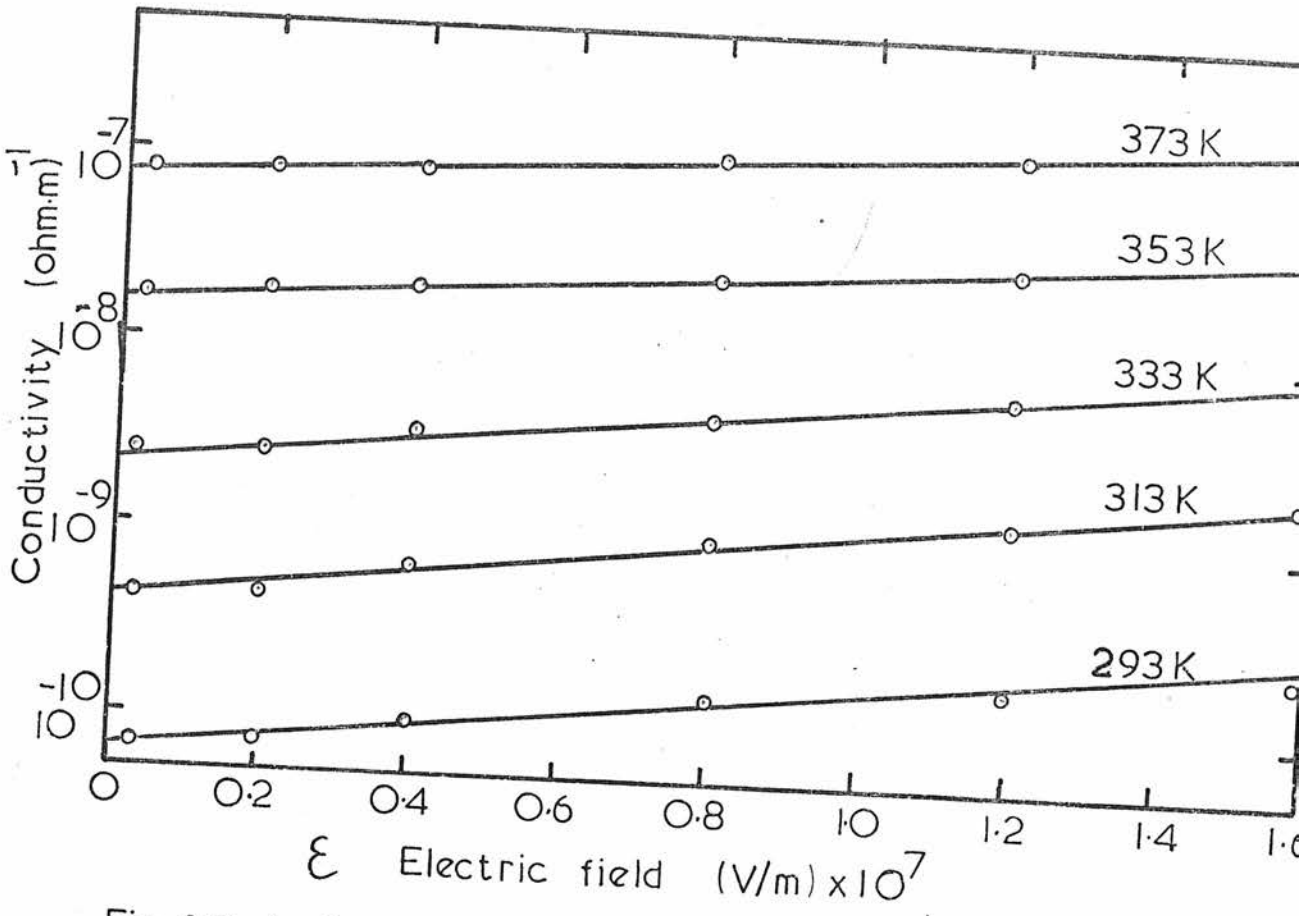

Fig 9.5 As_2Se_3 log conductivity vs electric field strength

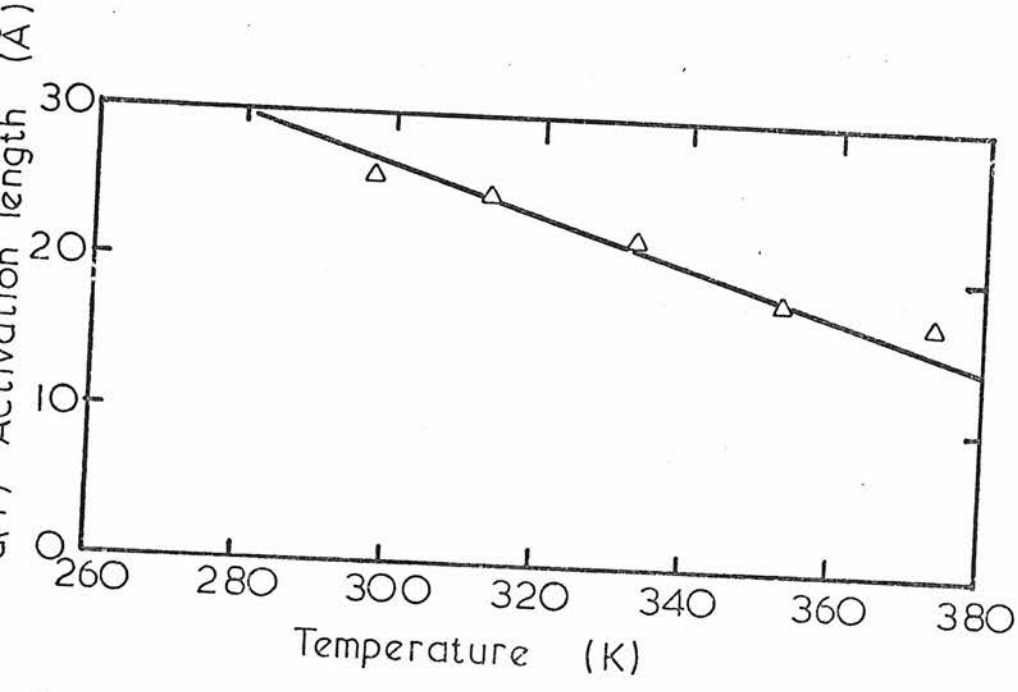

Fig 9.5a Activation length vs Temperature

As_2Se_3

$$\sigma(\mathcal{E}) = \sigma_o \exp[-\{E_\sigma - e\, a(T)\, \mathcal{E}\}/kT]$$

and figure 9.6 shows a(T) vs T, for sample C-8, giving a room temperature value between 20 Å and 30 Å, although the data are not as accurate as the data for As_2Te_3.

Figure 9.3 includes the temperature dependence of the high field conductivity, at $\mathcal{E} = 1.2 \times 10^7$ V m^{-1}, for sample C-7 showing a reduction in activation energy, by 0.12 eV, to 0.8 eV. This implies an extrapolated value of $a(0) \approx 80 - 100$ Å which seems rather high when compared with the data of figure 9.6, but which is perhaps a more accurate estimate.

Field enhanced band-tail hopping was again considered as a possible mechanism, and discounted for the same reasons as applied to As_2Te_3. The value of σ_o (1.3×10^4 Ω^{-1} m^{-1}) implies extended state conduction, while the hopping distance must be large - i.e. ≥ 20 Å. The hyperbolic sine behaviour predicted below $\sim 5 \times 10^6$ V m^{-1} was not observed in this work, nor in the work of de Witt and Crevecoeur[65].

It is possible that field induced delocalisation of shallow localised states is responsible for the high field behaviour of As_2Se_3 - i.e. the 'mobility edge' effect discussed in 2.2.5.

9.6 PHOTOCONDUCTIVITY : SPECTRAL RESPONSE

The spectral response of a number of co-planar As_2Se_3 samples was measured, over a range of temperature

(294 - 373 K) and electric field (4×10^5 - 1.6×10^7 V m^{-1}). It was found that under the conditions of temperature and excitation employed, bimolecular recombination prevailed, and this was taken into account when the 'raw' data were normalised to photocurrent per unit incident photon flux.

Figure 9.6 shows the normalised response at low applied field ($\mathcal{E} = 4 \times 10^5$ V m^{-1}). For sample C-8 (0.87 μm thick) at 294 K and 373 K. (Measurements were also made at 314, 333, and 353 K, but are omitted, for clarity). The shape of the spectral response, rising with photon energy, to a peak, and falling off at higher photon energies, is similar to the response of As_2Te_3, in the bimolecular recombination regime.

It is again proposed that the fall off at high photon energies is associated with a reduction of the bimolecular bulk lifetime τ_{pb}, with decreasing absorption depth. Writing equation 8.5.7 as

$$\Delta I = we\mu_{po} \ (4\eta F(1-R_1)/\theta)^{\frac{1}{2}} \ Z(\alpha,d) \qquad 9.6.1$$

$Z(\alpha,d)$ represents the effects of changing α on the generation rate and lifetime in a sample. Figure 9.7 shows $Z(\alpha,d)$ vs α, for two thicknesses, 0.87 μm and 1.35 μm. The function first increases with α, as more photons are absorbed, but eventually decreases, as the bimolecular lifetime falls, with decreasing absorption depth. Returning to figure 9.6, the relative low field quantum efficiency η, at 294 K and 373 K is also shown,

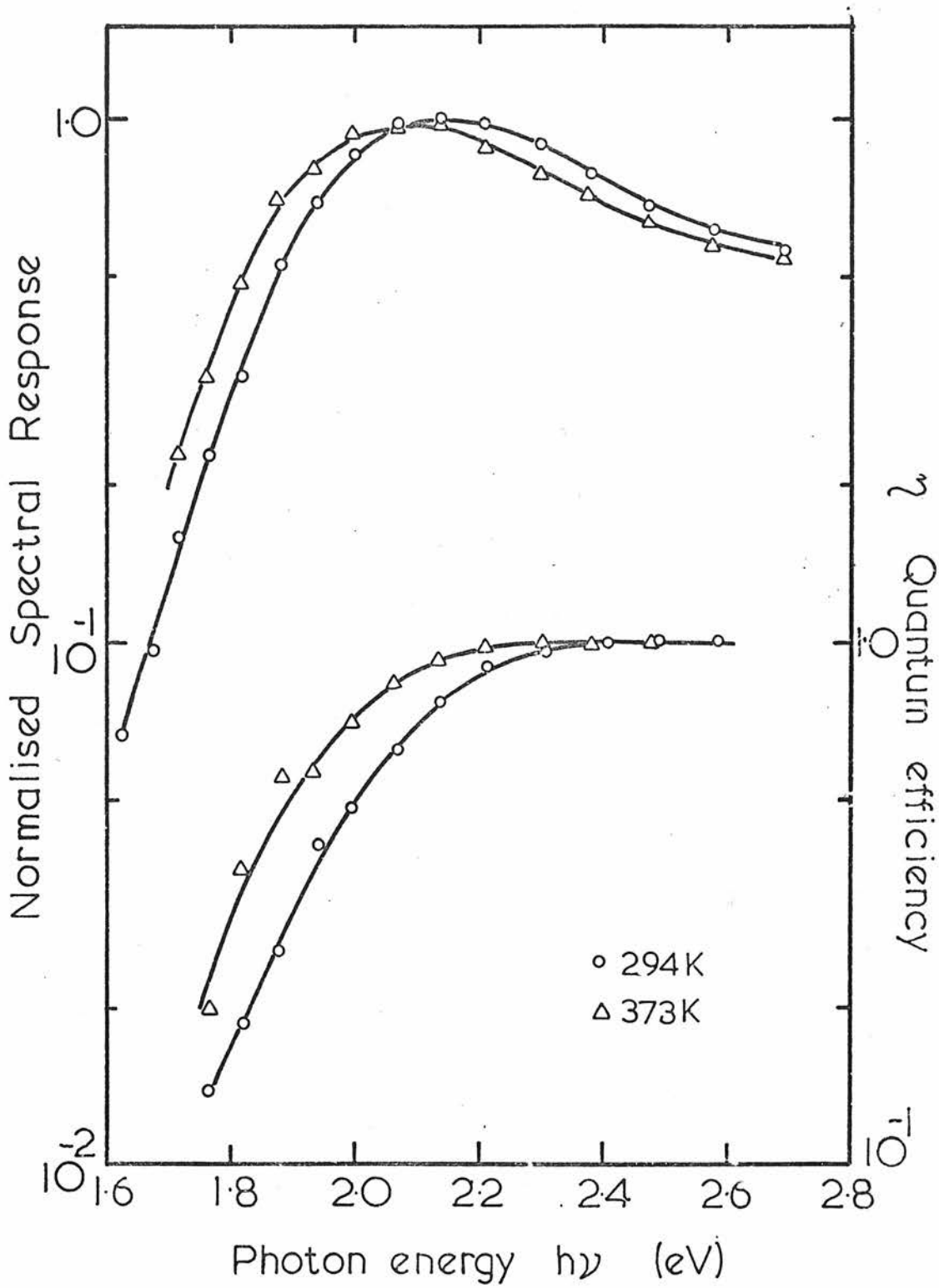

Fig 9.6 As_2Se_3 Normalised Spectral response & Quantum efficiency vs photon energy at 294K & 373K

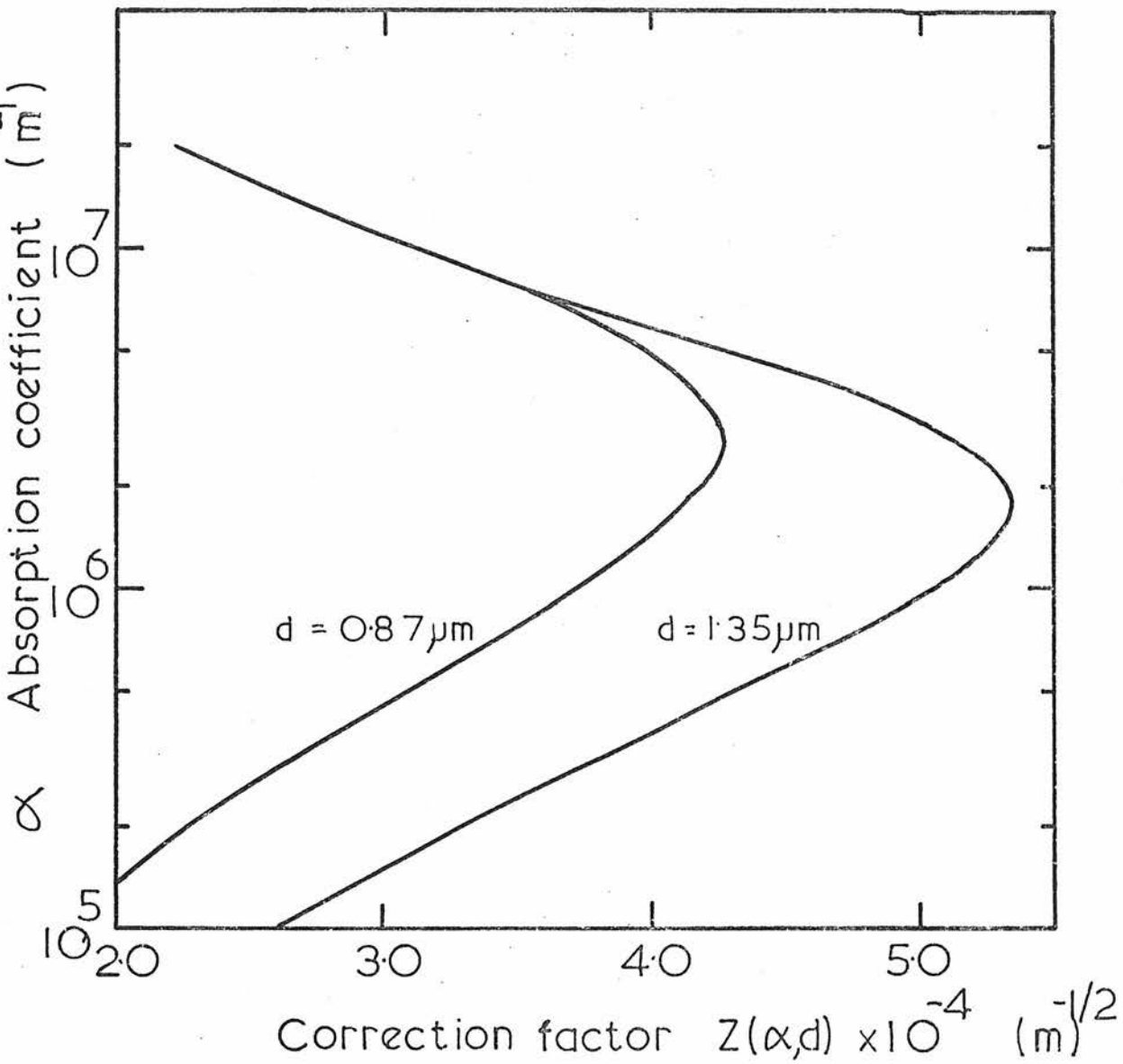

Fig 9.7 Factor Z (see text) vs α for two film thicknesses As_2Se_3

calculated from equation 8.5.7, assuming no spatial dependence of recombination kinetics. The curve for 373 K was obtained using extrapolated values for α, from figure 9.1.

It can be seen that at the nominal optical gap energy, the relative quantum efficiency is well below its maximum, and does not saturate until the photon energy is ~ 0.5 eV above E_{opt} (e.g. at 294 K E_{opt} = 1.86 eV, and η does not saturate until $h\nu \approx 2.4$ eV). In this respect, As_2Se_3 is similar to Se.

The shape of the photon energy dependence of the quantum efficiency was the only point of marked similarity between As_2Se_3 and Se. Other features observed in Se, and predicted by the Davis-Mott[17] analysis, such as temperature activation, and a large field dependence, were not apparent.

The shift of the spectral response and relative quantum efficiency curves to lower photon energy with increasing temperature can be almost totally accounted for, by the contraction of the optical gap and shift of the absorption edge. There are two effects here - the macroscopic effect of a change in α, which affects the the generation rate in the sample, and the more fundamental change, in the band structure. It is this latter change which is revealed in the shift of the relative quantum efficiency curve with temperature.

Thus, if the quantum efficiency is activated at all, the activation energy is independent of photon energy. It will be assumed, by arguments similar to those used for

As_2Te_3, that the flat high energy region corresponds to $\eta = 1$, and that the quantum efficiency is therefore not activated. (Figure 9.6 therefore represents absolute quantum efficiencies).

Figure 9.8 shows the spectral response and quantum efficiency for C-7, at 294 K, for low and high applied fields. (4×10^5 and 1.6×10^7 V m^{-1}). Measurements were also made at a number of intermediate fields - but as can be seen, the effect is small, so these curves have been omitted.

The problem in this measurement is to separate out the effects of field on transport and recombination from the effects on generation. In calculating the quantum efficiency, it was assumed that the field affected transport and recombination independently of photon energy, and that the effect on η at high photon energies ($h\nu > 2.6$ eV, $\eta \approx 1$) was very small. Hence, placing the high energy portions of the spectral response in coincidence would be a better representation than that shown.

Figure 9.8 shows that the effect of high fields on the quantum efficiency is very small, again in contrast to observations on Se, and Xerographic discharge experiments on As_2Se_3 [160], although it must be noted that the maximum field employed in this work is somewhat lower than the fields used in those investigations.

It appears, then, that theories involving geminate recombination of the photogenerated electron-hole pair,

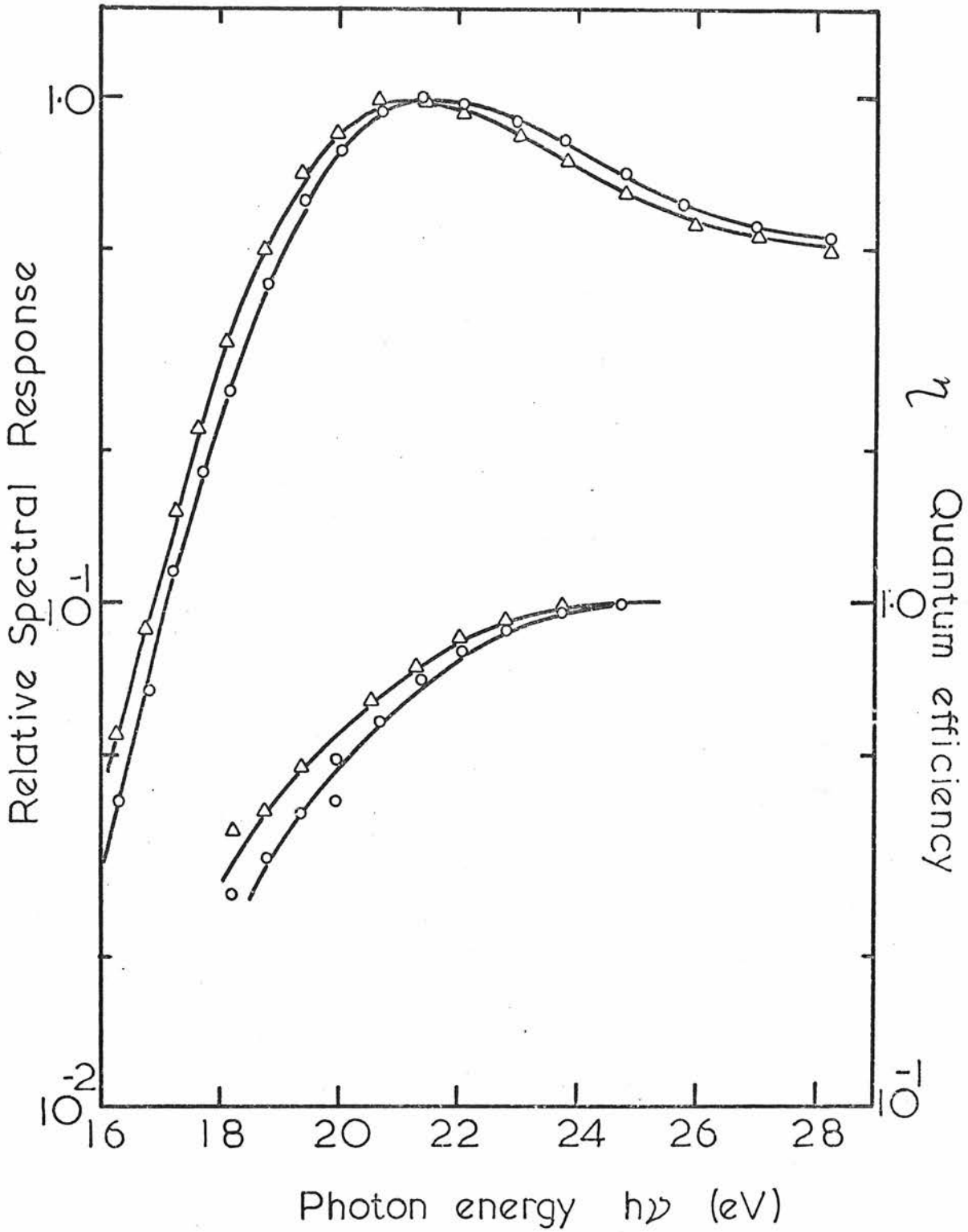

Fig 9.8 As_2Se_3 Normalised Spectral response & Quantum efficiency vs photon energy. at low & high electric fields

∘ 4×10^5 △ 1.6×10^7 (V/m)

resulting in an activated field dependent quantum efficiency are perhaps inappropriate, in the light of the present results. It could be that some absorption produces a bound exciton - say as an excited molecular state, which cannot be disscciated. This is only speculation, as the existence of particular molecular entities in amorphous As_2Se_3, analogous to the Se_8 rings in Se, is not known.

9.7 PHOTOCURRENT INTENSITY DEPENDENCE

It was noted in 9.6 that the photocurrent was proportional to the square root of the excitation intensity employed in the spectral response measurements. The relation between ΔI and photon flux density F was measured in sample C-7 using a Monsanto MV4H GaAsP l.e.d., with peak emission at 0.655 μm (1.89 eV). Although the quantum efficiency is less than unity at this wavelength, it is not dependent on intensity.

Figure 9.9 shows log (ΔI) vs log (F) at three temperatures using 'd.c. illumination' on sample C-7, and $\mathcal{E} = 4 \times 10^5$ V m^{-1}. The transition from linear (monomolecular) to square root (bimolecular) behaviour is evident, as is the reversal of temperature dependence between the two regimes. The dark current (for the whole sample) for each temperature is also indicated, showing that the transition is from small to large signal conditions. Note that there was no absorption depth 'scaling' of I_o, as the generation at this wavelength is fairly uniform. ($T_r \approx 0.35$).

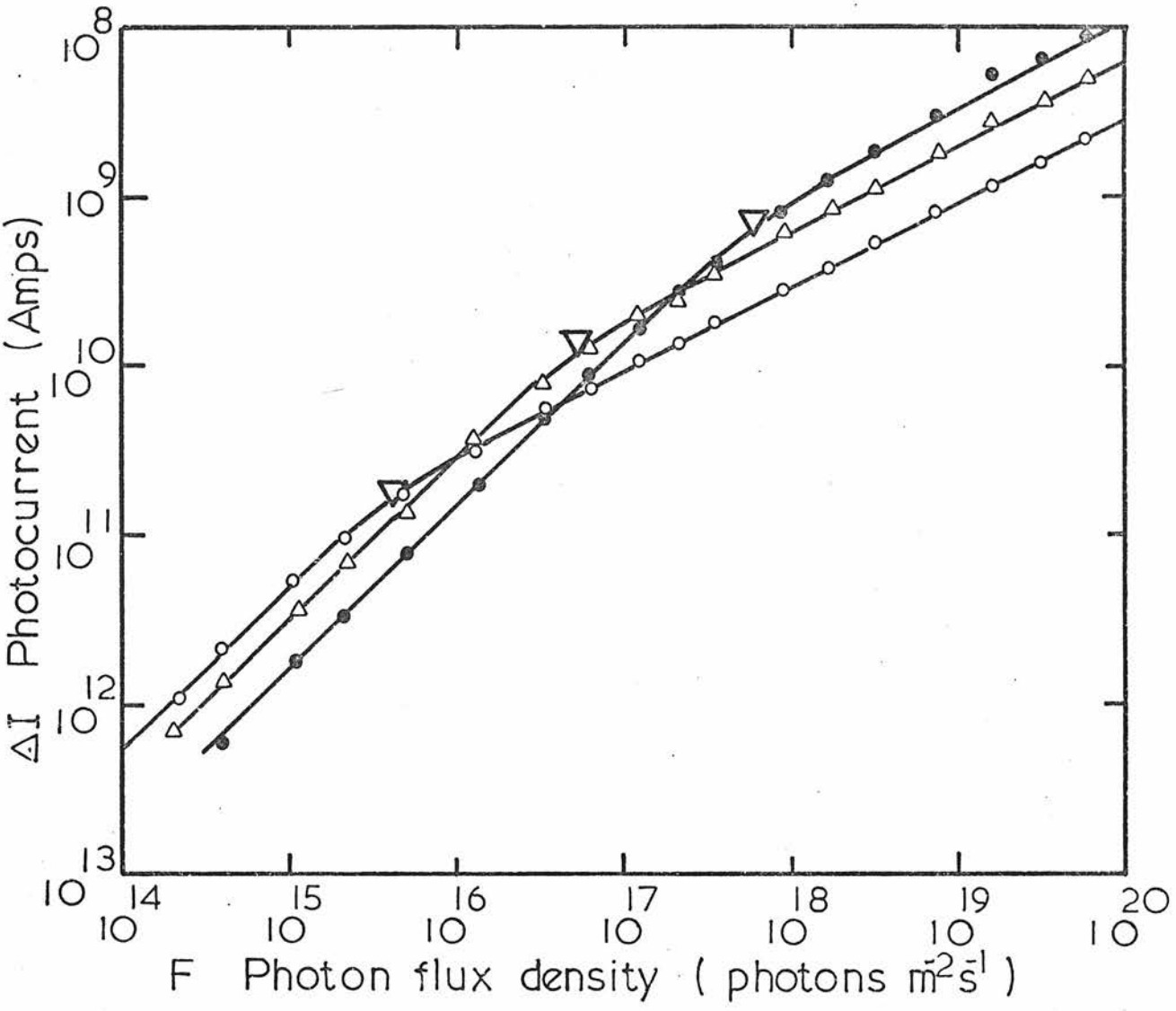

Fig 99 Photocurrent vs photon flux density for As_2Se_3

- ∘ 342 K
- △ 368 K
- • 392 K
- ▽ Dark current

9.8 PHOTOCURRENT TEMPERATURE DEPENDENCE

Figure 9.10 shows log (ΔI) vs $10^3/T$ for two photon flux densities, 5×10^{15} and 10^{19} photons m^{-2} s^{-1} at $\mathcal{E} = 4 \times 10^5$ V m^{-1} using sample C-7, and 1.89 eV 'd.c. excitation' from the MV4H l.e.d. Also shown is the dark current. The familiar peak in ΔI can be seen, and the reversal of temperature dependence between the low and high excitation regimes. From these data, $\Delta E_m \approx 0.37 \pm 0.3$ eV, and $\Delta E_b \approx 0.37$ eV. In the temperature range covered, there was no break to a lower slope, as in As_2Te_3.

The temperature dependence of the optical gap does have a significant effect on the apparent value of ΔE_b for 1.89 eV photon energy. Referring to equation 9.6.1, if the temperature dependence of the absorption factor Z, is included, and the shift of η to lower photon energies, then the true value of ΔE_b is $\sim 0.32 - 0.33$ eV.

Figure 9.11 shows the values of ΔE_b obtained at various photon energies, from 1.55 eV, to 2.75 eV, using sample C-23, at $\mathcal{E} = 4 \times 10^4$ V m^{-1}, and temperature range 294 - 373 K. The dependence of ΔE_b on $h\nu$ is reminiscent of Pai and Ing's results for η in Se[88], and the Davis-Mott analysis, given in equation 3.2.3. When correction is made to the ΔI vs $10^3/T$ data, however, for the changes in Z and η, caused by contraction of E_{opt} with temperature, the corrected values of ΔE_b all lie close to ~ 0.33 eV. This is merely a different way of stating the conclusion of section 9.6, that η is probably not activated. Corrections to ΔE_m are small, and will be neglected.

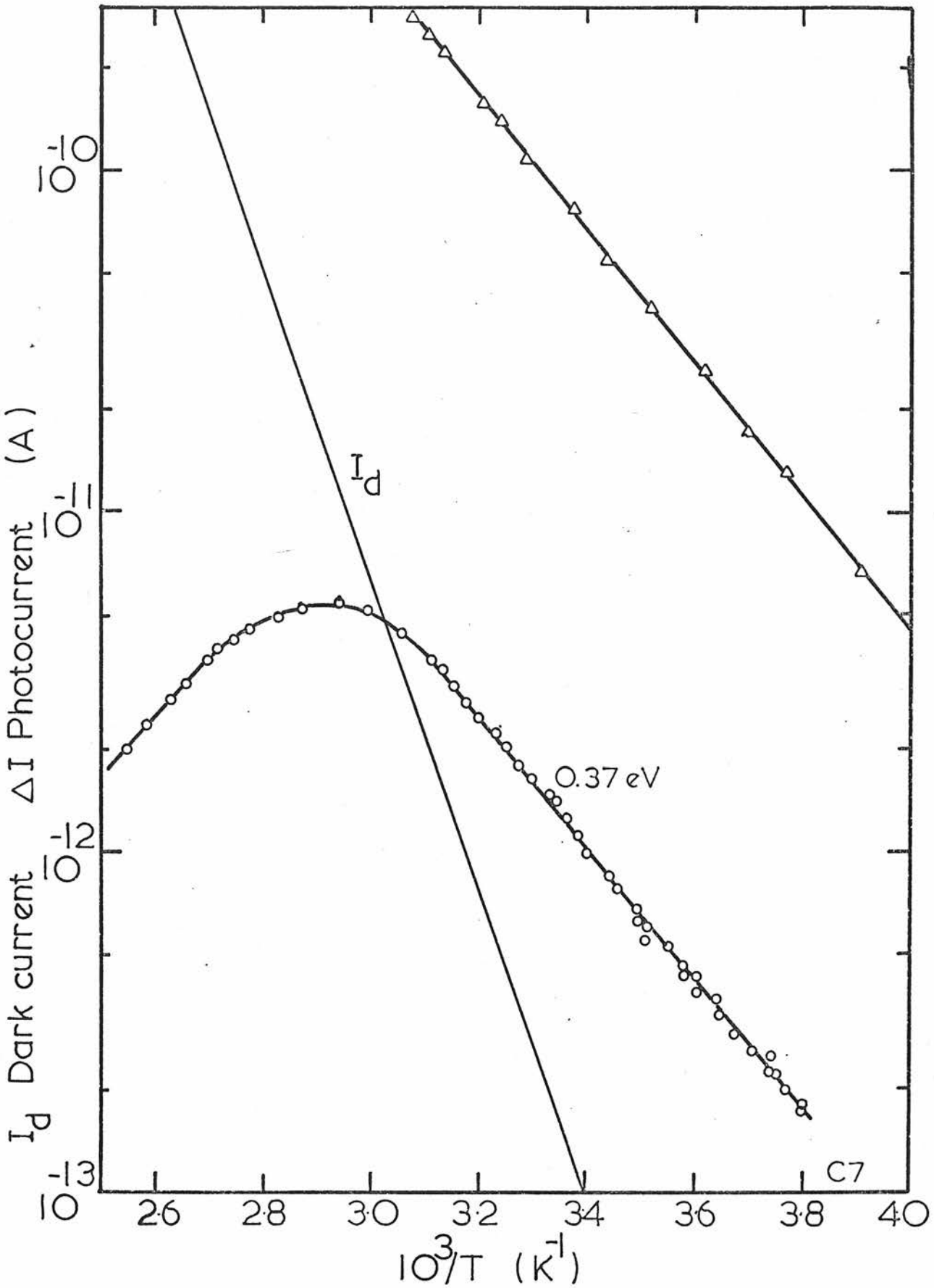

Fig 9 10 As_2Se_3 Photocurrent vs $10^3/T$ at two illumination levels
∘ 5×10^{15}
△ 10^{19} (photons $m^{-2}s^{-1}$)

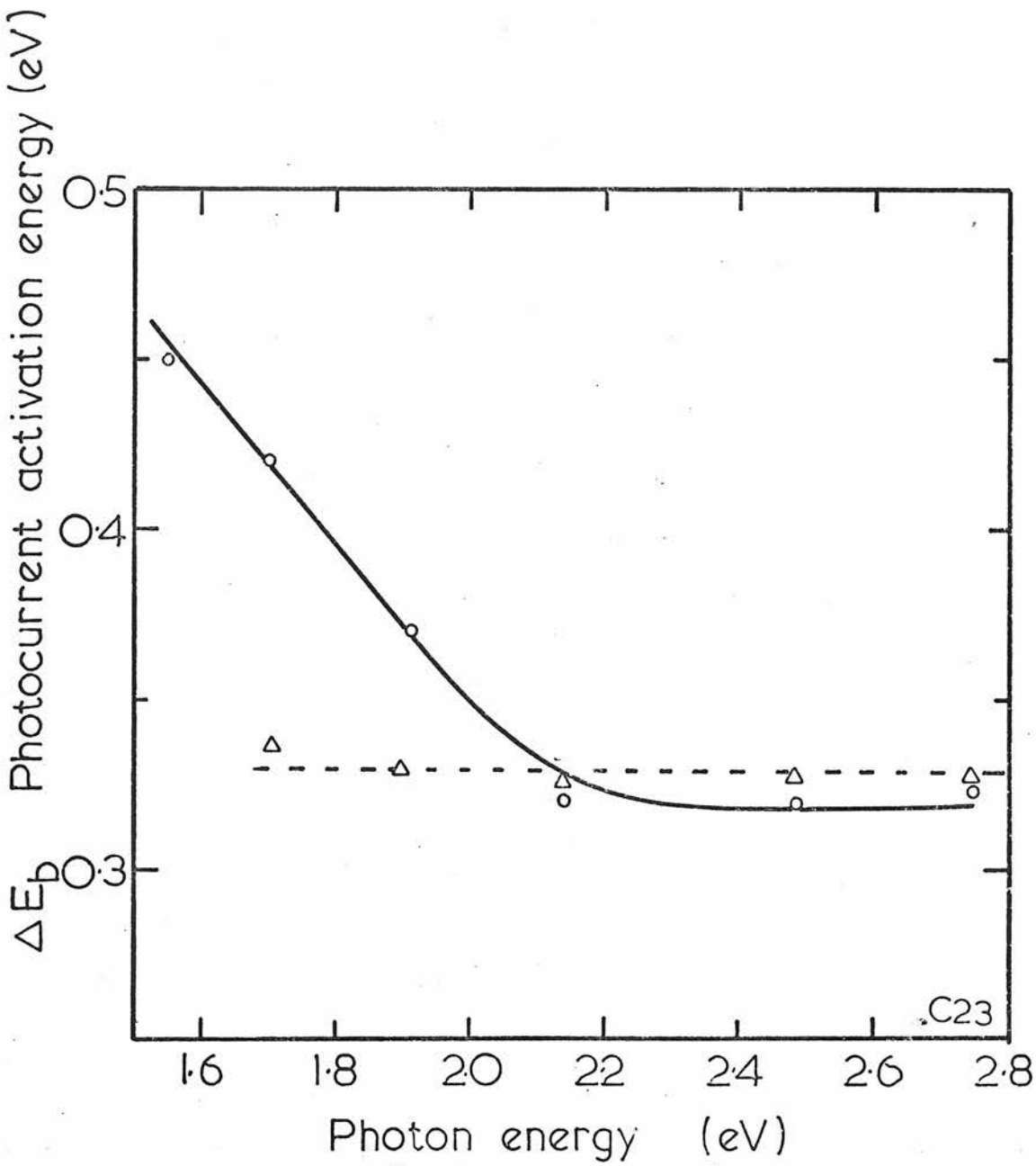

Fig 9.11 As_2Se_3 ΔE_b Photocurrent activation energy vs Photon energy

∘ original data

△ data corrected for absorption edge shift with Temperature

9.9 PHOTOCURRENT FIELD DEPENDENCE

Photocurrent - voltage measurements were carried out in the high excitation region, using a range of photon energies but with most emphasis on measurement at the l.e.d. energy of 1.89 eV. Figure 9.12 shows log (photoconductance) vs $\mathcal{E}$ at several temperatures for C-5. Again, a good straight line fit is obtained, and the value of the activation length parameter a(T) is ~15 Å at 294 K, reducing to ~ 12 Å at 373 K. At shorter wavelengths, ($h\nu$ = 2.58 eV) the field dependence is slightly smaller, (2 - 3 Å smaller). This is in agreement with the assumptions of section 9.6, - i.e. the field dependence at high photon energies, is associated with transport only, while at lower photon energies, the quantum efficiency is also slightly field dependent.

The values of a(T) obtained from these measurements are significantly lower than for the dark current (25 - 30 Å at 294 K) as was the case for As_2Te_3, and it is possible that a combination of bimolecular recombination kinetics and a 'mobility edge' high field effect is again responsible for this (see 8.10).

Data for high fields ($\mathcal{E}$ = 1.2 x 10^7 V m^{-1}), from ΔI vs $10^3/T$, at $h\nu$ = 1.89 eV for C-7 (see figure 9.13), give a reduction in ΔE_b, by ~ 0.05 eV, from 0.37 eV, to ~ 0.32 eV, i.e. about half the reduction of the dark conductivity activation energy. This is in agreement with the above assumption, but the implied value of a(0) ~ 40 Å, is somewhat higher than might be expected from the results of figure 9.12.

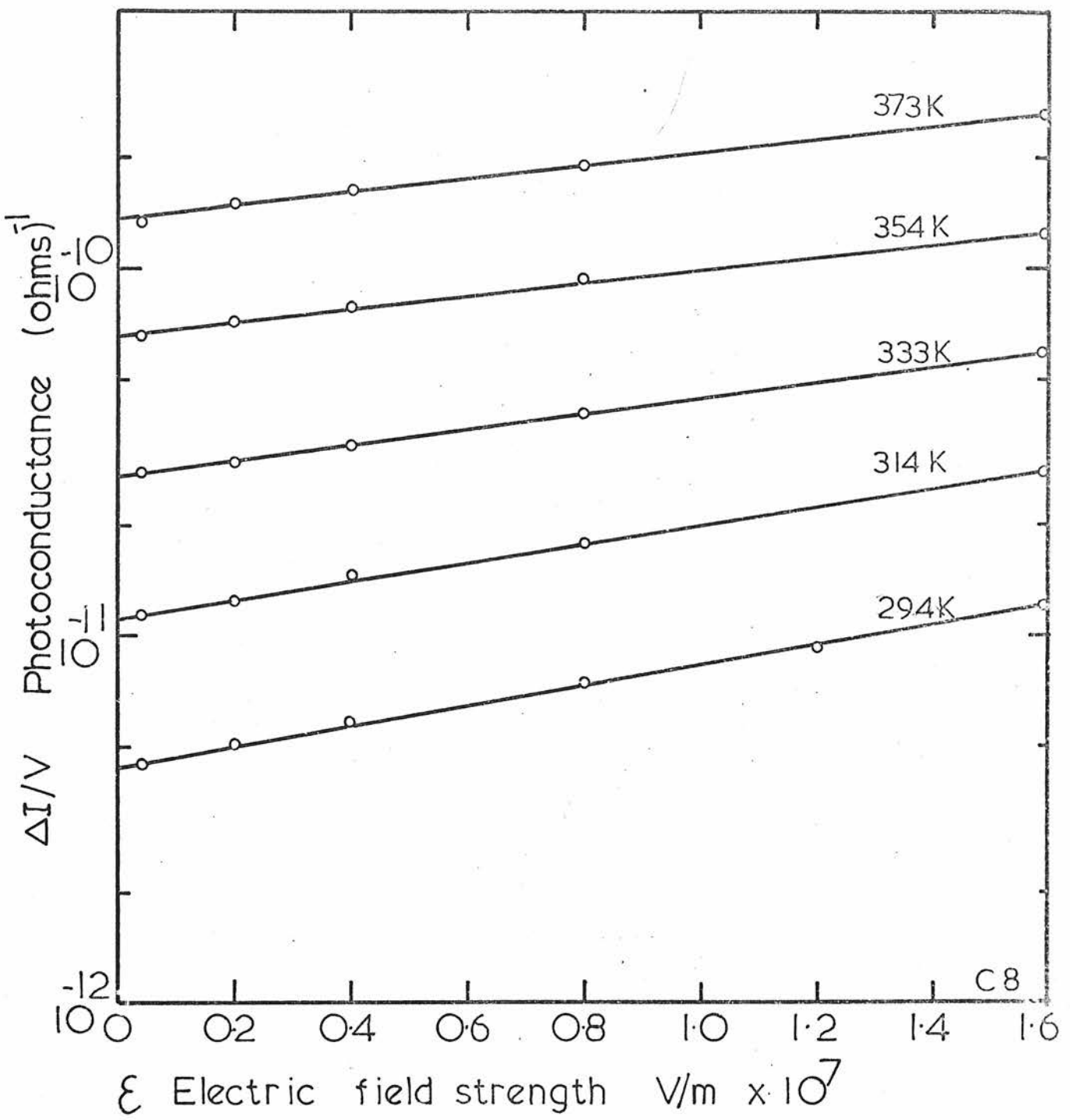

Fig 9.12 As_2Se_3 log photoconductance vs Electric field strength.

9.10 PHOTODECAY TIME

As was the case with As_2Te_3, the steady state results could be interpreted in terms of B-L or L-L recombination. The photodecay results can be used again to resolve any ambiguities. In the case of As_2Se_3 the evidence, corroborated by photomobility measurements, is even more in favour of a B-L mechanism.

Pulsed illumination was provided by the MV4H l.e.d. and the circuit of figure 4.10. Excitation rise and fall times were ~0.2 μs, and the instrumental rise time was 2 μs, much shorter than the shortest photodecay time observed (8 μs).

Figure 9.13 shows the photodecay time τ_c, vs $10^3/T$, for sample C-7, at two photon flux densities, 10^{19}, and 2×10^{19} photons m^{-2} s^{-1}. The photocurrent for $F = 10^{19}$ is also shown for $\mathcal{E} = 2 \times 10^7$ V m^{-1}. The behaviour is similar to that of As_2Te_3, exhibiting a steep temperature dependence in the monomolecular regime, with $\Delta E_\tau(m) \approx 0.95$ eV, and independence of excitation. The decay is accurately exponential in this region. There is some sample to sample variation, and C-8 gives $E_\tau(m) \sim 1.05$ eV. In the bimolecular regime, the decay time τ_{cb} is excitation dependent, and <u>increases</u> with 1/T, with activation energy $\Delta E_\tau(b) \approx 0.08$ eV. The decay has a long 'tail' and <u>appears</u> to be hyperbolic. This may not be the case, as will be discussed in 9.13.

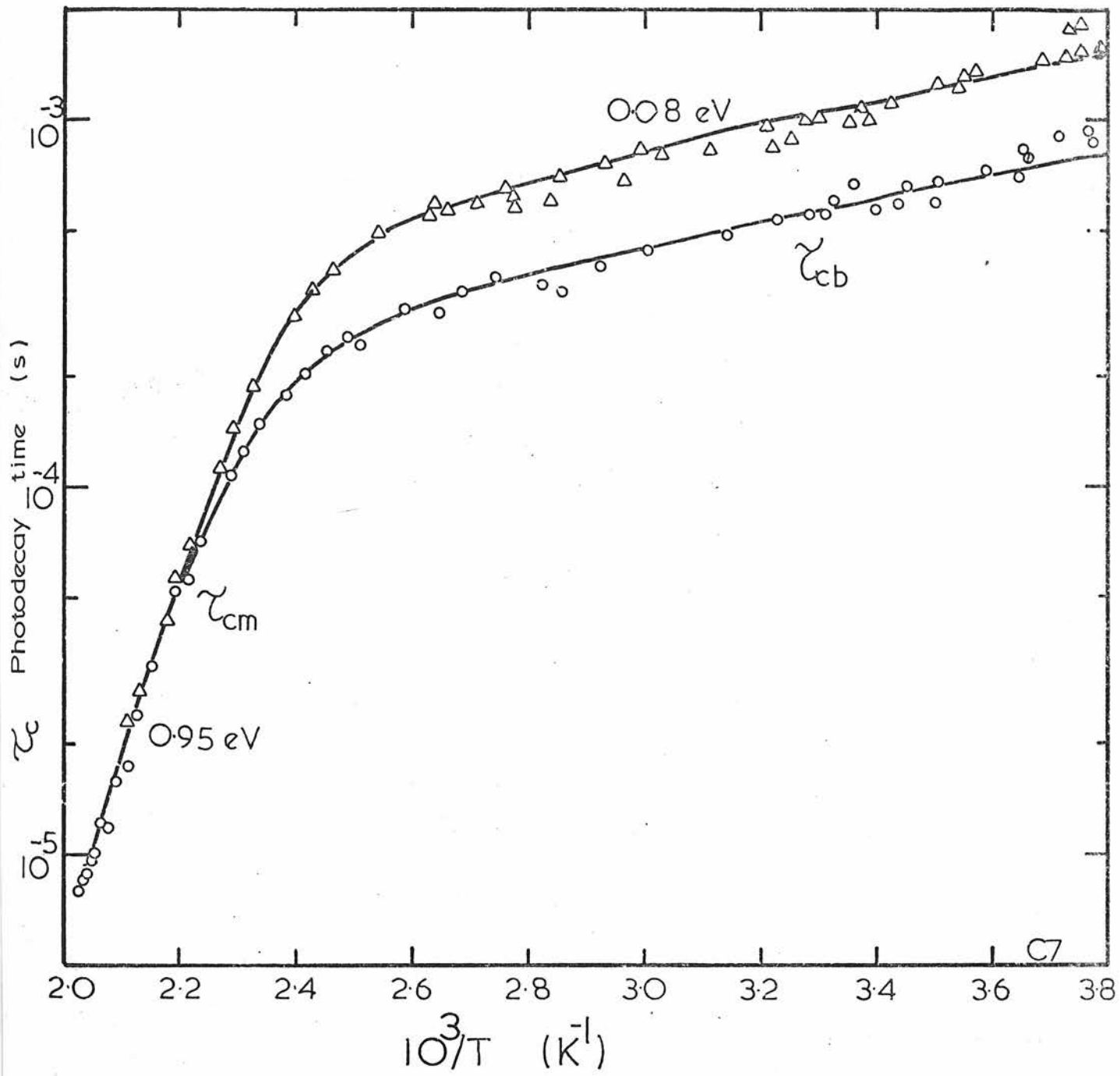

Fig 9.13 As_2Se_3 Photodecay time τ_c vs $10^3/T$ for two illumination levels

△ 10^{19}

○ 2×10^{19} (photons $m^{-2}s^{-1}$)

9.11 PRELIMINARY MODEL FOR As_2Se_3

The data obtained so far were analysed in the same way as in the case of As_2Te_3, using a 4-level model, of figure 3.10, to determine the prevailing recombination paths, and likely distribution of localised states. The data used are :

Optical gap (OK)	E_{opt}	2.0	eV
Dark conductivity activation energy	E_σ	0.92	eV
Steady state monomolecular 'activation'	ΔE_m	0.37	eV
Steady state bimolecular 'activation'	ΔE_b	0.33	eV
Monomolecular decay time 'activation'	$\Delta E_\tau(m)(aV)$	1.0	eV

It turns out again that the simple model of B-L recombination, and extended state hole conduction fits the data best. As an illustration of the process of elimination, the values of E_1 and E_2 in the simple 4-level model can be found from the dark and steady-state data, and then used as a test of consistency, to predict $E_\tau(m)$, for three possible models. (a) B-L recombination only (b) B-L recombination in the monomolecular regime, and L-L in the bimolecular regime (c) L-L recombination only. The values obtained are listed in table 9.11.1.

	(a) B-L	(b) B-L ⟶ L-L	(c) L-L
$E_2 - E_v$	0.66 eV	0.33 eV	0.33 eV
$E_1 - E_v$	1.29	1.29	1.62
$E_F - E_v$	0.92	0.92	0.92
$\Delta E_\tau(m)$(predicted)	1.03	0.70	0.70
$\Delta E_\tau(m)$(measured)		1.0 eV	

Table 9.11.1. Comparison of energy values obtained from different photoconductivity models.

It is evident that (a) B-L (path 1) recombination gives the best fit to the data, as models (b) and (c) predict a value for $E_\tau(m)$ which is far too low. In the case of As_2Se_3, <u>all</u> of the models require some states to pin E_F.

Some of the parameters of the model (a) can now be estimated, using the high temperature monomolecular data, of figure 9.13 (say, T = 455 K).

$$\sigma_o = e\mu_{po}N_v = 1.3 \times 10^4\ \Omega^{-1}\ m^{-1} \qquad 9.11.1$$

$$\tau_{cm} = (N_2/p_2)\tau_{pm} = 50\ \mu s \qquad 9.11.2$$

$$\Delta I = we\mu_{po}\mathcal{E}\{\tau_{pm}\ \eta\ F(1 - R_1 - T_r)\} = 2.5 \times 10^{-8}\ A \qquad 9.11.3$$

The factor $\eta(1 - R_1 - T_r) = \eta A$ in 9.11.3 is estimated by extrapolation of low temperature data, to be ~ 0.25 at 455 K, to within a factor of 2, for sample C-7.

From 9.11.1, the product $\mu_{po}N_v \approx 8 \times 10^{22}$ m^{-1} V^{-1} s^{-1}, so $N_v \sim 8 \times 10^{25}$ m^{-3}, gives,

$$N_v \approx 8 \times 10^{25} \text{ m}^{-3}$$

$$N_2 \approx 7 \times 10^{22} \text{ m}^{-3}$$

$$\mu_{po} \approx 10^{-3} \text{ m}^2 \text{ V}^{-1} \text{ s}^{-1}$$

$$\tau_{pm} \approx 2 \times 10^{-8} \text{ s (455 K)}$$

(including as far as possible, gap temperature dilation effects).

Estimates can be made for C_{p2} (σ_{p2}) if $\tau_{t2} < 2 \times 10^{-8}$ s, as implied by the data, giving $\sigma_{p2} > 10^{-20}$ m^2, a reasonable value for coulombic capture, and not impossible for neutral centre capture. If the latter is true, then the density of charged states pinning E_F, need only be greater than 2×10^{20} m^{-3}. Note that these states must again play an insignificant role in recombination, as in As_2Te_3.

Room temperature small signal, or dark values can be calculated or extrapolated from this model, giving

free lifetime (294 K) $\tau_{pm} \approx 3 \times 10^{-6}$ s

monomolecular decay time (294 K) $\tau_{cm} \approx 30$ s

ratio of free/trapped holes $p_o/N_2\bar{f}_{20} \approx 10^{-7}$

Many of these values are verified by photomobility measurements, which also give information on other sets of localised states.

9.12 PHOTOCURRENT GROWTH

Measurements of the initial growth of photocurrent, in response to step excitation, before recombination was significant, proved to be straightforward, as the instrumental rise time was ~ 2 μs, and the shortest photocurrent rise time in the temperature range covered (273 - 373 K) was > 100 μs. An interesting feature of the growth curve was the appearance of two distinct growth regions with quite different slopes, indicating trapping in two distinct levels. The two rise curves shown in figure 9.14 illustrate this, for $F = 1.0 \times 10^{19}$ and 2.0×10^{19} photons m^{-2} s^{-1}, and $\mathcal{E} = 1.2 \times 10^{7}$ V m^{-1}, at 294 K.

The analysis of the growth of photoconductivity while recombination is insignificant, given in 3.3.3 can easily be extended to include two trapping levels. Figure 9.15 shows the situation to be analysed, with a set of 'fast' traps at energy E_3, (trapping and release times τ_{t3}, and τ_{tr3}) and a deeper set, at E_2 (trapping and release times τ_{t2} and τ_{tr2}). This choice of subscripts presupposes the experimental results of this section which identify the 'slow growth' region with the centres at E_2, already known from steady state results.

Assuming that $\tau_{t3} \ll \tau_{t2}$, and that the occupation of states at E_3 is much less than the occupation at E_2 (giving $\tau_{tr3}/\tau_{t3} \ll \tau_{tr2}/\tau_{t2}$) simplifies the analysis, and leads to :

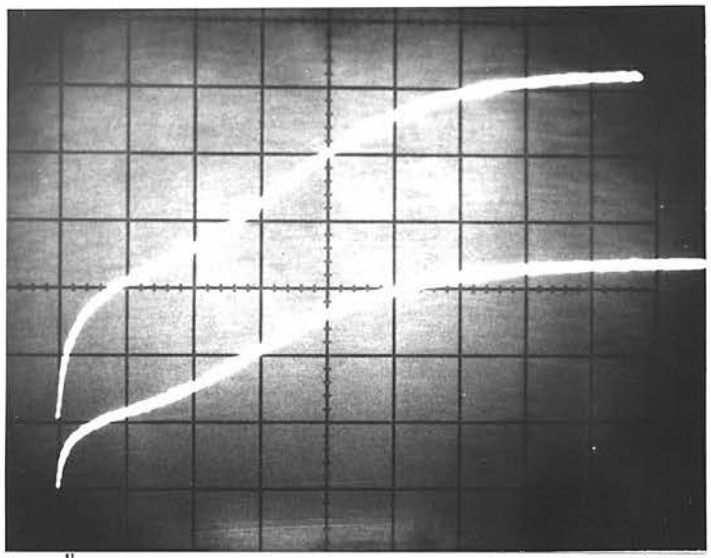

Fig 9.14 As_2Se_3 Photoresponse to step function excitation showing two distinct growth regions

vertical scale 2nA/cm

horizontal scale $\frac{1}{2}$ ms/cm upper / lower

upper trace 2

lower trace 1

$\times 10^{19}$ photons $m^{-2} s^{-1}$

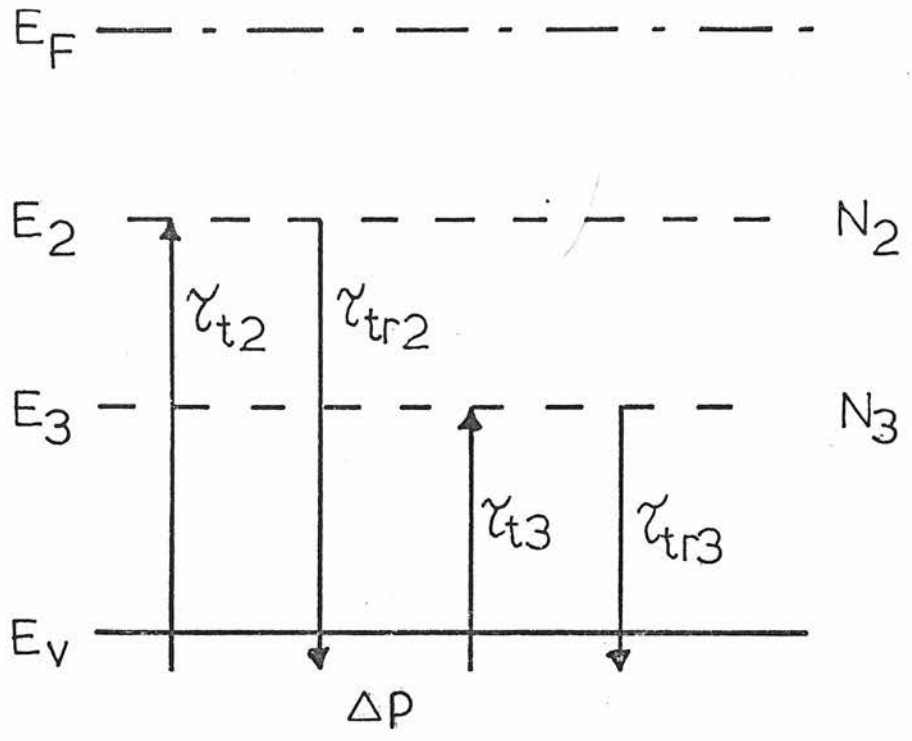

Fig 9.15 As_2Se_3 Two trap model for photoconductivity growth analysis

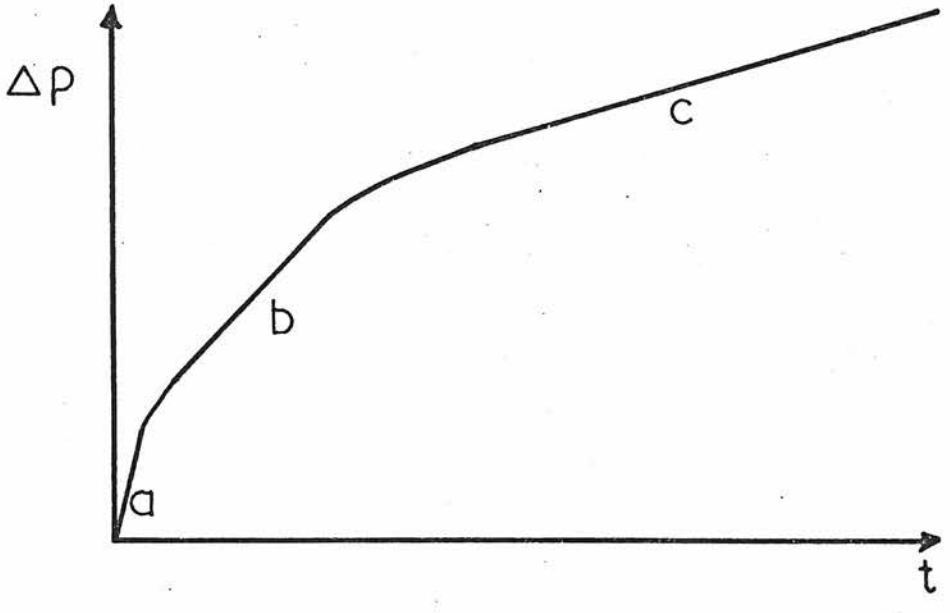

Fig 9.16 Growth of excess hole density showing three regions.

$$\Delta p(t) \approx \Delta G(\tau_{t2} + (\tau_{t2}/\tau_{tr2})t - \tau_{t3} \exp(-t/\tau_{t3}) - \tau_{t2} \exp(-t\,\tau_{t3}/\tau_{t2}\,\tau_{tr3})) \qquad 9.12.1$$

The shape of this growth curve is shown schematically in figure 9.16. The three distinct slopes, in regions (a), (b) and (c), when translated to photocurrent growth, correspond to three 'mobilities'

(a) $\frac{d\Delta I}{dt} \alpha \Delta G \mu_{po}$ free mobility

(b) $\frac{d\Delta I}{dt} \alpha \Delta G \mu_{po}\, \tau_{t3}/\tau_{tr3} \longrightarrow \mu_{d3}$ drift mobility, trap-limited by set '3'.

(c) $\frac{d\Delta I}{dt} \alpha \Delta G \mu_{po}\, \tau_{t2}/\tau_{tr2} \longrightarrow \mu_{d2}$ drift mobility, trap-limited by set '2'.

Region (a) is inaccessible, experimentally, and accurate measurements of region (c) could only be made at high fields. The slight inflexion or S-shaped appearance in figure 9.14 is not predicted by the simple analysis, as $d^2\Delta p/dt^2$ is always negative. This will be discussed later.

Irrespective of whether excitation is uniform through the sample or not, the appropriate mobility can be obtained from the simple relation - e.g. for slope region (b),

$$\mu_{d3} = (\frac{d\Delta I}{dt})\ (b)\ (F(1 - R_1 - T_r)\,\eta.e\mathcal{E}w) \qquad 9.12.2$$

Note that this linear form applies for all levels of excitation - even when the final steady state indicates

bimolecular recombination, as the particular experimental conditions employed remove recombination considerations.

The field and temperature dependence of the mobility μ_{d3} was investigated in some detail from 273 - 376 K, and a field range of 8×10^5 - 1.6×10^7 V m^{-1}. It was found that in this fairly limited range, the data fitted either Poole-Frenkel, or $\exp(\mathcal{E}^1)$ plots, as shown in figures 9.17 and 9.18. The value of μ_{d3} at room temperature and 10^7 V m^{-1}, is 3×10^{-9} m^2 V^{-1} s^{-1}, in good agreement with previous measurements carried out by transit-time techniques[20,160]. From figure 9.17 a value for the Poole-Frenkel constant β at 294 K, of 1.4×10^{-5} eV $V^{-\frac{1}{2}}$ $m^{\frac{1}{2}}$ is obtained, in reasonable agreement with the value of 1.5×10^{-5} obtained from conductivity measurements, although at higher temperatures the value is rather smaller. Note that these values are rather smaller than the one-dimensional theory prediction, i.e. 2.3×10^{-5} eV $V^{-\frac{1}{2}}$ $m^{\frac{1}{2}}$, and also lower than the value of 2.6×10^{-5}, which Marshall and Owen obtained from transit time techniques[20].

In the light of the evidence from high-field conductivity measurements[65,66], it appears that the $\exp(\mathcal{E}^1)$ dependence shown in figure 9.18 is more appropriate. This gives an activation length parameter a(T) which varies between 25 Å and 15 Å, from 273 K to 353 K, in good agreement with the high field conductivity data.

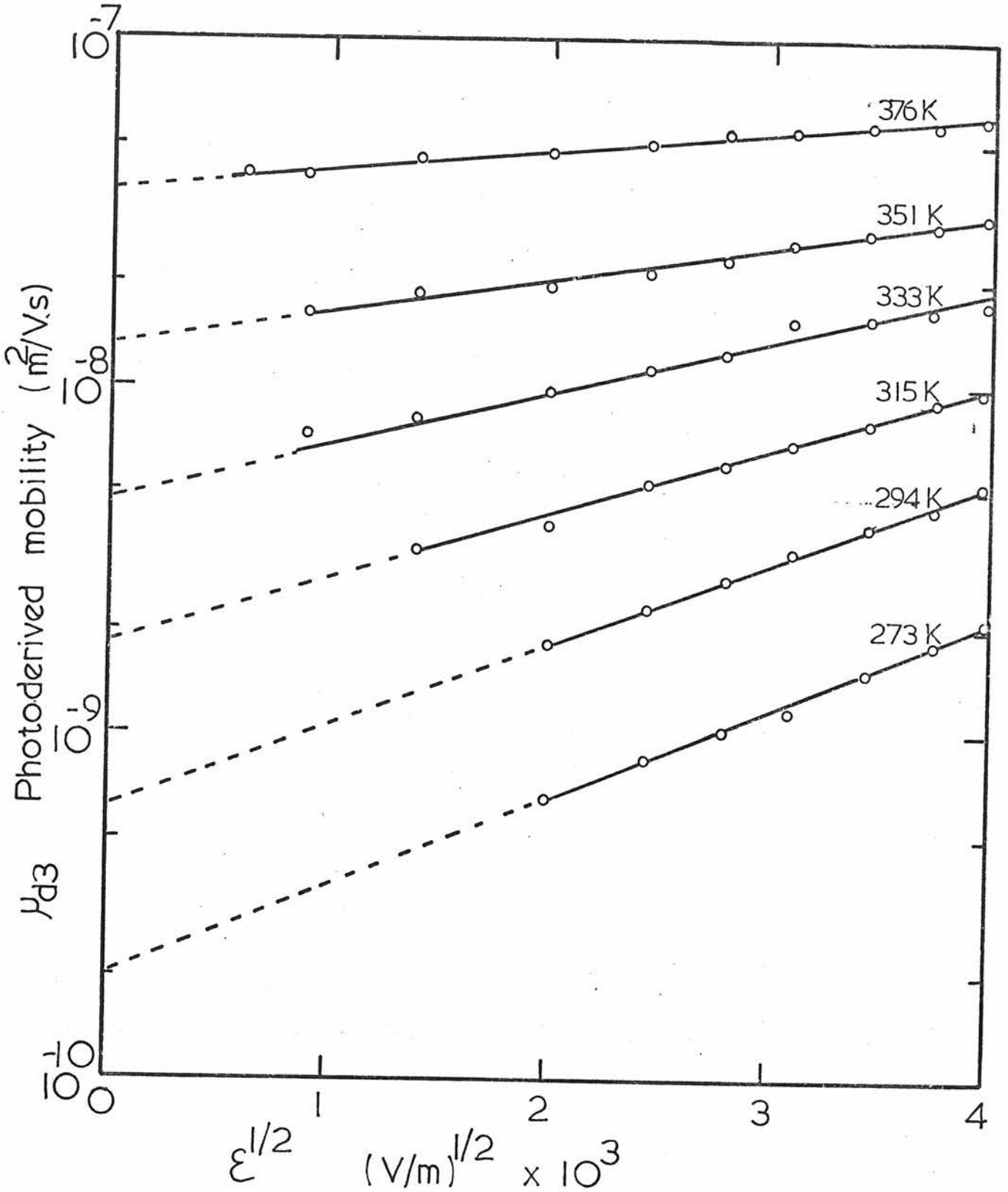

Fig 9.17 Photoderived drift mobility (trap limited by set 3) vs $\mathcal{E}^{1/2}$.

As_2Se_3

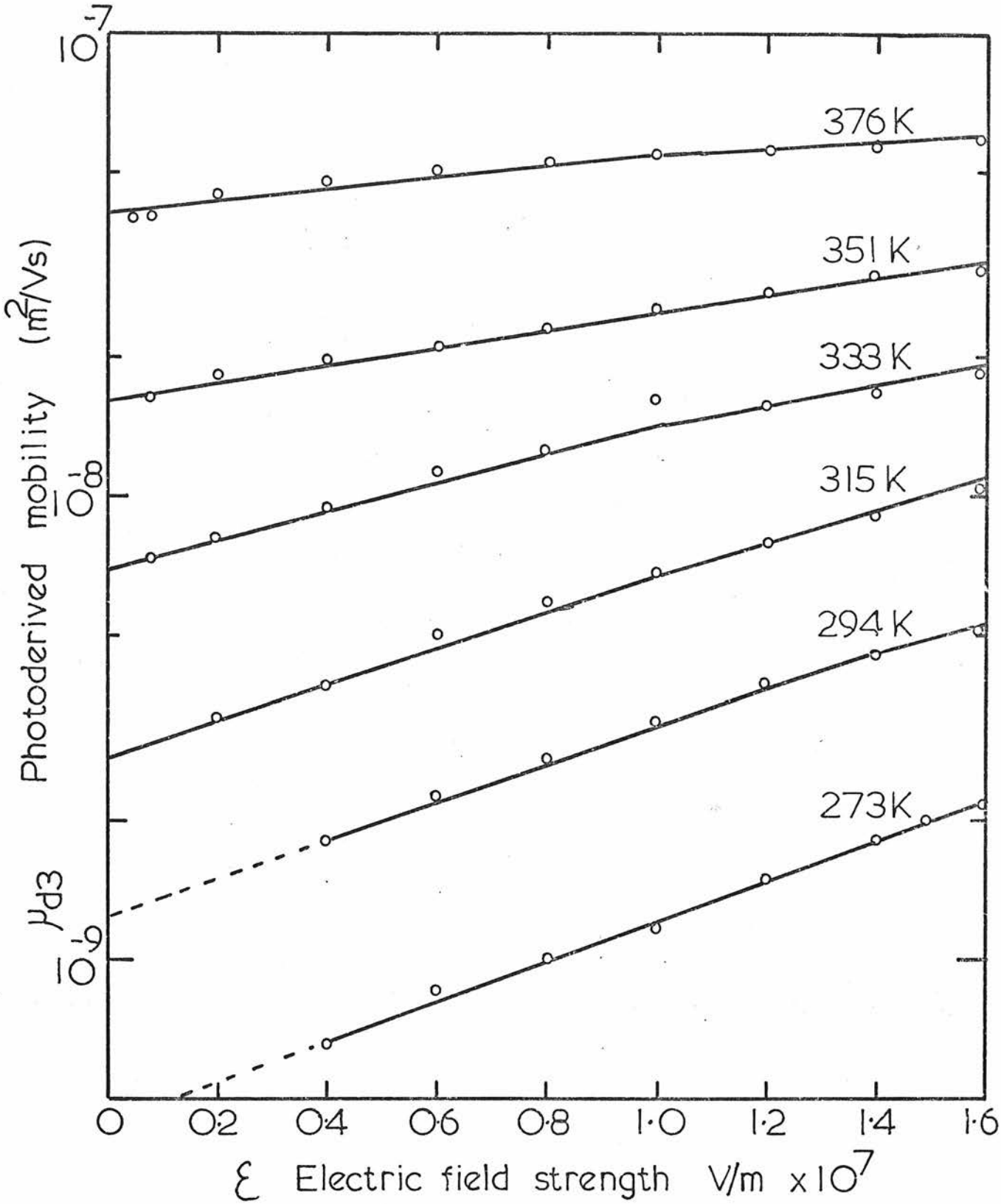

Fig 9.18 As_2Se_3 μ_{d3} Trap limited drift mobility vs applied field $\mathcal{E}$

Note that the mobility measurement, carried out in the absence of recombination effects, gives a higher value for a(T) than the steady state measurements. This justifies the contention of 8.10, that a kind of 'field quenching' could effectively lower the photoconductivity field dependence, in the presence of bimolecular recombination. It can also be noted that the similarity of the high field dependence of the mobility and conductivity implies that injection effects are not responsible for the field enhancement of the conductivity.

Figure 9.19 shows μ_{d3} vs $10^3/T$, at several applied fields, and also an extrapolated 'zero field' temperature dependence (obtained from figure 9.18). The zero field activation energy is ~0.44 eV, reducing to 0.33 eV at 1.2×10^7 V m^{-1}. This reduction of 0.11 eV is in good agreement with the reduction of the conductivity activation energy at the same field (~0.12 eV). Note that extrapolating the exp ($\mathcal{E}^{\frac{1}{2}}$) behaviour of figure 9.17, to zero field, gives an activation energy of ~0.47 eV.

These values are in good agreement with the results of Marshall and Owen[20], who obtained a zero field activation energy of 0.43 eV (from a Poole-Frenkel extrapolation), and with the TSC results of Street and Yoffe[164], indicating a level at 0.40 ± 0.03 eV.

The magnitude and temperature dependence of the mobility indicate a trap-limited process, rather than hopping. It cannot be determined whether a discrete level or a band tail 0.44 eV deep, is involved, but a

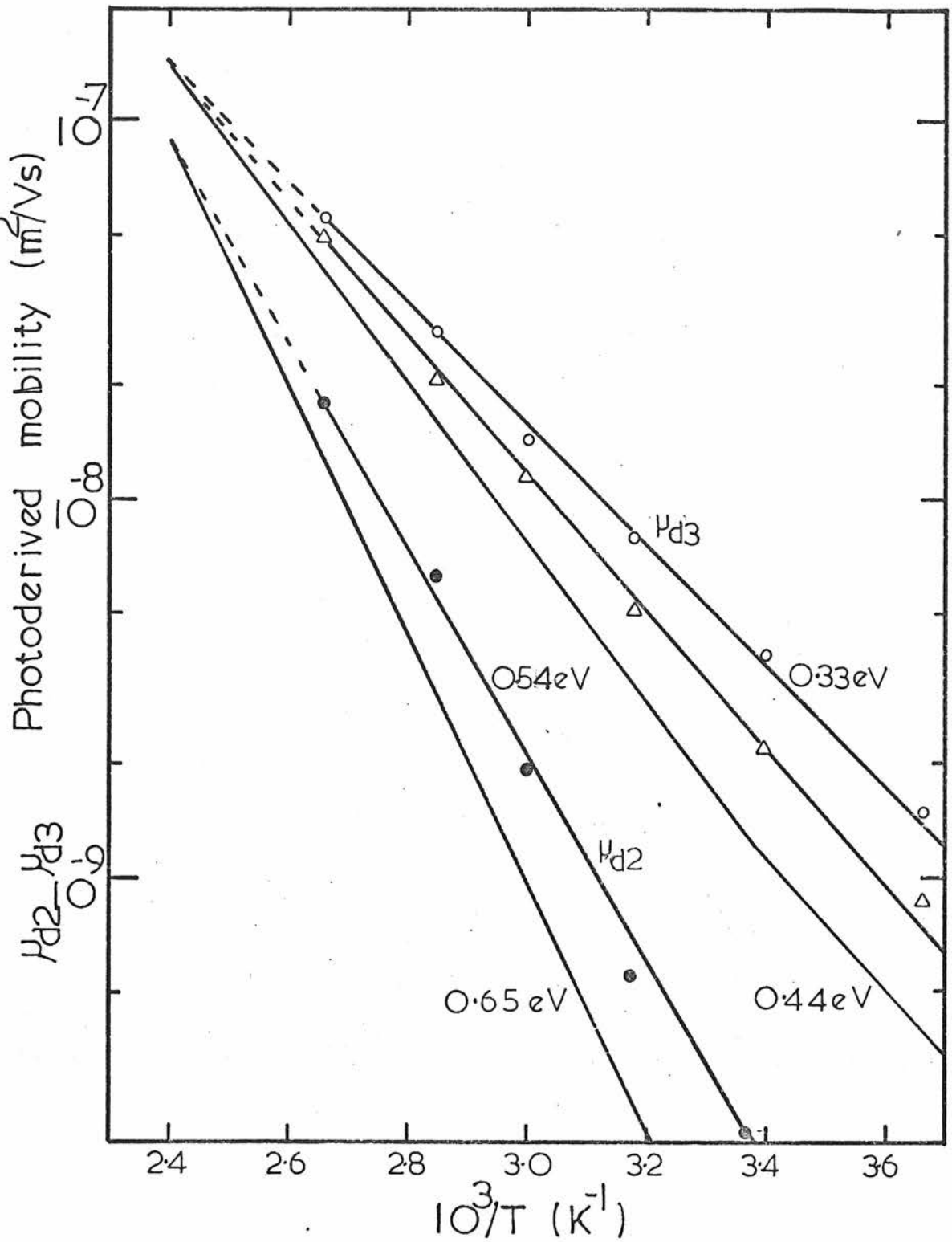

Fig 9.19 As_2Se_3 Trap limited drift mobilities μ_{d2}, μ_{d3} vs $10^3/T$ at various fields

•• 12×10^7 V/m △ 6×10^4 V/m

zero field extrapolation

tail of this depth in a simple compound chalcogenide is perhaps unlikely. As mentioned in 2.2.1, band tailing in such materials is probably limited to < 0.2 eV.

Assuming a discrete trap-level, then, the trap limited mobility may be written

$$\mu_{d3} \approx (\mu_{po}N_v/N_3)\exp[-(E_3-E_v)/kT]\exp[(0.44/2.0) \times \gamma/k] \quad 9.12.3$$

including a factor for the temperature dependence of the gap.

As $\mu_{po}N_v = 8 \times 10^{22}$ m^{-1} V^{-1} s^{-1} (form 9.11.1), $N_3 \approx 10^{24}$ m^{-3}, somewhat lower than the estimate of $10^{25} - 10^{26}$ m^{-3}, of Marshall and Owen[20], for vitreous 'bulk' samples. Marshall and Owen attributed the large field dependence of the mobility to a Poole-Frenkel effect, on coulombic traps (negatively charged when empty of holes). The 'mobility edge' field delocalisation, proposed by Marshall and Miller on the other hand effectively lowers the mobility edge, making all traps shallower, regardless of charge type. Thus a mobility, limited by trapping by neutral centres can also display a large field dependence.

The trapping time and capture cross sections of the traps at E_3 and E_2 can also be estimated. Firstly, inspection of equation 9.12.1, and figure 9.14, shows that the effective equilibration time for traps at E_2 is

$$\tau'_{t2} = \tau_{t2} \times (\tau_{tr3}/\tau_{t3}) >> \tau_{t2} \quad 9.12.4$$

i.e. trapping in shallower states slows the filling of the deeper states. This time is marked on figure 9.14, and the excess hole density at this turnover point, is

$$\Delta p(b) \approx \Delta G \, \tau_{t2} \qquad 9.12.5$$

It is worth noting that the measured value for τ'_{t2} is ~ 180 μs at room temperature, in reasonable agreement with the 'deep trapping' time of ≥ 125 μs which Marshall and Owen[20] obtained from a 'Hecht curve' analysis of transit time data.

Similarly, the excess hole density after equilibration with the shallower states at E_3 is achieved, is

$$\Delta p(a) \approx \Delta G \, \tau_{t3} \qquad 9.12.6$$

To obtain a value for $\Delta p(a)$, the instrumental rise time was reduced to ~ 100 ns, by using a 50 KΩ sampling resistor. As this resulted in reduced sensitivity, a high intensity light pulse was used ($F = 2 \times 10^{20}$ m^{-2} s^{-1}, $\Delta G \approx 1.5 \times 10^{25}$ m^{-3} s^{-1}), and a high field, $\mathcal{E} = 1.6 \times 10^{7}$ V m^{-1}. After an equilibration time of 2 μs, which indicated slowing down by yet another set of even shallower traps (perhaps band-tail states), $\Delta I = 7 \times 10^{-9}$ A, and assuming $\mu_{po} = 10^{-3}$ m^2 V^{-1} s^{-1}, gives $\Delta p(a) = 6.6 \times 10^{14}$ m^{-3}, and

$$\tau_{t3} \approx 4 \times 10^{-11} \text{ s}$$

$$C_{p3} \approx 2 \times 10^{-14} \text{ m}^3 \text{ s}^{-1}$$

$$\sigma_{p3} \approx 2 \times 10^{-19} \text{ m}^2$$

i.e. a very short free trapping time, and a cross-section which could indicate coulombic or neutral centres.

The temperature dependence of the mobility μ_{d2} at $\mathcal{E} = 1.2 \times 10^{7}$ V m^{-1} obtained from the growth slope in region (c) is also shown on figure 9.19. The room temperature value, at this field is $\approx 2 \times 10^{-10}$ m^2 V^{-1} s^{-1} and the activation energy is 0.54 eV. The zero field line, shown on figure 9.19, is obtained by assuming that the field reduction in activation energy is 0.11 eV, and by noting from the μ_{d3} data that a(T) extrapolates to zero at $10^3/T = 2.4$. The depth obtained, 0.65 eV, is in close agreement with the value from steady state photoconductivity data (0.66 eV). This trap depth is also close to levels reported by Kolomiets, by TSC measurements[163], and Bishop et al, by optical quenching of photoluminescence[166].

By a calculation similar to that of equation 9.12.2, $N_2 \approx 1.1 \times 10^{23}$ m^{-3}, and from equation 9.12.5 and figure 9.14

$$\tau_{t2} \approx 4 \times 10^{-10} \text{ s}$$

$$C_{p2} \approx 2 \times 10^{-14} \text{ m}^3 \text{ s}^{-1}$$

$$\sigma_{p2} \approx 2 \times 10^{-19} \text{ m}^2$$

i.e. the traps are very similar in type to those at E_3, but less dense. The value for N_2 is in good agreement with that obtained from straightforward photoconductivity measurements in 9.11.

From figure 9.14, the bimolecular steady state recombination time, at $F = 2 \times 10^{19}$ m^{-2} s^{-1} is, from $\Delta p_{ss} = \Delta G \, \tau_{pb}$,

$$\tau_{pb} \approx 8 \times 10^{-10} \text{ s}$$

somewhat longer than the value obtained from the low field steady state data of figure 9.10 ($\tau_{pb} \approx 4 \times 10^{-10}$ s, $F = 1 \times 10^{19}$ m^{-2} s^{-1}). The cross-section and density of the states at E_1 can, now be estimated. The preceding data, with figure 9.10, give the following room temperature values, for $\mu_{po} \approx 10^{-3}$ m^2 V^{-1} s^{-1}

	p_o	3.8×10^{11}	m^{-3}
	Δp	2.6×10^{14}	
	$N_2\Delta\bar{f}_2$	5.0×10^{21}	equal
$F = 10^{19}$ m^{-2} s^{-1}	$N_1\Delta f_1$	5.0×10^{21}	equal
$\mathcal{E} \longrightarrow \mathcal{E}0$	$N_3\Delta\bar{f}_3$	2.6×10^{20}	

Thus $\tau_{pb} = (C_{p1} N_1 \Delta f_1)^{-1} \approx 5 \times 10^{-10}$ s. giving $C_{p1} \approx 4 \times 10^{-13}$ m^3 s^{-1}, $\sigma_{p1} \approx 4 \times 10^{-18}$ m^2, a large cross-section which perhaps implies coulombic capture (i.e. states at E_1 are negative when occupied). Furthermore, as $f_{10} = \exp(-0.37 \text{ eV/kT}) \exp[(\gamma/k)(0.37/2.0)]$

$= 1.6 \times 10^{-6}$ at 294 K,

and $\tau_{pm} \approx 3 \times 10^{-6}$, (section 9.11)

then $N_1 \approx 4 \times 10^{24}$ m^{-3}.

The S-shaped appearance of the rise curves of figure 9.14 has all the hall-marks of a non-linear trapping effect, discussed by Ryvkin[167] and Boer and Vogel[168]. In its simplest form, this can occur with a

single trap-level. During excitation, before recombination has become significant, the level 'fills' to such an extent, that the trapping time increases drastically. At this point, time t_f say, the free carrier density begins to climb again, with a slope equal to the pre-trapping slope.

A similar situation can arise when shallower traps are also present, slowing down the whole process. This type of analysis was applied to the situation of figure 9.15, but proved inadequate, for several reasons. Firstly, if the level at E_2 becomes nearly full, bimolecular conditions cease to exist and there should be a linear relationship between ΔI and F. This did not occur, and $\bar{f}_2$ was always less than unity. Also, the slope of region (c) would be the same as the slope of region (b) according to this analysis, and this is patently not so.

A possible explanation is that traps near E_F are filled in time t_f, as the total generated density ($\Delta G t_f$) in this time is roughly independent of temperature, and is $\sim 10^{21}$ m^{-3}, in rough agreement with the estimate of 9.11 . This argument implies a short hole capture time, however, which may not be compatible with the apparently small role played by those states in recombination. Perhaps the electron capture cross-section is very small. Radiative transitions to those states may account for the photoluminescence observed by Kolomiets[165], at 77 K, which peaks at ~ 0.88 eV.

9.13 LOW TEMPERATURE PHOTODECAY

The analysis of section 8.12 for the anomalously rapid photodecay at low temperatures in As_2Te_3, also applies to As_2Se_3. The simple theory of 3.3.2, predicts that τ_{cb} increases with 1/T with activation energy $\Delta E_\tau(b) \approx 0.37$ eV (or 0.33 eV when corrected), while the observed activation energy is ~ 0.08 eV.

The theory of 8.12, which involves decay of the excess population of the valence band plus traps at E_3 in time τ'_{cb} before traps at E_2 are significantly affected seems appropriate here, as the free recombination time τ_{pb} (see 9.12) is reduced, in bimolecular conditions, to the same order of magnitude as τ_{t2}. Thus the activation energy predicted by equation 8.12.4 is

$$\Delta E_\tau(b) = (E_3 - E_v) - \tfrac{1}{2}(E_2 - E_v)$$

$$\approx 0.11 \text{ eV}$$

in rough agreement with the measured value.

To verify whether this argument is correct, consider the times τ_{pb}, τ'_{cb} and τ_{cb} predicted at room temperature. The theory of 8.12 predicts

$$\tau_{cb}/\tau'_{cb} \approx (N_2/N_3) \exp[+(E_2 - E_3)/kT] \approx 20$$

$$\tau'_{cb}/\tau_{pb} \approx (N_3/N_v) \exp[+(E_3 - E_v)/kT] \approx 10^6$$

As $\tau_{pb} \approx 5 \times 10^{-10}$ s ($F = 10^{19}$ m^{-2} s^{-1}) at 294 K, the predicted values of τ_{cb} and τ'_{cb} are 10^{-2} s and 5×10^{-4} s respectively. Clearly, τ'_{cb} is the more

appropriate, as the measured value is $\sim 10^{-3}$ s, thus justifying the above arguments.

9.14 MODEL FOR As_2Se_3

Figure 9.20 shows in schematic form the band model and distribution of localised states identified in this work. Some of the estimated parameters are listed below.

Energy (eV)	Density (m^{-3})	Capture coefficient ($m^3\ s^{-1}$)
E_c 2.0	N_c	
E_1 1.29	N_1 4×10^{24}	$C_{p1} \approx 4 \times 10^{-13}$
E_F 0.92	$N_F \geq 10^{20}$	
E_2 0.66	N_2 1×10^{23}	$C_{p2} \approx 2 \times 10^{-14}$
E_3 0.44	N_3 1×10^{24}	$C_{p3} \approx 2 \times 10^{-14}$
E_v 0	N_v 1×10^{26}	

Free Mobility $\mu_{po} \approx 10^{-3}\ m^2\ V^{-1}\ s^{-1}$

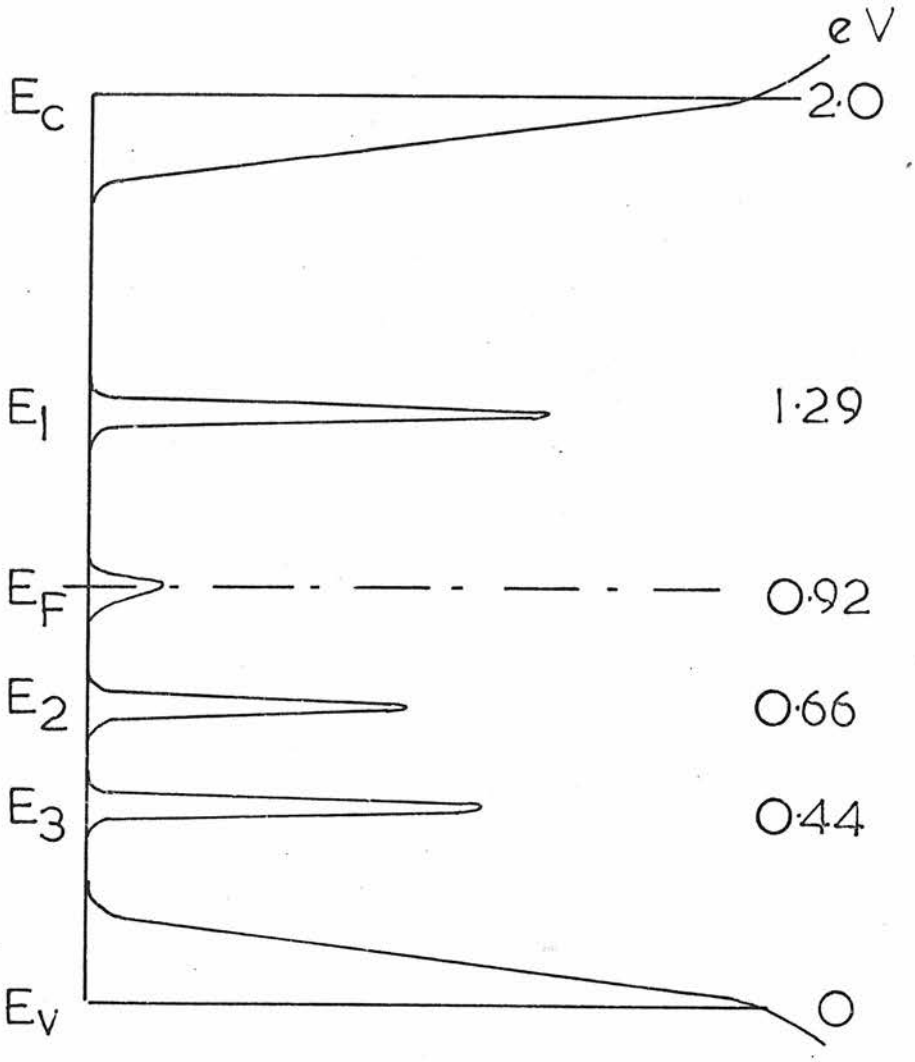

Fig 9.20 As_2Se_3 Schematic band diagram

APPENDIX

DIFFUSION EFFECTS

As promised in chapter 3, the effects of diffusion of excess carriers, in the x-direction, may be assessed, for various experimental situations which arose.

The starting point is the spatial distribution (x-direction) of excess carriers, arising from optical absorption in the sample, in the absence of diffusion effects. A crude method of assessment is to compare the rate of loss of carriers from a region of the sample at the surface by diffusion into the bulk, with the generation rate in this region - i.e. compare the terms in the continuity equation 3.21. If the diffusion terms are significant, the distribution is altered, and the original solutions for excess carrier density, may be incorrect. In the 'worst-case' situation, only hole diffusion is considered, and internal fields are neglected.

In the small signal, monomolecular recombination regime, such considerations are not important for homogeneous samples. A redistribution of excess carriers does not affect the total excess densities as the lifetime is independent of position and excitation. In the bimolecular regime, however, the carrier lifetime depends upon the excess density, and hence upon position in the sample.

At the photon energy used for most of the quantitative measurements in As_2Se_3 - i.e. 1.89 eV, the absorption constant α, is low, $\sim 5 \times 10^5$ m^{-1}, and excitation is fairly homogeneous. This leaves the case of As_2Te_3, in the bimolecular regime, with GaAs excitation at 1.37 eV ($\alpha \sim 10^7$ m^{-1}).

The comparison to be made is between the terms

$$D_p \frac{\partial^2 p}{\partial x^2}\Big)_{x=o} \quad \text{and} \quad \Delta G\Big)_{x=o}$$

$$\text{Now} \qquad \Delta G\Big)_{x=o} = \eta \alpha F(1 - R_1) \qquad \text{A.1.}$$

$$\text{and} \qquad \Delta p(x) = \Delta p(0) \exp(-\alpha x/2) \qquad \text{A.2.}$$

The value of $\Delta p(0)$ can be obtained from the photocurrent ΔI

$$\Delta I = \Delta p(0)\, 2/\alpha\, we\, \hat{\mathcal{E}}\, \mu_{po} \qquad \text{A.3.}$$

$$\therefore D_p \frac{\partial^2 p}{\partial x^2}\Big)_{x=o} = \frac{\Delta I\, \alpha^3\, kT}{8\mathcal{E} we\, e} \qquad \text{A.4.}$$

assuming the Einstein relation between D_p and μ_{po}. Notice that μ_{po} does not appear in equation A.4. Comparing A.1. and A.4., for the data of figure 8.10 at 166 K, ($F = 9 \times 10^{19}$ m^{-2} s^{-1}), gives

$$\left(\Delta G/D_p \frac{\partial^2 \Delta p}{\partial x^2}\right)_{x=o} = \frac{\eta F(1 - R_1)\, 8\, w\, \mathcal{E} e^2}{\Delta I\, \alpha^2\, kT} \approx 10^2 \qquad \text{A.5.}$$

so diffusion effects are small.

The calculation carried out above, ignored trapped carriers, but is correct if the Quasi-thermal equilibrium condition holds. In this situation, trap-limited

mobilities may be substituted for μ_{po} and again cancel out. This argument, applied to the worst case of diffusion from the surface, also applies to successively deeper layers, in the sample, and thus to the whole sample.

As the ratio in A.5. is proportional to $F^{\frac{1}{2}}$, diffusion may become important at low excitations. However, this was a worst case analysis, and probably overestimated the effect by several orders of magnitude.

REFERENCES

1. Lax, M. J. Phys. Chem. Solids, 8, 66, 1959.
2. Rose, A. Concepts in Photoconductivity and allied problems : Interscience Publishers, New York, 1963, Chapter 3.
3. Shockley, W., and Bardeen, J. Phys. Rev., 77, 407, 1950.
4. Conwell, E.M., and Weisskopf, V.F. Phys. Rev., 77, 338, 1950.
5. Smith, R.A. Semiconductors, Cambridge University Press, (1964), Chapter 5.
6. Rose, A. R.C.A. Review, 12, 362, 1951.
7. Mott, N.F., and Davis, E.A. Electronic Processes in Non-crystalline Materials, Oxford University Press, 1971, Chapter 7.
8. Fritzche, H. J. Non-cryst. Solids, 6, 49, 1971.
9. Vaipolin, A.A., and Porai-Koshits, E.A. Sov. Phys. - Solid State, 5, 186, 1963.
10. Ioffe, A.F., and Regel, A.R. Prog. in Semiconductors, 4, 239, 1960.
11. Lucovsky, G. et al. Solid State Comm., 5, 113, 1967.
12. Gubanov, A. Quantum Theory of Amorphous Semiconductors, New York, Consultants Bureau, 1965.
13. Cohen, M.H. J. Non-cryst. Solids, 4, 326, 1970.
14. Mott, N.F. Phil. Mag., 22, 1, 1970.
15. Anderson, P.W. Phys. Rev, 109, 1492, 1958.
16. Fitzpatrick, J.R., and Maghrabi, C. Phys. Chem. Glasses, 12, 105, 1971.

17. Davis, E.A., and Mott, N.F. Phil. Mag., 22, 903, 1970.

18. Marshall, J.M., and Owen, A.E. Phys. Stat. Sol.(a) 12, 181, 1972.

19. Mott, N.F. Phil. Mag.,

20. Marshall, J.M., and Owen, A.E. Phil. Mag, 24, 1281, 1971.

21. Vaipolin, A.A., and Porai-Koshits, E.A. Sov. Phys. - Solid State, 5, 178, 1963.

22. Vaipolin, A.A., and Porai-Koshits, E.A. Ibid 497, 1963.

23. Vaipolin, A.A. Sov. Phys. - Crystallography, 10, 509, 1966.

24. Andrievskii, A.I. et al. Sov. Phys. - Crystallography, 6, 534, 1962.

25. Carron, G.J. Acta. Cryst., 16, 338, 1963.

26. Zallen, R. et al. Phys. Rev., B3, 4257, 1971.

27. Mooser, E., and Pearson, W.B. Prog. in Semicond., 5, 104, 1960.

28. Kastner, M. Phys. Rev. Letts., 28, 355, 1972.

29. Tabak, M.D. Solid State Comm., 7, No.11, p.viii, (abstr.) 1969.

30. Marshall, J.M., and Owen, A.E. Phys. Stat. Sol.(a), 12, 181, 1972.

31. Economou, E.N. et al. Phys. Rev. Letts., 25, 520, 1970.

32. Mott, N.F. Phil. Mag., 19, 835, 1969.

33. Emin, D. et al. Phys. Rev. Letts., 28, 813, 1972.

34. Howard, W.E., and Tsu, R. Phys. Rev, B1, 4709, 1970.

35. Edmond, J.T. J. Non-cryst. Solids, 1, 39, 1968.

36. Stuke, J. J. Non-cryst. Solids, 4, 1, 1970.

37. Mott, N.F., and Davis, E.A. Electronic Processes in Non-Crystalline Solids, Oxford University Press, 1971, p.205.

38. Fagen, E.A., and Fritzsche, H. J. Non-cryst. Solids, 2, 170, 1970.

39. Owen, A.E. Contemp. Phys., 11, 227, 1970.

40. Edmond, J.T. Br. J. App. Phys., 17, 979, 1966.

41. Uphoff, H.L., and Healy, J.H. J. App. Phys., 32, 950, 1961.

42. Owen, A.E., and Robertson, J.M. J. Non-cryst. Solids, 2, 40, 1971.

43. Male, J.C. Brit. J. App. Phys., 18, 1543, 1967.

44. Roilos, M. J. Non-cryst. Solids, 6, 5, 1971.

45. Dresner, J. J. Phys. Chem. Solids., 28, 505, 1964.

46. Kolomiets, B.T., and Nazarova, T.F. Sov. Phys. - Solid State, 2, 369, 1960.

47. Friedman, L., and Holstein, T. Ann. Phys., 21, 494, 1963.

48. Klinger, M.I. Phys. Stat. Sol., 11, 499, 1965.

49. Emin, D., and Holstein, T. Ann. Phys., 53, 439, 1969.

50. Friedman, L. Proc. International Conference on Low Mobility Materials, Eliat, Israel, Taylor and Francis, London, 1971.

51. Schnakenberg, J. Phys. Stat. Sol., 28, K135, 1968.

52. Firsov, Y.A. Sov. Phys. - Solid State, 5, 1566, 1964.

53. Austin, I.G., and Mott, N.F. Adv. Phys., 18, 41, 1969.

54. Spear, W.E. J. Non-cryst. Solids, 1, 197, 1969.

55. Ivkin, E.V., and Kolomiets, B.T. J. Non-cryst. Solids, 3, 41, 1970.

56. Rockstad, H.K. Solid State Comms., 9, 2233, 1971.

57. Pollack, M. Phil. Mag., 23, 519, 1971.

58. Mott, N.F., and Davis, E.A. Electronic Processes in Non-Crystalline Materials, Oxford University Press, 1971, p.250.

59. Weiser, K., and Brodsky, M.H. Phys. Rev., B1, 791, 1970.

60. Tauc, J. Optical Properties of Solids. ed. Abeles, F., North-Holland, Amsterdam, 1972, Chapter 5.

61. Kolomiets, B.T. et al. J. Non-Cryst. Solids, 4, 289, 1970.

62. Kolomiets, B.T. Phys. Stat. Sol., 7, 359, and 713, 1964.

63. Kolomiets, B.T. et al. Proc. Int. Conf. Phys. Semicond., Exeter, 1962, p.259.

64. Hurst, C.H. Ph.D. Thesis, Cambridge, 1972.

65. de Witt, H.J., and Crevecoeur, C. Phys. Lett., 33A, 25, 1970.

66. Marshall, J.M., and Miller, G.R. Phil. Mag., 27, 1151, 1973.

67. Marshall, J.M. Private Communication.

68. Lampert, M.A., and Mark, P. Current Injection in Solids, Academic Press, New York, 1970.

69. Bagley, B.G. Solid State Comm., 8, 345, 1970.

70. Hill, R.M. Phil. Mag., 24, 1307, 1971.

71. Mott, N.F. Phil. Mag., 19, 835, 1969.

72. Frenkel, J. Phys. Rev., 54, 647, 1938.

73. Hartke, J.L. J. App. Phys., 39, 4871, 1968.

74. Ieda, M. et al. J. App. Phys., 42, 3737, 1971.

75. Poole, H.H. Phil. Mag., 32, 112, 1916.

76. Schottky, N., and Spenke, E. Wiss. Veroff. Siemens Werke, 18, 1, 1939.

77. Hindley, N.K. J. Non-cryst. Solids, 5, 17, 1970.

78. Optical Properties of Solids ed. Abeles, F. North-Holland, Amsterdam, 1972.

79. Smith, R.A. Semiconductors, Cambridge University Press, 1964, Chapter 7.

80. Tauc, J. Optical Properties of Solids, (ed. Abeles, F.) North-Holland, Amsterdam, 1970.

81. Kubo, R. Phys. Rev., 86, 929, 1952.

82. Lanyon, H.P.D. Phys. Rev., 130, 134, 1963.

83. Mott, N.F. and Davis, E.A. Electronic Processes in Non-Crystalline Materials. Oxford University Press, 1971, p.238.

84. Toyozawa, Y. Prog. Theor. Phys., 22, 455, 1959.

85. Dow, J.D. and Redfield, D. Phys. Rev., B1, 3358, 1970.

86. van Roosbroeck, W. Phys. Rev., 123, 474, 1961.

87. Tabak, M.D. and Warter, P.J. Phys. Rev., 173, 899, 1968.

88. Pai, D., and Ing, S.W. Phys. Rev., 173, 729, 1968.

89. Fagen, E.A., and Fritzsche, H. J. Non-cryst. Solids, 2, 180, 1970.

90. Hartke, J.L., and Regensburger, P.J. Phys. Rev., 139, A970, 1965.

91. Felty, E.J., and Myers, M.B. quoted by Davis, E.A. and Mott, N.F. in Phil. Mag. 22, 903, 1970.

92. Davis, E.A., and Shaw, R.F. J. Non-cryst. Solids, 2, 406, 1970.

93. Weimer, P.K., and Cope, A.D. R.C.A. Rev., 12, 314, 1951.

94. Gilleo, M.A. J. Chem. Phys., 19, 1291, 1951.

95. Keck, P.H. J. Opt. Soc. Am., 42, 221, 1952.

96. Fotland, R.A. J. Appl. Phys., 31, 1558, 1960.

97. Dresner, J. J. Chem. Phys., 35, 1628, 1961.

98. Knights, J. Ph.D. Thesis, Cambridge University, 1972, Chapter 6.

99. Arnoldussen, T.C. et al. J. Appl. Phys., 43, 1798, 1972.

100. Weiser, K. et al. Proc. Tenth Int. Conf. Phys. Semicond., Cambridge, Mass., U.S. Atomic Commission, Oak Ridge, Tennessee, 1970, p.667.

100a. Lucovsky, G. Ibid. p 797

101. Kolomiets, B.T., and Lyubin, V.M. Sov. Phys. Doklady, 4, 1345, 1960.

102. Kolomiets, B.T. et al. J. Non-cryst. Solids, 5, 389, 1970.

103. Kolomiets, B.T. et al. Ibid, 402.

104. Kolomiets, B.T. et al. Sov. Phys. - Solid State, 9, 19, 1967.

105. Rockstad, H.K. J. Non-cryst. Solids, 2, 192, 1970.

106. Simmons, J.G., and Taylor, G.W. Phys. Rev., B4, 502, 1971.

107. Taylor, G.W., and Simmons, J.G. J. Non-cryst. Solids, 8 - 10, 940, 1972.

108. Simmons, J.G., and Taylor, G.W. Ibid, 946.

109. Mott, N.F., and Davis, E.A. Electronic Processes in Non-Crystalline Materials, Oxford University Press, 1971, p.229.

110. Dobrego, V.P., and Ryvkin, S.M. Sov. Phys. - Solid State, 6, 928, 1964.

111. Rose, A. Concepts in Photoconductivity and Allied Problems. Interscience Publishers, New York, 1963, chapter 3.

112. van Roosbroeck, W., and Shockley, W. Phys. Rev., 94, 1558, 1954.

113. Stern, F. J. Non-cryst. Solids, 8 - 10, 954, 1970.

114. Shockley, W., and Read, W.T. Phys. Rev., 87, 835, 1952.

115. Blakemore, J.S. Semiconductor Statistics, Pergamon Press, 1962.

116. Fischer et al. Phys. Rev. Lett., 26, 1182, 1971.

117. Weiser, K. J. Non-cryst. Solids, 8 - 10, 922, 1970.

118. Stern, F. Phys. Rev., B3, 2636, 1971.

119. Weiser, K., and Brodsky, M.H. Phys. Rev., B1, 791, 1970.

120. Mott, N.F., and Davis, E.A. Electronic Processes in Non-Crystalline Materials, Oxford University Press, 1971, chapter 7.

121. Garbuny, M. et al. Rev. Sc. Inst., 28, 826, 1957.

122. Mancebo, L. Rev. Sc. Inst., 35, 969, 1964.

123. Johnson, J.B. Phys. Rev., 32, 97, 1928.

124. van Vliet, K.M., and Fasset, J.R. Fluctuation Phenomena in Solids (ed. Burgess, R.E.) Academic Press, New York, 1965, chapter V11.

125. Wiener, N. Acta. Math., 55, 117, 1930.

126. Nyquist, H. Phys. Rev., 32, 110, 1928.

127. van Vliet, K.M., and Blok, J. Physica, 22, 231, 1956.

128. Rollin, B.V., and Templeton, I.M. Proc. Phys. Soc., London, B66, 259, 1953.

129. Hyde, F.J. Proc. Phys. Soc. London, B69, 242, 1956.

130. Bell, D.A. Electrical Noise, Van Nostrand, London, 1960.

131. Van der Ziel, A. Fluctuation Phenomena in Semiconductors. Butterworths, London, 1959, p.62.

132. Montgomery, H.C. Bell. Syst. Tech. J., 31, 950, 1952.

133. Maple, et al. J. Appl. Phys., 26, 490, 1955.

134. Van der Ziel, A. Fluctuation Phenomena in Semiconductors, Butterworths, London, 1959, p.56.

135. Brophy, J.J. Phys. Rev., 122, 26, 1961.

136. McWhorter, A.L. Lincoln Lab. Report No. 80, 1955.

137. Petritz, R.L. in semiconductor Surface Physics, University of Pennsylvania Press, 1957.

138. Bess, L. Phys. Rev., 91, 1569, 1953.

139. Hooge, F.N. Phys. Lett., 29A, 139, 1969.

140. Langevin, M.P. Compt. Rend., 146, 530, 1908.

141. Burgess, R.E. Physica, 20, 1007, 1954.

142. Van Vliet, K.M. Physica, 23, 248, 1957.

143. Kornfel'd, M.I., and Sochova, L.S. Sov. Phys. - Solid State, 1, 1960.

144. Kornfel'd, M.I., and Sochova, L.S. Sov. Phys. - Solid State, 1, 1960.

144a. Main, C., and Owen, A.E. Phys. Stat. Sol.(a), 1, 297, 1970.

144b. Baxandall, P.J. Wireless World, 74, 388, 1968.

145. Van der Ziel, A. Fluctuation Phenomena in Semiconductors, Butterworths, London, 1959, p.8.

146. Croitoru, N.L. et al. J. Non-cryst. Solids, 4, 493, 1970.

147. Mott, N.F., and Davis, E.A. Electronic Processes in Non-Crystalline Materials, Oxford University Press, 1971, p.361.

148. Shaw, R.F. et al. J. Non-cryst. Solids, 4, 29, 1970.

149. Zallen, R. et al. Phys. Rev. Lett., 26, 1564, 1971.

150. Owen, A.E. Contemp. Phys., 11, 257, 1970.

151. Vengel, T.N., and Kolomiets, B.T. Sov. Phys. - Tech. Phys., 2, 2314, 1957.

152. Owen, A.E. Glass. Ind., 48, 637, 1967.

153. Mott, N.F., and Davis, E.A. Electronic Processes in Non-Crystalline Materials, Oxford University Press, 1971, p.204.

154. Lakatos, A.I., and Abkowitz, M. Phys. Rev., B3, 1791, 1971.

155. Taylor, P.C. et al. Solid State Comm., 8, 1783, 1970.

156. Crevecoeur, C., and de Witt, H.J. Solid State Comm., 9, 445, 1971.

157. Felty, E.J. et al. Solid State Comm., 5, 555, 1967.

158. Mazets, T.F. Ph.D. Thesis, Leningrad University, 1969, quoted by Adler, D., in Amorphous Semiconductors, Butterworths, London, 1972.

159. Kolomiets, B.T., and Lyubin, Sov. Phys. - Solid State, 4, 291, 1962.

160. Scharfe, M.E. Phys. Rev., B2, 5025, 1970.

161. Kolomiets, B.T., and Lebedev, E.A. Sov. Phys. - Semiconductors, 1, 244, 1967.

162. Kolomiets, B.T. Proc. Ninth. Int. Conf. Phys. Semicond. Moscow, Nauka, Leningrad, 1968, p.1259.

163. Kolomiets, B.T., and Mazets, T.F. J. Non-cryst. Solids, 3, 46, 1970.

164. Street, R.A., and Yoffe, A.D. Thin Solid Films, 11, 161, 1972.

165. Kolomiets, B.T. et al. J. Non-cryst. Solids, 4, 289, 1970.

166. Bishop, S.G., and Guenzer, C.S. Phys. Rev. Lett., 30, 1309, 1973.

167. Ryvkin, S.M. Photoelectric effects in Semiconductors, Consultants Bureau, New York, 1964, p.149.

168. Boer, K.W., and Vogel, H. Ann. Physik, 17, 10, 1955.